Bursts of beta oscillations across the brain as a neurophysiological correlate of contextual novelty

Submitted by Callum Walsh to the University of Exeter

As a thesis for the degree of

Doctor of Philosophy in Medical Studies

In September 2021

I certify that all material in this thesis which is not my own work has been identified and that no material has previously been submitted and approved for the award of a degree by this or any other University.

Signature: ……...

Abstract

The retrosplenial cortex and hippocampus are brain regions which have been shown to be highly involved in contextual memory. In order to discover neurophysiological correlates of contextual memory in these regions, we used *in vivo* electrophysiology in awake, behaving mice while they explored a series of novel and familiar environments. Additionally, in order to better understand the specific neurophysiological effects of Alzheimer's disease-associated amyloid pathology on the retrosplenial cortex and hippocampus, we compared network activity between wild-type mice and J20 mice, a transgenic mouse model which develops widespread age-related amyloid pathology and memory impairments. We detected transient bursts of beta oscillations in both the retrosplenial cortex and hippocampus that were synchronous between these regions and upregulated during contextual novelty. Moreover, spiking of neurons in the retrosplenial cortex was significantly increased during beta bursts. In J20 mice, we noted numerous examples of altered network activity, including aberrant beta bursting which is not coupled to neuronal spiking. Through the use of EEG recordings in mice, we demonstrated that beta bursts can be detected across the cortex, and are highly synchronous between different brain regions. Finally, we demonstrated that it is possible to pharmacologically induce beta bursting in the retrosplenial cortex *in vitro* through the use of carbachol, a muscarinic acetylcholine receptor agonist, providing an assay for better understanding the mechanisms underlying beta bursting. These findings suggest that transient beta bursting across the brain provides brief windows of effective communication between brain regions, which may underlie the formation of cortical representation of contexts, and may be impaired in Alzheimer's disease.

Acknowledgments

I would first like to thank my supervisors, Dr Jonathan Brown and Professor Andrew Randall, who provided so much support over the course of my PhD, but always allowed me enough room to develop myself as an independent scientist. I will be forever grateful that I had the opportunity to work on such a fascinating topic, and that I had supervisors who granted me the freedom to explore all of the wonderful little avenues which appeared throughout my research.

I would also like to thank everybody in the Brown Lab, in particular Dr Thomas Ridler and Dr Maria Garcia Garrido, who were always happy to help teach me or answer all of my questions, as incessant as they may have sometimes been. Having such fantastic scientists to look up to has been a constant source of inspiration for me.

Many thanks to my parents, who have always supported me and pushed me to go as far as I can. I never in my wildest dreams thought I could have done this, but it was your encouragement led me on this path in the first place.

Finally, I would thank Martha, who has given me an endless amount of support throughout the entirety of my PhD, and who has kept be going through the up's and down's. Taking this journey has been made infinitely easier with you by my side.

Table of Contents

Abstract 3

Acknowledgments 5

Figures 14

Abbreviations 18

1 Introduction 20

1.1 Retrosplenial Cortex 20

1.1.1 Anatomy 20

1.1.2 Connectivity 20

1.1.3 Role in Contextual Memory 23

1.2 Hippocampus 24

1.2.1 Anatomy 24

1.2.2 Connectivity 25

1.2.3 Role in Contextual Memory 28

1.3 Neuronal Oscillations 29

1.3.1 Oscillatory frequency bands 30

1.3.2 Theta Oscillations 31

1.3.3 Gamma Oscillations 32

1.3.4 Beta Oscillations 32

1.3.5 Phase-amplitude coupling 33

1.3.6 Neuronal spiking recordings 36

1.4 Alzheimer's Disease 37

1.4.1 Dementia 37

1.4.2 Pathological hallmarks of Alzheimer's disease 38

1.4.3 Amyloid Pathology and the Amyloid Cascade Hypothesis 40

1.4.4 Tau Pathology 43

1.4.5 Treatment of Alzheimer's Disease 44
1.4.6 Mouse models of Dementia 45
1.5 Aims 49
2 General Methods 51
2.1 Animals 51
2.2 In Vivo Data Collection 51
2.3 Data Analysis 53
2.4 Power Spectral Analysis 54
2.5 Beta Burst Detection 55
2.6 Beta Burst Characteristics 56
2.7 Phase-Amplitude Coupling 60
2.8 Multi-Unit Activity 63
2.9 Coherence Analysis 64
2.10 Granger Causality Analysis 65
2.11 Beta Burst Cross-Correlation 66
2.12 Histology 67
2.13 Statistics 67
3 Chapter 3 69
3.1 Authors Note 69
3.2 Introduction 69
3.3 Methods 71
3.3.1 Animals 71
3.3.2 Surgery 72
3.3.3 Behaviour 72
3.3.4 Data Analysis 73
3.3.5 Histology 76

3.4 Results 78
3.4.1 Behaviour 78
3.4.2 Dysgranular Spectral Analysis 82
3.4.3 Dysgranular Beta Bursting Activity 89
3.4.4 Dysgranular Beta Burst Characteristics 96
3.4.5 Dysgranular Phase-amplitude Coupling 100
3.4.6 Dysgranular Spiking Activity 104
3.4.7 Granular Spectral Analysis 107
3.4.8 Granular Beta Bursting Activity 111
3.4.9 Granular Beta Burst Characteristics 114
3.4.10 Granular Phase-amplitude Coupling 117
3.4.11 Granular Spiking Activity 120
3.5 Discussion 122
3.5.1 Summary 122
3.5.2 Power Spectral Analysis 122
3.5.3 Beta Bursting Activity 124
3.5.4 Beta Bursting Characteristics 126
3.5.5 Phase-Amplitude Coupling 127
3.5.6 Neuronal spiking during Beta Bursts 129
3.5.7 Neurophysiological changes in J20 mice 131
3.5.8 Conclusions 133
4 Chapter 4 134
4.1 Introduction 134
4.2 Methods 136
4.2.1 Author's Note 136
4.2.2 Animals 136

4.2.3 Surgery 137
4.2.4 Data Analysis 137
4.3 Results 138
4.3.1 Hippocampal Spectral Analysis 138
4.3.2 Hippocampal Beta Bursting Activity 143
4.3.3 Hippocampal Beta Burst Characteristics 146
4.3.4 Hippocampal Phase-amplitude Coupling 149
4.3.5 Hippocampal Spiking Activity 152
4.3.6 Intra-Retrosplenial Coherence 154
4.3.7 Hippocampal-Retrosplenial Coherence 159
4.3.8 Intra-Retrosplenial Granger Causality 163
4.3.9 Hippocampal-Retrosplenial Granger Causality 168
4.3.10 Burst Cross-Correlation 172
4.4 Discussion 176
4.4.1 Summary 176
4.4.2 Power Spectral Analysis 176
4.4.3 Beta Bursting Activity 178
4.4.4 Beta Bursting Characteristics 180
4.4.5 Phase-Amplitude Coupling 181
4.4.6 Neuronal spiking during Beta Bursts 182
4.4.7 Intra-retrosplenial Coherence 183
4.4.8 Hippocampal-Retrosplenial Coherence 185
4.4.9 Intra-retrosplenial Granger Causality 187
4.4.10 Hippocampal-Retrosplenial Granger Causality 188
4.4.11 Burst Cross Correlation 190
4.4.12 Conclusions 191

5 Chapter 5 192
5.1 Introduction 192
5.2 Methods 193
5.2.1 Animals 193
5.2.2 Surgery 194
5.2.3 Behaviour 195
5.2.4 Data Analysis 195
5.3 Results 198
5.3.1 Cortical Spectral Analysis 200
5.3.2 Cortical Beta Bursting Activity 205
5.3.3 Cortical Beta Burst Characteristics 209
5.3.4 Burst Cross-Correlation 214
5.4 Discussion 217
5.4.1 Summary 217
5.4.2 Power Spectral Analysis 217
5.4.3 Beta Bursting Activity 219
5.4.4 Beta Bursting Characteristics 220
5.4.5 Burst Cross Correlation 221
5.4.6 Experimental Design 223
5.4.7 Conclusions 223
6 Chapter 6 225
6.1 Introduction 225
6.2 Methods 227
6.2.1 Slice Preparation 227
6.2.2 Data Collection 227
6.2.3 Experimental Protocol 228

6.2.4 Solutions 228
6.3 Results 230
6.3.1 Retrosplenial Spectral Activity *In Vitro* 231
6.3.2 Retrosplenial Beta Bursting Activity *In Vitro* 235
6.3.3 Retrosplenial Beta Burst Characteristics *In Vitro* 239
6.4 Discussion 246
6.4.1 Summary 246
6.4.2 Power Spectral Analysis 246
6.4.3 Beta Bursting Activity 248
6.4.4 Beta Bursting Characteristics 250
6.4.5 Conclusions 252
7 General Discussion 253
7.1 Key Findings 253
7.2 Beta Bursting across the Brain 253
7.3 Additional Functional Correlates of contextual novelty 256
7.4 Aberrant beta bursting in J20 mice 259
7.5 Altered network activity in J20 mice 262
7.6 Potential mechanisms underlying beta bursting 263
7.7 Animal models of Alzheimer's disease 264
7.8 Implications for Future Study 266
7.9 Future Directions 269
7.10 Final Conclusions 272
8 References 273
9 Appendix 1 304
9.1 Power Spectral Analysis - SpectraWYW (While-You-Work) 304
9.2 Beta Burst Detection - BurstDetectionWYW (While-You-Work) 308

9.3 Phase Amplitude Coupling Analysis (Tort Method) - PhaseAmplitudeCouplingTort 319
9.4 Multi-Unit Activity Analysis - SimpleMUADuringBursts 324
9.5 Beta Burst Cross-Correlation Analysis - BurstXCorr 329
9.6 Coherence Analysis - CoherenceWYW (While-You-Work) 334
9.7 Granger Causality Analysis - GrangerGram 338
10 Appendix 2 343

Figures

Figure 1.1 Anatomy and connectivity of the retrosplenial cortex. 22

Figure 1.2 Anatomy and connectivity of the hippocampal formation 27

Figure 1.3 Phase-amplitude cross-frequency coupling..... 35

Figure 1.4 Spatiotemporal progression of amyloid and tau pathology in Alzheimer's disease. 39

Figure 1.5 Schematic of the original amyloid cascade hypothesis 42

Figure 1.6 Amyloid pathology in the J20 model of Alzheimer's Disease 48

Figure 2.1 Photograph of the entire recording and behaviour setup..... 52

Figure 3.1 Experimental Design 75

Figure 3.2 Amylo-glo staining of J20 mouse brains reveals amyloid plaques .. 77

Figure 3.3 Beta (20-30 Hz) power is significantly higher during novelty in the dysgranular retrosplenial cortex in wild-type and J20 mice. 85

Figure 3.4 Retrosplenial local field potentials are marked by short, phasic increases in beta power, referred to as beta bursts..... 87

Figure 3.5 Beta bursting activity in the dysgranular retrosplenial cortex (RSCdg) is significantly higher during novelty. 93

Figure 3.6 Novelty-associated beta bursting in the dysgranular retrosplenial cortex (RSCdg) can be detected with a lower amplitude threshold. 94

Figure 3.7 Novelty-associated beta bursting in the dysgranular retrosplenial cortex (RSCdg) can be detected with a lower duration threshold. 95

Figure 3.9 Beta burst characteristics in the dysgranular retrosplenial cortex (RSCdg). 99

Figure 3.10 Theta-alpha/beta phase-amplitude coupling is increased in the dysgranular retrosplenial cortex (RSCdg) during novelty. 102

Figure 3.11 Phase-amplitude coupling during the final minute of each session in the dysgranular retrosplenial cortex. 103

Figure 3.12 Spiking activity in RSCdg is coupled to beta bursting in wild-type mice, but disrupted in J20 mice. 106

Figure 3.13 Beta (20-30 Hz) power is significantly higher during novelty in the granular retrosplenial cortex in wild-type and J20 mice. 109

Figure 3.14 Beta bursting activity in the granular retrosplenial cortex (RSCg) is significantly higher during novelty. 113

Figure 3.15 Beta burst characteristics in the dysgranular retrosplenial cortex (RSCdg). 116

Figure 3.16 Theta-alpha/beta phase-amplitude coupling is increased in the granular retrosplenial cortex (RSCg) during novelty. 118

Figure 3.17 Phase-amplitude coupling during the final minute of each session in the granular retrosplenial cortex. 119

Figure 3.18 Spiking activity in RSCg is coupled to beta bursting in wild-type and J20 mice. 121

Figure 4.1 Beta (20-30 Hz) power is marginally higher during novelty in the hippocampus. 141

Figure 4.2 Beta bursting activity in the hippocampus. 145

Figure 4.3 Beta burst characteristics in the hippocampus. 148

Figure 4.4 Theta-gamma phase-amplitude coupling is increased in the hippocampus during novelty. 150

Figure 4.5 Phase-amplitude coupling during the final minute of each session in the granular retrosplenial cortex. 151

Figure 4.6 The overall firing rate of hippocampal neurons in J20 mice is increased. 153

Figure 4.7 Intra-retrosplenial coherence varies depending on novelty. 157

Figure 4.8 Hippocampal-retrosplenial coherence is generally unaffected by novelty. 161

Figure 4.9 Granger Causality is higher from the RSCg to the RSCdg. 166

Figure 4.10 Granger causality from the RSCg to the hippocampus is increased during familiar sessions. 170

Figure 4.11 Beta bursts in the RSC and hippocampus are highly correlated and synchronous. 175

Figure 5.1 Experimental Design. 197

Figure 5.2 Various spectral changes are observed across the cortex in J20 mice. 202

Figure 5.3 Heat maps illustrating the mean power in each frequency band across the entire cortical surface, during the first minute (Novel) and last 10 minutes (Familiar) of the session, in both genotypes. 203

Figure 5.4 Beta bursting activity across the cortex. 207

Figure 5.5 Beta burst distribution and rate across the cortex. 208

Figure 5.6 Beta burst magnitude and duration across the cortex. 212

Figure 5.7 Beta burst frequency profile and rhythmicity across the cortex. 213

Figure 5.8 Beta bursts are highly correlated and synchronous across the cortex. 216

Figure 6.1 Experimental Design. 229

Figure 6.2 Carbachol induced a broadband increase in spectral power that peaked around 7 Hz. 234

Figure 6.3 Carbachol induces transient epochs of high beta power and beta rhythmicity in the retrosplenial cortex in vitro, that are reminiscent of beta bursts. 235

Figure 6.4 Beta burst distribution and rate in the deep layers of the retrosplenial cortex in vitro. 237

Figure 6.5 Beta burst distribution and rate in the shallow layers of the retrosplenial cortex in vitro. 238

Figure 6.6 Beta burst number, magnitude and duration in the deep layers of the retrosplenial cortex in vitro..... 240

Figure 6.7 Beta burst number, magnitude and duration in the shallow layers of the retrosplenial cortex in vitro..... 241

Figure 6.8 Beta burst frequency profile and rhythmicity in the deep layers of the retrosplenial cortex in vitro..... 244

Figure 6.9 Beta burst frequency profile and rhythmicity in the shallow layers of the retrosplenial cortex in vitro..... 245

Tables

Table 1 Dysgranular spectral analysis - Summary of significant results 86

Table 2 Dysgranular spectral analysis - Summary of significant results 110

Table 3 Hippocampal spectral analysis - Summary of significant results 142

Table 4 Intra-Retrosplenial Coherence - Summary of significant results 158

Table 5 Hippocampal-Retrosplenial Coherence - Summary of significant results 162

Table 6 Intra-Retrosplenial Granger Causality - Summary of significant results 167

Table 7 Hippocampal-Retrosplenial Granger Causality - Summary of significant results 171

Abbreviations

Aβ	Amyloid β
aCSF	Artificial Cerebrospinal Fluid
AMPA	α-amino-3-hydroxy-5-methyl-4-isoxazolepropionic acid
AP	Anteroposterior
APP	Amyloid Precursor Protein
APV	(2R)-amino-5-phosphonovaleric acid
CNQX	Cyanquixaline
dB	Decibels
DV	Dorsoventral
EEG	Electroencephalography
EPSP	Excitatory Postsynaptic Potential
FDG-PET	Fluorodeoxyglucose-Positron Emission Tomography
GABA	γ-aminobutyric acid

HC	Hippocampus
IIR	Infinite Impulse Response
IPSP	Inhibitory Postsynaptic Potential
LED	Light Emitting Diode
LFP	Local Field Potential
MEG	Magnetoencephalography
MI	Modulation Index
ML	Mediolateral
MRI	Magnetic Resonance Imaging
NMDA	N-methyl-D-aspartate
PAC	Phase-Amplitude Coupling
PBS	Phosphate Buffered Saline
PFA	Paraformaldehyde
RSC	Retrosplenial Cortex
RSCdg	Dysgranular Retrosplenial Cortex
RSCg	Granular Retrosplenial Cortex
SEM	Standard Error of the Mean
WT	Wild-type

1 Introduction

1.1 Retrosplenial Cortex

1.1.1 Anatomy

The retrosplenial cortex is made up of Brodmann areas 29 and 30 in humans (Brodmann, 1909), and named as such because it is found posterior to the thickest and most caudal part of the corpus callosum, known as the splenium (Morris et al., 2000). The anatomy of the retrosplenial cortex varies slightly between humans and rodents (Figure 1.1). In humans, the retrosplenial cortex is located deep within the brain, and forms part of the posterior cingulate cortex (Brodmann, 1909). In rodents, the retrosplenial cortex is far larger in comparison to the size of the brain, and found on the cortical surface, and due to the absence of Brodmann areas 23 and 31, makes up the entirety of the posterior cingulate cortex (Vogt et al., 2004). Brodmann areas 29 and 30 are also commonly referred to as the granular and dysgranular retrosplenial cortex, with dysgranular referring to the poorly defined layer IV (Vogt, 1976). In rodents, the dysgranular retrosplenial cortex is found on the ventral surface of the cortex, while the granular retrosplenial cortex is folded deep within the longitudinal fissure, directly above the corpus callosum.

1.1.2 Connectivity

In both primates and rodents, the retrosplenial cortex is reciprocally connected to specific thalamic nuclei and the subicular regions of the hippocampal formation (Figure 1.1, Groen and Wyss, 1990; van Groen and Wyss, 1992; Kobayashi and Amaral, 2003, 2007; Van Groen and Wyss, 2003). The retrosplenial cortex has a high degree of cortico-cortical connectivity, with reciprocal connections between

the entire retrosplenial cortex and the prefrontal and anterior cingulate cortices, and more specific connections between the dysgranular retrosplenial cortex and the visual and motor cortices (Vogt and Miller, 1983; Morris et al., 1999). In addition to the connections with the thalamic nuclei, the retrosplenial cortex receives inputs from other subcortical nuclei such as the diagonal band of Broca (Bigl et al., 1982). Many of these subcortical and cortico-cortical connections form part of the cingulum bundle, a white matter tract that runs adjacent to the cingulate cortex and projects extensively to the retrosplenial cortex (Mufson and Pandya, 1984; Bubb et al., 2018). The anatomical connectivity of the retrosplenial cortex places it as an anatomical interface between the cortex, thalamic nuclei and hippocampus, and as such the retrosplenial cortex is thought to be highly involved in numerous hippocampal functions (Vann et al., 2009).

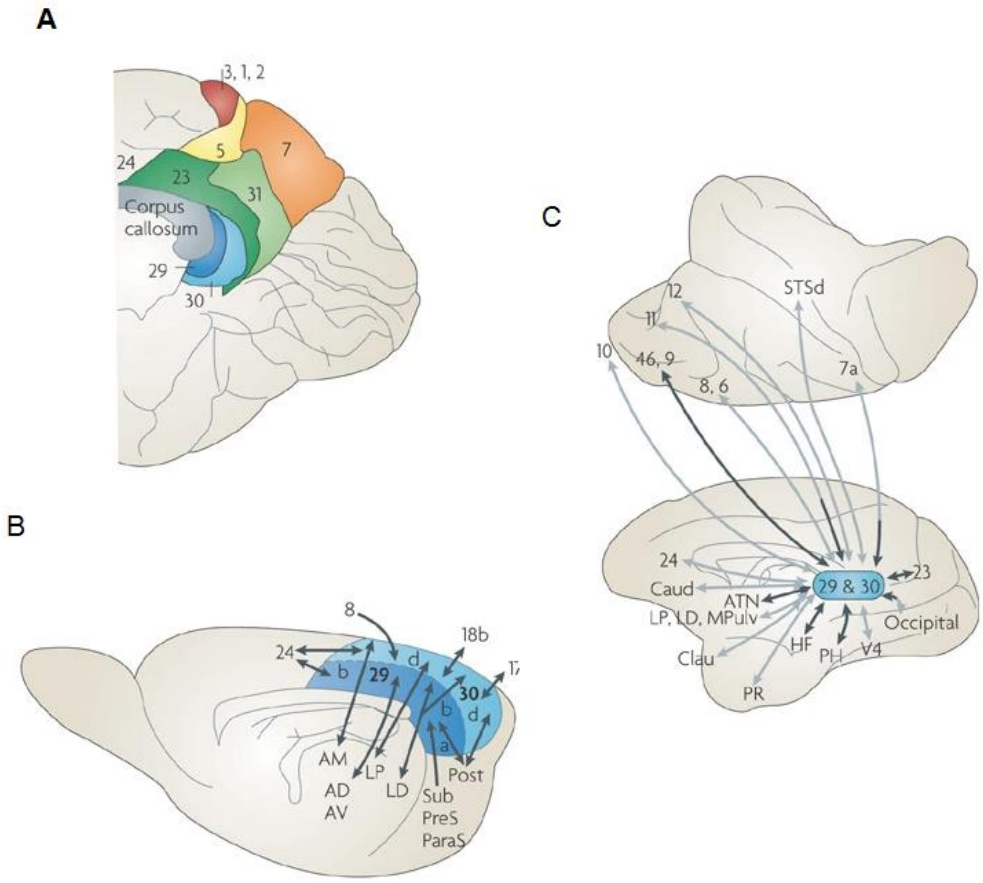

Figure 1.1 Anatomy and connectivity of the retrosplenial cortex.
A. The retrosplenial cortex is made up of Brodmann areas 29 and 30, and is located posterior to the thickest part of the corpus callosum. In humans, the retrosplenial cortex is located deep within the brain, and along with Brodmann areas 23 and 31 makes up the posterior cingulate cortex. B. In rodents, the retrosplenial cortex is found on the dorsal surface of the cortex, and due to the absence of Brodmann areas 23 and 31 in rodents, makes up the entire posterior cingulate cortex. C. Some notable connections of the retrosplenial cortex include visual cortex, numerous thalamic nuclei as well as the subicular complex of the hippocampal formation. AD, anterodorsal thalamic nucleus; AM, anteromedial thalamic nucleus; AV, anteroventral thalamic nucleus; Caud, caudate nucleus; Clau, claustrum; HF, hippocampal formation; LD, laterodorsal thalamic nucleus; LP, lateroposterior thalamic nucleus; MPulv, medial pulvinar; ParaS, parasubiculum; PH, parahippocampal cortex; Post, postsubiculum; PR, perirhinal cortex; PreS, presubiculum; STSd, dorsal superior temporal sulcus; Sub, subiculum; V4, visual area 4. Image modified from (Vann et al., 2009)

1.1.3 Role in Contextual Memory

A large body of evidence exists that indicates the importance of the retrosplenial cortex in contextual memory and spatial navigation. Inhibition of protein synthesis in the retrosplenial cortex before contextual fear acquisition results in contextual memory impairment (Kwapis et al., 2015) and while temporary inactivation of the retrosplenial cortex with the AMPA receptor antagonist CNQX impaired performance in the Morris Water Maze, a spatial memory task (Czajkowski et al., 2014). Numerous lesion studies have been performed to attempt to investigate the specific role of the retrosplenial cortex in memory. Excitotoxic lesions in the retrosplenial cortex after a spatial memory test resulted in the loss of these memories, and subsequently learned spatial memories were poorly retained (Haijima and Ichitani, 2008). In a contextual fear conditioning experiment, rats with lesions in the retrosplenial cortex had reduced fear responses to the context but not the auditory tone (Keene and Bucci, 2008). Lesions of the entire retrosplenial cortex impaired object-in-place memory, but spared recognition of the object itself (Vann and Aggleton, 2002). Due to the importance of both the hippocampus and cortex in learning and memory, it has been hypothesised that memories are rapidly stored in the hippocampus and slowly transferred to the cortex for long term storage (Marr, 1971), or concurrently stored in both regions (O'Reilly and Rudy, 2001). Considering that the retrosplenial cortex is highly involved in contextual memory process, it is thought that this may be a site where this contextual memory information is stored. Optogenetic stimulation of retrosplenial cortex neurons is able to retrieve (Cowansage et al., 2014) and consolidate contextual memories (De Sousa et al., 2019). Functional magnetic resonance imaging in humans revealed that the retrosplenial cortex was active

during both the formation and retrieval of contextual information (Iaria et al., 2007). Finally, the retrosplenial cortex is highly affected during the earliest stages of Alzheimer's disease, and is affected by both regional hypometabolism and atrophy (Minoshima et al., 1997; Choo et al., 2010), resulting in spatial memory deficits that are thought to be specific to the retrosplenial cortex (Laczó et al., 2009; Vann et al., 2009; Morganti et al., 2013). It is hoped that future work into the role of the retrosplenial cortex in contextual memory will elucidate how contextual memory is encoded in this region, and how the retrosplenial cortex interacts with the hippocampus and other cortical areas to create contextual representations.

1.2 Hippocampus

1.2.1 Anatomy

The hippocampal formation is a group of brain structures found in the medial temporal lobe which includes the entorhinal cortex, subicular complex and hippocampus proper (Schultz and Engelhardt, 2014). The different structures that make up the hippocampal formation are contiguous and highly folded, with relatively unidirectional intrinsic connectivity through the whole structure (Per et al., 2009). Despite some differences, much of the structure and neuroanatomy of the hippocampal formation is highly conserved within mammals. The hippocampus proper is split into 3 major numbered subregions: CA1, CA2 and CA3, with CA referring to 'cornu ammonis' after the curved horn of the Egyptian god ammon (Lorente de Nó, 1934), however there is considerable disagreement about the CA2 as an independent region (Dudek et al., 2016). The hippocampus contains a wide variety of different cell types and has a highly laminar structure, with a single densely packed layer of pyramidal cell bodies (Per et al., 2009). Due

to the laminar structure of the pyramidal cell layer, the dendritic arbors are aligned, with the basal dendrites located in the stratum oriens, and the apical dendrites extending into stratum radiatum and stratum lacunosum-moleculare. A wide variety of interneurons are found within all layers of the hippocampus and have a variety of morphologies and functions (Klausberger and Somogyi, 2008).

1.2.2 Connectivity

The intrinsic connectivity within the hippocampal formation is thought to be relatively unidirectional, with the main pathways within the formation often referred to as the “trisynaptic circuit” (Andersen et al., 1971). First, the entorhinal cortex projects to the dentate gyrus via the perforant path, forming a key cortical input to the hippocampus (Witter and Amaral, 1991). Next, the granule cells of the dentate gyrus project to the CA3 region, known as the mossy fibre pathway (Schultz and Engelhardt, 2014). The final part of this circuit is the Schaffer collateral pathway from the CA3 which projects to the CA1 and terminates in stratum oriens and stratum radiatum (Ishizuka et al., 1990). These three pathways form the major pathways within the hippocampus, but there are numerous additional pathways of note within the hippocampal formation and between the hippocampal formation and the rest of the brain. The CA1 projects to the subiculum, which subsequently projects to numerous brain regions, including a variety of subcortical structures and perirhinal and retrosplenial cortices, making it a major output hub in the hippocampus (Witter and Groenewegen, 1990). In fact, projections from the subiculum to the retrosplenial cortex are dense compared to sparse projections to the nearby anterior cingulate cortex (Wyss and Van Groen, 1992). Subiculum projections to the entorhinal

cortex essentially closes the loop which returns to the start of the trisynaptic circuit.

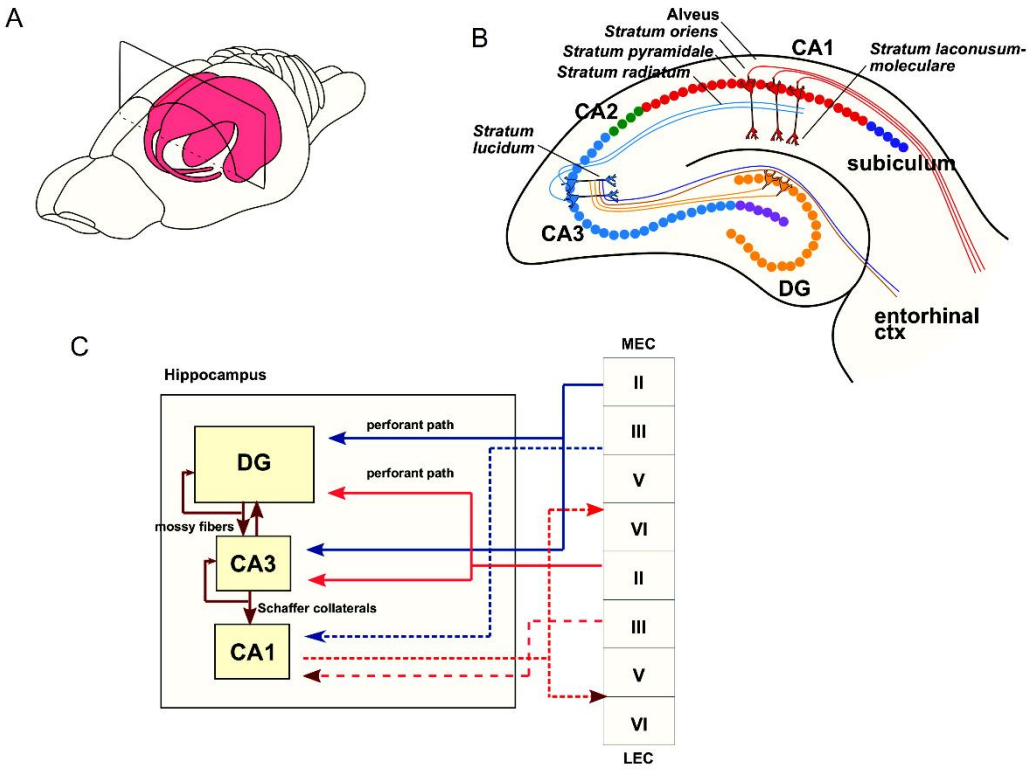

Figure 1.2 Anatomy and connectivity of the hippocampal formation
A. Rodent brain with the hippocampal formation highlighted in pink. The hippocampal formation is large in rodents compared to the rest of the brain, and curves in a C shape. B. Cross section of the hippocampus with the main regions, layers and pathways of the trisynaptic circuit. The first part of the trisynaptic circuit is the perforant path, made up of projections from the entorhinal cortex which perforate the hippocampal fissure and target the dentate gyrus (dark blue). The dentate gyrus projects to the CA3 region via the mossy fibre pathway (orange), which projects onwards to the CA1 region via the Schaffer collateral pathway (blue). Finally, projections from the CA1 to the entorhinal cortex complete the loop (red). C. Circuit diagram of the hippocampal trisynaptic circuit, showing additional connectivity and the specific layers of the entorhinal cortex where inputs and outputs are found.

1.2.3 Role in Contextual Memory

The hippocampus, along with the retrosplenial cortex, are both part of the Papez circuit, once thought to be a key brain network for emotion (Papez, 1937). More recently, some of the key functions of the hippocampus are thought to be spatial learning and navigation and contextual memory (for review, see Burgess et al., 2002), and there is thought to be a high degree of overlap of these processes in the hippocampus (Hirsh, 1974; Smith and Bulkin, 2014). As with the retrosplenial cortex, lesions of the hippocampus impair responses to contexts during contextual fear conditioning, but preserve responses to other stimuli such as auditory tones (Kim and Fanselow, 1992; Phillips and LeDoux, 1992). The hippocampal formation receives a great deal of highly processed multimodal sensory information via a range of cortical regions, and as such, hippocampal neurons have been shown to respond to visual (Save et al., 2000), auditory (Itskov et al., 2012), and somatosensory stimuli (Stackman et al., 2002). Hippocampal neurons have been shown to have spatially modulated firing, with changes in firing rate depending on place (O'Keefe and Dostrovsky, 1971), and a variety of other spatially modulated cells have been discovered elsewhere in the hippocampal formation such as head direction cells (Taube et al., 1990; Sargolini et al., 2006) and boundary cells (Solstad et al., 2008; Lever et al., 2009; Boccara et al., 2010). Finally, reactivation of hippocampal neuronal ensembles active during a contextual fear conditioning task was sufficient to elicit a fear response in the absence of that context, demonstrating that contextual information is represented by hippocampal ensembles (Garner et al., 2012; Liu et al., 2012; Ramirez et al., 2013). The hippocampus is highly affected by during the early stages of Alzheimer's disease, with amyloid plaque deposition (Thal et

al., 2002) and neurofibrillary tangle formation (Braak and Braak, 1995). Furthermore, volumetric magnetic resonance imaging (MRI) studies show that the hippocampus undergoes severe atrophy during Alzheimer's disease, as shown by (Jack et al., 1997, 1998). Finally, synapse loss occurs in the hippocampus early in Alzheimer's disease and is one of the best correlates of cognitive impairment (DeKosky and Scheff, 1990; Terry et al., 1991; DeKosky et al., 1996; Scheff et al., 2006).

1.3 Neuronal Oscillations

The activity of neurons within the brain generates electromagnetic fields within the extracellular space which can be measured in order to investigate the activity of neuronal networks (Buzsáki et al., 2012). This electrical activity can be measured from within the brain, known as the local field potential (LFP), or from outside the brain, known as an electroencephalogram (EEG). The movement of ions across cellular membranes creates current sources and sinks, and therefore one of the largest sources of electrical activity within the brain is from postsynaptic currents. The flow of positively charged ions such as Na+ ions through postsynaptic ion channels results in an excitatory postsynaptic potential (EPSP). Conversely, the flow of negatively charged ions such as Cl- ions through postsynaptic ion channels such as γ-aminobutyric acid (GABA) receptors results in an inhibitory postsynaptic potential (IPSP). Summation of numerous EPSPs or IPSPs in large populations of neurons can result in substantial electrical fields. Since the inception of EEG and the first human EEG recordings by Berger (1934), rhythmic oscillations have been demonstrated across the brain. These neural oscillations are thought to arise from the synchronous firing of large populations of neurons, and occur at a range of different frequencies all the way from 600

cycles per second to a single cycle every 40 seconds (Buzsáki and Draguhn, 2004). Neuronal oscillations are not merely a passive product of ongoing electrical activity, however. Neural oscillations can coordinate the activity of large groups of neurons through a process called phase-locking, where neuronal firing "locks" to a specific phase of an oscillatory cycle (Jensen, 2005).

1.3.1 Oscillatory frequency bands

Different oscillatory frequency ranges are often associated with different behavioural states or brain functions, and as such, neural oscillations are generally classified into one of a number of frequency bands. These frequency bands are highly variable between groups and as such there is little consistency with nomenclature, but some of these frequency bands are delta (1-5 Hz), theta (5-12 Hz), alpha (12-20 Hz), beta (20-30 Hz) and gamma (30-100 Hz). Oscillations also occur at a range of frequencies below 1 Hz and above 100 Hz, but oscillations in the frequency range 1-100 Hz are some of the most well studied. It is important to note that oscillations may vary dramatically between species; theta oscillations for example are found at a much lower frequency of around 1-4 Hz in humans, which explains some of the discontinuity in nomenclature and highlights the difficulty in directly translating findings in rodents to the human brain (Jacobs, 2014). Two of the most dominant oscillations in the rodent cortex and hippocampus during active wakefulness are theta and gamma oscillations, and both oscillations are strongly associated with memory processes (Vanderwolf, 1969; Buzsáki, 2002; Sirota et al., 2008; Lisman, 2010). Furthermore, while beta oscillations are far less established, a variety of studies have demonstrated the relevance of oscillations of this frequency band in both

health and disease (Sharott et al., 2005; McCarthy et al., 2011; Sherman et al., 2016; Tinkhauser et al., 2018).

1.3.2 Theta Oscillations

Theta oscillations are prominent throughout the hippocampus and in numerous cortical regions and are present during active wake and paradoxical sleep (Jouvet, 1969; Vanderwolf, 1969; Mitchell and Ranck, 1980; Leung and Borst, 1987). Theta-phase locking has been demonstrated in the hippocampus and cortex, with different neuronal subtypes firing at different phases of the theta cycle (Jensen, 2005; Klausberger and Somogyi, 2008). Furthermore, dynamic changes in the phase at which neurons fire, known as theta-phase precession, is thought to be one means by which information of encoded within the brain (O'Keefe and Recce, 1993; Jensen and Lisman, 2000; Hasselmo et al., 2002). Moreover, theta synchrony between the hippocampus and other brain regions, such as the prefrontal cortex, in combination with theta phase-locking of neurons may provide a means of communication and information flow between different brain regions (Siapas et al., 2005). It is thought that there is no single generator of theta oscillations within the brain. The cholinergic antagonist atropine only partially blocks theta oscillations in the hippocampus (Buzsáki et al., 1983), however in however this "atropine-resistant" theta is completely abolished by lesions of the entorhinal cortex (Vanderwolf and Leung, 1982). While this may suggest that the entorhinal cortex is the source of atropine-resistant theta oscillations in the hippocampus, it has been shown that atropine-resistant theta oscillations can emerge within the isolated hippocampus *in vitro*, indicating that theta oscillations can be generated independently in this region, and that different theta oscillators couple *in vivo* (Goutagny et al., 2009).

1.3.3 Gamma Oscillations

Gamma oscillations are also a common feature of hippocampal and cortical network activity, and are often found during periods of theta oscillations (Buzsáki et al., 1983; Chrobak and Buzsáki, 1998; Sirota et al., 2008). The gamma band is often subdivided into low gamma (30-50 Hz) and high gamma (60-120 Hz), and work by Colgin et al. (2009) has suggested that gamma oscillations in different frequency bands differentially mediate the flow of information within the hippocampal formation. High oscillatory synchrony in the slow gamma was demonstrated between the CA1 and CA3 regions of the hippocampus, while oscillatory synchrony between the CA1 and medial entorhinal cortex was greater in the high gamma range. Despite gamma oscillations being generally considered as local oscillations (Von Stein and Sarnthein, 2000; Montgomery and Buzsáki, 2007), gamma synchrony has been demonstrated between distant brain regions (Engel et al., 1991), and is thought to organise neuronal spiking into cell assemblies (Buzśaki and Wang, 2012). Network models of gamma oscillations have demonstrated the important of inhibitory interneurons to the formation of gamma oscillations (Whittington et al., 1995; Wang and Buzsáki, 1996), and gamma oscillations can be generated by interneuron-only networks (ING) or by networks of pyramidal cells and interneurons (PING) (Whittington et al., 2000).

1.3.4 Beta Oscillations

Beta oscillations are far less established, and are associated with a wide range of disparate behaviours, from motor control (Engel and Fries, 2010) to working memory (Lundqvist et al., 2016) and sensory processing (Leventhal et al., 2012). This diversity of behavioural correlates has precluded the development of an overarching hypothesis regarding the general role of beta oscillations within the

brain. Furthermore, beta oscillations are thought to be highly dependent on inhibitory interneurons (Faulkner et al., 1999; Traub et al., 1999), and as such are often conflated with gamma oscillations (Carr et al., 2012; Remondes and Wilson, 2015). Recent studies have suggested that beta oscillations can occur in discrete bursts, rather than continuous oscillations, and that the rate and timing of beta bursts has functional relevance across a range of behaviours (Leventhal et al., 2012; Lundqvist et al., 2016; Shin et al., 2017; Tinkhauser et al., 2018). Finally, beta bursting has gained a great deal of attention recently as pathological beta bursting is seen throughout the cortex and basal ganglia during Parkinson's disease, and is strongly associated with the severity of motor impairments in this disease (Brown et al., 2001; Brittain et al., 2014; Tinkhauser et al., 2018).

1.3.5 Phase-amplitude coupling

Neural oscillations in the brain do not exist in isolation, and a variety of forms of "cross-frequency coupling" have been described, where oscillations of one frequency interact with those of another frequency (Canolty et al., 2006; Onslow et al., 2011; Belluscio et al., 2012). One of the best studied forms of cross-frequency coupling is phase-amplitude coupling, where the amplitude of faster oscillation, such as gamma is coupled to the phase of a slow oscillation, such as theta. This "nesting" of gamma oscillations can be seen as a clear rhythmic change in gamma amplitude in time series data (Buzśaki and Wang, 2012). Theta-gamma coupling has been strongly associated with working memory (Tort et al., 2009; Axmacher et al., 2010; Lisman and Jensen, 2013), and memory encoding and retrieval have been demonstrated at different phases of theta oscillations (Kragel et al., 2020), or different frequencies of gamma (Colgin, 2015a), providing a valuable functional framework for memory processing.

Finally, the coupling of large-scale oscillations such as theta with more local oscillations such as gamma is thought to allow coordination of local network activity across the brain (Sirota et al., 2008).

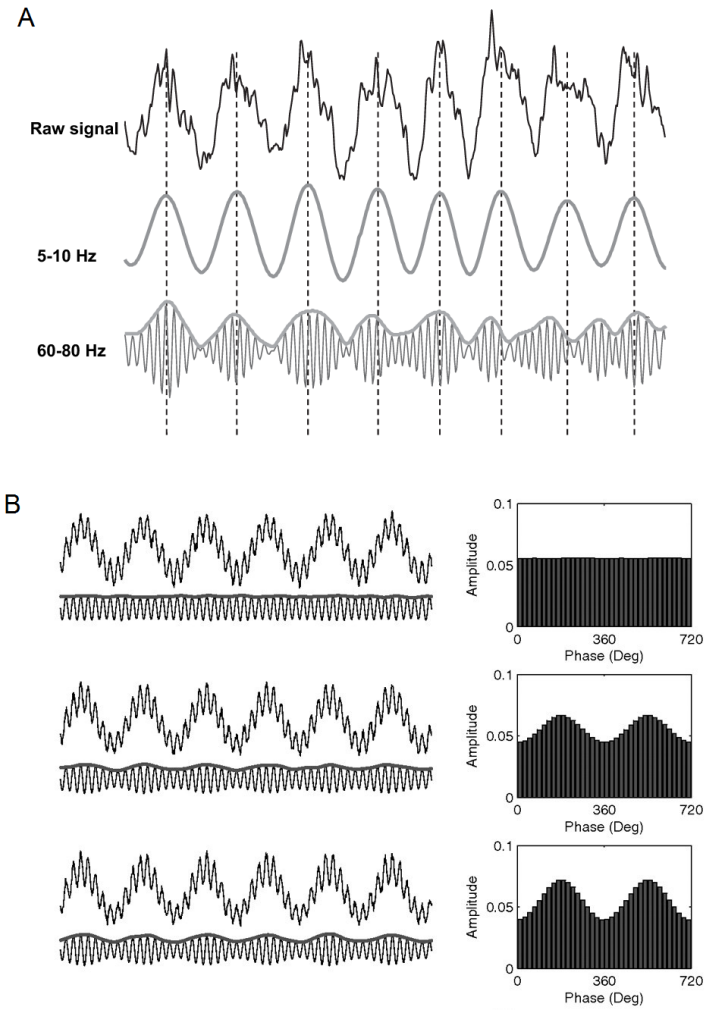

Figure 1.3 Phase-amplitude cross-frequency coupling

A. Cross-frequency oscillatory coupling can occur in a number of ways, including phase-amplitude coupling, where the amplitude of a fast oscillation, in this case gamma, is coupled to the phase of a slower oscillation, such as theta. Gamma oscillations of different frequencies can differentially couple to the phase of the theta cycle. In this example, gamma amplitude peaks at the peak of the theta cycle. B. Histograms of the mean amplitude of a fast oscillation for each phase of a slow oscillation can reveal phase-amplitude coupling. An absence of phase-amplitude coupling appears as a uniform amplitude that does not vary with phase. The Tort method of quantifying phase-amplitude coupling involves calculating the Kullback-Leibler distance of this distribution. A modified from Onslow et al. (2011), B modified from Tort et al. (2010).

1.3.6 Neuronal spiking recordings

Action potentials can also be recorded in the extracellular space as large, high frequency deflections which last around 1 millisecond. These spikes are largest in amplitude near the soma, with amplitude decreasing dramatically with increasing distance from the cell. Neuronal spiking in extracellular recording that arises from multiple different neurons is known as multi-unit activity, while spikes from a single neuron are known as single-units. While multi-unit activity itself can provide a broad estimation of neuronal spiking (Stark and Abeles, 2007), variations in activity between different types of neurons may be diluted in multi-unit data. Spike sorting is an analytical technique by which neuronal spikes are grouped into single units, in order to investigate the spiking activity of individual neurons. A variety of different methods can be employed to differentiate spikes for different neurons, such as analysing spike waveform features, and grouping spikes base on these features (Caro-Martín et al., 2018). Tetrode recordings, or high-density silicon probes, can make use of the fact that spikes from individual neurons are likely to have a distinct spatiotemporal profile that appears on multiple recording sites in order to cluster spikes together (Harris et al., 2000; Henze et al., 2000; Quiroga et al., 2004; Rossant et al., 2016). Spike sorting also allows tentative classification of cells as excitatory neurons or interneurons based on the waveform features or firing rates (Frank et al., 2001). The development of ultra-high-density silicon probes with high channel counts has made it possible to record from hundreds of individual neurons at once, making automated spike sorting a priority (Rossant et al., 2016; Jun et al., 2017).

1.4 Alzheimer's Disease

1.4.1 Dementia

Dementia refers to a group of symptoms associated with impaired brain function, such as memory loss and cognitive impairment, which can result in difficulty performing normal daily activities, and can be caused by a wide range of diseases and pathologies. Some causes of dementia include Parkinson's disease and vascular pathologies, but the most common cause of dementia is Alzheimer's disease, which accounts for between 60-80% of all cases (Alzheimer's Association, 2015). Dementia greatly increases in prevalence with age, but is not a normal feature of aging, as it was once thought to be (Berchtold and Cotman, 1998; Nelson et al., 2011). Approximately 7% of people over the age of 65 have dementia, and in people over the age of 95, this number increases dramatically to around 40% (Prince et al., 2014). Aside from the emotional burden of living with dementia, there is also a huge socioeconomic burden. In England alone, the estimated annual cost of dementia was estimated to be £24.2 billion in 2015, with a large proportion of that cost taken on as unpaid care by those with dementia and their families (Wittenberg et al., 2019). Gradual increases in life expectancy alongside a variety of other societal factors have resulted in an aging global population, meaning age-related diseases such as dementia will likely increase in prevalence over time, creating a potentially disastrous public health problem in the future (United Nations, Department of Economic and Social Affairs, 2015). Importantly, for many of the underlying causes of dementia, there are no effective treatments which stop or even slow the progression of the disease, making research into dementia and discovery of novel therapeutics highly important.

1.4.2 Pathological hallmarks of Alzheimer's disease

Alzheimer's disease is a progressive neurodegenerative disease that is associated with the appearance of a number of pathological hallmarks in the brain. In Alzheimer's disease, progressive loss of neurons in the brain results in gross atrophy of a number of brain regions, including the hippocampus, but it is the loss of synapses that best correlates with the severity of cognitive impairment in Alzheimer's disease (DeKosky and Scheff, 1990; DeKosky et al., 1996). Alzheimer's disease was first described by Alois Alzheimer in 1907, who noted the presence of protein deposits throughout the cortex during a post-mortem analysis of the brain of a woman with severe dementia (Alzheimer, 1907). These protein deposits are known as senile plaques and neurofibrillary tangles, and are two of the two main pathological hallmarks of Alzheimer's disease. Senile plaques, or amyloid plaques, are deposits of insoluble amyloid β (Aβ) protein which generally form in the extracellular space (Figure 1.4a, Glenner and Wong, 1984). Conversely, neurofibrillary tangles are intracellular deposits of insoluble, hyperphosphorylated tau protein, that accumulate in the somatodendritic compartment of neurons (Figure 1.4b, Kosik et al., 1987). These two pathologies progressively spread throughout the brain in relatively stereotypical patterns, and their presence is considered the gold-standard for diagnosis of Alzheimer's disease (Braak and Braak, 1991; Thal et al., 2002; Jucker and Walker, 2013).

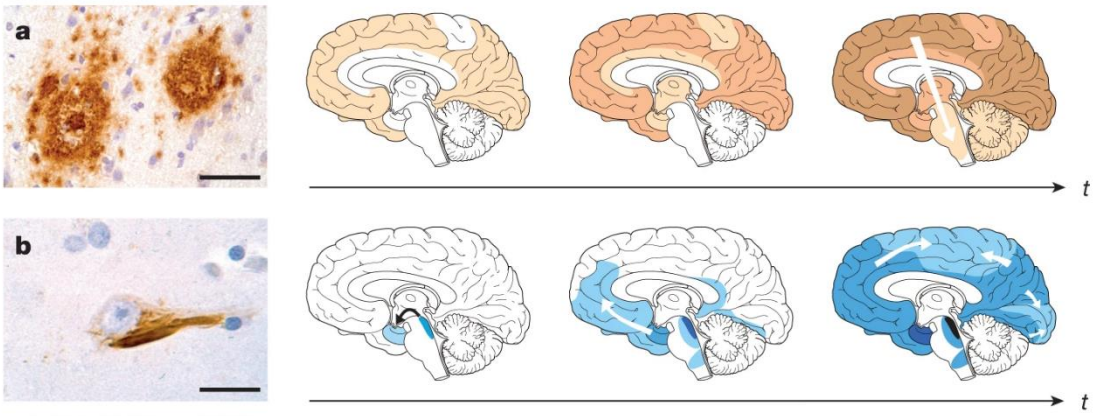

Figure 1.4 Spatiotemporal progression of amyloid and tau pathology in Alzheimer's disease.

A. Extracellular senile plaques formed of amyloid β can be found throughout the brain in Alzheimer's disease. Amyloid pathology appears diffusely throughout the neocortex, and progressively worsens, spreading into the hippocampus and other subcortical regions, before spreading to the brainstem and cerebellum in the latter stages of the disease. This spread has been staged according to Thal et al. (2002). B. Insoluble deposits of hyperphosphorylated tau protein, known as neurofibrillary tangles, can be found within neurons in Alzheimer's disease. The spread of tau pathology is very different to the spread of amyloid pathology, and is thought to begin in the brainstem locus coeruleus and transentorhinal region, before spreading further into the hippocampal formation and the rest of the cortex. The spread of tau pathology has been thoroughly investigated, and staged according to Braak & Braak (1991). Figure modified from Jucker and Walker (2013).

1.4.3 Amyloid Pathology and the Amyloid Cascade Hypothesis

Amyloid β is a protein created by the cleavage of amyloid precursor protein (APP) by two membrane-bound enzymes: β-secretase and γ-secretase (Nunan and Small, 2000). This pathway is considered to be amyloidogenic, but APP can also be processed through a non-amyloidogenic pathway, where it is cleaved by α-secretase, before being cleaved by γ-secretase (Nunan and Small, 2000). APP is thought to have a number of functions in the healthy brain, such as promoting synaptogenesis (Ouimet et al., 1994; Wang et al., 2005). Amyloid β peptides can vary in length, but the most common forms are between 40 and 42 amino acids long, and are prone to aggregation into plaques due to the hydrophobic nature of Aβ42 (Jarrett et al., 1993). A number of missense mutations were discovered at codon 717 of the APP that are associated with familial Alzheimer's disease including the 'Indiana' (V717F, Murrell et al., 1991) and 'London' mutations (V717I, Chartier-Harlin et al., 1991), which change valine for phenylalanine and isoleucine, respectively. Furthermore, the high prevalence of Alzheimer's disease in Down's syndrome was determined to arise from the trisomy of Chromosome 21, where the gene for APP is found (Fried, 1959; Lejeune et al., 1959). These discoveries formed the basis of the Amyloid Cascade Hypothesis by Hardy and Higgins (1992) (Figure 1.5). This hypothesis states that the accumulation of amyloid β results in a cascade of neuropathology seen in Alzheimer's disease, including tau pathology and neurodegeneration. Numerous genetic mutations in the APP gene are associated with familial Alzheimer's disease (for review, see TCW and Goate, 2017), and have a number of pathological consequences, such as overproduction of APP (Citron et al., 1992), or increasing the production of aggregation-prone Aβ42 (Murrell et al., 1991). Conversely, the missense

‘Icelandic’ mutation (A673T), located near the site of β-secretase cleavage results in an approximate 40% reduction in the production of Aβ40 and Aβ42 (Jonsson et al., 2012). Additionally, gain-of-function mutations in presenilin 1 and 2, which form part of the γ-secretase complex (De Strooper et al., 1998), are the most common genetic cause of familial Alzheimer’s disease, and are associated with increased production of Aβ42 (Iwatsubo et al., 1994; Scheuner et al., 1996).The aggregation of amyloid β into oligomers, and then fibrils, results in the formation of amyloid plaques, but recent work has suggested that much of the toxic effect of amyloid β may arise from the oligomeric form of the protein (Hayden and Teplow, 2013). Reducing levels of amyloid beta oligomers without reducing plaque load results in cognitive improvement in transgenic mice (Lesné et al., 2008). Amyloid β oligomers have been shown to disrupt N-methyl-D-aspartate (NMDA) receptor function, causing impaired excitatory synaptic transmission and the loss of dendritic spines, demonstrating that amyloid β may have affect neuronal function independent of its toxic effects (Snyder et al., 2005; Shankar et al., 2007).

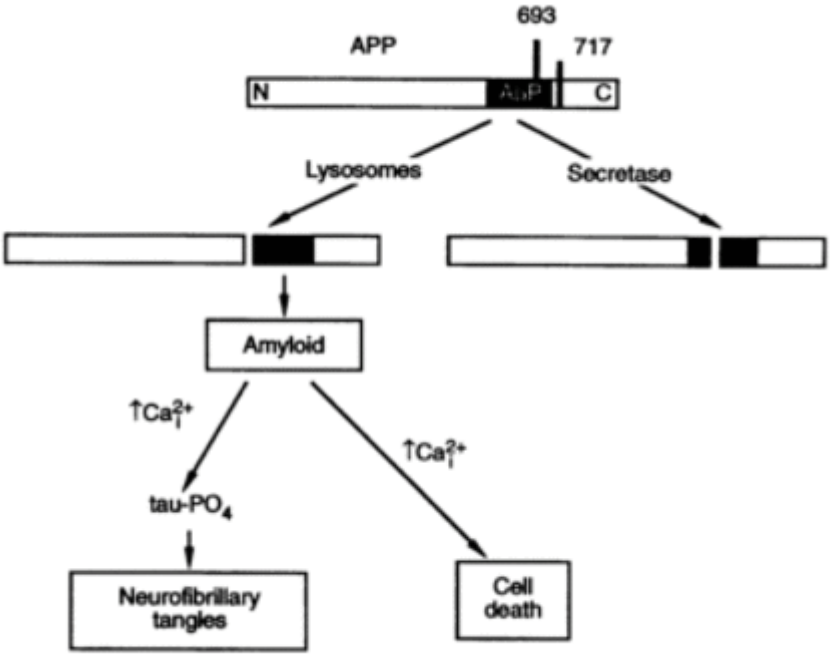

Figure 1.5 Schematic of the original amyloid cascade hypothesis

According to the amyloid cascade hypothesis, cleavage of amyloid precursor protein in the endolysosome results in the formation of amyloid β peptide which forms amyloid plaques, and results in the formation of neurofibrillary tangles and cell death. The hypothesised pathway underlying these changes was thought to be due to increased intraneuronal calcium, resulting in hyperphopshorylation of tau protein and excitotoxicity. Figure reproduced from Hardy and Higgins (1992).

1.4.4 Tau Pathology

Tau is a microtubule-associated protein generally found in the axons of neurons, where it stabilises microtubules (Weingarten et al., 1975; Binder et al., 1985). The binding of tau to microtubules varies depending on its phosphorylation states at specific sites (Lindwall and Cole, 1984), and hyperphosphorylation of tau causes it to disassociate from microtubules and aggregate in the somatodendritic compartment of neurons, forming neurofibrillary tangles (Kosik et al., 1987; Goedert et al., 1989). It is therefore thought that toxicity due to tau protein could be due to both the toxicity of hyperphosphorylated tau and the loss of normal axonal transport due to microtubule destabilisation (Trojanowski and Lee, 2005). Tau pathology is another key pathological hallmark of Alzheimer's disease, in that neurofibrillary tangles made up of insoluble tau protein can be found throughout the brain (Kosik et al., 1987). In the early stages of Alzheimer's disease, tau pathology is found in a limited number of brain regions, including the entorhinal cortex, but over time spreads to numerous other brain regions in a sequence that varies very little between individuals, and is correlated with the progression of cognitive impairment (Braak and Braak, 1991). Tau pathology has been shown in a number of other neurodegenerative diseases, now known as tauopathies (Williams, 2006). The spatial patterns of tau pathology within the brain, as well as the species of pathological tau vary between different tauopathies, but progressive neurodegeneration is a common feature of all tauopathies (Williams, 2006). Unlike amyloid β, there are no tau mutations associated with Alzheimer's disease, however a number of mutations are associated with other tauopathies, such as frontotemporal dementia and parkinsonism linked to chromosome 17 (FTDP-17, Hutton et al., 1998; Spillantini et al., 1998).

1.4.5 Treatment of Alzheimer's Disease

There have been numerous attempts to develop disease modifying agents for Alzheimer's disease which are able to slow or stop the progression of the disease. From the year 2002 to the year 2012, the approval rate for Alzheimer's disease drugs was around 0.4%, and those compounds that were approved were symptomatic treatments rather than disease-modifying agents (Cummings et al., 2014). Three of these compounds, donepezil, galantamine and rivastigmine primarily inhibit the enzyme acetylcholinesterase, which catalyses the breakdown of acetylcholine (Sharma, 2019). Cholinergic signalling has been shown to be impaired in Alzheimer's disease, likely due to neurodegeneration in the nucleus basalis of Meynert (Bartus et al., 1982), and blocking cholinergic signalling has been shown to cause cognitive impairment which worsen with age (Molchan et al., 1992), therefore treatment with acetylcholinesterase inhibitors is thought to increase concentrations of acetylcholine in the synaptic cleft and improve cognition. While these drugs improve cognition, they do not target the disease.

A large number of experimental disease-modifying agents targeted amyloid β in an attempt to clear plaques or reduce the generation of amyloid β from APP. Some examples include the gamma secretase inhibitor semagacestat, and the amyloid β antibodies, bapineuzumab and solanazeumab, which aimed to clear plaques and reduce soluble amyloid β respectively (DeMattos et al., 2002; Kopan and Ilagan, 2004; Rinne et al., 2010). A number of these compounds were able to clear amyloid pathology in the brain, but failed to show improvements in cognition in humans (Schenk et al., 1999; DeMattos et al., 2001; Hyslop et al., 2004). This lack of success caused many in the field, including Hardy himself, to re-examine the amyloid cascade hypothesis (Hardy, 2009; Karran and De

Strooper, 2016). While tau pathology and large-scale neurodegeneration are thought to be downstream of amyloid pathology according to the amyloid cascade hypothesis, both are notably absent in amyloid mouse models, despite widespread amyloid pathology (Karran and De Strooper, 2016). Furthermore, as previously mentioned, clearance of amyloid pathology did little to improve cognition in humans in Phase 3 clinical trials (Cummings et al., 2014), although it is important to note that, unlike tau, the extent of amyloid pathology in Alzheimer's disease is not correlated with the severity of cognitive symptoms (Arriagada et al., 1992; Braak and Braak, 1995). Finally, many of these compounds had previously showed cognitive enhancing potential in preclinical rodent models, which has raised a number of questions about the translational value and validity of these models (Philipson et al., 2010).

1.4.6 Mouse models of Dementia

Numerous transgenic mouse models have been generated which recapitulate a number of the pathological hallmarks of Alzheimer's disease. One of the first mouse models of Alzheimer's disease was the PDAPP model which overexpressed human APP with the Indiana mutation (V717F), which results in an increased ratio of Aβ42/Aβ40 (Murrell et al., 1991; Tamaoka et al., 1994; Games et al., 1995). These mice begin to develop amyloid plaques in the hippocampus and cortex at around 6-9 months of age, and show memory impairments, including object recognition memory and spatial memory, as measured using the radial-arm maze (Dodart et al., 1999). Another commonly used model is the Tg2576 line, which overexpresses mutant APP with the Swedish mutation (KM670/671NL), which results in increased production and secretion of Aβ42 and Aβ40 (Citron et al., 1992; Mullan et al., 1992; Hsiao et al.,

1996; Scheuner et al., 1996). Amyloid plaques were present in the hippocampus and cortex at around 11-13 months of age (Hsiao et al., 1996). Furthermore, contextual memory deficits have been demonstrated as early as 5 months of age (Jacobsen et al., 2006), and spatial memory deficits in the Morris Water maze around 6 months of age (Westerman et al., 2002).

A model we have used extensively throughout this thesis is the J20 mouse line which overexpresses human APP with both the Indiana (V717F) and Swedish (KM670/671NL) mutations (Murrell et al., 1991; Mullan et al., 1992; Mucke et al., 2000). The combination of these mutations accelerates plaque formation in these mice, with plaques appearing in the hippocampus and the deep layers of the neocortex around 5-7 months of age (Mucke et al., 2000). J20 mice have been shown to present with spatial memory deficits in both the Morris water maze and radial-arm maze at 4 months of age, prior to the appearance of amyloid plaques (Cheng et al., 2007; Wright et al., 2013). The rapid development of amyloid pathology in these mice, as well as the spatial distribution of amyloid plaques in the retrosplenial cortex and throughout the hippocampus (Figure 1.6, Whitesell et al., 2019), make the J20 mouse line a valuable mouse model for our experiments.

Combined mutant models with APP and presenilin mutations have been developed that have even more severe pathology (Holcomb et al., 1998; Oakley et al., 2006; Whitesell et al., 2019), however some have suggested that presenilin mutations result in pathology independent of amyloid pathology, thus producing confounding factors (Shen and Kelleher, 2007). It is notable that none of the models previously discussed demonstrate either tau pathology, or significant neurodegeneration. Tau pathology has been modelled in mice, using mutations

commonly found in frontotemporal dementia with Parkinsonism linked to chromosome 17, another tauopathy (Lewis et al., 2000; Santacruz et al., 2005). These mice show widespread neurofibrillary tangle formation, and neurodegeneration, indicating the importance of tau pathology to this phenotype, and highlight the importance of completely recapitulating all aspects of Alzheimer's disease. More recent models which express both amyloid and tau mutations show both plaque and tangle formation, and demonstrate that the presence of tau accelerates amyloid pathology, demonstrating an important interaction between these pathologies (Oddo et al., 2003).

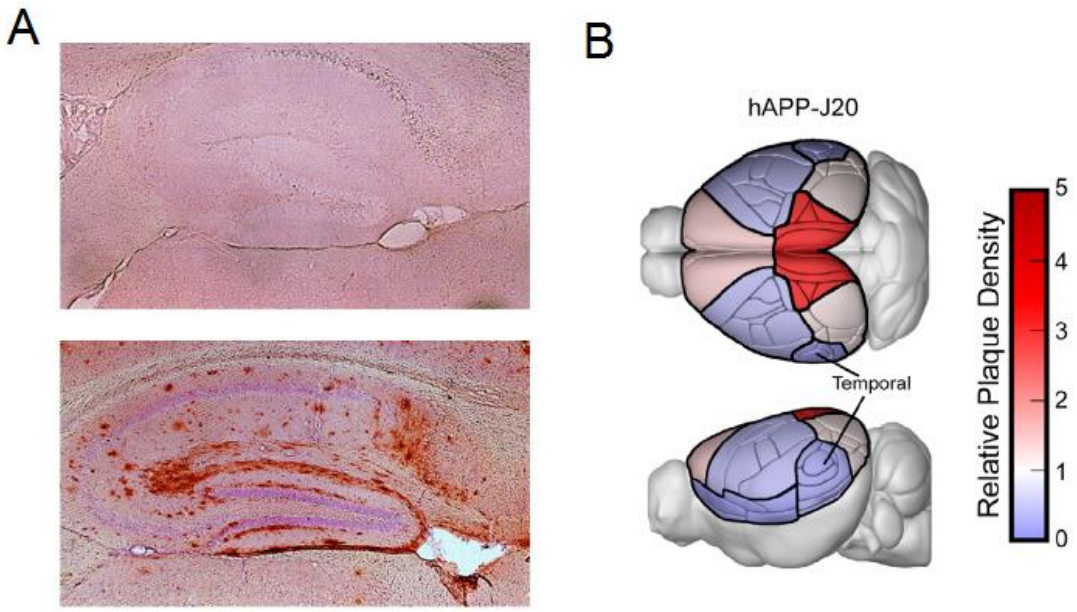

Figure 1.6 Amyloid pathology in the J20 model of Alzheimer's Disease

A. Photomicrographs of the hippocampus from light microscopy at 4x of mouse brains stained for amyloid β using the 3D6 antibody. Above is the hippocampus from a 15-month old wild-type (WT) mouse, and below is the hippocampus from a 10-month old J20 mouse. Amyloid plaques can be seen throughout the hippocampus of J20 mice, particularly in the outer molecular layer of the dentate gyrus. B. Relative plaque density across the cortex of 13-month old J20 mice, as quantified using methoxy-X04 labelling and serial two-photon tomography. Amyloid plaques are highest in density within the retrosplenial cortex, with other regions of the neocortex demonstrating far lower relative plaque density. A modified from Mucke et al. (2000), B modified from Whitesell et al. (2019).

1.5 Aims

As we have previously discussed, a large body of evidence has indicated the importance of the retrosplenial cortex in contextual memory, but the neurophysiological mechanisms underlying these memory processes in this region are unclear. While the role of the hippocampus in memory has been extensively studied throughout the last century, until recently the retrosplenial cortex has been generally overlooked. The first aim of this project was to attempt to further understand the specific role of the retrosplenial cortex in contextual memory, by investigating functional correlates of environmental novelty and familiarity through the use of *in vivo* electrophysiology. *In vivo* electrophysiology is an invaluable technique to probe the activity of both large-scale neuronal networks and of individual neurons, in awake, behaving animals, and functional correlates of behaviour allow us to better understand the specific processes that underlie the many functions performed by the brain. Our second aim was to investigate how the retrosplenial cortex interacts with other areas of the brain during contextual memory process. While there are countless studies detailing the anatomical connectivity of the retrosplenial cortex, few studies have investigated the functional connectivity of this region. Pure anatomical studies may provide an incomplete picture of the functional networks that make up the brain. A specific focus in this thesis is the interactions between the retrosplenial cortex and the hippocampus. As we have previously discussed, both regions are highly involved in contextual memory, and often appear to have overlapping functions, so these studies may provide insight into the dynamics which underlie communication between these two regions. The final main aim of this project is to investigate how the retrosplenial cortex network activity is affected by

Alzheimer's disease-associated amyloid pathology, through parallel investigations using the J20 transgenic mouse line. The retrosplenial cortex is highly affected during the early stages of Alzheimer's disease (Minoshima et al., 1997; Choo et al., 2010), however the physiological consequences of amyloid pathology on neuronal network activity are unclear. Functional correlates of behaviour can provide measurable benchmarks of health against which the effects of neuropathology can be tested against.

2 General Methods

2.1 Animals

All procedures were carried out in accordance with the UK Animal (Scientific Procedures) Act 1986 65 and were approved by the University of Exeter Animal Welfare and Ethical Review Body. Access to food and water was provided ad libitum. All animals were kept on a 12-hour light/dark cycle, with the light/dark cycle matching the normal daylight/night-time cycle, meaning all interactions including handling, surgery and behaviour took place during the light cycle. Surgical mice were group housed prior to surgery, and single housed post-surgery, in order to prevent damage to the surgical implants.

2.2 In Vivo Data Collection

Throughout experimental sessions, Local Field Potentials (LFPs) and Electroencephalograms (EEGs) were recorded using an Open Ephys Acquisition board (Open Ephys), which was tethered to the probe via a headstage (RHD 16-Channel Recording Headstage or RHD 32-Channel Recording Headstage, Intan Technologies), and SPI cables (Intan Technologies). LFPs and EEGs on each channel were sampled at 30 kHz, while the animal's location was monitored using a pair of light-emitting diodes (LED) soldered to the headstage, and a video camera, placed directly above the arena. The location of these LEDs was tracked using Bonsai tracking software, so the location and running speed of the animal could be estimated offline. In order to aid tracking, and to minimise stress and promote exploration, the arena was dimly lit from above by a faint light emitting diode (LED) light. All analysis was performed offline. The entire recording setup can be seen in (Figure 2.1).

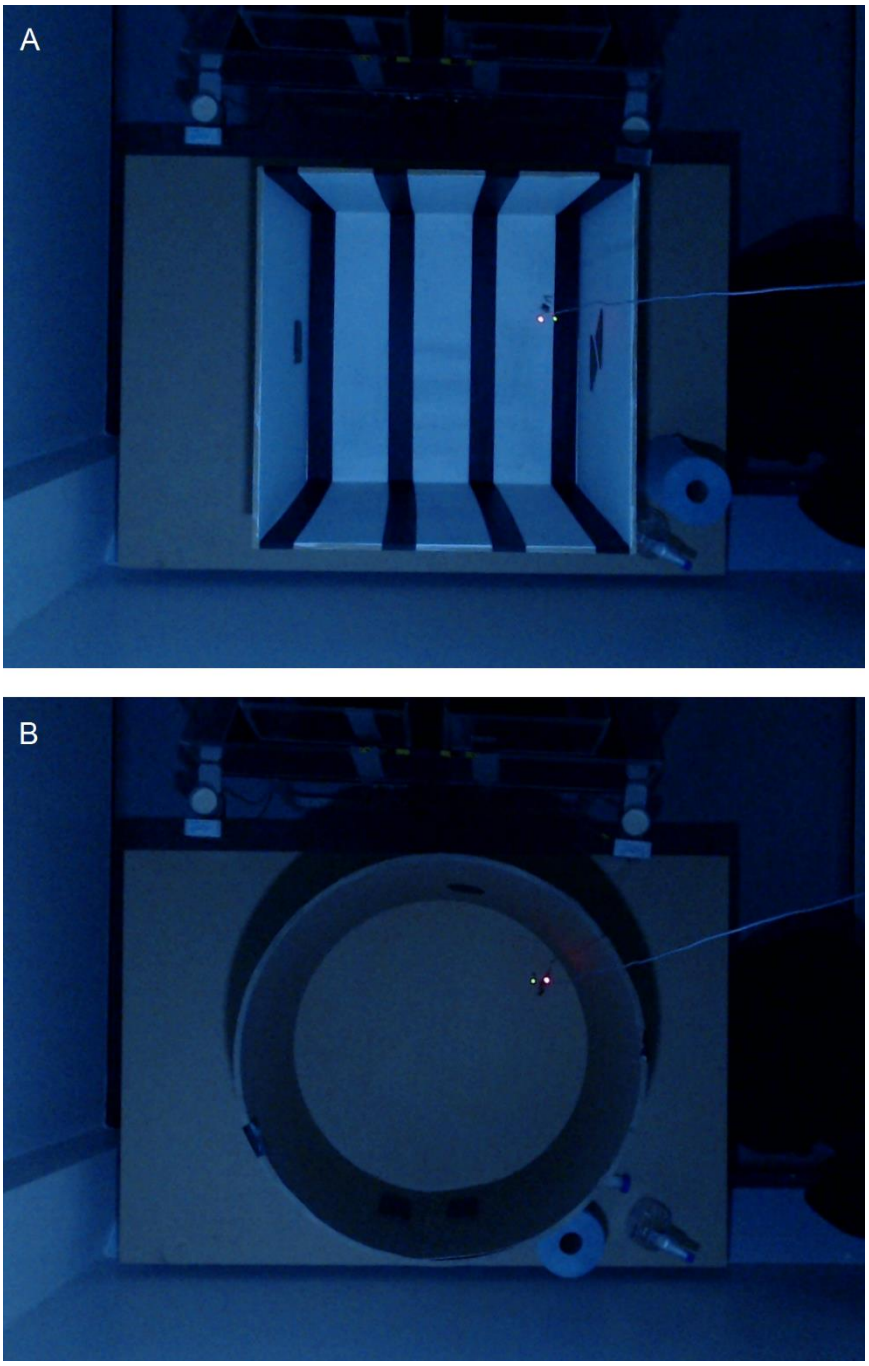

Figure 2.1 Photograph of the entire recording and behaviour setup

Experimental setup showing both the square (A) and circular arenas (B). Photograph was taken by an overhead camera used to track behaviour. The room was dimly lit by a small LED light on the ceiling, just out of shot. The animal was tethered to an Open Ephys acquisition board (Open Ephys) via a headstage (Intan Technologies) with a red and green LED soldered onto it to allow behavioural tracking, which can be seen in both images. Arenas were cleaned with 70% ethanol between behavioural recording sessions. Photographs courtesy of Maria Garcia Garrido.

2.3 Data Analysis

LFPs were down-sampled by different amounts depending on the analysis used, and de-trended in order to remove any slow linear drift of the baseline that may occur across the session. Down-sampling was used in the experiments detailed in this thesis in order to reduce computation time, which was especially important for some of the more complex analyses, however for some analyses signals were not downsampled in order to preserve temporal precision. For each analysis the minimum amount of down-sampling was performed in order to retain temporal precision while reducing computation time. When digital filters were used, the order of each filter was chosen to achieve a balance between a sharp roll off rate at the edges of the pass band, while minimising the creation of spurious oscillations that may arise from filtering spikes of noise with high order filters (de Cheveigné and Nelken, 2019). Butterworth filters were used as they have a smooth frequency response with no ripples. The Chronux toolbox (Mitra and Bokil, 2008, http://chronux.org/) was used for a number of functions including the mtspecgramc and mtcohgramc functions, as well as a number of built in MATLAB functions. Additionally, a number of functions from the MVGC Multivariate Granger Causality toolbox were used to perform Granger causality analysis (Barnett and Seth, 2014). Finally, some functions from the MATLAB File Exchange were used including shadedErrorBar (Campbell, 2021) and polyfitZero (Mikofski, 2021). All other scripts used in this study were written in house, and are included in the Appendices of this thesis. In order to select channels in specific brain regions and to ensure these channels which were at equivalent depths between animals, a combination of post-hoc histology and functional outputs were used to determine the exact locations of each channel. One

functional output makes use of the fact that the phase of theta oscillations reverses across the pyramidal cell layer of the hippocampus (Buzsáki, 2002), so for probes which reached or crossed this layer, it is possible to work backwards to find the exact location of each channel to less than 100 µm. This allows us to greatly reduce variability between animals and is a worthwhile validation.

2.4 Power Spectral Analysis

LFPs for power spectral analysis were downsampled by 30 times to a sampling rate of 1000 Hz. Multi-taper spectral analysis was performed using the mtspecgramc function from the Chronux Toolbox (Mitra and Bokil, 2008), with a time-bandwidth product of 2 (1 second x 2 Hz), and 3 tapers, resulting in some smoothing of resulting spectra. Multi-taper spectral analysis was used to reduce spectral variance and improve the signal-to-noise ratio of power spectra, especially for the high frequency bands (Mitra and Bokil, 2008), and the parameters used allowed for a sufficient temporal and frequency resolution for our analyses. The mtspecgramc function generates a power spectrogram by generating multiple power spectra for short segments of time series data, using a moving window; in our case with the window size of 1 s with no overlap. As spectral power decreases with a 1/f distribution, power at high frequencies can be hard to visualise so in order to correct for this, spectrograms were then logged to the base 10, and multiplied by 10, in order to convert to decibels (dB). These individual spectra were averaged, resulting in a single mean power spectrum for the entire 15-minute session, or for the first minute of each session, as specified in the results. Spectral data from 47to 53 Hz, which incorporates line frequency noise (50 Hz), were removed and linearly interpolated between the nearest neighbours. The power of each frequency band was calculated as the mean

power in each of the following frequency ranges: delta (1-5 Hz, Joho et al., 1999), theta (5-12 Hz, Vanderwolf, 1969), alpha (12-20 Hz), beta (20-30 Hz, Sherman et al., 2016), gamma (30-100 Hz, Buzsáki et al., 2003). These frequency bands were similar to those used in the literature, however there is a great deal of variability in the field regarding these frequencies. Furthermore, while some studies subdivide the gamma band into low gamma and high gamma, we saw no evidence of divergence within this frequency range that would warrant this for these data.

For some spectral analysis in this paper, the continuous wavelet transform was performed instead of the fast Fourier transform used in the mtspecgramc function, due to its superior temporal resolution in the frequency domain for short time series (Moca et al., 2021). Wavelet analysis was performed using the cwt function in MATLAB, with a Morlet wavelet with equal variance and time and frequency. The scale to frequency conversions are set by the sampling rate of 30 kHz. For all other power spectral analysis, such high temporal resolution was unnecessary, so the fast Fourier transform was used due to its lower computational power requirements.

2.5 Beta Burst Detection

LFPs for beta burst detection were downsampled by 10 times to a sampling rate of 3000 Hz, and band-pass filtered between 20-30 Hz to isolate the beta frequency band, using a Butterworth IIR filter with order 2. The amplitude and phase of this beta signal were calculated as the real and imaginary components of the Hilbert transform, respectively. Due to the sensitivity of this beta burst detection algorithm to noise, epochs were the beta amplitude exceeded 10 median absolute deviations from the median were removed from the data. The

beta amplitude was subsequently z-scored, to standardise the data and investigate epochs where the beta amplitude deviated strongly from the mean. Epochs of the signal where this z-score exceeded 2 standard deviations from the mean amplitude were detected, as were the corresponding “edges” of these epochs, where the signal magnitude surpassed 1 standard deviation either side of the 2-standard deviation threshold. This was done in order to capture the time-course of these high beta amplitude epochs. Events that did not persist longer than a minimum duration of 150 ms (i.e. fewer than 3 oscillation cycles) were discarded. These remaining events were then considered beta-bursts. A number of characteristics were calculated, including the magnitude of the bursts, as given by the amplitude from peak to trough. Beta bursts with magnitudes that exceeded 3 median absolute deviations from the median were considered outliers and discarded.

In order to investigate the distribution of beta bursting within sessions, the cumulative sum of beta bursts was calculated in 1-second bins for the whole session. This cumulative frequency data was used to estimate the rate of beta bursting during the first minute and the final 10 minutes of each session, by independently fitting linear regressions to the data, with the linear fit for the first minute constrained to zero using the function polyfitZero from the MATLAB file exchange (Mikofski, 2021). The rate of beta bursting, in beta bursts per minute, was calculated from the slope of these fits.

2.6 Beta Burst Characteristics

Following beta burst detection, a number of different beta burst characteristics were calculated. First, the duration and magnitude of each beta burst was calculated, and subsequently the frequency profile and rhythmicity. In order to

investigate the frequency profile of beta bursts, power spectral analysis was performed on each burst and epochs of equal length before and after each burst, using the Chronux function mtspectrumc. The time-bandwidth product of this analysis was 1 (1 second x 1 Hz), with a single taper, in order to account for the shorter time periods. All burst and pre-burst epochs were averaged, across all sessions. The final beta burst characteristic of interest was the extent of rhythmicity during, and outside, beta bursts in order to attempt to understand whether beta bursts are generated by a "dynamic amplitude modulation" mechanism or a "bursty generator" (Shin et al., 2017; van Ede et al., 2018), as illustrated in Figure 2.2 Dynamic amplitude modulation and bursty generator mechanisms are two theoretical models for transient neural oscillations. In order to investigate the rhythmicity of beta oscillations during burst and non-burst epochs, first the signal was band-pass filtered between 20-30 Hz to isolate the beta frequency band, using a Butterworth IIR filter with order 2. The start times and stop times of each beta burst were used to isolate burst and non-burst epochs, with non-burst epochs defined as time segments before the first beta burst or between beta bursts. Any non-burst epochs shorter than 66 ms (equivalent to two cycles of a 30 Hz oscillation) were discarded in order to focus on longer time segments which likely better represent the inter-burst interval. The built-in function findpeaks was used to find the peaks of the beta-filtered signal, with a minimum distance of 25 ms between adjacent peaks (equivalent to a 40 Hz oscillation), for all burst and non-burst epochs, and the time between adjacent peaks was taken as the period of the beta oscillation. For each recording session, a histogram of the burst and non-burst beta periods was generated, in order to visualise the consistency of beta periods, which we considered as a measure of beta rhythmicity.

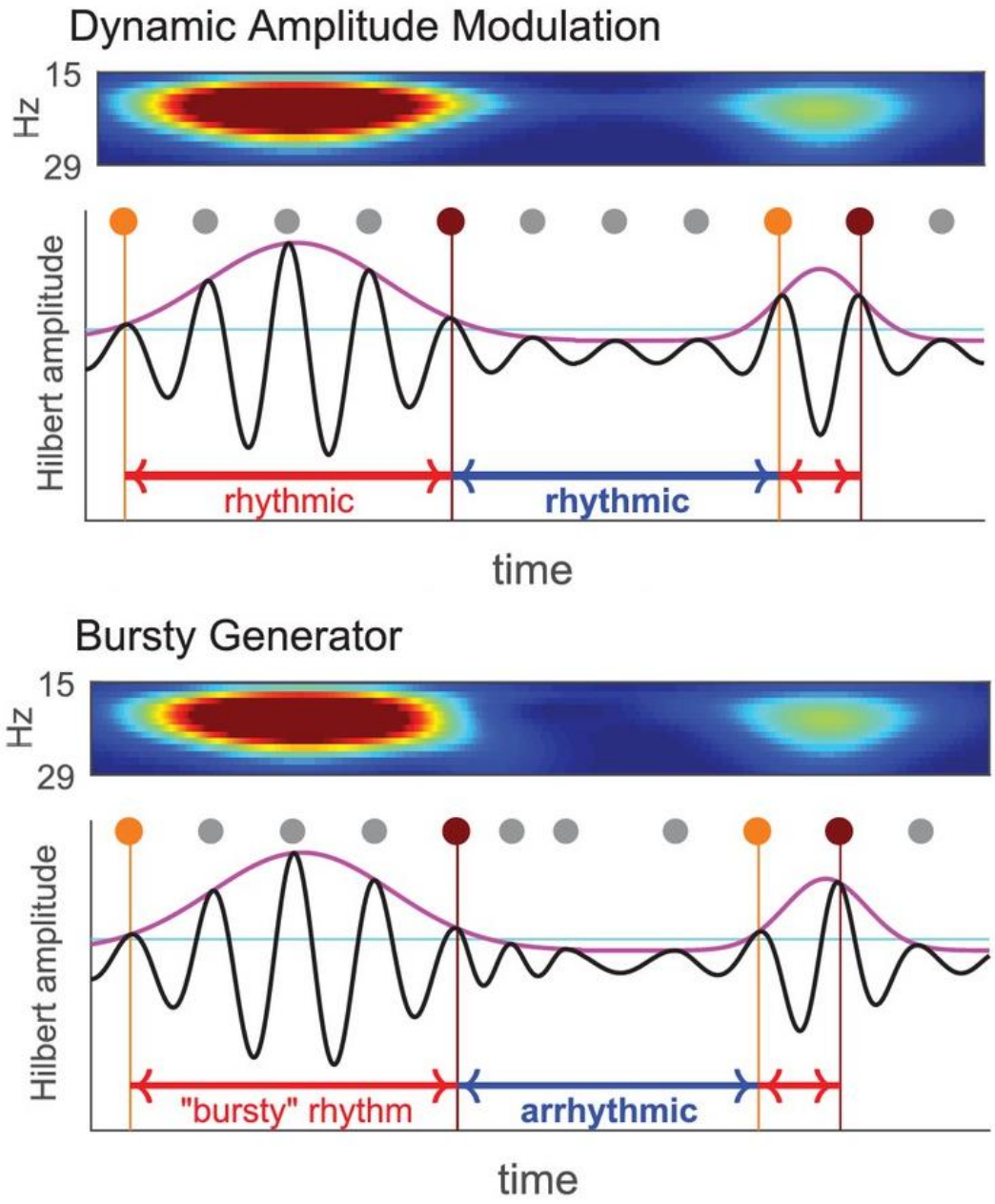

Figure 2.2 Dynamic amplitude modulation and bursty generator mechanisms are two theoretical models for transient neural oscillations.
Illustration demonstrating two theoretical models of neural oscillations which may support the generation of transient neural oscillations such as beta bursts, as theorised by van Ede et al. (2018). While both dynamic amplitude modulation and bursty generator models are likely to produce oscillations which are visually similar in the frequency domain, as shown by the spectrograms above each trace, the key divergence between these two models can be seen in the time domain. Dynamic amplitude modulated signals are consistently rhythmic during, and outside, high amplitude events (as shown by the constant oscillatory period demonstrated by regular spacing between the dots). Conversely, bursty generators could be expected to produce oscillations which are tightly rhythmic during high amplitude events, and highly arrhythmic outisde these events. Figure modified from Shin et al. (2017).

2.7 Phase-Amplitude Coupling

To calculate phase-amplitude coupling, and create phase-amplitude coupling comodulograms, modulation index (MI) was calculated individually for each pair of phase and amplitude frequencies as described by Tort et al. (2009). This method has been shown to be superior to alternative methods, and is less sensitive to changes in amplitude. A full explanation of this method can be found in (Tort et al., 2009), but will be briefly explained here. Phase-amplitude coupling was calculated between phase frequencies in bins of 0.25 Hz from 2 to 12 Hz, and amplitude frequencies in bins of 2 Hz from 10 to 100 Hz. For each pair, local field potentials were filtered in the phase frequency band and the amplitude frequency band, after which the instantaneous phase and amplitude of each filtered signal was calculated, respectively, using the Hilbert transform. The phases of the “phase signal” were binned in 10° bins, and the average amplitude of the “amplitude signal” was calculated for each phase bin, after which this “amplitude distribution” was normalised so that the sum of all bins is equal to 1. The existence of phase-amplitude coupling can be seen in these amplitude distributions as a non-uniform amplitude across the phase bins, and as such, the Kullback-Leibler distance was calculated to quantify the divergence of this amplitude distribution from the uniform distribution (Kullback and Leibler, 1951). In order to convert to Kullback-Leibler distance to Modulation Index, with a scalar value between 0 and 1, this value is divided by the natural logarithm of the number of phase bins, which in this case is 18. Although this method is far less sensitive to spurious coupling than other methods, we still normalised the resulting modulation index, as suggested in Tort et al. (2010). This was done by the generation of 100 surrogates, where the data was time shifted by a random

amount between 1 and 59 seconds, for which the modulation index was calculated. A gaussian distribution was then fitted to these surrogate modulation indicies and the actual modulation index was calculated as a z-score from the mean of this distribution. This same mathematical operation was performed for all phase and amplitude frequency pairs to create a comodulograms, and in order to smooth the resulting comodulograms, the data matrix was linearly interpolated in both dimensions by a factor of 2.

As previously mentioned, In order to generate these comodulograms, signals were filtered in very narrow frequency bands in order to get a high degree of resolution in the frequency range. For the amplitude axis the width of this band was 2 Hz, while for the phase axis this band was even smaller at 0.25 Hz. In order to confirm that filtering in such narrow bands did not cause significant distortion to the waveform of the oscillation, a selection of these bandpass filtered signals was inspected, using the same frequency bands used in the phase-amplitude coupling analysis. An example of these signals can be seen in Figure 2.3a, which shows that these waveforms are free of any notable distortions, likely due to the lack of ripples in the frequency response of the Butterworth filter used. Furthermore, in order to verify that phase-amplitude coupling could be estimated from such narrow bandpass filtered signals, we investigated the strength of theta-beta and theta-gamma coupling as previously described, using the same frequency bands shown in Figure 2.3a. As shown in Figure 2.3b, clear phase-amplitude coupling can be seen from the probability distributions for beta amplitude (left) and gamma amplitude (right) at different phases of the theta oscillation, as shown by the non-uniform distribution across theta phase, and the modulation index (MI) values shown above both graphs.

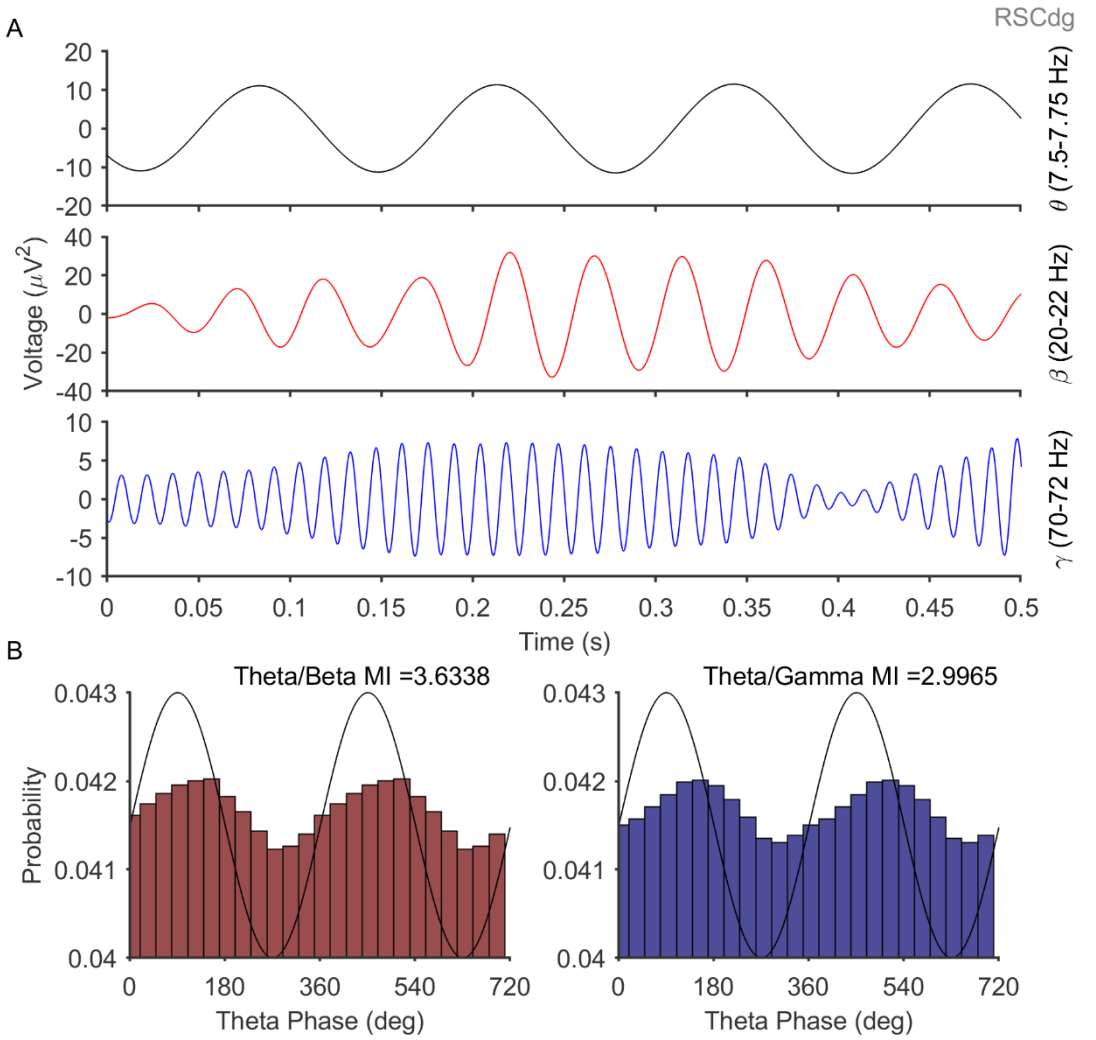

Figure 2.3 Phase-amplitude coupling can be estimated even with narrow bandpass filtered local field potentials.
A. Example bandpass filtered local field potentials from a single animal, filtered in a small subsection of the theta (top), beta (middle) and gamma (bottom) freqency bands, as used in our phase-amplitude coupling analysis. These signals are free from any notable distortions which may arise as an artefact of filtering.
B. Example probability distributions for beta (left) and gamma amplitude (right) at different phases of the theta oscillation, using signals filtered in the same narrow bands as those shown in the traces above. The probability distributions shown here show a high degree of non-uniformity, suggesting the presence of phase-amplitude coupling, which is further supported by the high modulation index (MI) values calculated using these probability distributions (shown above). These data together support the validity of narrow bandpass filtered signals for phase-amplitude coupling analysis across a large frequency range. All data comes from a single recording from the dygranular retrosplenial cortex of a single mouse.

2.8 Multi-Unit Activity

Due to the distance between adjacent channels on the recording probe (100 µm) it is highly unlikely that activity of a single neuron would appear on multiple channels. This precluded the possibility of using standard spatiotemporal clustering techniques (Quiroga et al., 2004; Rossant et al., 2016). Consequently, individual channels were treated as individual multi-units. Raw local field potentials were first common average-referenced, using a mean of the signals from all other 15 channels, then filtered in the range of 500-5000 Hz, using a Butterworth IIR filter with order 4, in order to isolate the spiking frequency band. This common average-referencing allowed us to remove potential noise from the data, as spikes appearing simultaneously on many channels at once are unlikely to be biological and therefore are probably recording artefacts. Spikes were detected as peaks that crossed a threshold given by 4 medians of the absolute voltage of the signal divided by 0.6745, as suggested by Quiroga, Nadasdy and Ben-Shaul (2004), and had a minimum separation of 0.5 ms, equivalent to the time to peak amplitude for a spike waveform with a duration of 1 ms. According to Donoho and Johnstone (1994), the median of the absolute voltage of the signal divided by 0.6745 is an estimate of the standard deviation of the background noise. Average multi-unit waveforms were generated by averaging across all spike waveforms in all sessions, for all animals, while average firing rate was calculated as the average firing rate across all sessions, for all animals. In order to investigate multi-unit activity during beta bursts, bursts were detected as previously mentioned, and bursts that occurred within a second of each other were discarded, to remove overlapping segments. A single peri-burst histogram was created for each channel by taking the total number of spikes in 50 ms time

bins from 500 ms before burst onset, to 500 ms after, for all beta bursts. Each histogram was then normalised by dividing the count in each bin by the total number of spikes in all bins, averaged across all sessions and z-scored with respect to the baseline epoch (0.5 second pre-burst). The spike rate during beta bursting was calculated as the mean z-scored firing rate during the first 250 ms after burst onset, as this was determined to be the approximate time course of high beta amplitude.

2.9 Coherence Analysis

Coherence analysis is commonly used in neuroscience to investigate phase-locking between neural oscillators and quantify this in the frequency domain (Lowet et al., 2016). Analysis was performed in a similar way to power spectral analysis, in that data processing prior to analysis was the same, as were the multi-taper parameters. LFPs for coherence analysis were downsampled by 30 times to a sampling rate of 1000 Hz. Multi-taper coherence analysis was performed using the cohgramc function from the Chronux Toolbox (Mitra and Bokil, 2008), with a time-bandwidth product of 2 (1 second x 2 Hz), and 3 tapers, resulting in some smoothing of resulting spectra. The mtspecgramc function generates a power spectrogram by generating multiple power spectra for short segments of time series data, using a moving window; in our case with the window size of 1 s with no overlap. These individual spectra were averaged, resulting in a single mean coherence spectrum for the entire 15-minute session, or for the first minute of each session, as specified in the results. Coherence data from 47 to 53 Hz, which incorporates line frequency noise (50 Hz), were removed and linearly interpolated between the nearest neighbours. The coherence in each frequency band was calculated as the mean coherence in each of the following

frequency ranges: delta (1-5 Hz), theta (5-12 Hz), alpha (12-20 Hz), beta (20-30 Hz), gamma (30-100 Hz). As before, we saw no evidence of divergence within the gamma frequency range that would warrant subdividing the gamma band for these data.

2.10 Granger Causality Analysis

Granger causality analysis is a technique by which potential directional interactions between neural oscillators can be investigated by determining whether the past of one time series can predict the future of another (Seth et al., 2015). Granger causality analysis in this study was performed using the MVGC Multivariate Granger Causality toolbox (Barnett and Seth, 2014). First local field potentials were downsampled 30 times to a sampling rate of 1000 Hz. The signals were then segmented into 1-minute epochs, with each epoch analysed individually, in order to investigate the time course of Granger causality changes over the session. In order to estimate a suitable model order for vector autoregression, the Akaike information criteria was calculated for vector autoregression models up to a maximum model order of 20, using Morf's version of the locally weighted regression algorithm. This estimated model order was then used to fit a vector autoregression model to the data, using the ordinary least squares solution. The resulting residuals covariance matrix and vector autoregression coefficients matrix were then used to calculate the autocovariance sequence up to a maximum lag of 50,000 samples. Spectral pairwise-conditional Granger causalities are then calculated from the autocovariance sequence up to the Nyquist frequency, or half the sampling rate, which in this instance is 500 Hz. The frequency resolution is set to be the number of autocovariance lags. In order to standardise between Granger causalities with

different frequency resolutions, these underwent 1-dimensional interpolation, in 0.25 Hz steps from 0 to 120 Hz. A final check is performed to ensure that spectral multivariate Granger causalities integrate back to multivariate Granger causalities in the time domain, with minimal absolute difference less than 1e-5. These frequency domain Granger causality spectra were combined to produce ‘Grangerograms’ for each direction, showing Granger causality across the session in 1-minute bins, and subtracted from each other in order to visualise the balance between both directions.

2.11 Beta Burst Cross-Correlation

For beta burst cross correlation, beta burst detection was performed as before, however local field potentials were not downsampled in order to maximise the temporal resolution of the analysis. Data signals from all channels were filtered in the beta frequency range as before, and beta burst detection was performed on the data from a single “reference” channel. The starts and stops of these reference channel beta bursts were used to isolate these burst epochs from all other channels. xcorr, a built-in MATLAB function was used to investigate the cross-correlation between each beta burst detected at the reference channel, and the time-locked beta signal from each other “test” channel. These cross correlations were normalised as a correlation coefficient, so the autocorrelation of the reference beta burst would be equal to 1 at zero lag. The peak cross correlation was calculated from these cross-correlations, as well as the lag at which this peak cross-correlation occurs. This process was repeated for all test channels and all beta bursts.

2.12 Histology

Upon completion of the *in vivo* experiments, mice were killed using an overdose of sodium pentobarbital (Euthetal). For brain from experimental mice fitted with silicon depth probes, an isolated stimulator was used to produce electrolytic lesions at the recording sites. Mice were then transcardially perfused with 40% paraformaldehyde (PFA), and their brains were extracted and stored in 40% PFA for 24 hours, after which they were transferred to phosphate-buffered saline (PBS) prior to sectioning. Brains were sliced into 100 µm sagittal sections using a Lecia VT1200 vibratome (Leica), and stained depending on the desired protocol. For simple electrode location verification, brains were stained with 1% Cresyl Violet solution. For visualisation of amyloid plaque pathology, brains were stained with amylo-glo stain (Schmued et al., 2012). Slides were visualised on a Nikon Eclipse E800 microscope (Nikon), using either a 5x or 10x objective. Digital pictures were taken using either QCapture Pro 7 software (Qimaging) or SPOT Image Capture software (SPOT Imaging), and electrode sites were verified by comparing the lesion sites in these photographs to The Allen Mouse Brain Atlas (https://mouse.brain-map.org/static/atlas) and the Mouse Brain in Stereotaxis Coordinates by Paxinos and Franklin (2012). Due to the high channel count of these probes, as well as their linear geometry, it was possible to account for small differences in the depth of each probe by selecting channels of similar depths across different probes. This resulted in reduced variability between animals in a range of neurophysiological measures.

2.13 Statistics

All statistical analysis was performed in MATLAB using a number of different built-in functions. Statistical analysis varied depending on the type of analysis

performed, however the majority of statistical analysis was performed using mixed ANOVA with varying number of factors. The Novel/Familiar environment task involved 2 novel sessions and 8 familiar sessions, so in order to account for this imbalance, data was averaged across all novel and all familiar sessions. For the majority of analyses, mixed ANOVAs had two factors, with genotype as the between-subjects factor, and novelty as the within-subjects factor. Other additional factors included region for the EEG analysis, and slice plane for the *in vitro* slice analysis. Significant main effects or interactions from an ANOVA was subsequently followed up with relevant planned comparisons. Statistical tests used for each analysis are noted alongside the results of that analysis, throughout this thesis.

3 Chapter 3

3.1 Authors Note

Some of the content of this Chapter has been previously submitted for publication, and is available on the preprint server bioRxiv (Walsh et al., 2021). In order to adhere to restrictions on word counts, the amount of content in this published work is greatly reduced compared to the work presented in this Chapter, and a variety of material changes have since been made, including key analytical changes. As such, the content of this published work is highly different to the work shown here, but for the sake of transparency, this work has been provided as an appendix to this thesis.

3.2 Introduction

The retrosplenial cortex (RSC) is considered to play a critical role in spatial learning and memory. Damage to this region results in severe impairments in navigation and landmark processing (see Mitchell *et al.*, 2018 for review). There is a large body of experimental evidence suggesting the retrosplenial cortex is involved in the encoding, retrieval and consolidation of spatial and contextual memory (see Todd and Bucci, 2015 for review). Optogenetic stimulation of RSC neurons is sufficient to elicit retrieval and consolidation of contextual memories (Cowansage et al., 2014; De Sousa et al., 2019). RSC neurons encode a range of contextual information during navigation (Koike et al., 2017), and inactivation of the RSC during spatial memory and contextual fear memory tasks impairs performance in these tasks (Czajkowski et al., 2014; Kwapis et al., 2015), suggesting the RSC is involved in the storage of spatial information. Finally, Iaria *et al.*, (2007) demonstrated that while hippocampal subregions are differentially

involved in the encoding and retrieval of spatial information, the entire RSC is active during both processes. Spatial learning and memory impairments have been shown to be one of the earliest aspects of cognitive impairment in Alzheimer's disease (AD). Patients exhibit disturbances in specific spatial memory processes associated with the RSC (Laczó et al., 2009; Vann et al., 2009; Morganti et al., 2013). During the early stages of AD, the retrosplenial gyrus has been shown to exhibit regional hypometabolism (as measured by FDG-PET), and considerable atrophy (Minoshima et al., 1997; Choo et al., 2010). As such, the RSC is a region of great interest in research into the brain's function in health and AD.

Measurable correlates of brain function can have great value in fundamental neuroscience. They can aid the understanding of the complex ways in which the brain processes information and performs its many tasks, and also indicate how such functionality may be affected in disease. Similarly, these "functional biomarkers" can provide measurable benchmarks against which to test interventions which may affect or restore normal brain function (Walsh et al., 2017). Of the growing number of methodologies available for investigating brain function, *in vivo* electrophysiology remains a powerful tool with a superior temporal resolution to all others. The temporal resolution of electrophysiology combined with the spatial specificity afforded by intracranial recordings make *in vivo* electrophysiology an invaluable tool for discovering functional correlates of brain function and disease-associated dysfunction. Few local field potential studies have been performed in the RSC to date, and those which have focus on the relationships between the RSC and the hippocampus. Alexander et al (2018) demonstrated the presence of theta and gamma oscillations in the RSC during

wake, spiking of RSC neurons was phase locked to these theta and gamma oscillations, and that gamma amplitude was coupled to theta phase in this region.

In order to investigate the role of the RSC in spatial learning and memory, we recorded LFPs and multi-unit spiking activity from this region, while mice freely explored either a novel or familiar environment. To probe the effects of AD-associated amyloid pathology on RSC function we used J20 mice, a widely employed mouse model of amyloidopathy. In this Chapter, we describe short, phasic bursts of beta (20-30 Hz) oscillations, termed “beta bursts”, that occur within the RSC, while mice freely explore an environment. Beta bursting activity is significantly increased during exposure to a novel environment, and these bursts are correlated with increased neuronal spiking in the RSC. These data demonstrate that beta bursting in the RSC is a robust neurophysiological correlate of environmental novelty and may have a role in the storage and retrieval of cortical spatial representations. Finally, we observed aberrant beta bursting activity and an uncoupling of beta bursting from neuronal spiking in the RSC in J20 mice, which may disrupt its function, and underlie spatial learning and memory deficits seen in these mice (Cheng et al., 2007).

3.3 Methods

3.3.1 Animals

8 male J20 mice and 6 wild-type littermates were bred at the University of Exeter and housed on a 12-hour light/dark cycle. All procedures were carried out in accordance with the UK Animal (Scientific Procedures) Act 1986 65 and were approved by the University of Exeter Animal Welfare and Ethical Review Body. Access to food and water was provided ad libitum. All animals were kept on a 12-hour light/dark cycle, with the light/dark cycle matching the normal daylight/night-

time cycle, meaning all interactions including handling, surgery and behaviour took place during the light cycle. Mice were group housed prior to surgery, and single housed post-surgery, in order to prevent damage to the surgical implants. All mice were between 6 to 8 months of age at the time of recordings.

3.3.2 Surgery

Mice were unilaterally implanted with a 16 channel, single shank silicon probe (NeuroNexus Technologies, A1x16-5mm-100-177-CM16LP), in the right retrosplenial cortex (AP –2 mm, ML +0.5 mm, DV +1.75 mm, 0° Pitch, Figure 3.1c). Mice were anaesthetised using isoflurane and fixed into a stereotaxic frame. A small craniotomy was drilled over the desired co-ordinate, and at least one hole was drilled in each of the major skull plates, in which miniature screws were placed to act as supports (Antrin Miniature Specialties). The probe was slowly lowered into the desired location, and fixed in place with dental cement (RelyX Unicem, 3M). The ground wire from the probe was connected to a silver wire, attached to a screw overlying the cerebellum. Throughout surgery, body temperature was monitored with a rectal probe and regulated by a feedback-controlled heat mat. Animals were kept hydrated by subcutaneous injections of Hartmann's solution once per hour of surgery (0.01 ml/g body weight).

3.3.3 Behaviour

The Novel/Familiar environment task was used to probe the neurophysiological responses to contextual novelty (Figure 3.1). Individual mice were tethered to the recording apparatus, and placed in one of two high-sided recording arenas: one square, with black and white stripes, and one circular and lacking stripes (Figure 3.1a). These arenas were custom built by another member of our lab and this behavioural paradigm has been previously validated. These two arenas were

similar in size; the square arena measured 56x56 cm and the circular arena had a diameter of 62 cm, while the height of both arenas measured 65 cm. Both arenas each had two internal visual cues, placed on opposite sides of the arena. The experimental procedure is illustrated in (Figure 3.1b). Firstly, the animals were places into the area and were allowed to freely explore their environment for 15 minutes, after which, they were returned to their home cage. After 15 minutes in their home cage, the animal was returned to the same recording arena for another 15 minutes, and allowed to freely explore. Following this, the animal was returned to its home cage. This protocol was repeated at the same time of day, for 5 consecutive days, but on the fifth day, the animal was placed in the other, previously unseen arena. The order of exposure to these arenas was counterbalanced between animals. Each session can therefore be described by the experimental day, and the particular session within that day, with session A being the first, and session B being the second. Using this nomenclature, Sessions 1a and 5a were 'novel' sessions, while the remaining sessions were 'familiar' sessions. In order to reduce the stress associated with the recording process, animals were acclimatised to this process during 10-minute test session 3 days prior to the start of the experiment, in which the animal was tethered and recorded from while in its home cage. An added benefit of this was to familiarize the animals with this experimental procedure, thus ensuring that perceived novelty during the first experimental session was limited to the environment, and not the experience of being tethered to the recording apparatus.

3.3.4 Data Analysis

All analyses were performed for a single central channel in the dysgranular and a separate single central channel in granular RSC. The location of each channel

was estimated from post-hoc histology. Due to a surgical inaccuracy in a single wild-type animal, the probe was too deep to isolate any channels in the dysgranular RSC. It is for that reason that for all analyses, n = 8 for J20 mice in both granular and dysgranular RSC, while in wild-type mice n = 5 in the dysgranular RSC and n = 6 in the granular RSC. Fourteen mice in total were used in this study, 6 wild-type and 8 J20, with each mouse undergoing a total of ten recording sessions (5 days, 2 sessions per day). Unfortunately, the local field potential data from Day 3 session 1 (i.e. session 3a) was corrupted for a single wild-type mouse, and therefore data for this mouse from this session was omitted from all figure making and statistics.

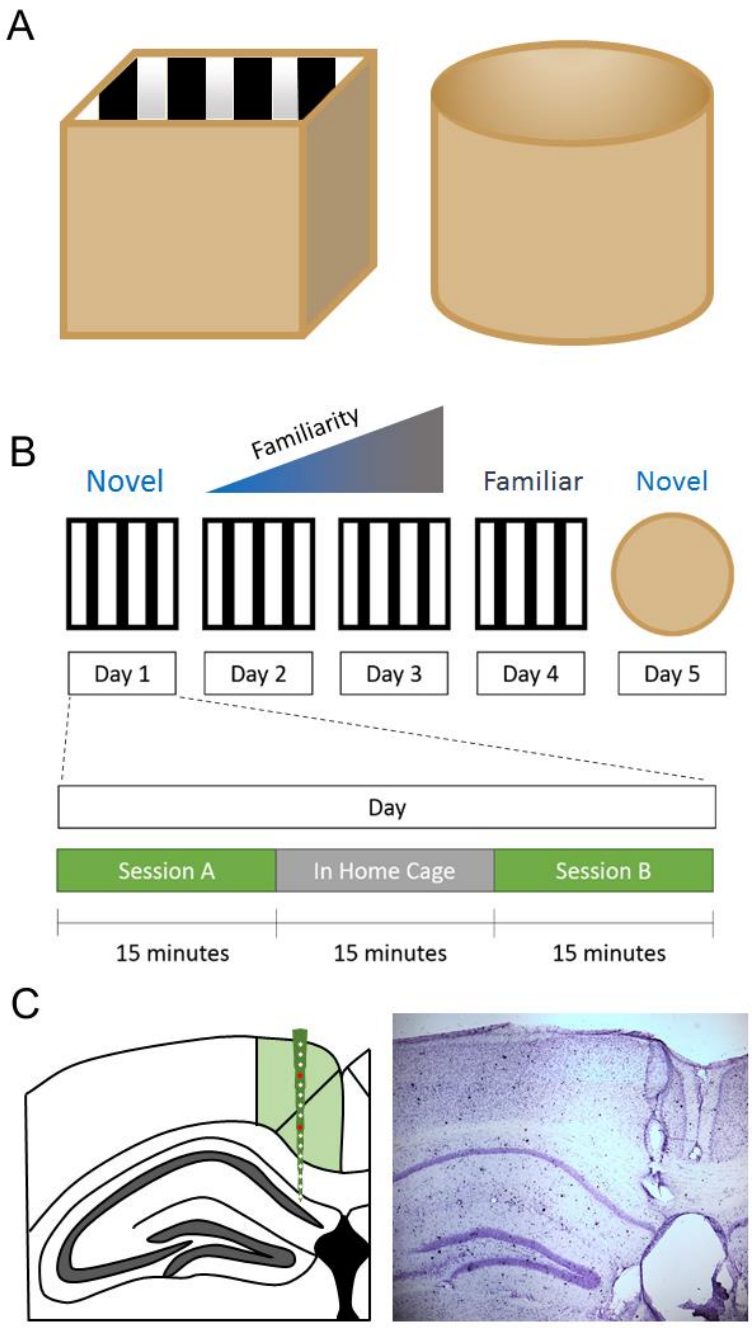

Figure 3.1 Experimental Design
A. Diagrams of the recording arenas used for this study. Both are roughly equal sized, one is square, with black and white stripes along the walls and floor (left) and the other is cylindrical with plain brown floor and walls. B. Experimental procedure for the novel/familiar environment task. A mouse is placed in one of the recording arenas for two 15-minute sessions, referred to as sessions A and B, with a 15-minute break in their home cage between the two sessions. This is repeated in the same arena for 4 consecutive days, after which the arena is switched for the 5th and final day. C. Single shank, 16 channel silicon probe electrodes were implanted in the retrosplenial cortex (green), so that they spanned the dysgranular (upper green section) and granular (lower green section) subregions. In order to verify the location of the electrodes, electrolytic lesions were made prior to perfusion, and slices were histologically prepared using Cresyl Violet stain. An example is shown (right).

3.3.5 Histology

Upon completion of the experiments, mice were killed using an overdose of sodium pentobarbital (Euthetal), and an isolated stimulator was used to produce electrolytic lesions at the recording sites. Mice were then transcardially perfused with 40% paraformaldehyde (PFA), and their brains were extracted and stored in PFA for 24 hours, after which they were transferred to phosphate-buffered saline (PBS) prior to sectioning. Brains were sliced into 100 µm sagittal sections using a vibratome (Leica VT1200), and stained with Cresyl Violet (Figure 3.1c, right). Digital pictures were taken using QCapture Pro 7 software (Qimaging), and electrode sites were verified by comparing the lesion sites in these photographs to The Allen Mouse Brain Atlas (https://mouse.brain-map.org/static/atlas). Due to the high channel count of these probes, as well as their linear geometry, it was possible to account for small differences in the depth of each probe by selecting channels of similar depths across different probes. This resulted in reduced variability between animals in a range of neurophysiological measures. As previously mentioned, in order to confirm age-related amyloid pathology in our J20 mice, we performed amylo-glo staining to stain for plaques in both 8-month old and 12-month old J20 mice, as well as age-matched wild-type littermates (Figure 3.2). This staining revealed an age-related deposition of amyloid plaques in both the hippocampus and retrosplenial cortex, with low levels of plaques in 8-month old animals, but widespread plaques by 12 months of age.

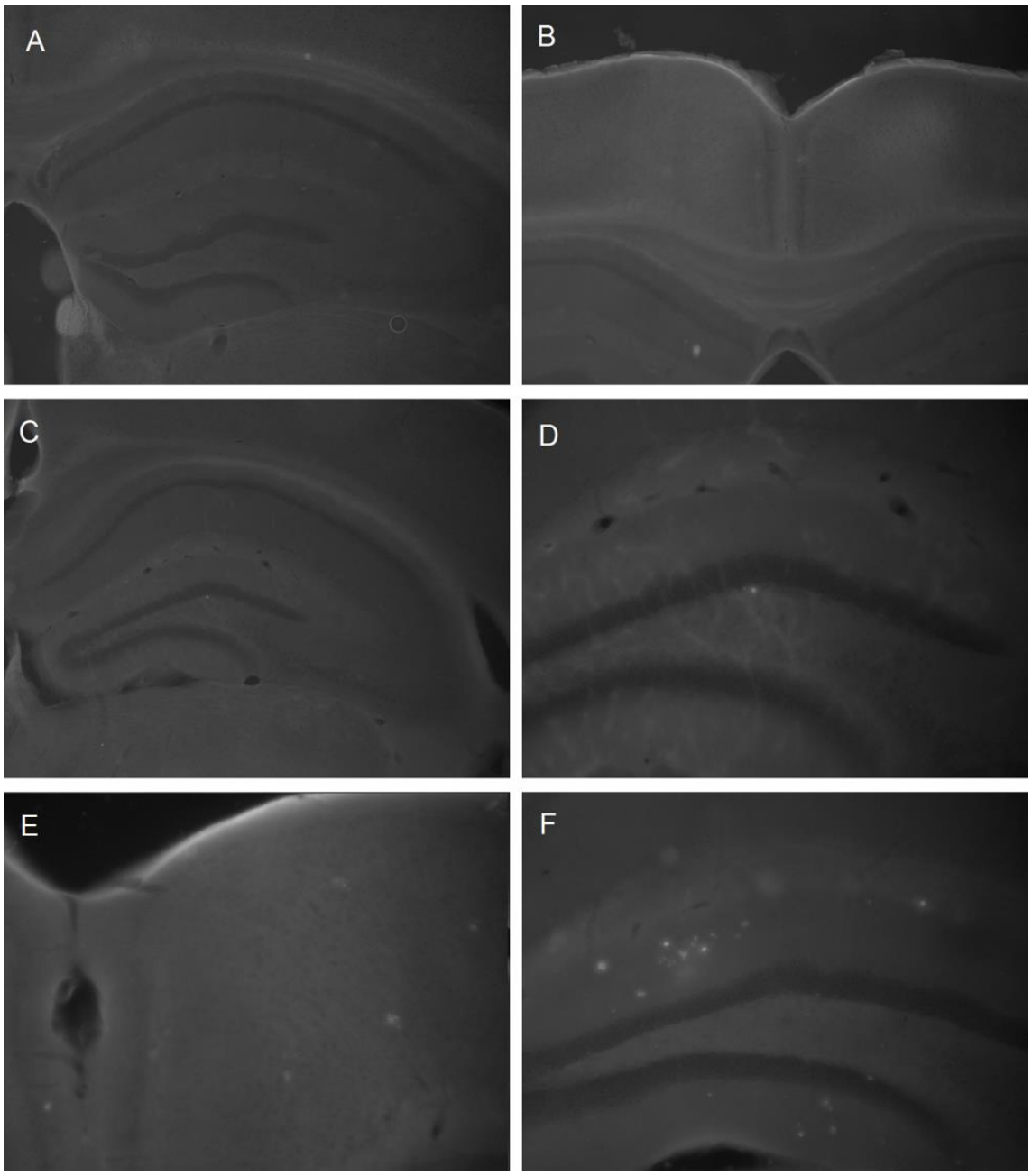

Figure 3.2 Amylo-glo staining of J20 mouse brains reveals amyloid plaques

Brains from 8-month old and 12-month old J20 mice, and age matched littermates were sectioned and stained for amyloid plaques using amylo-glo staining. Amyloid plaques are completely absent from both the hippocampus (A) and retrosplenial cortex (B) of 12-month old wild-type mice. In 8-month old J20 mice, amyloid pathology is sparse, with only a few amyloid plaques in the hippocampus (C). These plaques appear small and dense, and are generally seen in the dentate gyrus (D). In 12-month old J20 mice, there are numerous plaques throughout both the retrosplenial cortex (E) and hippocampus (F). In the hippocampus these are most prevalent in the molecular layer of the dentate gyrus, and are more diffuse than plaques in 8-month old J20 mice. Magnifications: A-C, 4x; D-F, 10x.

3.4 Results

To investigate neurophysiological correlates of spatial learning and memory in the retrosplenial cortex (RSC), local field potentials were recorded from across the entire dorsoventral axis of the RSC, while animals underwent a novel/familiar environment task. The RSC is made up of two distinct subdivisions: dysgranular (RSCdg), and granular (RSCg). While these regions are strongly interconnected, the neuroanatomical connectivity of these regions has been shown to differ (van Groen and Wyss, 1992; Van Groen and Wyss, 2003), therefore it is possible that the functional neurophysiology may vary as well, especially during a behavioural paradigm such as this, where spatial learning and memory processes may be stimulated. Due to the anatomical positioning of these subdivisions in rodents, it is possible to record from both RSCdg and RSCg simultaneously, using a single, vertical silicon probe (Figure 1C). Therefore, for this study, our analyses were performed for both subdivisions.

3.4.1 Behaviour

In order to investigate the behavioural response to environmental novelty, tracking data was used to investigate how locomotor activity varied between, and within recording sessions, and to determine whether there were any differences in locomotor activity between wild-type and J20 mice. Moreover, it is important to note that oscillatory activity in the brain can change dramatically with changes in running speed. In the hippocampus for example, theta and gamma power have been shown to be positively correlated with running speed (Chen et al., 2011; Ahmed and Mehta, 2012). It is for this reason that locomotor activity must be considered when interpreting changes in oscillatory activity.

As shown in (Figure 3.3a), location tracking reveals that during novel sessions, animals explore the environment thoroughly and continue exploring throughout the recording session. Conversely, during familiar sessions, animals explore a far smaller area of the arena, tending to spend most of the session at the edges of the arena and in the corners (Figure 3.3b). Running speed was calculated from tracking data and averaged across the entire 15 minutes of each recording session (Figure 3.3c, left). Average running speed was significantly higher overall during novel sessions (Main Effect Novelty - $F(1,12) = 29.4$, $p = 1.5e\text{-}4$, Mixed ANOVA). Running speed was higher on average during novel sessions for both wild-type (Nov: 6.8 ± 0.3; Fam: 5.1 ± 0.4, $p = 0.002$) and J20 mice (Nov: 8 ± 0.5; Fam: 6.7 ± 0.5, $p = 0.003$), and there was no significant overall difference between average running speed in wild-type and J20 mice (Main Effect Genotype - $F(1,12) = 2.7$, $p = 0.13$, Mixed ANOVA). In these experiments, the most important part of the session with regards to behaviour is likely to be the first minute or so, as the animal rapidly processes its environment and determines it to be either novel or familiar. For this reason, we repeated the previous running speed analysis but instead for only the first minute of each session (Figure 3.3c, right). As before, average running speed was significantly higher overall during novel sessions (Main Effect Novelty - $F(1,12) = 33.7$, $p = 8.4e\text{-}5$, Mixed ANOVA). Running speed was higher during the first minute of novel sessions than the first minute of familiar sessions for both wild-type (Nov: 8.4 ± 0.5; Fam: 4.3 ± 0.5, $p = 4.9e\text{-}4$) and J20 mice (J20 - Nov: 9.6 ± 1; Fam: 7 ± 0.7, $p = 0.005$), and as before, there was no significant overall difference between average running speed in wild-type and J20 mice (Main Effect Genotype - $F(1,12) = 2.1$, $p = 0.2$, Mixed ANOVA). Finally, we calculated the total distance travelled during each second of each recording session in order to further quantify the animals

behaviour within sessions, and produced cumulative frequency graphs shown in Figure 3.3d. During both novel (left) and familiar sessions (right), animals move at a relatively steady pace throughout the entire 15 minutes of each session, as indicated by the linear relationship between total distance travelled and time. In order to quantify this, average running speed during the initial part of the session (first minute) and the final part of the session (last 10 minutes) were calculated for each session and averaged across novel (Figure 3.3e, left) and familiar sessions (Figure 3.3c, right). Average running speed was significantly higher overall during novel sessions (Main Effect Novelty - $F(1,12) = 35$, $p = 7e\text{-}5$, Mixed ANOVA), however there was no significant overall difference in running speed between the initial and final part of the recording sessions or between the two genotypes.

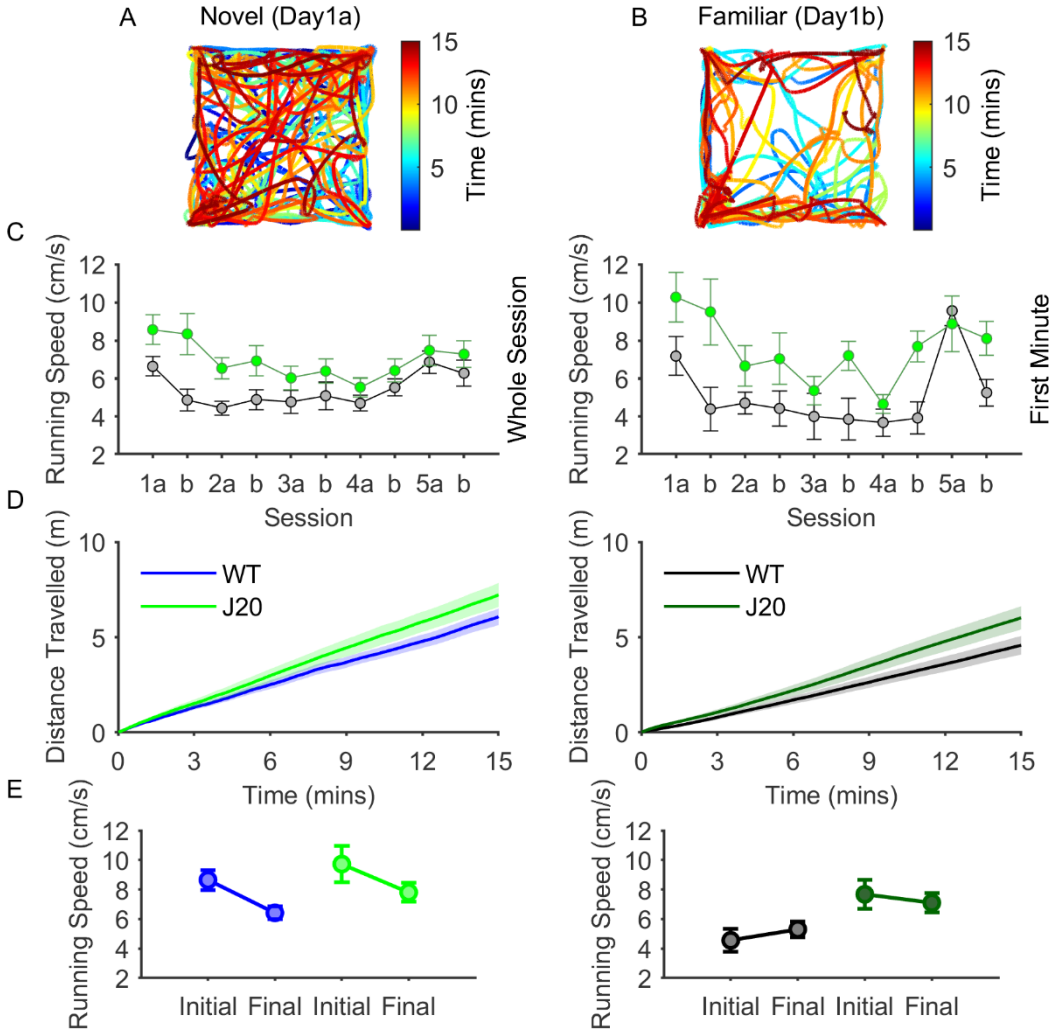

Figure 3.3 Animals explore significantly more during novel sessions.
A. Graph showing the location of a single wild-type animal across the entire 15 minutes of a novel session (Day1a), with the time represented by the color of the line. During novel sessions, animals thoroughly explore the arena, throughout the session. B. Graph showing the location of the same wild-type animal in A, but in the subsequent familiar session (Day1b). During familiar sessions, animals are far less exploratory and spend much more time at the edges of the arena.
C. Graphs showing the average running speed of wild-type and J20 mice in each session, averaged across the whole session (left), and the first minute of each session (right). Average running speed was higher overall during novel sessions, for both the whole session ($p = 1.5e-4$) and first minute ($p = 8.44e-5$). There was no significant difference between average running speeds in wild-type and J20 mice. D. Cumulative frequency graphs showing the total distance travelled by wild-type and J20 mice during novel (left) and familiar sessions (right). Animals appear to explore throughout both novel and familiar sessions. E. Graphs showing running speed during novel (left) and familiar sessions (right), for wild-type and J20 mice. Running speed was quantified for the initial minute of each session, and final 10 minutes. Running speed was significantly higher overall during novel sessions ($p = 7e-5$), however there was no significant effect of time or genotype on running speed. (Data shown as mean ± SEM, WT: n = 6, J20: n = 8).

3.4.2 Dysgranular Spectral Analysis

Local field potentials from RSCdg show a clear, continuous peak in theta frequency band (5-12 Hz) throughout recording sessions (Figure 3.4a), as well as less distinct peaks at higher frequencies. In order to investigate any changes in oscillatory activity in RSCdg during environmental novelty, power spectral analysis was performed on the entire 15 minutes of each session. These power spectra were averaged across novel and familiar sessions for wild-type and J20 mice. Significant findings are summarised in Table 1, however a more detailed account of these findings, including descriptive statistics, will be listed here in-text. Gamma power was significantly higher overall during novel sessions (Gamma: Main Effect Novelty - $F(1,11) = 21.6$, $p = 7e\text{-}4$, Mixed ANOVA). Gamma power was significantly higher during novel sessions in wild-type (WT - Nov: 10.6 ± 0.1 dB; Fam: 10.2 ± 0.1 dB, $p = 0.01$) and J20 mice (J20 - Nov: 11.2 ± 0.2 dB; Fam: 10.8 ± 0.2 dB, $p = 0.004$). There were significant interactions between the effects of genotype and novelty on delta, alpha and beta power (Delta: Interaction - $F(1,11) = 9.4$, $p = 0.01$, Mixed ANOVA; Alpha: Interaction - $F(1,11) = 6$, $p = 0.03$, Mixed ANOVA; Beta: Interaction - $F(1,11) = 5.2$, $p = 0.04$, Mixed ANOVA). Delta power was significantly higher during familiar sessions in wild-type (WT - Nov: 22.1 ± 0.7 dB; Fam: 22.5 ± 0.7 dB, $p = 0.02$), but not J20 mice. Beta power was significantly higher during novel sessions in both wild-type (WT - Nov: 14.2 ± 0.2 dB; Fam: 13.7 ± 0.2 dB, $p = 0.02$) and J20 mice (J20 - Nov: 16.7 ± 0.3 dB; Fam: 15.8 ± 0.3 dB, $p = 2e\text{-}5$). Moreover, beta power was significantly higher in J20 mice than in wild-type mice, for both novel (Nov - WT: 14.2 ± 0.2 dB; J20: 16.7 ± 0.3 dB, $p = 0.001$) and familiar sessions (Fam - WT: 13.7 ± 0.2 dB; J20: 15.8 ± 0.3 dB, $p = 0.002$).

Upon closer inspection of power spectrograms (Figure 3.4a), it was clear that spectral activity changed within novel sessions. Power in the 20 – 40 Hz range appeared to be higher in the first minute of the session and diminish over time. As exemplified in (Figure 3.4c), transient epochs of high power in the 20-40 Hz range are seen throughout the early stages of the session. By performing the same power spectral analysis as before on only the first minute of each session, clearer differences appeared between novel and familiar sessions. Theta, alpha, beta and gamma power were significantly higher overall during novel sessions (Theta: Main Effect Novelty - $F(1,11) = 14.7$, $p = 0.003$, Mixed ANOVA; Alpha: Main Effect Novelty - $F(1,11) = 24.3$, $p = 4e\text{-}4$, Mixed ANOVA; Beta: Main Effect Novelty - $F(1,11) = 47.5$, $p = 3e\text{-}5$, Mixed ANOVA; Gamma: Main Effect Novelty - $F(1,11) = 19.9$, $p = 0.001$, Mixed ANOVA). There was a significant interaction between the effects of genotype and novelty on delta power (Interaction - $F(1,11) = 8.3$, $p = 0.01$, Mixed ANOVA). Delta power was significantly higher during novel sessions in J20 mice (J20 - Nov: 22.8 ± 0.2 dB; Fam: 21.8 ± 0.2 dB, $p = 0.006$), but not wild-type mice. Moreover, alpha and beta power were significantly higher overall in J20 mice (Alpha: Main Effect Genotype - $F(1,11) = 7.2$, $p = 0.02$, Mixed ANOVA; Beta: Main Effect Genotype - $F(1,11) = 21.9$, $p = 7e\text{-}4$, Mixed ANOVA).

Across these time series, increased beta power occurred in brief, discrete epochs, as shown in the expanded power spectrogram in (Figure 3.5a). This can also be seen clearly in beta-filtered local field potentials, where these periods of high beta amplitude intersperse an otherwise very low amplitude oscillation. In order to understand the timescale and frequency domains of these events, wavelet analysis was used to investigate their time course and frequency profile

further. As exemplified in (Figure 3.5c), these individual events were short in duration, and peaked in the 20-30 Hz, beta band.

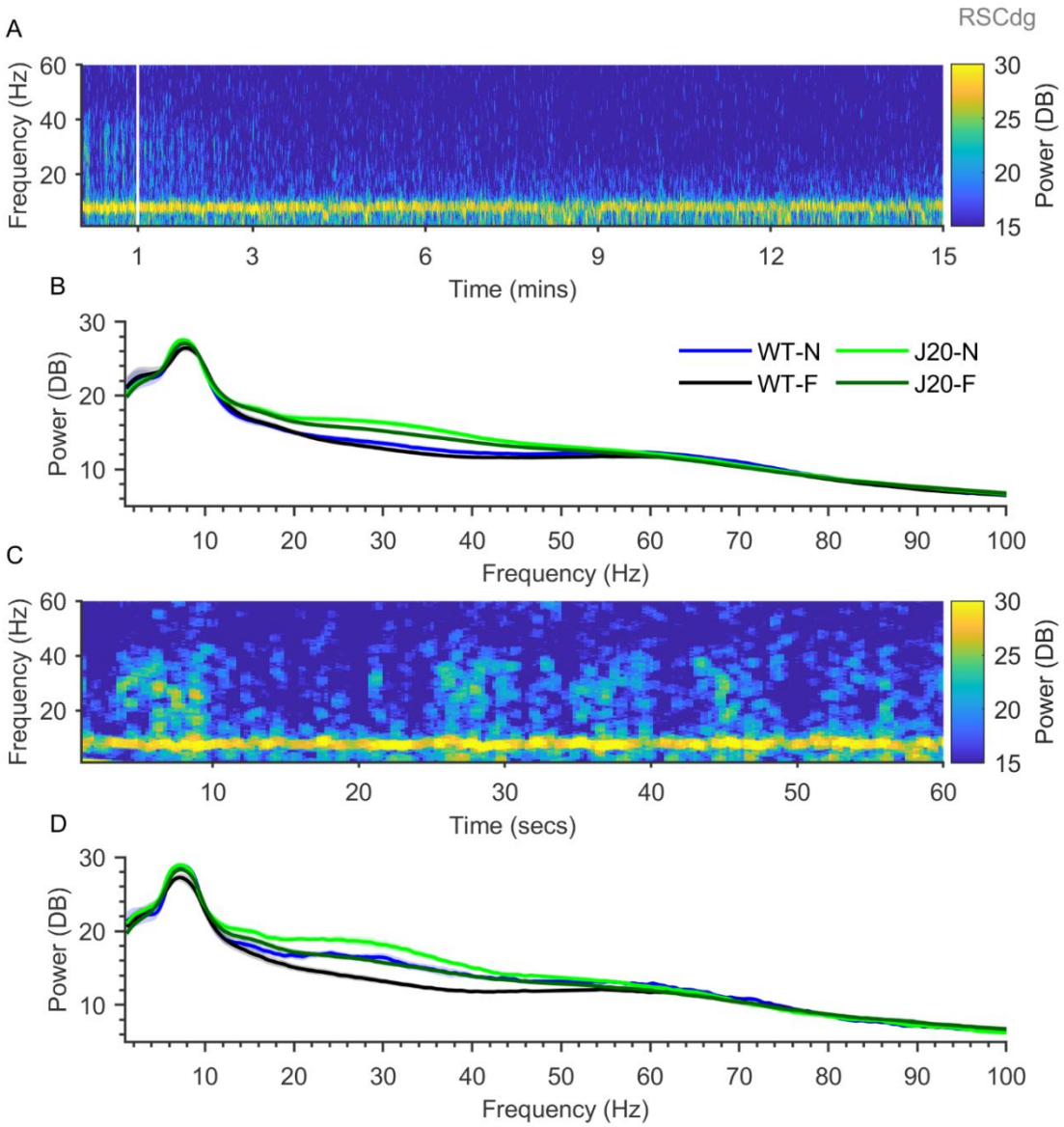

Figure 3.4 Beta (20-30 Hz) power is significantly higher during novelty in the dysgranular retrosplenial cortex in wild-type and J20 mice.
A. Example power spectrogram for an entire novel session in a wild-type mouse. B. Average power spectra for the entire 15 minutes of all novel and familiar sessions, for wild-type and J20 mice. Beta power was significantly higher during novel sessions in both wild-type ($p = 0.02$) and J20 mice ($p = 2e\text{-}5$). Moreover, beta power was significantly higher in J20 mice than in wild-type mice, during novel ($p = 0.001$) and familiar sessions ($p = 0.002$). C. Example power spectrogram shown in A, expanded to show the first 60 seconds of the session (before the white line). Short epochs of increased power in the 20-40 Hz range can be seen. D. Average power spectra for the first minute of all novel and familiar sessions, for wild-type and J20 mice. Beta power was significantly higher overall during novel sessions ($p = 3e\text{-}5$), and was significantly higher overall in J20 mice ($p = 7e\text{-}4$). (Data shown as mean ± SEM, WT: n = 5, J20: n = 8).

Table 1 Dysgranular spectral analysis - Summary of significant results

Analysis Type	Frequency Band	Relationship	p-value
Whole Session	δ	N X G	0.01
	δ	$f_{WT} > n_{WT}$	0.02
	α	N X G	0.03
	β	N X G	0.04
	β	$n_{WT} > f_{WT}$	0.02
	β	$n_{J20} > f_{J20}$	2.00E-05
	β	$n_{J20} > n_{WT}$	0.001
	β	$f_{J20} > f_{WT}$	0.002
	γ	n > f	7.00E-04
	γ	$n_{WT} > f_{WT}$	0.01
	γ	$n_{J20} > f_{J20}$	0.004
First Minute	δ	N X G	0.01
	δ	$n_{J20} > f_{J20}$	0.006
	θ	n > f	0.003
	α	n > f	4.00E-04
	α	J20 > WT	0.02
	β	n > f	3.00E-05
	β	J20 > WT	7.00E-04
	γ	n > f	0.001

N, novelty; G, genotype; N X G, interaction between novelty and genotype; n, novel; f, familiar; WT, wild-type; J20, J20; δ, delta; θ, theta; α, alpha; β, beta; γ, gamma

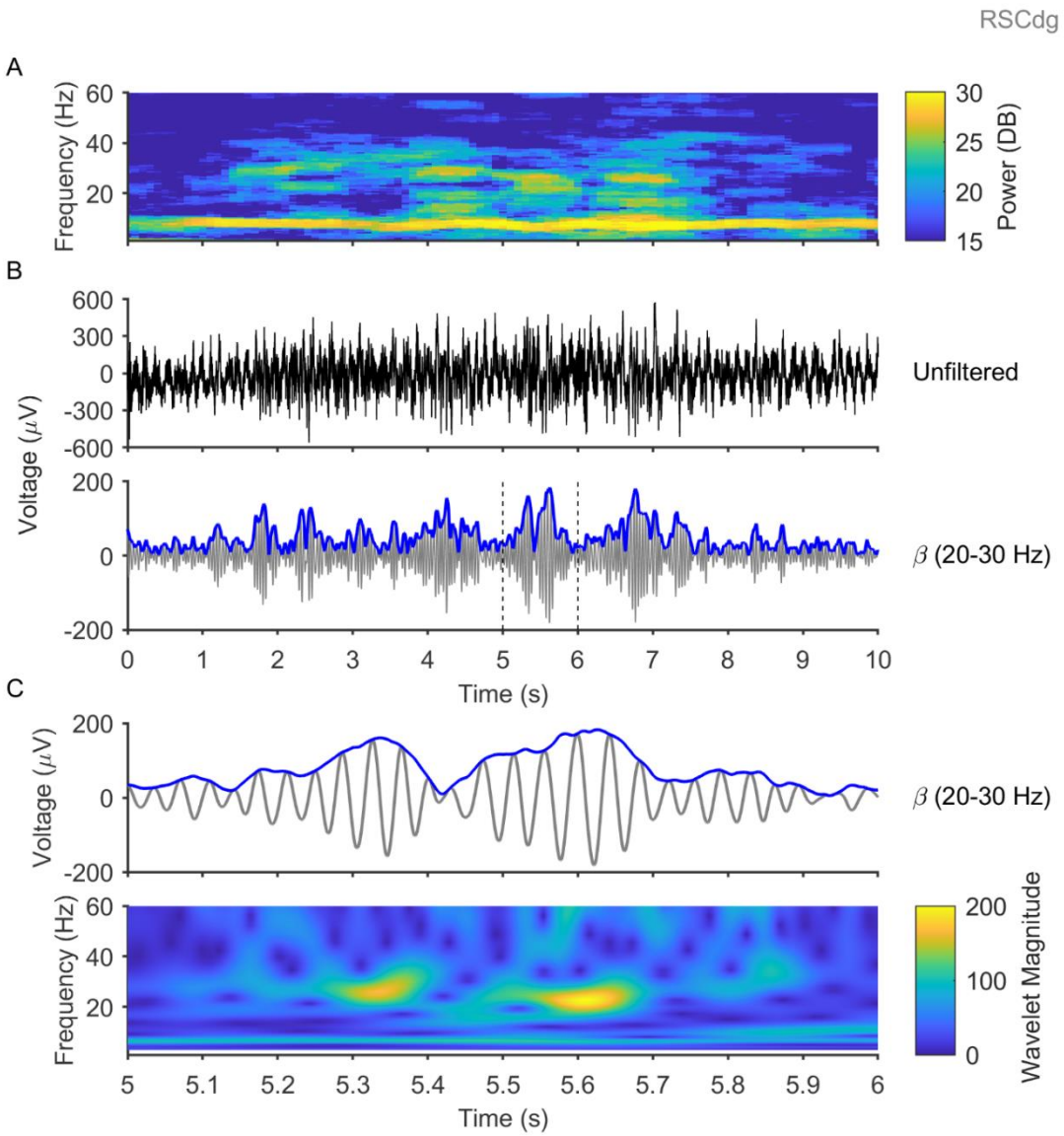

Figure 3.5 Retrosplenial local field potentials are marked by short, phasic increases in beta power, referred to as beta bursts.
A. Example power spectrogram showing transient increases in beta power. B. Local field potentials of data shown in A, both unfiltered (top), and filtered in the beta band (bottom), with the envelope amplitude in blue for clarity. The beta-filtered local field potential shows clear epochs of high beta amplitude, which intersperse a low amplitude continuous beta oscillation. C. Expanded trace of the dashed area in shown in B (top), and a continuous wavelet spectrogram of this time series (bottom). Due to the high temporal resolution of wavelet-based methods, these periods of high beta amplitude can be seen to be brief in duration, only lasting around 100-200 ms.

It is important to note here that as we previously mentioned, neural oscillations can change depending on the running speed of the animal, which may confound data such as those just shown. In order to counteract this, it is common to “speed control” the data in order to analyse and compare epochs during which the animal is running at a certain speed (Booth et al., 2016). For the data shown throughout this thesis, we decided not to speed control our data for several reasons. Firstly, as shown in (Figure 3.3), we found no significant differences between running speed in wild-type and J20 mice, demonstrating that local field potential data is coming from comparable locomotor states, and therefore any differences between network activity in these animals is unlikely to arise from differences in locomotor activity. Secondly, we also found no significant differences between running speed during the first minute of recording sessions and the last 10 minutes of recording sessions (Figure 3.3), again demonstrating that local field potential data is coming from comparable locomotor states, and that any differences in network activity between these two time points is not merely resulting from higher levels of locomotor activity in the first minute of the recording session, for example. Finally, as previously mentioned, an interesting feature of this data which will be explored in great detail throughout this thesis is the presence of transient oscillatory events in the 20-30 Hz band. Due to the transient nature of these oscillations, speed controlling this data would likely result in the exclusion of a large number of these events due to the discarding of epochs not in the speed band of interest, and therefore deprive us of a great deal of information such as the distribution of these events over time. With this decision in mind, it is therefore important to note that due to the significant overall increase in running speed during novel sessions in both wild-type and J20 mice, it is not possible to completely discount the effect this may have on network activity.

3.4.3 Dysgranular Beta Bursting Activity

In order to investigate this phasic beta activity in more depth, an algorithm was written to detect and analyse these “beta bursts”; the basis of this algorithm is illustrated in (Figure 3.6a). Briefly, epochs where beta amplitude exceeded a “hard threshold” of 2 standard deviations from mean for longer than 150 milliseconds were detected. The start and stop of each putative burst were determined as the moment the amplitude crossed a “soft threshold” of 1 standard deviation, prior to and following each burst.

With these transient epochs of high beta power now classified as discrete beta bursts, it was possible to compare this beta activity between sessions. As shown in (Figure 3.6b), there were significantly more beta bursts detected overall during novel sessions (Main Effect Novelty - $F(1,11) = 20.9$, $p = 8e\text{-}4$, Mixed ANOVA). Furthermore, there were significantly more beta bursts detected overall in J20 mice (Main Effect Genotype - $F(1,11) = 16.8$, $p = 0.002$, Mixed ANOVA).

Moreover, from the cumulative frequency plots shown in (Figure 3.6c), it is possible to visualise the rate of beta bursting over time, within sessions. As illustrated by the slope of these lines, the rate of beta bursting was reasonably steady throughout familiar sessions (Figure 3.6c, right), but substantially higher during the first few minutes of novel sessions, for both genotypes (Figure 3.6c, left). Beta bursting rate during the initial part of the session (first minute) and the final part of the session (last 10 minutes), was calculated for each session and averaged across novel and familiar sessions (Figure 3.6d). The rate of beta bursting was significantly higher overall during novel sessions (Main Effect Novelty - $F(1,11) = 18.6$, $p = 0.001$, Mixed ANOVA), and also significantly higher overall during the initial part of recording sessions (Main Effect Time - $F(1,11) =$

24.5, p = 4e-4, Mixed ANOVA). During novel sessions, initial burst rate was significantly higher than final burst rate for wild-type (WT - Nov Initial: 13 ± 1.6; Final: 0.9 ± 0.1, p = 0.01), and J20 mice (J20 - Nov Initial: 14.1 ± 3.6; Final: 2.0 ± 0.4, p = 0.004). Furthermore, there was no significant difference between wild-type and J20 mice for initial burst rate or final burst rate (Nov Initial - WT: 13 ± 1.6; J20: 14.1 ± 3.7, p = 0.8; Nov Final - WT: 0.9 ± 0.1; J20: 2 ± 0.4, p = 0.08).

During familiar sessions, initial burst rate was significantly higher than final burst rate for J20 mice (J20 - Fam Initial: 5.1 ± 0.5; Final: 2.1 ± 0.2, p = 1e-4), but not wild-type mice (WT - Fam Initial: 2.7 ± 0.5; Final: 1.4 ± 0.1, p = 0.07). Furthermore, initial burst rate and final burst rate were significantly higher in J20 mice than in wild-type mice (Fam Initial - WT: 2.7 ± 0.5; J20: 5.1 ± 0.5, p = 0.006; Fam Final - WT: 1.4 ± 0.1; J20: 2.1 ± 0.2, p = 0.03).

The minimum amplitude (2 standard deviations from mean) and duration thresholds (150 ms) used in this burst detection algorithm were chosen in order to detect the most significant events, however these thresholds were selected from visual inspection of the data and do not have any pre-existing physiological basis. While our minimum burst duration threshold was set at 150 ms, Sherman et al. (2016) noted that transient beta events in human neocortex typically lasted less than 150 ms. Therefore, we decided to perform the same burst detection analysis with different thresholds, in order to determine how sensitive our findings are to different algorithm parameters.

Firstly, instead of a minimum amplitude threshold of 2 standard deviations from the mean, we tested our burst detection algorithm with a minimum amplitude threshold of 1 standard deviation from the mean (Figure 3.7 Novelty-associated beta bursting in the dysgranular retrosplenial cortex (RSCdg) . As shown in

(Figure 3.7b), there was a significant interaction between novelty and genotype on the total number of beta bursts detected (Interaction - $F(1,11) = 7.9$, $p = 0.02$, Mixed ANOVA). There were significantly more beta bursts detected during novel sessions for J20 mice (J20 - Nov: 152 ± 4.9; Fam: 115 ± 3, $p = 8.9e\text{-}5$), but not wild-type mice (WT - Nov: 103 ± 4.7; Fam: 94 ± 1.5, $p = 0.27$). As shown in (Figure 3.7d), the rate of beta bursting was significantly higher overall during novel sessions (Main Effect Novelty - $F(1,11) = 26.3$, $p = 3e\text{-}4$, Mixed ANOVA), and also significantly higher overall during the initial part of recording sessions (Main Effect Time - $F(1,11) = 44.3$, $p = 3.6e\text{-}5$, Mixed ANOVA). During novel sessions, initial burst rate was significantly higher than final burst rate for wild-type (WT - Nov Initial: 29.6 ± 1.4; Final: 3.6 ± 0.3, $p = 0.002$), and J20 mice (J20 - Nov Initial: 29.4 ± 5.4; Final: 6.5 ± 1, $p = 8e\text{-}4$). Furthermore, there was no significant difference between wild-type and J20 mice for initial burst rate or final burst rate (Nov Initial - WT: 29.6 ± 1.4; J20: 29.4 ± 5.4, $p = 0.97$; Nov Final - WT: 3.6 ± 0.3; J20: 6.5 ± 1, $p = 0.05$). During familiar sessions, initial burst rate was significantly higher than final burst rate for wild-type (WT - Fam Initial: 9.9 ± 0.7; Final: 5.8 ± 0.2, $p = 0.01$), and J20 mice (J20 - Fam Initial: 14.7 ± 0.9; Final: 7.2 ± 0.6, $p = 2.3e\text{-}5$). Furthermore, initial burst rate was significantly higher in J20 mice than in wild-type mice (Fam Initial - WT: 9.9 ± 0.7; J20: 14.7 ± 0.9, $p = 0.003$).

Secondly, instead of a minimum duration threshold of 150 ms, we tested our burst detection algorithm with a minimum duration threshold of 100 ms (Figure 3.8). As shown in (Figure 3.8b), there were significantly more beta bursts detected overall during novel sessions (Main Effect Novelty - $F(1,11) = 16.4$, $p = 0.002$, Mixed ANOVA). Furthermore, there were significantly more beta bursts detected overall in J20 mice (Main Effect Genotype - $F(1,11) = 28.1$, $p = 3e\text{-}4$, Mixed ANOVA).

There were significantly more beta bursts detected during novel sessions for J20 mice (J20 - Nov: 212 ± 5.7; Fam: 177 ± 3.8, p = 8e-4), but not wild-type mice (WT - Nov: 166 ± 4.9; Fam: 151 ± 2.3, p = 0.16). As shown in (Figure 3.8d), the rate of beta bursting was significantly higher overall during novel sessions (Main Effect Novelty - F(1,11) = 24.3, p = 5e-4, Mixed ANOVA), and also significantly higher overall during the initial part of recording sessions (Main Effect Time - F(1,11) = 44.8, p = 3.4e-5, Mixed ANOVA). During novel sessions, initial burst rate was significantly higher than final burst rate for wild-type (WT - Nov Initial: 45.4 ± 2.7; Final: 6.4 ± 0.3, p = 0.001), and J20 mice (J20 - Nov Initial: 41.1 ± 7.7; Final: 9 ± 1.4, p = 1e-3). Furthermore, there was no significant difference between wild-type and J20 mice for initial burst rate or final burst rate (Nov Initial - WT: 45.4 ± 2.7; J20: 41.1 ± 7.7, p = 0.7; Nov Final - WT: 6.4 ± 0.3; J20: 9 ± 1.4, p = 0.2). During familiar sessions, initial burst rate was significantly higher than final burst rate for wild-type (WT - Fam Initial: 15.9 ± 1.2; Final: 9.5 ± 0.2, p = 0.006), and J20 mice (J20 - Fam Initial: 21.2 ± 1.3; Final: 11 ± 0.7, p = 3.3e-5). Furthermore, initial burst rate was significantly higher in J20 mice than in wild-type mice (Fam Initial - WT: 15.9 ± 1.2; J20: 21.2 ± 1.3, p = 0.02).

These results show that reducing the amplitude and duration thresholds in the beta burst detection algorithm results in a dramatic increase in the number of beta bursts detected, however the dramatic increases in the rate of beta bursting during novelty are consistent across all thresholds tested. While this validates our findings, in order to focus on the most significant transient beta events we will continue with the original thresholds for all for the remainder of this thesis.

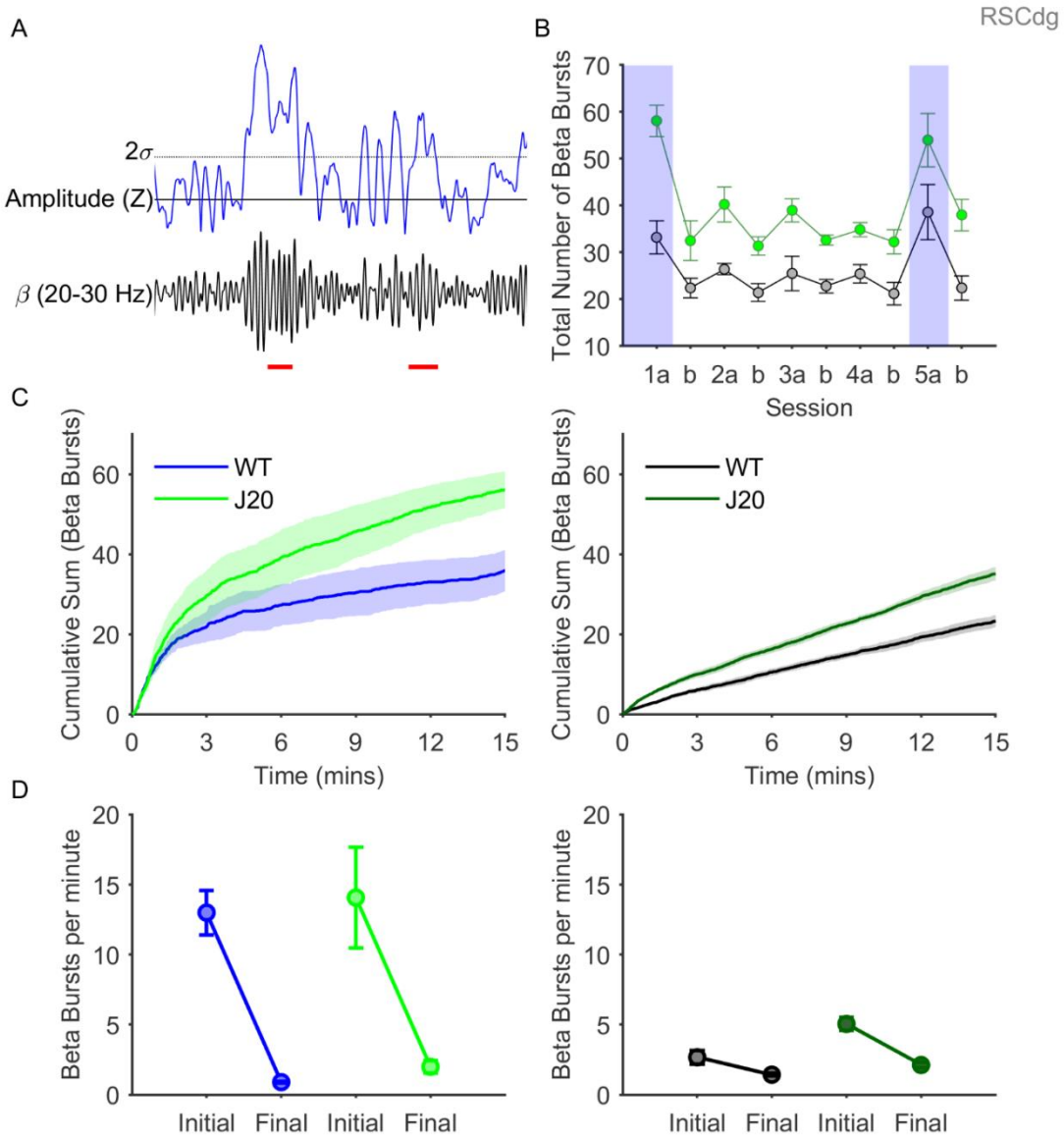

Figure 3.6 Beta bursting activity in the dysgranular retrosplenial cortex (RSCdg) is significantly higher during novelty.

A. Diagram illustrating how beta bursts were detected. B. Graph showing the average number of beta bursts detected in RSCdg in each session, for wild-type (black) and J20 mice (green). Novel sessions Day1a and Day5a are highlighted in blue for clarity. Significantly more beta bursts were detected during novel sessions than during familiar sessions ($p = 8e\text{-}4$). Moreover, significantly more beta bursts were detected overall in J20 mice ($p = 0.002$). C. Cumulative frequency graphs of beta bursts detected in novel (left) and familiar sessions (right), for wild-type and J20 mice. While beta bursting occurred monotonically during familiar sessions, during the first minute of a novel session, beta bursting was substantially increased. D. Graphs showing beta burst rate during novel (left) and familiar sessions (right), for wild-type and J20 mice. Burst rate was quantified for the initial minute of each session, and final 10 minutes. Beta burst rate was significantly higher overall during the initial minute of novel sessions than during the final 10 minutes of novel sessions for both wild-type ($p = 0.01$) and J20 mice ($p = 0.004$). (Data shown as mean ± SEM, WT: n = 5, J20: n = 8).

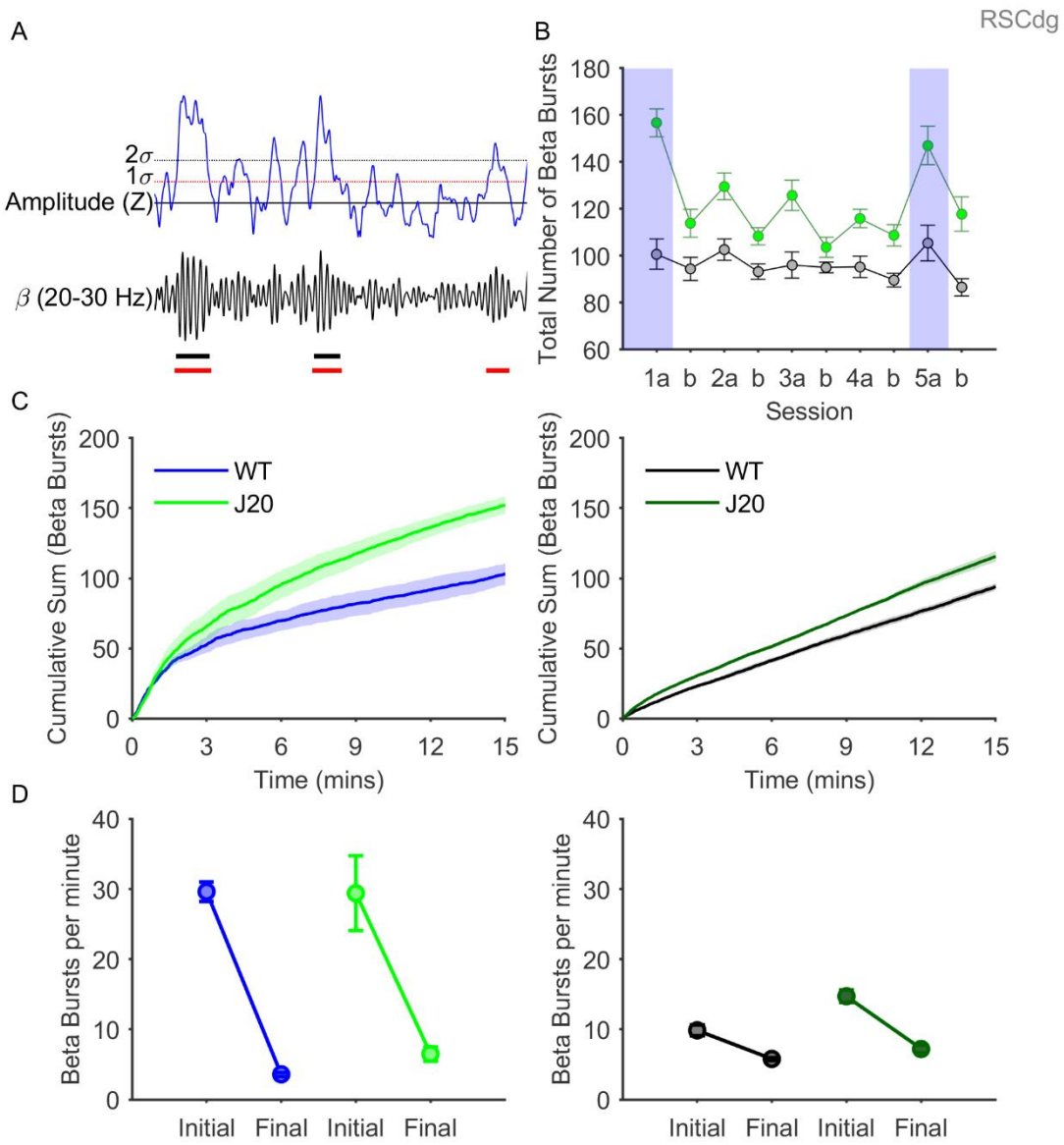

Figure 3.7 Novelty-associated beta bursting in the dysgranular retrosplenial cortex (RSCdg) can be detected with a lower amplitude threshold.
A. Diagram illustrating how beta bursts were detected, with the lower amplitude threshold (dotted) and detected beta bursts (solid) in red. B. Graph showing the average number of beta bursts detected in RSCdg in each session, for wild-type (black) and J20 mice (green). Novel sessions Day1a and Day5a are highlighted in blue for clarity. Significantly more beta bursts were detected during novel sessions than during familiar sessions for J20 mice ($p = 8.8e-5$) but not wild-type mice ($p = 0.27$). C. Cumulative frequency graphs of beta bursts detected in novel (left) and familiar sessions (right), for wild-type and J20 mice. While beta bursting occurred monotonically during familiar sessions, during the first minute of a novel session, beta bursting was substantially increased. D. Graphs showing beta burst rate during novel (left) and familiar sessions (right), for wild-type and J20 mice. Burst rate was quantified for the initial minute of each session, and final 10 minutes. Beta burst rate was significantly higher overall during the initial minute of novel sessions than during the final 10 minutes of novel sessions for both wild-type ($p = 0.002$) and J20 mice ($p = 8e-4$). (Data shown as mean ± SEM, WT: $n = 5$, J20: $n = 8$).

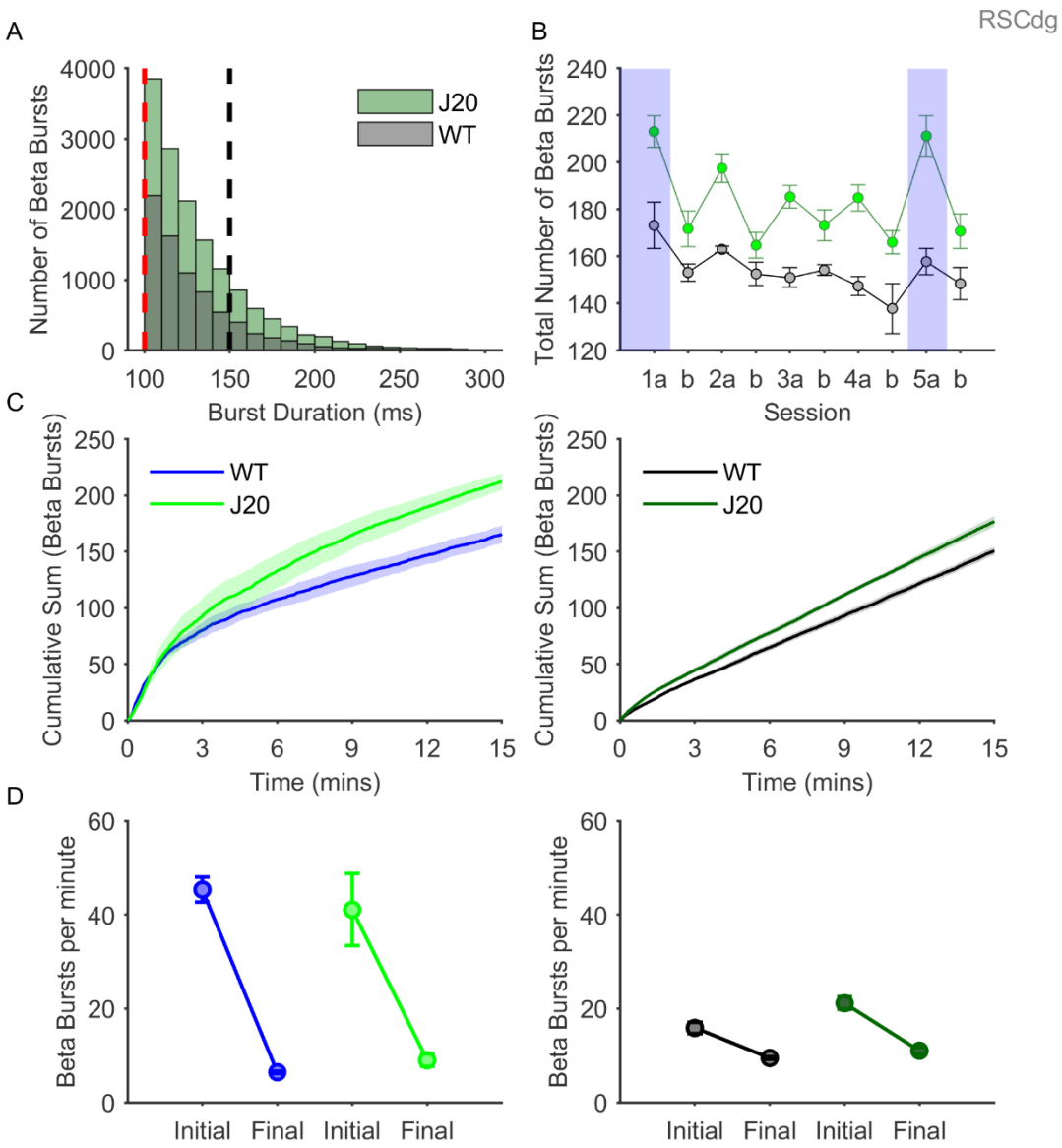

Figure 3.8 Novelty-associated beta bursting in the dysgranular retrosplenial cortex (RSCdg) can be detected with a lower duration threshold.
A. Histogram showing the duration of all beta bursts detected across all sessions for wild-type (grey) and J20 mice (green), with the lower duration threshold in red. B. Graph showing the average number of beta bursts detected in RSCdg in each session, for wild-type (black) and J20 mice (green). Novel sessions Day1a and Day5a are highlighted in blue for clarity. Significantly more beta bursts were detected during novel sessions than during familiar sessions for J20 mice ($p = 7.6e-4$) but not wild-type mice ($p = 0.16$). C. Cumulative frequency graphs of beta bursts detected in novel (left) and familiar sessions (right), for wild-type and J20 mice. While beta bursting occurred monotonically during familiar sessions, during the first minute of a novel session, beta bursting was substantially increased. D. Graphs showing beta burst rate during novel (left) and familiar sessions (right), for wild-type and J20 mice. Burst rate was quantified for the initial minute of each session, and final 10 minutes. Beta burst rate was significantly higher overall during the initial minute of novel sessions than during the final 10 minutes of novel sessions for both wild-type ($p = 0.001$) and J20 mice ($p = 0.001$). (Data shown as mean ± SEM, WT: n = 5, J20: n = 8).

3.4.4 Dysgranular Beta Burst Characteristics

In order to attempt to understand the nature of retrosplenial beta bursts, and the mechanisms which underlie them, a number of beta burst characteristics were investigated. For each beta burst, the duration and magnitude were calculated, as shown in (Figure 3.9a). Beta burst magnitude was significantly higher overall during novel sessions (Main Effect Novelty - $F(1,11) = 43.6$, $p = 4e\text{-}5$, Mixed ANOVA). As shown in (Figure 3.9b), beta bursts were significantly larger in magnitude during novel sessions in wild-type (Nov: 93.3 ± 3 µV; Fam: 78.5 ± 2.7 µV, $p = 0.004$) and J20 mice (J20 - Nov: 121 ± 4.4 µV; Fam: 102 ± 3.3 µV, $p = 8e\text{-}5$). Moreover, beta bursts were significantly larger in magnitude overall in J20 mice (Main Effect Genotype - $F(1,11) = 14.3$, $p = 0.003$, Mixed ANOVA). Beta burst duration was also significantly higher overall during novel sessions (Main Effect Novelty - $F(1,11) = 28.1$, $p = 3e\text{-}4$, Mixed ANOVA). As shown in (Figure 3.9c), beta bursts were significantly longer in duration during novel sessions in wild-type (WT - Nov: 190 ± 2.5 ms; Fam: 177 ± 1 ms, $p = 0.003$) and J20 mice (J20 - Nov: 189 ± 2 ms; Fam: 180 ± 0.9 ms, $p = 0.004$).

In order to understand the frequency profile of beta bursts, and to determine whether these oscillations conformed to the beta frequency band (20-30 Hz), power spectral analysis was performed on individual beta bursts. As a control, these burst spectra were compared to power spectra of epochs of equal length directly prior to each burst. These power spectra were averaged across all bursts and “pre-bursts”, for wild-type and J20 mice (Figure 3.9d). Overall, beta bursts were associated with a large significant increase in beta power (Main Effect Burst - $F(1,11) = 4811$, $p = 7e\text{-}16$, Mixed ANOVA), and smaller significant increases in alpha and gamma power (Alpha: Main Effect Burst - $F(1,11) = 169$, $p = 5e\text{-}8$,

Mixed ANOVA; Gamma: Main Effect Burst - F(1,11) = 46, p = 3e-5, Mixed ANOVA). Alpha, beta and gamma power were significantly higher during beta bursts in both wild-type (Alpha: WT – Pre-Burst: 16.5 ± 0.4 dB; Burst: 17.6 ± 0.3 dB, p = 3e-6; Beta: WT – Pre-Burst: 12.8 ± 0.3 dB; Burst: 19.9 ± 0.3 dB, p = 9e-14; Gamma: WT – Pre-Burst: 8.3 ± 0.2 dB; Burst: 8.6 ± 0.1 dB, p = 0.002), and J20 mice (Alpha: J20 – Pre-Burst: 17.7 ± 0.4 dB; Burst: 18.6 ± 0.4 dB, p = 7e-7; Beta: J20 – Pre-Burst: 15.2 ± 0.3 dB; Burst: 22.3 ± 0.3 dB, p = 8e-15; Gamma: J20 – Pre-Burst: 9.4 ± 0.2 dB; Burst: 9.8 ± 0.2 dB, p = 1e-4).

As illustrated by van Ede *et al.* (2018), continuous oscillations may appear as phasic burst events if their amplitude varies greatly over time. The time taken to complete one cycle of an oscillation is known as the period of the oscillation, and therefore how consistent this period is over a certain length of time can be considered as a measure of how rhythmic the oscillation is. The rhythmicity of beta oscillations during and outside of beta burst epochs can suggest potential mechanisms underlying their generation. Beta oscillations that are rhythmic both during and outside of bursts could be suggestive of a “dynamic amplitude modulation” mechanism, in that beta oscillations are a continuous oscillatory rhythm where the amplitude varies over time. Conversely, a loss of beta rhythmicity outside beta bursts may imply a “bursty generator” (Shin et al., 2017; van Ede et al., 2018), in that true beta oscillations only occur as transient bursts. Previous work suggests beta oscillations have a bursty generator, which we hoped to verify ourselves in this study (Shin et al., 2017). The period of beta oscillations was calculated for all beta bursts and all epochs without beta bursts, as described in the methods in Chapter 2, and the distribution of these beta periods were calculated and averaged across all burst and non-burst epochs, in

all sessions, for wild-type and J20 mice (Figure 3.9e). While the distribution of beta periods during beta bursts was reasonably consistent, peaking around 0.04s, equivalent to a 25 Hz oscillation, the distribution of beta periods in non-burst epochs was far more variable, with a large proportion of periods outside beta range. These data suggests that beta oscillations during beta bursts are highly rhythmic, while rhythmicity is far lower during non-burst epochs, suggesting a “bursty generator” model put forward by van Ede et al. (2018), however it is important to note that the data presented does not provide any conclusive proof of either mechanism, as neural oscillations are generated by synchronous firing of large populations of neurons, so more synchronous firing could be expected to result in both increased oscillatory amplitude, and increased rhythmicity. Furthermore, another caveat to this analysis is that digital filtering of complex signals is rarely perfect, and spectral leakage close to the band edges may result in irregular oscillations, especially when the oscillations are low in amplitude.

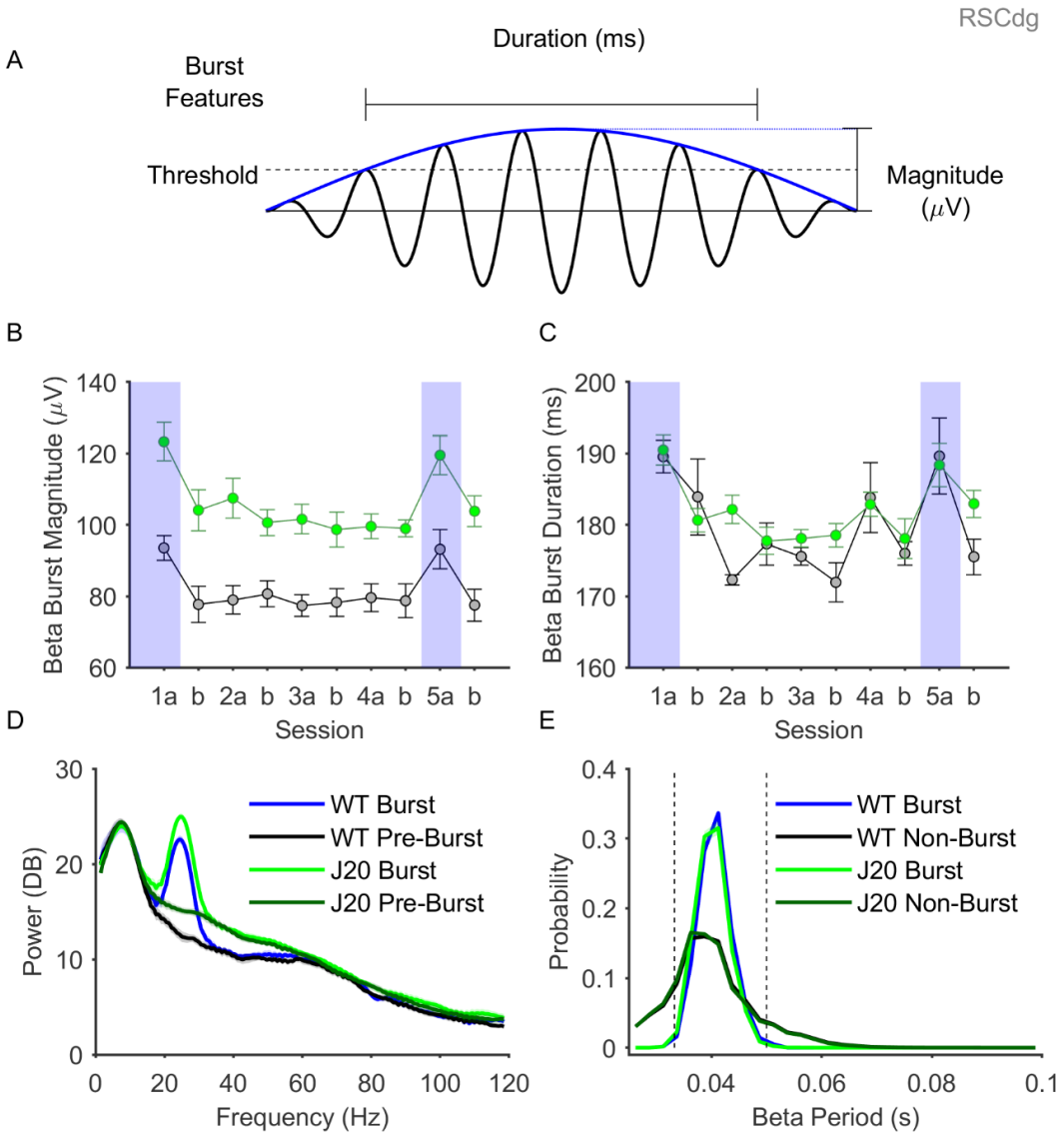

Figure 3.9 Beta burst characteristics in the dysgranular retrosplenial cortex (RSCdg).

A. Diagram illustrating how the magnitude and duration of beta bursts were calculated. B. Graph showing the average beta burst magnitude in RSCdg in each session, for wild-type and J20 mice. Beta bursts were overall significantly larger in magnitude during novel sessions ($p = 4e\text{-}5$). Moreover, beta bursts were also significantly larger overall in J20 mice ($p = 8e\text{-}5$). C. Graph showing the average duration of beta bursts in RSCdg in each session, for wild-type and J20 mice. Beta bursts were overall significantly longer in duration during novel sessions ($p = 3e\text{-}4$), however there was no significant overall difference between beta burst duration in wild-type and J20 mice. D. Average power spectra for beta burst, and pre-burst epochs. Beta bursts were associated with a large, significant increase in beta power during beta bursts ($p = 7e\text{-}16$). E. Average distributions of beta oscillation period for burst and non-burst epochs, in wild-type and J20 mice. Beta oscillations are tightly rhythmic during beta bursts, but highly arrhythmic during non-burst epochs. (Data shown as mean ± SEM, WT: n = 5, J20: n = 8).

3.4.5 Dysgranular Phase-amplitude Coupling

Phase-amplitude coupling (PAC) involves coupling between the amplitude of an oscillation and the phase of a lower frequency oscillation (Canolty et al., 2006). This interaction is generally thought to allow slow, large amplitude oscillations to coordinate faster, small amplitude local oscillations. Theta-gamma coupling is the most well studied form of PAC but PAC has been previously demonstrated for a range of other oscillation frequencies (Canolty et al., 2006; Tort et al., 2009; Daume et al., 2017). We investigated PAC across a range of frequencies in this study to determine whether retrosplenial PAC was associated with contextual novelty. Additionally although our beta rhythmicity data argues against a dynamic amplitude modulation mechanism underlying beta bursts (van Ede et al., 2018), coupling of beta amplitude to the phase of a slower oscillation could modulate beta bursting in the retrosplenial cortex.

Phase-amplitude coupling efficacy was calculated for a range of phase and amplitude frequencies, and plotted as comodulograms, showing the strength of coupling for pairs of frequencies. As shown in (Figure 3.10a), there were two large peaks in these comodulograms: one between theta phase and gamma amplitude, and another between theta phase and 12-30 Hz amplitude. This second peak did not conform to a single frequency band, and as such was treated as a composite of alpha and beta frequency. The strength of phase-amplitude coupling was quantified for theta-alpha/beta and theta-gamma coupling for each session (Figure 3.10b). There was a significant interaction between the effects of genotype and novelty on theta-alpha/beta coupling (Interaction - $F(1,11) = 8.9$, $p = 0.01$, Mixed ANOVA). Theta-alpha/beta coupling was significantly higher during novel sessions for wild-type (WT - Nov: 2.9 ± 0.1; Fam: 1.6 ± 0.1, $p = 4e\text{-}4$), but

not J20 mice (J20 - Nov: 2.3 ± 0.2; Fam: 2 ± 0.2, p = 0.15). There were no significant effects of novelty or genotype on theta-gamma coupling (Main Effect Novelty - $F(1,11) = 0.2$, $p = 0.7$, Mixed ANOVA; Main Effect Genotype - $F(1,11) = 0.7$, $p = 0.4$, Mixed ANOVA). It is important to note that in order to focus on the most physiologically and behaviourally relevant part of the session, this analysis was performed for the first minute of each session. When the same analysis was performed on the last minute of each session, there was no effect of genotype or novelty on coupling on either theta-alpha/beta coupling (Main Effect Genotype - $F(1,11) = 0.4$, $p = 0.56$, Mixed ANOVA; Main Effect Novelty - $F(1,11) = 4.6$, $p = 0.054$, Mixed ANOVA; Figure 3.11b, left) or theta-gamma coupling (Main Effect Genotype - $F(1,11) = 3.7$, $p = 0.08$, Mixed ANOVA; Main Effect Novelty - $F(1,11) = 0.2$, $p = 0.69$, Mixed ANOVA; Figure 3.11b, right).

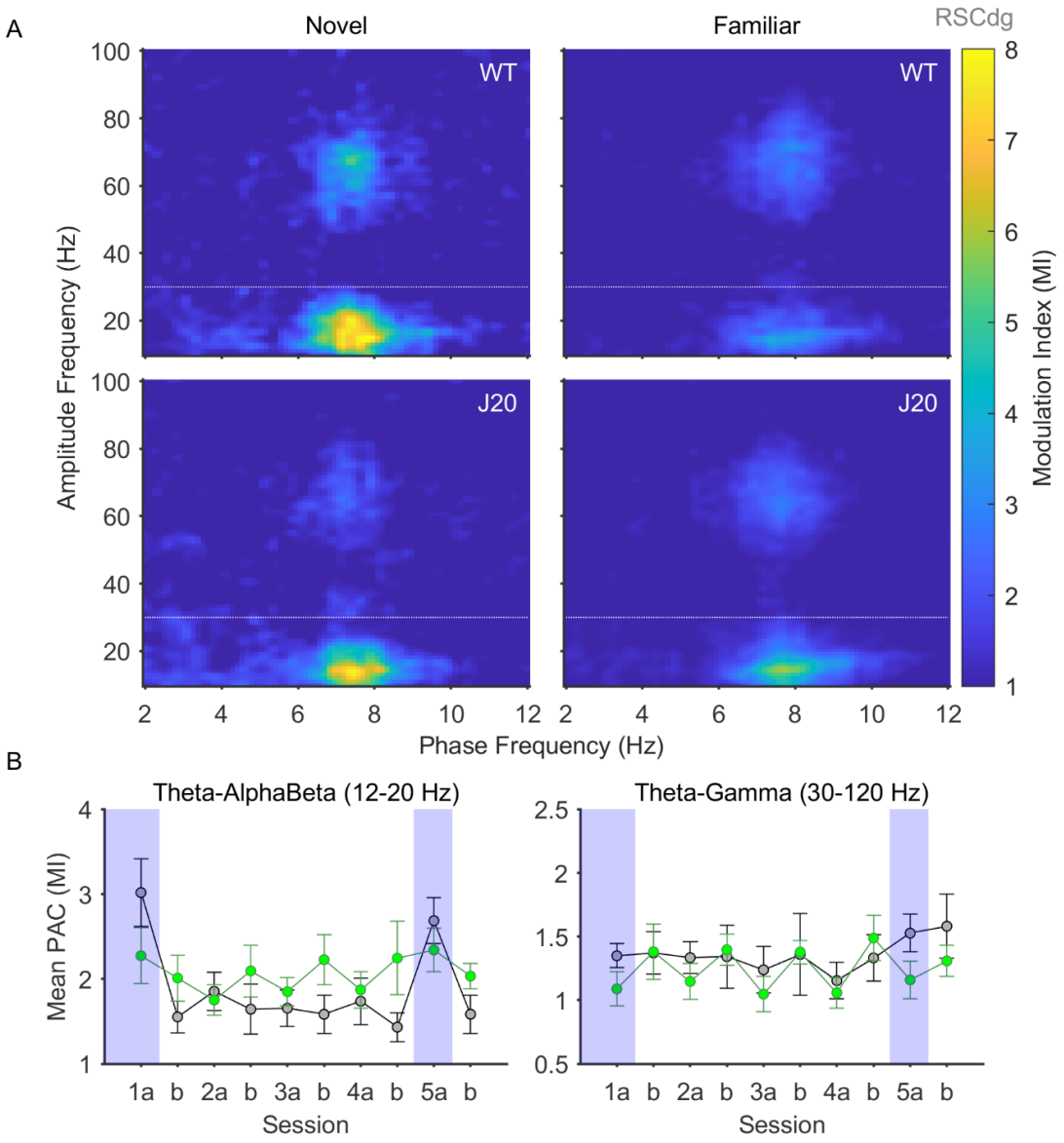

Figure 3.10 Theta-alpha/beta phase-amplitude coupling is increased in the dysgranular retrosplenial cortex (RSCdg) during novelty.
A. Average comodulograms showing the strength of cross-frequency phase-amplitude coupling in RSCdg during the first minute of novel and familiar sessions, for wild-type and J20 mice. Note the presence of two peaks in the theta-alpha/beta and theta-gamma ranges (the boundaries of which are denoted by the dotted lines). B. Average MI in the theta-alpha/beta (left) and theta-gamma ranges (right), for each session, for wild-type (black) and J20 mice (green). Novel sessions Day1a and Day5a are highlighted in blue for clarity. Theta-alpha/beta coupling was significantly higher during novel sessions for wild-type ($p = 0.01$), but not J20 mice ($p = 0.15$). There was no significant effect of genotype or novelty on theta-gamma coupling ($p = 0.4$, $p = 0.7$, respectively). (Data shown as mean ± SEM, WT: n = 5, J20: n = 8).

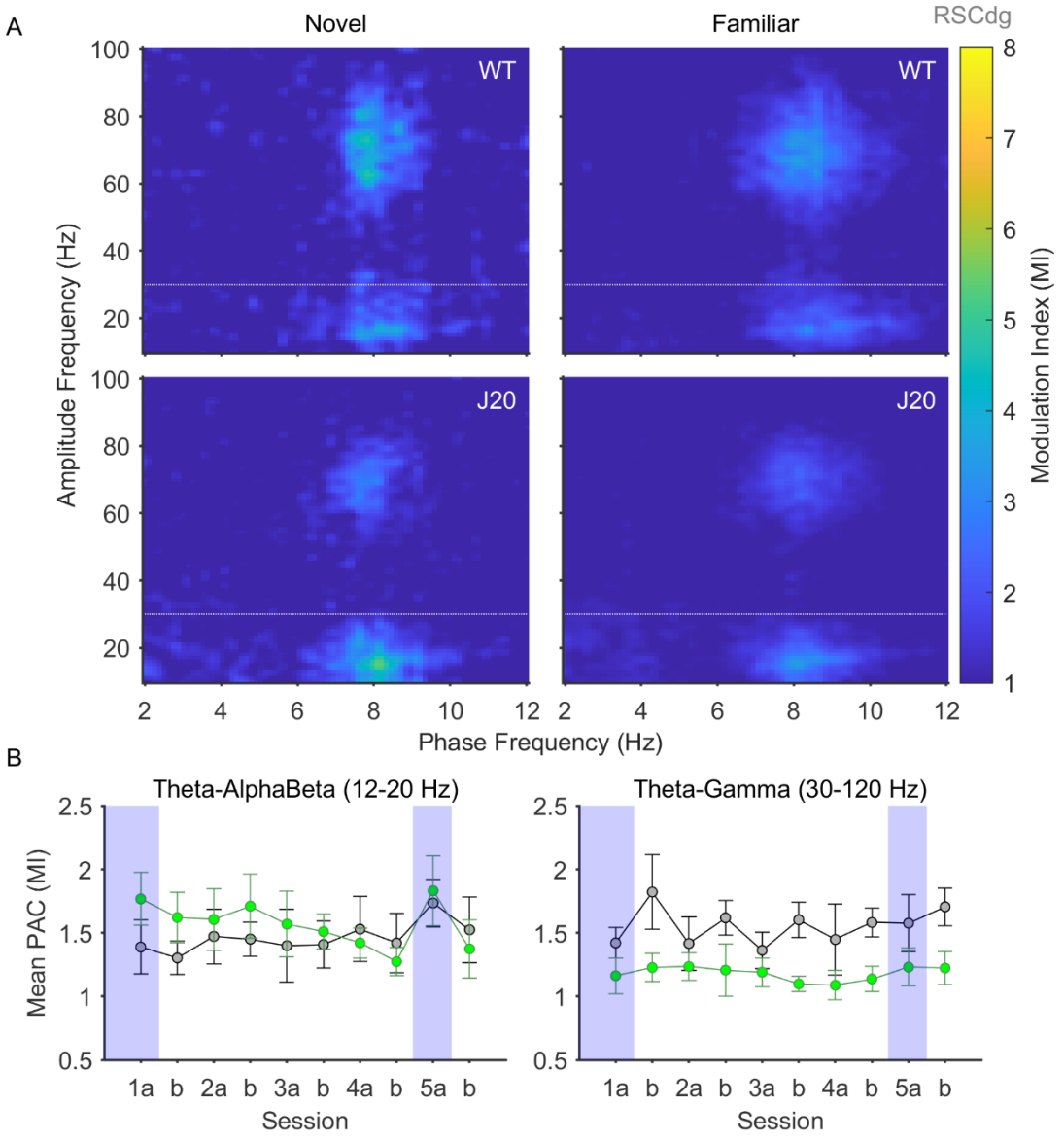

Figure 3.11 Phase-amplitude coupling during the final minute of each session in the dysgranular retrosplenial cortex.
A. Average comodulograms showing the strength of cross-frequency phase-amplitude coupling in RSCdg during the final minute of novel and familiar sessions, for wild-type and J20 mice. Note the presence of two peaks in the theta-alpha/beta and theta-gamma ranges (the boundaries of which are denoted by the dotted lines). B. Average MI in the theta-alpha/beta (left) and theta-gamma ranges (right), for each session, for wild-type (black) and J20 mice (green). Novel sessions Day1a and Day5a are highlighted in blue for clarity. There was no significant effect of genotype or novelty on theta-alpha/beta coupling ($p = 0.56$, $p = 0.054$, respectively). There was no significant effect of genotype or novelty on theta-gamma coupling ($p = 0.08$, $p = 0.69$, respectively). (Data shown as mean ± SEM, WT: n = 5, J20: n = 8).

3.4.6 Dysgranular Spiking Activity

In order to determine whether beta bursting was associated with a change in neuronal firing, multi-unit activity was investigated. Due to the linear geometry of the silicon probes, and the 100 μm distance between channels, it was not possible to reliably identify single unit activity, as activity from a single neuron was unlikely to appear on multiple channels, limiting spatiotemporal clustering methods generally used with tetrodes or higher density silicon probes. Therefore, spikes appearing on a single channel could be from one or more nearby neurons. This, however, does mean that it is possible to treat each individual probe channel as a single multi-unit, to facilitate investigation of the relationship between neuronal spiking activity and beta bursting. As shown in (Figure 3.12a, left), individual spike waveforms can be readily discerned, and there was no significant difference in the mean amplitude of these waveforms between wild-type (black) and J20 (green) mice (WT: -90.3 ± 6.4 μV; J20: -82 ± 7.7 μV; $t(11) = -0.8$, $p = 0.5$; unpaired t-test). Furthermore, as shown in (Figure 3.12a, right), there was no significant difference between average firing rate in wild-type and J20 mice (WT: 46.7 ± 10.1 Hz; J20: 43 ± 10.5 Hz; $t(11) = 0.24$, $p = 0.8$; unpaired t-test). One caveat to both of these measures is that spike amplitude is highly dependent on the distance between the recording channel and the neuron, and therefore so is spike rate, as reduced spike amplitude could result in reduced spike detection. Furthermore, as this data is from multi-units both the average spike waveform and average firing rate may therefore vary greatly between animals depending on the distance between all detected neurons and the recording channel, which itself depends on the probe location. The average beta amplitude during beta bursts is shown in (Figure 3.12b), averaged across all bursts with non-overlapping time segments. Beta bursts in both genotypes are associated with a

brief, monophasic increase in beta amplitude that lasts no more than 200 ms on average. Finally, (Figure 3.12c) shows peri-event time histograms for spike rate during beta bursts, as a Z score from the pre-burst baseline (left of the dotted line). In order to investigate statistically significant changes in spike rate during bursts, the mean z scored spike rate between 0 to 250 ms after burst onset was calculated, for each animal, and compared to the mean pre-burst spike rate (0 due to z scoring of spike rate to baseline) using a one-sample t-test. Beta bursting in the RSCdg of wild-type mice was associated with a significant increase in spike rate during beta bursts (Z-scored spike rate from baseline: 0.9 ± 0.3; $t(4) = 2.9$, $p = 0.04$; one-sample t-test; Figure 7c, left). Conversely there was no significant increase in spike rate during beta bursts in J20 mice (Z-scored spike rate from baseline: 0.48 ± 0.53; $t(7) = 0.9$, $p = 0.4$; one-sample t-test; Figure 7c, right). These data suggest that beta bursts are coupled to neuronal spiking in RSCdg in wild-type mice, and that this relationship is absent in J20 mice.

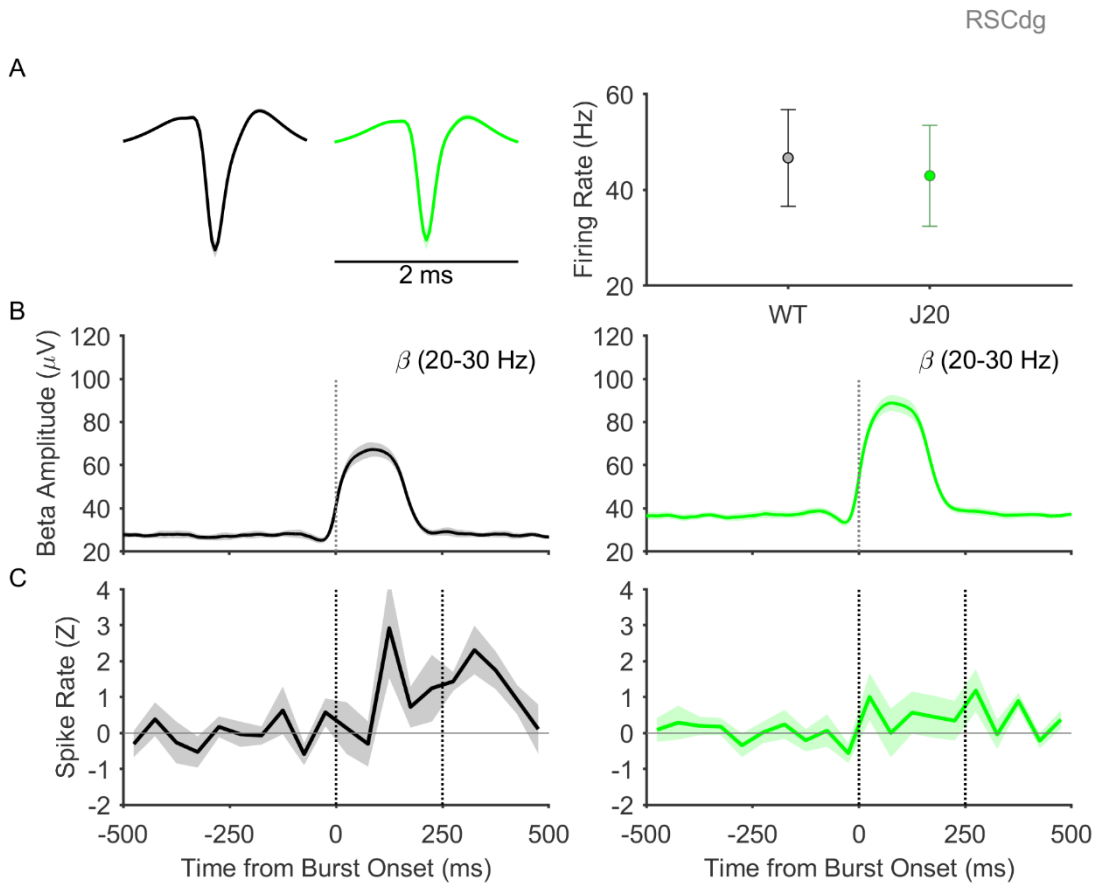

Figure 3.12 Spiking activity in RSCdg is coupled to beta bursting in wild-type mice, but disrupted in J20 mice.
A. Average spike waveforms for multi-unit activity in wild-type (black) and J20 (green) mice (left) and graph of average firing rate for detected multi-units across all sessions (right). There was no significant difference between the mean amplitude of spike waveforms in wild-type and J20 mice ($p = 0.5$). Moreover, there was no significant difference between average firing rate in wild-type and J20 mice ($p = 0.8$). B. Graphs showing beta amplitude over time for beta bursts, time locked to the onset of the burst (dotted line), and averaged across all detected bursts, for wild-type mice (left) and J20 mice (right). Beta bursting was associated with a monophasic increase in beta amplitude that returns to baseline after around 250 ms. C. Peri-event histograms showing multi-unit activity spike rate during beta bursts, for wild-type (left) and J20 mice (right). Data is shown as Z score from baseline (pre-burst epoch), and averaged across all beta bursts with non-overlapping time segments. Solid horizontal line is shown to indicate the baseline of zero, while the vertical lines indicate the time window of interest used to calculate the average spike rate during beta bursts. Beta bursts were associated with a significant increase in spike rate in wild-type ($p = 0.04$), but not J20 mice ($p = 0.4$). (Data shown as mean ± SEM, WT: $n = 5$, J20: $n = 8$).

3.4.7 Granular Spectral Analysis

As in the RSCdg, in order to investigate any changes in oscillatory activity in RSCg during environmental novelty, power spectral analysis was performed on the entire 15 minutes of each session (Figure 3.13a). These power spectra were averaged across novel and familiar sessions for wild-type and J20 mice. Significant findings are summarised in Table 2, however a more detailed account of these findings, including descriptive statistics, will be listed here in-text. There was a significant interaction between the effects of genotype and novelty on beta power (Interaction - $F(1,12) = 7.9$, $p = 0.02$, Mixed ANOVA). Beta power was significantly higher during novel sessions in wild-type (WT - Nov: 14.4 ± 0.5 dB; Fam: 14 ± 0.5 dB, $p = 0.001$), and J20 mice (J20 - Nov: 17.8 ± 0.2 dB; Fam: 17 ± 0.2 dB, $p = 9e\text{-}7$). Moreover, beta power was significantly higher in J20 mice during both novel (Nov - WT: 14.4 ± 0.5 dB; J20: 17.8 ± 0.2 dB, $p = 4e\text{-}4$) and familiar sessions (Fam - WT: 14 ± 0.5 dB; J20: 17 ± 0.2 dB, $p = 8e\text{-}4$). Gamma power was significantly higher overall during novel sessions (Main Effect Novelty - $F(1,12) = 20.2$, $p = 7e\text{-}4$, Mixed ANOVA). Gamma power was significantly higher during novel sessions in wild-type (WT - Nov: 10.7 ± 0.4 dB; Fam: 10.4 ± 0.4 dB, $p = 0.008$) and J20 mice (J20 - Nov: 12.4 ± 0.3 dB; Fam: 12 ± 0.3 dB, $p = 0.008$). Finally, gamma power was also significantly higher overall in J20 mice (Main Effect Genotype - $F(1,12) = 6.9$, $p = 0.02$, Mixed ANOVA).

As in RSCdg, transient epochs of high power in the 20-40 Hz range are seen throughout the early stages of the session, as illustrated in Figure 3.13c. Power spectral analysis was performed on the first minute of each session (Figure 3.13d). Theta, alpha, beta and gamma power were significantly higher overall during novel sessions (Theta: Main Effect Novelty - $F(1,12) = 7$, $p = 0.02$, Mixed

ANOVA; Alpha: Main Effect Novelty - F(1,12) = 13.3, p = 0.003, Mixed ANOVA; Beta: Main Effect Novelty - F(1,12) = 47.8, p = 2e-5, Mixed ANOVA; Gamma: Main Effect Novelty - F(1,12) = 15, p = 0.002, Mixed ANOVA). Theta power was significantly higher during novel sessions in wild-type (WT - Nov: 25.8 ± 0.5; Fam: 25.2 ± 0.6, p = 0.01), but not J20 mice. Alpha power was significantly higher during novel sessions in J20 mice (J20 - Nov: 20.3 ± 0.3 dB; Fam: 19.5 ± 0.3 dB, p = 0.004), but not wild-type mice. Beta power was significantly higher during novel sessions in wild-type (WT - Nov: 16.3 ± 0.5 dB; Fam: 14.4 ± 0.5 dB, p = 4e-4), and J20 mice (J20 - Nov: 19.3 ± 0.3 dB; Fam: 17.6 ± 0.1 dB, p = 3e-4). Gamma power was significantly higher during novel sessions in wild-type (WT - Nov: 11 ± 0.4 dB; Fam: 10.4 ± 0.4 dB, p = 0.005), but not J20 mice (J20 - Nov: 12.4 ± 0.2 dB; Fam: 12 ± 0.3 dB, p = 0.08). Alpha, beta and gamma power were significantly higher overall in J20 mice (Alpha: Main Effect Genotype - F(1,12) = 7.9, p = 0.02, Mixed ANOVA; Beta: Main Effect Genotype - F(1,12) = 18.4, p = 0.001, Mixed ANOVA; Gamma: Main Effect Genotype - F(1,12) = 5.9, p = 0.03, Mixed ANOVA).

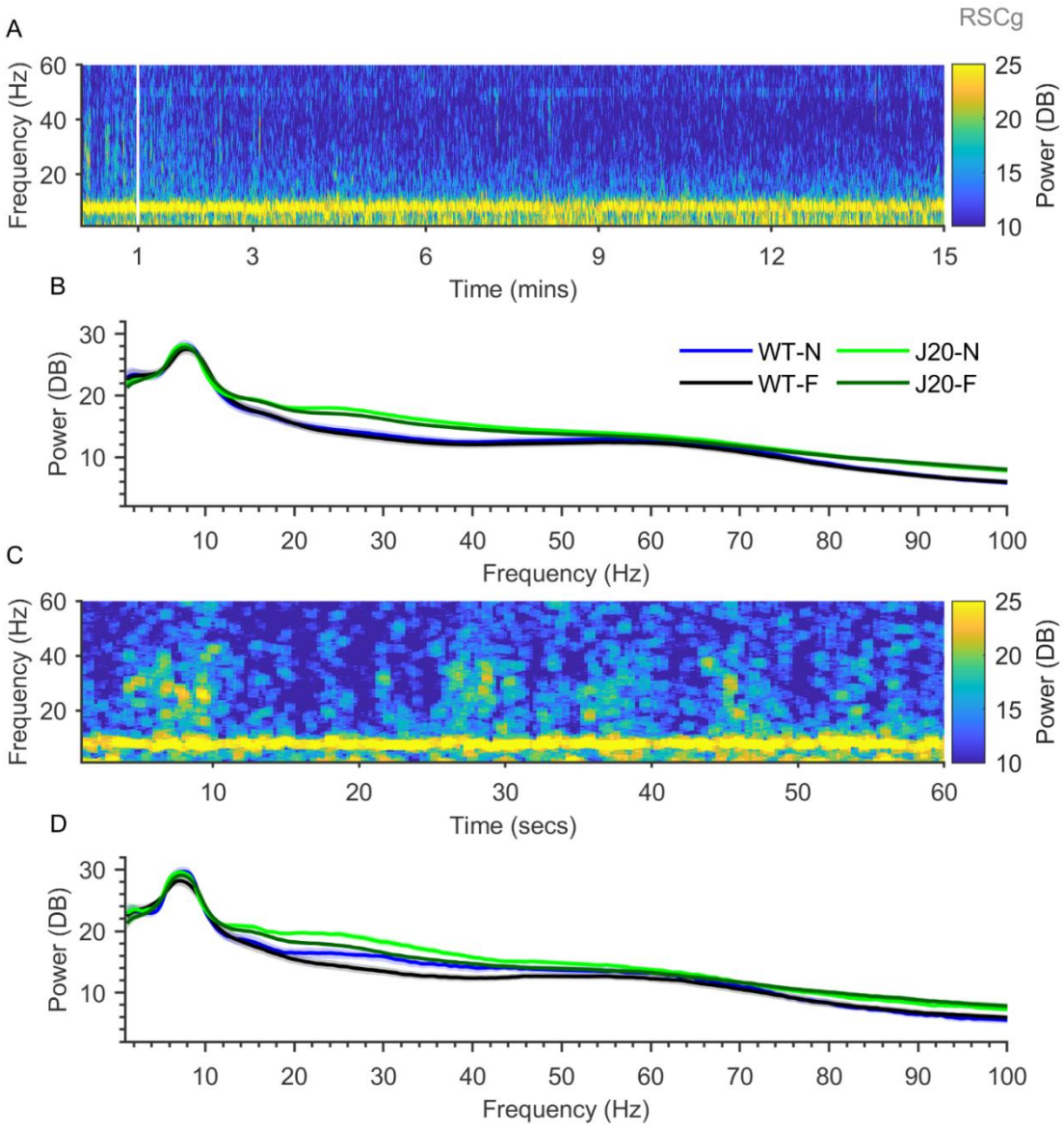

Figure 3.13 Beta (20-30 Hz) power is significantly higher during novelty in the granular retrosplenial cortex in wild-type and J20 mice.
A. Example power spectrogram for an entire novel session in a wild-type mouse. B. Average power spectra for the entire 15 minutes of all novel and familiar sessions, for wild-type and J20 mice. Beta power was significantly higher during novel sessions in wild-type ($p = 0.001$) and J20 mice ($p = 9e\text{-}7$). Moreover, beta power was significantly higher in J20 mice than in wild-type mice during both novel ($p = 4e\text{-}4$) and familiar sessions ($p = 8e\text{-}4$). C. Example power spectrogram shown in A, expanded to show the first 60 seconds of the session. Short epochs of increased power in the 20-40 Hz range can be seen. D. Average power spectra for the first minute of all novel and familiar sessions, for wild-type and J20 mice. Beta power was significantly higher overall during novel sessions ($p = 2e\text{-}5$). Moreover, beta power was significantly higher overall in J20 mice ($p = 0.001$). (Data shown as mean ± SEM, WT: n = 6, J20: n = 8).

Table 2 Dysgranular spectral analysis - Summary of significant results

Analysis Type	Frequency Band	Relationship	p-value
Whole Session	β	N X G	0.02
	β	$n_{WT} > f_{WT}$	0.001
	β	$n_{J20} > f_{J20}$	9.00E-07
	β	$n_{J20} > n_{WT}$	4.00E-04
	β	$f_{J20} > f_{WT}$	8.00E-08
	γ	n > f	7.00E-04
	γ	$n_{WT} > f_{WT}$	0.008
	γ	$n_{J20} > f_{J20}$	0.008
	γ	J20 > WT	2.00E-02
First Minute	θ	n > f	0.02
	θ	$n_{WT} > f_{WT}$	0.01
	α	n > f	0.003
	α	$n_{J20} > f_{J20}$	4.00E-03
	α	J20 > WT	0.02
	β	n > f	2.00E-05
	β	$n_{WT} > f_{WT}$	4.00E-04
	β	$n_{J20} > f_{J20}$	3.00E-04
	β	J20 > WT	0.001
	γ	n > f	0.002
	γ	$n_{WT} > f_{WT}$	5.00E-03
	γ	J20 > WT	0.03

N, novelty; G, genotype; N X G, interaction between novelty and genotype; n, novel; f, familiar; WT, wild-type; J20, J20; θ, theta; α, alpha; β, beta; γ, gamma

3.4.8 Granular Beta Bursting Activity

As in the RSCdg, beta bursts could be reliably detected in local field potential recordings from the RSCg (Figure 3.14a). As shown in (Figure 3.14b), there were significantly more beta bursts detected overall during novel sessions (Main Effect Novelty - $F(1,12) = 29$, $p = 2e\text{-}4$, Mixed ANOVA). Furthermore, there were significantly more beta bursts detected overall in J20 mice (Main Effect Genotype - $F(1,12) = 80.3$, $p = 1e\text{-}6$, Mixed ANOVA).

As shown in (Figure 3.14c, right), similar to the RSCdg, the rate of beta bursting was reasonably steady throughout familiar sessions, but substantially higher during the first few minutes of novel sessions, for both genotypes (Figure 3.14c, left). The rate of beta bursting was significantly higher overall during novel sessions (Main Effect Novelty - $F(1,12) = 18.8$, $p = 0.001$, Mixed ANOVA), and also significantly higher overall during the initial part of recording sessions (Main Effect Time - $F(1,12) = 22.9$, $p = 4e\text{-}4$, Mixed ANOVA). Additionally, the rate of beta bursting was significantly higher overall in J20 mice (Main Effect Genotype - $F(1,12) = 5.5$, $p = 0.04$, Mixed ANOVA). During novel sessions, initial burst rate was significantly higher than final burst rate for wild-type (WT - Nov Initial: 9.8 ± 1.5; Final: 1 ± 0.3, $p = 0.02$) and J20 mice (J20 - Nov Initial: 12.6 ± 3; Final: 2.6 ± 0.4, $p = 0.003$). Furthermore, while there was no significant difference between wild-type and J20 mice for initial burst rate (Nov Initial - WT: 9.8 ± 1.5; J20: 12.6 ± 3, $p = 0.5$), final burst rate was significantly higher in J20 mice (Nov Final - WT: 1 ± 0.3; J20: 2.6 ± 0.4, $p = 0.01$). During familiar sessions, initial burst rate was significantly higher than final burst rate for wild-type (WT - Fam Initial: 2.7 ± 0.5; Final: 1.2 ± 0.1, $p = 0.05$) and J20 mice (J20 - Fam Initial: 4.8 ± 0.5; Final: 2.5 ± 0.3, $p = 0.002$). Furthermore, initial burst rate and final burst rate were significantly

higher in J20 mice than in wild-type mice (Fam Initial - WT: 2.7 ± 0.5; J20: 4.8 ± 0.5, $p = 0.02$; Fam Final - WT: 1.2 ± 0.1; J20: 2.5 ± 0.3, $p = 0.001$).

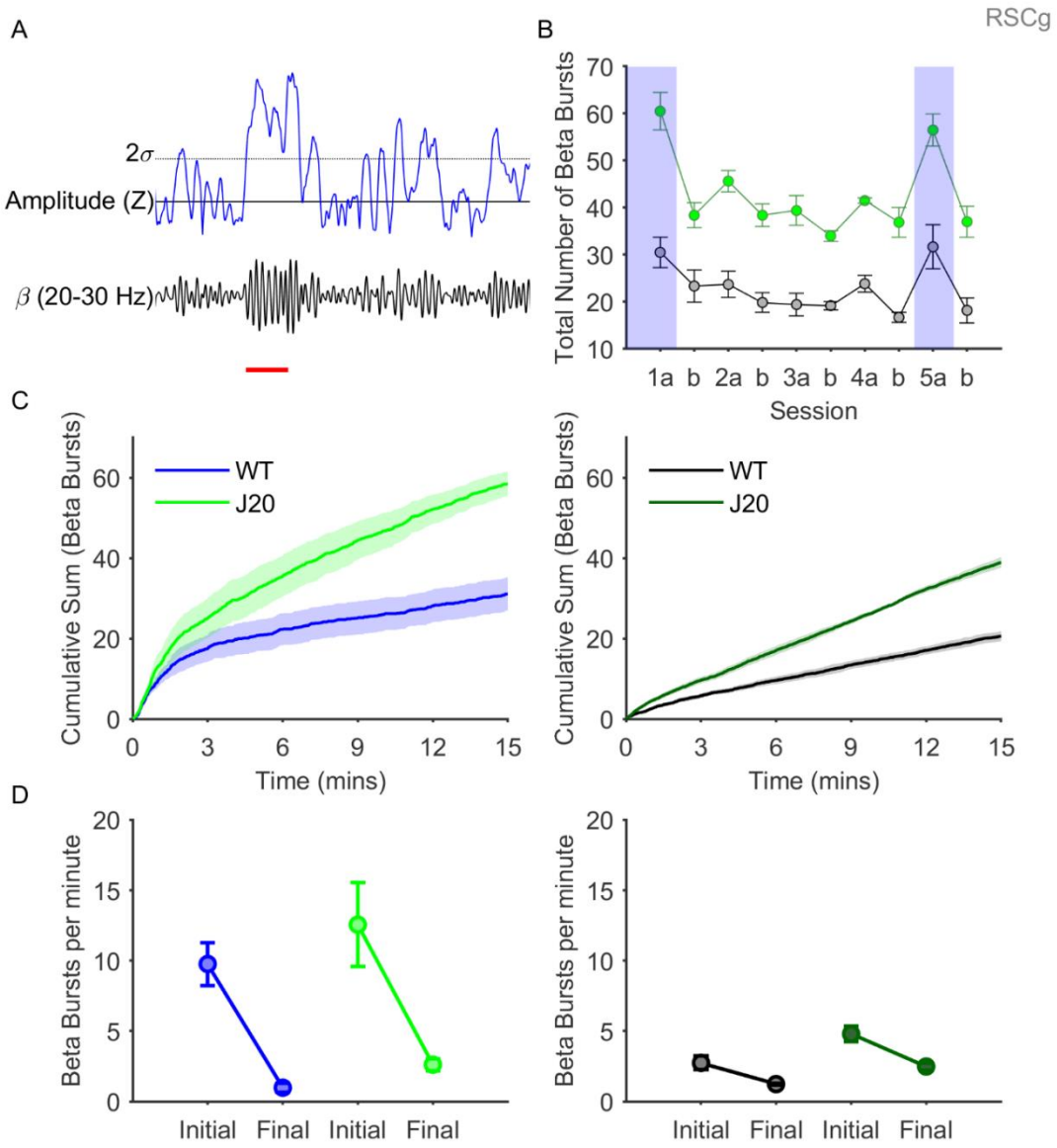

Figure 3.14 Beta bursting activity in the granular retrosplenial cortex (RSCg) is significantly higher during novelty.

A. Diagram illustrating how beta bursts were detected. B. Graph showing the average number of beta bursts detected in RSCdg in each session, for wild-type (black) and J20 mice (green). Novel sessions Day1a and Day5a are highlighted in blue for clarity. Significantly more beta bursts were detected overall during novel sessions ($p = 2e\text{-}4$). Moreover, significantly more beta bursts were detected overall in J20 mice ($p = 1e\text{-}6$). C. Cumulative frequency graphs of beta bursts detected in novel (left) and familiar sessions (right), for wild-type and J20 mice. As in the RSCdg, while beta bursting occurred monotonically during familiar sessions, during the first minute of a novel session, beta bursting was substantially increased. D. Graphs showing beta burst rate during novel (left) and familiar sessions (right), for wild-type and J20 mice. Burst rate was quantified for the initial minute of each session, and final 10 minutes. Beta burst rate was significantly higher overall during the initial minute of novel sessions than during the final 10 minutes of novel sessions, for wild-type ($p = 0.02$) and J20 mice ($p = 0.003$). (Data shown as mean ± SEM, WT: n = 6, J20: n = 8).

3.4.9 Granular Beta Burst Characteristics

The characteristics of beta bursts in the RSCg also vary depending on novelty and genotype. Beta burst magnitude was significantly higher overall during novel sessions (Main Effect Novelty - F(1,12) = 56.8, p = 7e-6, Mixed ANOVA). As shown in (Figure 3.15a), beta bursts were significantly larger in magnitude during novel sessions in wild-type (WT - Nov: 96.1 ± 5.3 μV; Fam: 131 ± 2.9 μV, p = 7e-4) and J20 mice (J20 - Nov: 131 ± 2.9 μV; Fam: 115 ± 2.1 μV, p = 4e-5). Moreover, beta bursts were significantly larger in magnitude overall in J20 mice (Main Effect Genotype - F(1,12) = 22.7, p = 5e-4, Mixed ANOVA). Beta burst duration was also significantly higher overall during novel sessions (Main Effect Novelty - F(1,12) = 23.2, p = 4e-4, Mixed ANOVA). As shown in (Figure 3.15b), beta bursts were significantly longer in duration during novel sessions in wild-type (WT - Nov: 189 ± 2.4 μV; Fam: 175 ± 0.5 μV, p = 0.001) and J20 mice (J20 - Nov: 188 ± 1.3 μV; Fam: 181 ± 0.9 μV, p = 0.04).

Power spectral analysis was also performed on beta bursts in the RSCg, as before (Figure 3.15c). Overall, beta bursts were associated with a large significant increase in beta power (Main Effect Burst - F(1,12) = 2906, p = 1e-15, Mixed ANOVA), small significant increases in alpha and gamma power (Alpha: Main Effect Burst - F(1,12) = 60.4, p = 5e-6, Mixed ANOVA; Gamma: Main Effect Burst - F(1,12) = 57.2, p = 7e-6, Mixed ANOVA), and a small significant decrease in theta power (Main Effect Burst - F(1,12) = 5.6, p = 0.04, Mixed ANOVA). Alpha, beta and gamma power were significantly higher during beta bursts in both wild-type (Alpha: WT – Pre-Burst: 17.5 ± 0.6 dB; Burst: 18.3 ± 0.5 dB, p = 2e-4; Beta: WT – Pre-Burst: 13 ± 0.5 dB; Burst: 20.3 ± 0.5 dB, p = 1e-13; Gamma: WT – Pre-Burst: 8.7 ± 0.3 dB; Burst: 9 ± 0.3 dB, p = 0.001), and J20 mice (Alpha: J20 –

Pre-Burst: 18.5 ± 0.3 dB; Burst: 19.3 ± 0.3 dB, p = 9e-5; Beta: J20 – Pre-Burst: 16.1 ± 0.3 dB; Burst: 23.3 ± 0.2 dB, p = 3e-14; Gamma: J20 – Pre-Burst: 10.6 ± 0.3 dB; Burst: 11 ± 0.2 dB, p = 2e-5). Theta power was significantly lower during beta bursts in J20 mice (J20 – Pre-Burst: 24.2 ± 0.2 dB; Burst: 23.8 ± 0.2 dB, p = 0.01), but not wild-type mice.

In order to investigate beta rhythmicity in RSCg, the period of beta oscillations was calculated for all beta bursts and all epochs without beta bursts, and the distribution of these beta periods were calculated and averaged across all burst and non-burst epochs, in all sessions, for wild-type and J20 mice (Figure 3.15d). As in the RSCdg, while the distribution of beta periods during beta bursts was reasonably consistent, peaking around 0.04s, equivalent to a 25 Hz oscillation, the distribution of beta periods in non-burst epochs was far more variable, with a large proportion of periods outside beta range. These data indicate that beta bursts are associated with high beta rhythmicity, while beta rhythmicity is far lower during non-burst epochs, suggesting a “bursty generator” model put forward by van Ede et al. (2018). As before it is important to note that this data presented does not provide any conclusive proof of either mechanism for the reasons stated earlier in this Chapter, and is included more as an attempt to better understand the nature of beta oscillations both during and outside the transient events outlined in this thesis.

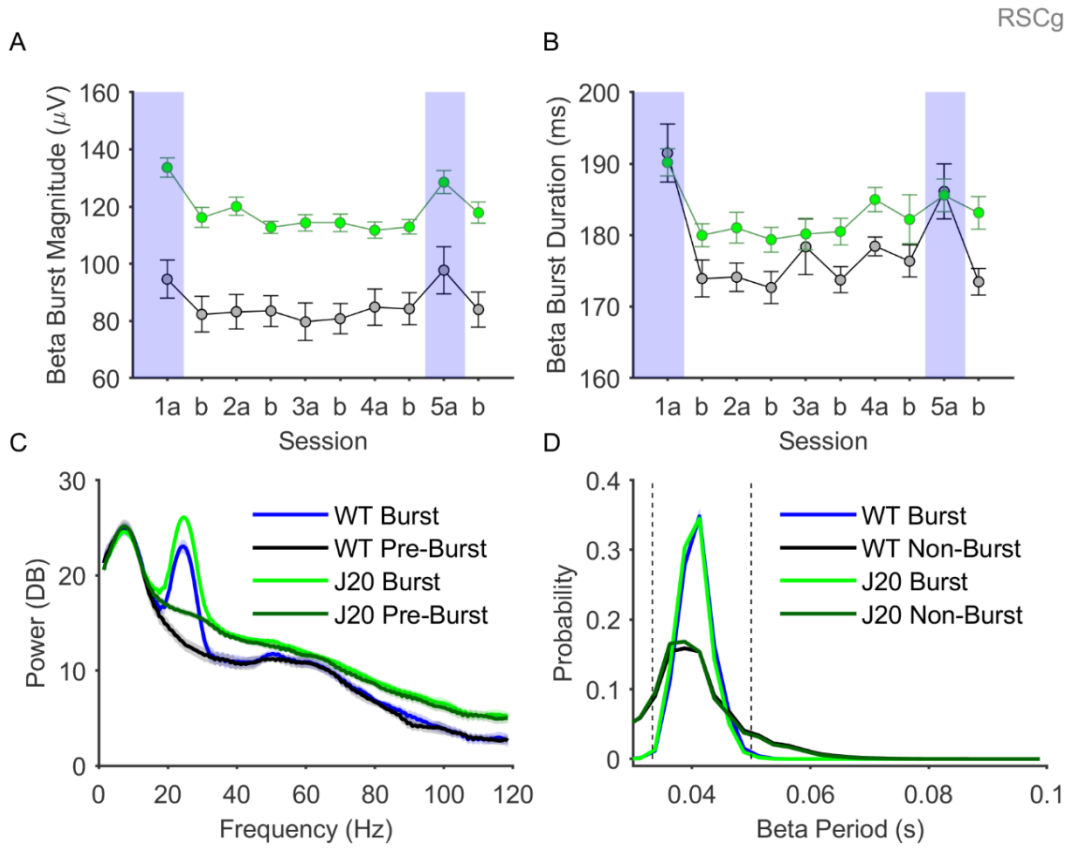

Figure 3.15 Beta burst characteristics in the dysgranular retrosplenial cortex (RSCdg).
A. Diagram illustrating how the magnitude and duration of beta bursts were calculated. B. Graph showing the average beta burst magnitude in RSCdg in each session, for wild-type and J20 mice. Beta bursts were overall significantly larger in magnitude during novel sessions (p = 7e-6). Moreover, beta bursts were also significantly larger overall in J20 mice (p = 5e-4). C. Graph showing the average duration of beta bursts in RSCdg in each session, for wild-type and J20 mice. Beta bursts were overall significantly longer in duration during novel sessions (p = 4e-4), however there was no significant overall difference between beta burst duration in wild-type and J20 mice. D. Average power spectra for beta burst, and pre-burst epochs. Beta bursts were associated with a large, significan increase in beta power during beta bursts (p = 1e-15). E. Average distributions of beta oscillation period for burst and non-burst epochs, in wild-type and J20 mice Beta oscillations are tightly rhythmic during beta bursts, but highly arrhythmic during non-burst epochs. (Data shown as mean ± SEM, WT: n = 6, J20: n = 8).

3.4.10 Granular Phase-amplitude Coupling

Phase-amplitude coupling efficacy was calculated for a range of phase and amplitude frequencies, and plotted as comodulograms, as shown in (Figure 3.16a). As in the RSCdg, there were two large peaks in these comodulograms, in the theta-gamma and theta-alpha/beta frequency ranges. The strength of phase-amplitude coupling was quantified for theta-alpha/beta and theta-gamma coupling for each session (Figure 3.16b). There was a significant interaction between the effects of genotype and novelty on theta-alpha/beta coupling (Interaction - $F(1,12) = 10.4$, $p = 0.007$, Mixed ANOVA). Theta-alpha/beta coupling was significantly higher during novel sessions for wild-type (WT - Nov: 3 ± 0.1; Fam: 1.9 ± 0.1, $p = 3e\text{-}4$), but not J20 mice (J20 - Nov: 2.4 ± 0.2; Fam: 2.3 ± 0.2, $p = 0.4$). There were no significant effects of novelty or genotype on theta-gamma coupling (Main Effect Novelty - $F(1,12) = 0.9$, $p = 0.4$, Mixed ANOVA; Main Effect Genotype - $F(1,12) = 2.7$, $p = 0.1$, Mixed ANOVA). As before, this analysis was performed for the first minute of each session, but when the same analysis was performed on the last minute of each session, there were a number of differences (Figure 3.17). There was a significant effect of novelty on theta-alpha/beta coupling (Main Effect Novelty - $F(1,12) = 5.5$, $p = 0.04$, Mixed ANOVA). Theta-alpha/beta coupling was significantly higher during novel sessions for J20 mice (J20 - Nov: 2.2 ± 0.2; Fam: 1.8 ± 0.1, $p = 0.04$), but not wild-type mice (WT - Nov: 1.9 ± 0.1; Fam: 1.7 ± 0.1, $p = 0.3$). While there was no significant effect of novelty on theta-gamma coupling (Main Effect Novelty - $F(1,12) = 1.3$, $p = 0.3$, Mixed ANOVA), theta-gamma coupling was significantly higher overall in wild-type mice (Main Effect Genotype - $F(1,12) = 8$, $p = 0.01$, Mixed ANOVA).

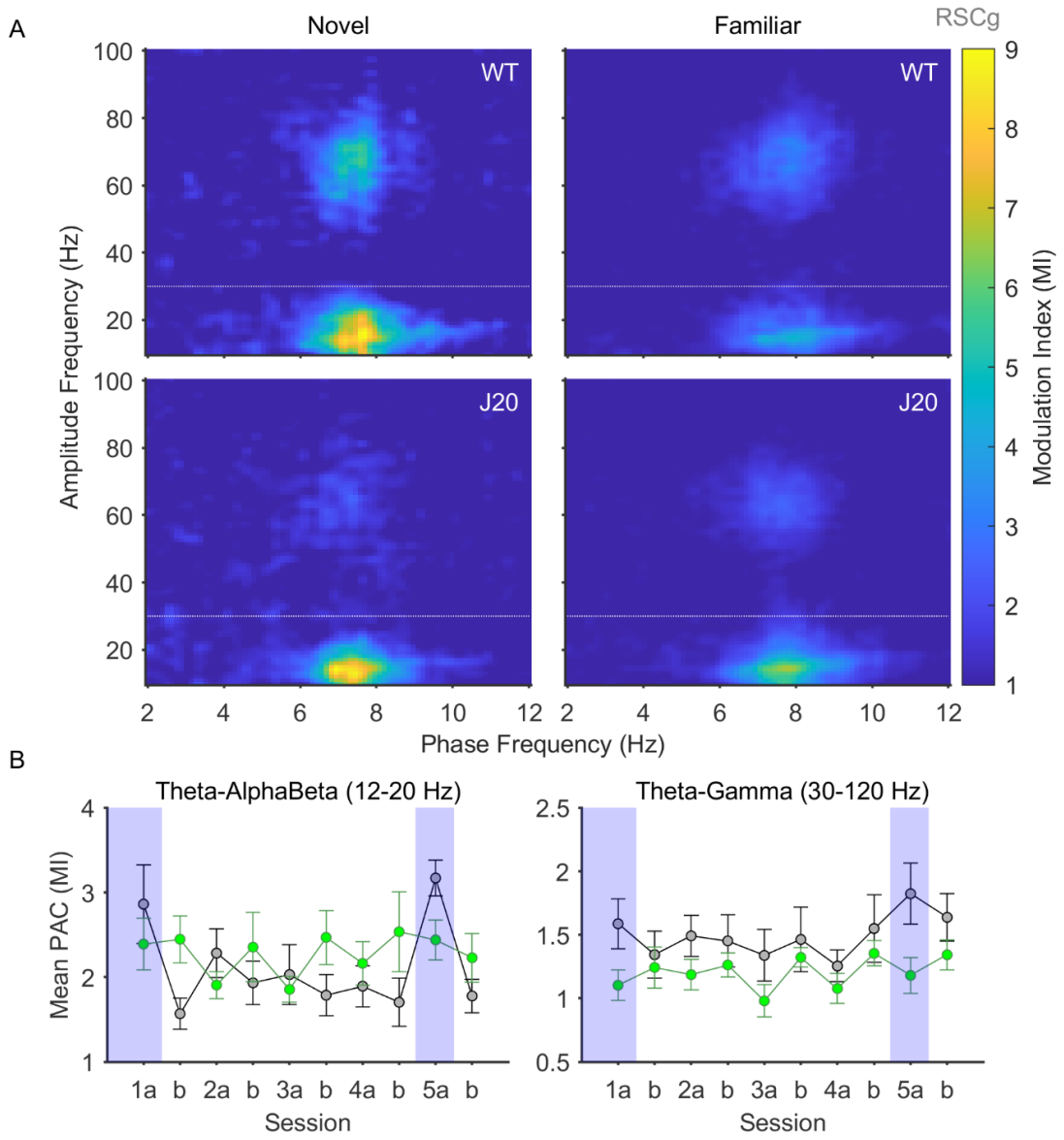

Figure 3.16 Theta-alpha/beta phase-amplitude coupling is increased in the granular retrosplenial cortex (RSCg) during novelty.
A. Average comodulograms showing the strength of cross-frequency phase-amplitude coupling in RSCg during the first minute of novel and familiar sessions, for wild-type and J20 mice. Note the presence of two peaks in the theta-alpha/beta and theta-gamma ranges (the boundaries of which are denoted by the dotted lines). B. Average MI in the theta-alpha/beta (left) and theta-gamma ranges (right), for each session, for wild-type (black) and J20 mice (green). Novel sessions Day1a and Day5a are highlighted in blue for clarity. Theta-alpha/beta coupling was significantly higher during novel sessions for wild type ($p = 3e-4$) but not J20 mice ($p = 0.4$). There was no significant effect of genotype or novelty on theta-gamma coupling ($p = 0.1$, $p = 0.4$, respectively). (Data shown as mean ± SEM, WT: n = 6, J20: n = 8).

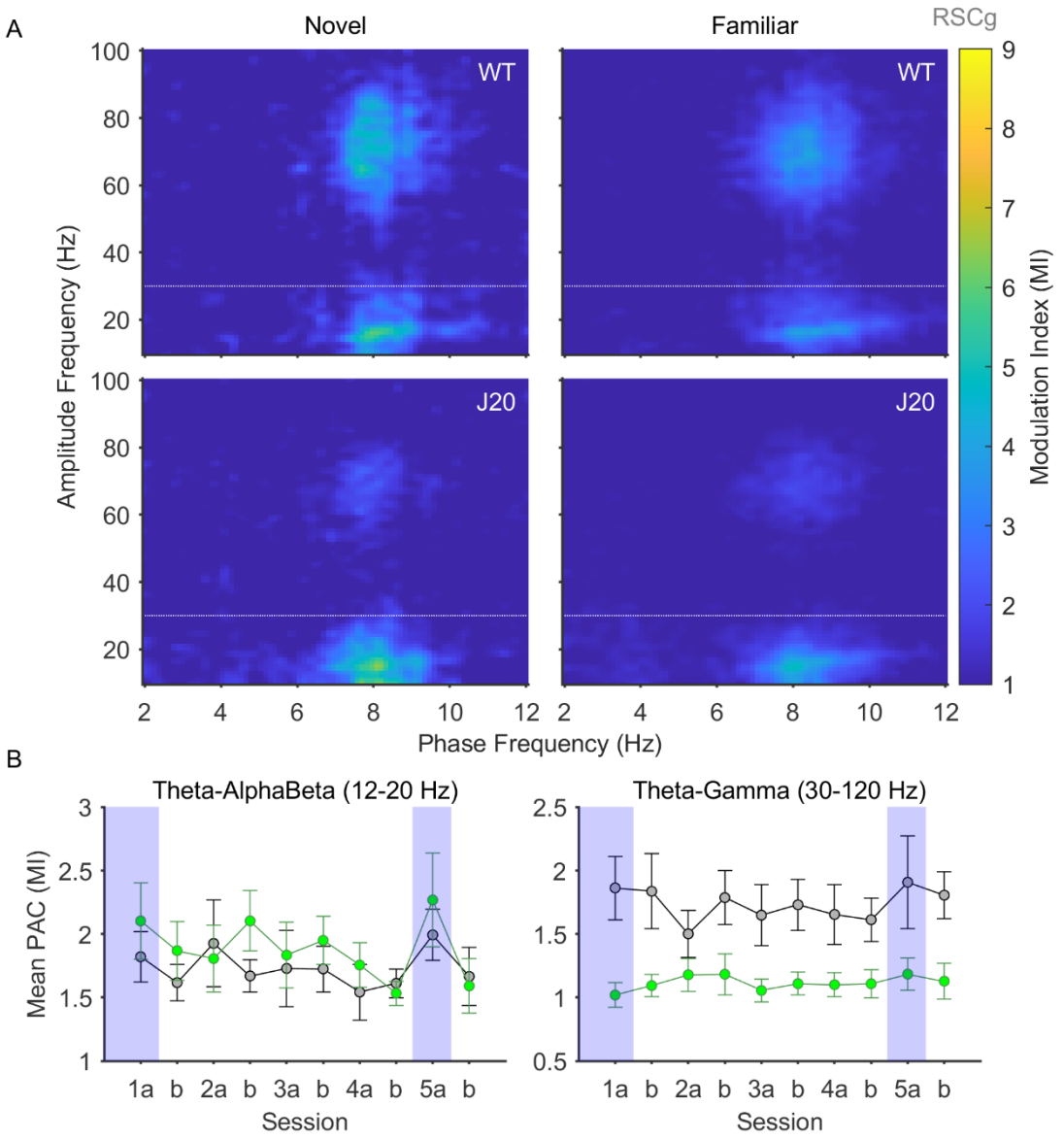

Figure 3.17 Phase-amplitude coupling during the final minute of each session in the granular retrosplenial cortex.
A. Average comodulograms showing the strength of cross-frequency phase-amplitude coupling in RSCg during the final minute of novel and familiar sessions, for wild-type and J20 mice. Note the presence of two peaks in the theta-alpha/beta and theta-gamma ranges (the boundaries of which are denoted by the dotted lines). B. Average MI in the theta-alpha/beta (left) and theta-gamma ranges (right), for each session, for wild-type (black) and J20 mice (green). Novel sessions Day1a and Day5a are highlighted in blue for clarity. Theta-alpha/beta coupling was significantly higher during novel sessions for J20 mice ($p = 0.04$) but not wild-type mice ($p = 0.3$). There was no significant effect of novelty on theta-gamma coupling ($p = 0.3$), but theta-gamma coupling was significantly higher overall in wild-type mice ($p = 0.015$). (Data shown as mean ± SEM, WT: $n = 6$, J20: $n = 8$).

3.4.11 Granular Spiking Activity

General neuronal spiking activity, as well as spiking during beta bursts was also investigated in the RSCg. As shown in (Figure 3.18a, left), the mean amplitude of spike waveforms was significantly higher in J20 mice (WT: -61.3 ± 2.9 μV; J20: -82 ± 7.8 μV; $t(12) = 2.2$, $p = 0.05$; unpaired t-test). Furthermore, as shown in (Figure 3.18a, right), there was no significant difference between average firing rate in wild-type and J20 mice (WT: 15.8 ± 8.8 Hz; J20: 36.6 ± 13.2 Hz; $t(12) = -1.2$, $p = 0.25$; unpaired t-test). It is important to note that, as mentioned before, both the average spike waveform and average firing rate may vary greatly between animals depending on the distance between all detected neurons and the recording channel. The average beta amplitude during beta bursts is shown in (Figure 3.18b), averaged across all bursts with non-overlapping time segments. As in the RSCdg, beta bursts in both genotypes are associated with a brief, monophasic increase in beta amplitude that lasts no more than 200 ms on average. Finally, (Figure 3.18c) shows peri-event time histograms for spike rate during beta bursts, as a Z score from the pre-burst baseline (left of the dotted line). Beta bursting in the RSCg was not associated with a significant increase in spike rate during beta bursts in either wild-type (Z-scored spike rate from baseline: 0.3 ± 0.3; $t(5) = 0.9$, $p = 0.4$; one-sample t-test; Figure 12c, left) or J20 mice (Z-scored spike rate from baseline: 1.1 ± 0.48; $t(7) = 2.2$, $p = 0.06$; one-sample t-test; Figure 12c right).

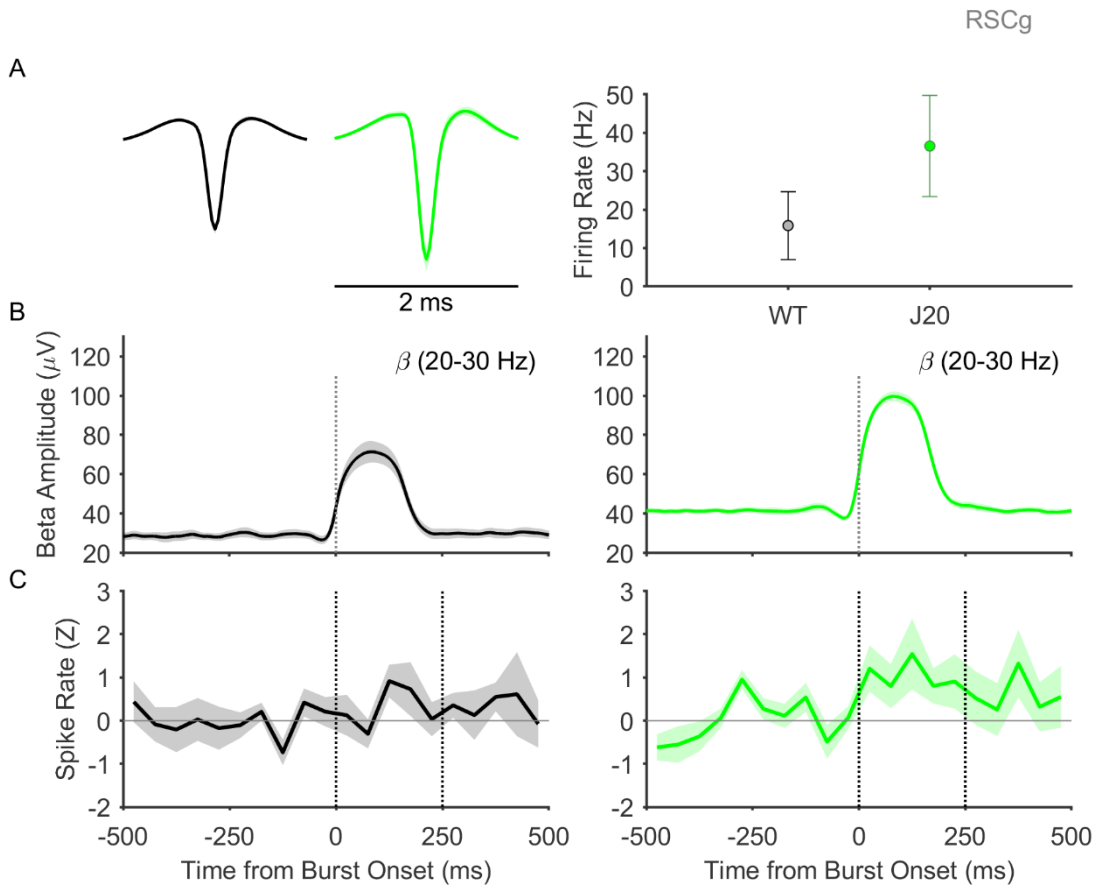

Figure 3.18 Spiking activity in RSCg is coupled to beta bursting in wild-type and J20 mice.

A. Average spike waveforms for multi-unit activity in wild-type (black) and J20 (green) mice (left) and graph of average firing rate for detected multi-units across all sessions (right). The mean amplitude of spike waveforms was significantly higher in J20 mice ($p = 0.05$), but there was no significant difference between average firing rate in wild-type and J20 mice ($p = 0.25$). B. Graphs showing beta amplitude over time for beta bursts, time locked to the onset of the burst (dotted line), and averaged across all detected bursts, for wild-type mice (left) and J20 mice (right). Beta bursting was associated with a monophasic increase in beta amplitude that returns to baseline after around 250 ms. C. Peri-event histograms showing multi-unit activity spike rate during beta bursts, for wild-type (left) and J20 mice (right). Data is shown as Z score from baseline (pre-burst epoch), and averaged across all beta bursts with non-overlapping time segments. Solid horizontal line is shown to indicate the baseline of zero, while the vertical lines indicate the time window of interest used to calculate the average spike rate during beta bursts. Beta bursts were not associated with a significant increase in spike rate in either wild-type ($p = 0.4$) or J20 mice ($p = 0.06$). (Data shown as mean ± SEM, WT: $n = 6$, J20: $n = 8$).

3.5 Discussion

3.5.1 Summary

The aim of this study was to identify electrophysiological correlates of environmental novelty across the mouse retrosplenial cortex (RSC), to understand the specific neurophysiological mechanisms which may support this region's role in contextual learning and memory. Furthermore, the inclusion of J20 mice in this study as a mouse model of Alzheimer's disease-related amyloidopathy allowed us to identify functional impairments in the RSC which may underlie cognitive impairments previously seen in these animals (Cheng et al., 2007; Wright et al., 2013).

3.5.2 Power Spectral Analysis

Power spectral analysis was performed in order to investigate oscillatory activity across a range of frequency bands, and compare the effects of novelty and genotype on retrosplenial cortex activity. When the entire 15-minute recording sessions were analysed, beta and gamma power were significantly higher during novelty, in both RSC subregions, for both genotypes. Furthermore, this increase was even greater when only the first minute of each session was analysed. Numerous studies have noted changes in beta activity in a range of brain regions, during a variety of behaviours (see Spitzer and Haegens, 2017 for review). It is important to note that due to variability between groups in the naming and frequency ranges of neural oscillation frequency bands, cross-study comparison is often complicated. What we have referred to as beta, has previously been called upper beta (Spitzer and Haegens, 2017), beta2 (França et al., 2014), or slow gamma (Carr et al., 2012; Remondes and Wilson, 2015). For the sake of clarity, references to beta oscillations in this thesis refer to the 20-

30 Hz frequency range. Beta oscillations have long been associated with motor activity and sensory processing, and a large body of work has also noted changes in beta activity in a range of brain regions during other cognitive tasks (see Engel and Fries, 2010 for review). Others have noticed similar novelty-induced beta oscillations in the hippocampus: Berke *et al.* (2008) reported a large increase in beta power that appeared when mice explored a novel environment, which persisted for around a minute, before returning to a lower level. The authors concluded that these oscillations may be a "dynamic state that facilitates the formation of unique contextual representations." Work by França *et al.* (2014) demonstrated that beta power was also transiently enhanced in the hippocampus during exploration of novel objects, but not previously experienced familiar items. Furthermore, they found that administration of an amnestic agent, namely haloperidol, resulted in a similar increased beta activity upon re-exposure to previously encountered objects, suggesting they had been "forgotten" and were therefore novel again. This further reinforces the idea that hippocampal beta activity is related to novelty, and extends the previous work by demonstrating that hippocampal-dependent novel object recognition can also elicit beta oscillations. Subsequently, França, Borgegius and Cohen (2020) investigated novelty-associated beta oscillations across a cortical-hippocampal novelty circuit, by simultaneously recording from hippocampus, prefrontal cortex and parietal cortex during environmental and object novelty. Novelty-associated increases in beta power were seen in the prefrontal cortex during environmental novelty.

Beta power was significantly higher overall in J20 mice, in both RSC subregions. Previous work in this strain has demonstrated a hyperexcitability phenotype, but to the author's knowledge, changes in the beta frequency band have yet to be

demonstrated in J20 mice (Palop et al., 2007; Palop and Mucke, 2009; Verret et al., 2012). Interestingly, aberrant beta oscillations have long been associated with another progressive neurodegenerative disease, Parkinson's disease. Increased beta oscillatory activity in the basal ganglia and cortex are associated with motor impairments in Parkinson's disease (for review see Brittain, Sharott and Brown, 2014), and administration of levodopa has been shown to improve motor function and reduce beta oscillations (Brown et al., 2001). The relationship between beta oscillations in the RSC and environmental novelty demonstrated in this study suggest these oscillations may have a potential role in contextual memory processes, and aberrant oscillatory power in this same frequency band in J20 mice may suggest a novel source of cognitive dysfunction in these animals (Cheng et al., 2007; Wright et al., 2013).

3.5.3 Beta Bursting Activity

Upon closer inspection of beta-filtered local potentials and power spectrograms, beta activity appears as discrete bursts rather than continuous oscillations. Due to the use of averaging across trials or analysis spanning long temporal segments, the phasic nature of transient oscillatory events can be easily lost. Previous studies into beta oscillations during novelty in rodents have generally viewed beta activity as continuous oscillations, rather than discrete events (Berke et al., 2008; França et al., 2014, 2020). This is despite Berke *et al.* (2008) noting that beta appears as pulses, and a brief mention of burst detection and characterisation by França *et al.* (2014). As demonstrated in this study, novelty-associated beta oscillations in the RSC conform well to a model of discrete bursts, where their rate and characteristics can vary depending on environmental novelty. Beta bursts are significantly more frequent during novel sessions, due to

a large increase in beta burst rate during the first minute of these sessions. During familiar sessions, the rate of beta bursting is far lower, and generally stable across the entire session. Previous work on beta bursting across the brain in a range of behaviours has led some to suggest that the unifying function of beta oscillatory activity is the maintenance of the “status-quo”, be it the current motor state, sensory stimulus or cognitive set (Engel and Fries, 2010). This theory would suggest that, beta activity would be decreased during novelty, and increased during familiarity. As we have shown, this is not the case. While steady and persistent beta bursting during familiarity may support the maintenance of the contextual “status-quo”, in this case the environment, this theory does not reconcile the significant increases in beta activity that occur during novelty. It is possible that high beta burst rate could signal the creation of a new “cognitive set”, which is maintained by persistent bursting. While the relationship between beta bursting and novelty is maintained in J20 mice, there is a significant increase overall in burst detection in these animals. Interestingly, this difference arises from a significant increase in burst rate throughout familiar sessions, and a trend towards increased beta burst rate during the final 10 minutes of novel sessions. Notably, there was no significant difference between beta burst rate during the initial minute of novel sessions. The rate of beta bursting during familiarity in J20 mice is approximately twice as high as that in wild-type mice, so a small increase in beta burst rate during novelty would be expected, and the absence of this difference may provide insight into the mechanisms underlying beta bursting. One possibility is that there is a theoretical maximum beta burst rate in the retrosplenial cortex, which could arise from the limitations of the local neuronal network physiology, or perhaps the slow firing rates of neurons from a distant projecting brain region. Another possibility is that there are different mechanisms

underlying the generation of slow “spontaneous” bursting, and rapid “induced” bursting. The steady beta bursting during familiarity suggests a “basal” beta bursting rate, but further investigation in a range of behavioural states would be required to confirm this.

3.5.4 Beta Bursting Characteristics

By treating transient beta oscillations as discrete events, a variety of characteristics can be investigated. Beta bursts are both larger in magnitude, and longer in duration during novelty. Due to the nature of our detection algorithm, this could partially support the increased beta burst detection seen during novelty. Increases in burst magnitude and duration could have beneficial effects on modulation of neuronal spiking activity. Greater amplitudes could allow modulation of larger populations of neurons, while longer durations could allow a wider temporal window for neuronal activation. In the somatosensory cortex, beta oscillations also appear as short events in both mice and humans; and beta burst characteristics, such as duration and frequency range, are highly conserved across tasks and species (Shin et al., 2017). On average, beta bursts were significantly larger in magnitude in J20 mice, but there was no change in burst duration between the two genotypes. The increase in burst magnitude may result from the same mechanisms underlying hyperexcitability and spontaneous epileptiform activity seen in this mouse model (Palop et al., 2007; Verret et al., 2012).

A notable discovery was that beta oscillations appear to be highly rhythmic during beta bursts, and more arrhythmic during non-burst epochs, which argues against the validity of averaging across burst and non-burst epochs when investigating beta activity. This mirrors data shown by Shin et al (2017), who demonstrated

that beta rhythmicity was absent outside beta burst epochs. As previously mentioned, other groups have characterised oscillations in the 20-30 Hz range as slow gamma (Carr et al., 2012; Remondes and Wilson, 2015). These data suggest that beta oscillations conform to a bursty generator model, while gamma oscillations have previously been shown to conform to a dynamic amplitude modulation model, where their amplitude is often coupled to theta phase (Canolty et al., 2006; Tort et al., 2009). This divergence supports the idea that beta is a valid frequency band that is distinct from the gamma band, arguing against this frequency range being named as “slow gamma” (Carr et al., 2012; Remondes and Wilson, 2015) and suggesting that beta oscillations may therefore arise from different mechanisms to those which underlie gamma oscillations (Buzśaki and Wang, 2012). Finally, spectral analysis of beta bursts demonstrate that the frequency range of beta bursts is firmly within the 20-30 Hz range, which both supports the classification of these transient events as “beta” bursts, and also validates the 20-30 Hz range as a distinct frequency band.

3.5.5 Phase-Amplitude Coupling

Lower frequency oscillations such as delta and theta have been shown to be highly correlated over large spatial distances within the brain, while fast oscillations such as gamma are generally thought to be more local, and spatially limited (Von Stein and Sarnthein, 2000). Therefore, phase-amplitude coupling is thought to allow for top-down coordination of local neuronal network activity by large-scale oscillatory activity (Canolty and Knight, 2010; Canolty et al., 2010). There are two main peaks in the phase-amplitude coupling comodulograms from the RSC, one between phase frequency at 7.5 Hz and amplitude frequency at 70 Hz, indicating theta-gamma coupling, while the other peaking between phase

frequency at 7.5 Hz and amplitude frequency at approximately 15-25 Hz, between the alpha and beta bands. While the majority of this coupling was at alpha frequency, there was sufficient coupling in the beta band to warrant treatment as a composite theta-alpha/beta coupling. Theta-gamma coupling is likely the most well studied form of phase-amplitude coupling, and has long been associated with memory processes (Lega et al., 2016). The presence of theta-gamma coupling in the RSC data was notable, as while previous work by Koike et al (2017) demonstrated strong theta-gamma phase-amplitude coupling in the RSC during paradoxical sleep (although at a higher gamma frequency of 120Hz), the authors did not see notable theta-gamma PAC during active waking. Theta-gamma coupling is generally the dominant form of phase-amplitude coupling in hippocampal and cortical recordings by a number of groups, and has been associated with a range of behaviours (for review, see Canolty and Knight, 2010). Interestingly, theta-gamma coupling was seemingly unaffected by novelty or familiarity in this study, remaining relatively constant between sessions. Furthermore, theta-alpha/beta was the dominant form of phase-amplitude coupling in the RSC during novelty.

The relationship between theta-alpha/beta PAC and beta bursting in this study is unclear. The rhythmicity data argues against a dynamic amplitude modulation model, and the absence of theta-beta coupling separate from theta-alpha coupling suggests that it is unlikely that phase amplitude coupling between theta phase and beta amplitude is the sole mechanism underlying beta bursting. This is supported by the finding that theta-alpha/beta coupling is uncoupled from novelty in J20 mice. However, theta-alpha/beta coupling may support beta bursting by coordinating the timing of beta bursts during novelty, and aberrant

beta bursting in J20 mice could result from this uncoupling of beta oscillations from theta phase. Others have noted theta-beta PAC in humans as well, both in the hippocampus during a working memory task (Axmacher et al., 2010), and in the inferior temporal cortex during object novelty (Daume et al., 2017). These data also raise the possibility that beta bursting in the retrosplenial cortex is either being driven or modulated by a distant brain region (Canolty and Knight, 2010). Synchrony between theta oscillations in the RSC and another brain region, in combination with theta-beta coupling in the RSC could allow for control of retrosplenial beta bursting by this distant region.

3.5.6 Neuronal spiking during Beta Bursts

To our knowledge, this is the first study that has demonstrated increased neuronal spiking during beta bursts. Work by Rule et al (2017) in non-human primates, demonstrated transient beta oscillations in local field potential recordings from motor and premotor cortex, but showed no difference in single-unit firing rates between high-beta and low-beta epochs. It is important to note that due to the geometry of the probes used in our study, it would not be possible to reliably isolate single units due to rapid decreases in amplitude with increasing distance from the soma (Buzsáki et al., 2012). By using multi-unit activity as a measure of overall spiking activity, it is possible to broadly investigate the effects of beta bursting on neuronal spiking, yet it is entirely possible that these multi-units are composed of different neuronal subtypes, which may respond differently to beta bursts. Different neuronal populations can have vastly different responses to oscillatory events; during transient high frequency oscillations known as sharp wave ripples, spiking of neurons in the RSC can vary dramatically, depending on neuronal subtype or cortical layer (Nitzan et al., 2020; Opalka et al., 2020).

Therefore, it is also possible that the multi-units in this study may be composed of single-units with vastly different responses to beta bursts, which would undoubtedly dilute the effects. Future work into beta bursting should attempt to isolate single-units, and classify them into subgroups such as putative interneurons or excitatory neurons, before investigating the effect of beta bursts on the firing of these individual neurons.

Many groups have previously shown that information may be rapidly represented and stored in the RSC (Cowansage et al., 2014; Czajkowski et al., 2014; Koike et al., 2017; Vedder et al., 2017). Beta oscillations have also been shown to carry a variety of different forms of contextual information in a range of brain regions, and phasic increases in beta power during working memory maintenance may represent reactivation of encoded information (Spitzer and Haegens, 2017). Supporting this is a study in which the authors employed transcranial magnetic stimulation to activate a currently unattended memory, as shown by an increase in content-specific beta activity (Rose et al., 2016). The theory put forth by Spitzer and Haegens (2017), is that beta oscillations can activate and reactivate neuronal ensembles to create and recall cortical representations. This theory is consistent with the data shown in this study: high beta bursting activity during perceived novelty activates neurons in the dysgranular RSC, which may encode content about the novel environment, and subsequent beta bursting may continuously reactivate these ensembles, further consolidating or altering this representation. Recent breakthroughs in real-time burst detection and neurofeedback have made it possible to artificially induce beta bursts in awake behaving animals, creating the possibility of testing this hypothesis directly (Karvat et al., 2020).

It was of note that beta bursting in wild-type mice was associated with an increase in neuronal spiking in the dysgranular RSC but not the granular RSC. This difference may due to layer specific differences, due to the location of the probe. In rodents, the retrosplenial cortex is found directly adjacent to the midline of the brain, and folds into the longitudinal fissure. The boundary between the two subregions is such that the superficial layer of the dysgranular RSC is visible on the dorsal surface of the cortex while the superficial layer of the granular RSC forms part of the longitudinal fissure. Due to the probe placement in this study, the silicon probe is perpendicular to the layers of the dysgranular RSC, yet parallel to those in the granular RSC, allowing us to sample from many layers of the RSCdg, but only a single, deep layer of the RSCg. Future work with probes angled away from midline could effectively record from the superficial layers of the dysgranular and granular RSC simultaneously, while avoiding damage to the sagittal sinus. In J20 mice, the coupling between beta bursting and neuronal spiking in the RSCdg was lost. Considering the hypothesised role of beta bursts in the activation of neuronal ensembles, this uncoupling would effectively render beta bursts ineffectual in this brain region, despite increased beta bursting in J20 mice.

3.5.7 Neurophysiological changes in J20 mice

As we have shown in this chapter, several neurophysiological changes were seen across the RSC in J20 mice. Beta power was significantly higher overall, beta bursts were more frequent, and bursts were far larger in magnitude, especially in the RSCg. Averaging across trials, or in this case, long recording sessions can cause transient oscillatory events to appear as continuous oscillations. However, while it may appear as though increased beta power is as a result of increased

beta bursting, and increased beta burst magnitude, spectral analysis of beta bursts and pre-burst epochs demonstrate that beta power appears to be elevated outside of beta bursts. These data suggest that perhaps increased beta bursting in J20 mice is as a consequence of persistently increased beta oscillatory activity. To the best of our knowledge, beta oscillations have yet to be investigated in this strain. Previous work in J20 mice has demonstrated spontaneous epileptiform discharges in the cortex, which were associated with increased alpha power, and decreased gamma power (Palop et al., 2007; Hanson et al., 2020). While variable increases in alpha and gamma power were detected in the retrosplenial cortex in the J20 mice in this study, we saw no evidence of epileptiform discharges. Increased transient oscillatory activity appeared as beta bursts rather than epileptiform discharges, which were centred around beta frequency rather than alpha. It is notable that despite the changes discussed above, certain relationships between neural network activity and novelty were maintained in J20 mice. During novelty, beta power was higher, beta bursting was increased, as was beta burst magnitude. This suggests that despite changes to retrosplenial beta oscillations in this strain, the mechanisms that underlie the beta response to novelty are functional.

At the age point used, amyloid pathology in J20 mice is thought to be predominantly located in the hippocampus in this model, although, amyloid pathology seems to develop in the RSC to a much greater extent than other cortical regions, especially in RSCg (Whitesell et al., 2019). Hyperexcitability of cortical neurons in a mouse model of amyloid pathology was more prevalent in neurones proximal to amyloid plaques (Busche et al., 2008), and inhibitory interneuron dysfunction in J20 mice has been shown to lead to cortical network

hypersynchrony and spontaneous epileptiform discharges (Verret et al., 2012). The hippocampus projects directly to RSCg, and indirectly, via the subiculum, to RSCdg (van Groen and Wyss, 1992; Van Groen and Wyss, 2003), so network dysfunction in RSC may be explained by its high levels of amyloid pathology or its anatomical connectivity with an increasingly dysfunctional hippocampus (Palop et al., 2007). These findings suggest a novel form of Alzheimer's disease (AD) related cortical dysfunction, which may underlie or exacerbate cognitive dysfunction seen in these mice, and in people with AD. Erroneous attribution of novelty to familiar environments, could cause memory impairments, and result in wandering and confusion. The loss of coupling between beta bursting and neuronal spiking seen in J20 mice suggest that attenuating bursting without restoring this coupling may be ineffective in AD.

3.5.8 Conclusions

In conclusion, phasic bursts of beta oscillations in the retrosplenial cortex are strongly associated with contextual novelty, and may be responsible for activating neural ensembles, and forming cortical representations of environments. Network dysfunction in J20 mice results in aberrant beta oscillatory activity and an uncoupling of beta bursting from spiking, which may underlie cognitive impairments in these mice.

4 Chapter 4

4.1 Introduction

In Chapter 3 we demonstrated a number of neurophysiological correlates of contextual memory in the retrosplenial cortex, including transient bursts of beta oscillations that were far more frequent when animals were exposed to a novel environment. Through our investigations in J20 mice, a mouse model of Alzheimer's disease-associated amyloidopathy, we demonstrated a range of neuronal network changes including altered oscillatory activity, aberrant beta bursting and an uncoupling of beta bursts from neuronal spiking. As we have previously discussed, much of the work into beta oscillations during novelty has been performed in the hippocampus, where novelty is associated with increased beta power (Berke et al., 2008; França et al., 2014, 2020). It was therefore of interest for us to extend our investigations to the hippocampus, to investigate how neurophysiological correlates of contextual novelty in this region compare to those in the retrosplenial cortex. This was made possible by our choice of silicon electrophysiology probes, as their length allowed us to span the entire retrosplenial cortex and reach the hippocampus, making conjunctive recording possible. Our hippocampal analysis had 3 main aims, firstly, to investigate whether contextual novelty was associated in increases in beta power, as previously seen (Berke et al., 2008; França et al., 2014, 2020), and to identify whether these beta oscillations conformed to a model of discrete beta bursts as in the retrosplenial cortex. Secondly, we aimed to investigate the extent of functional connectivity between the retrosplenial cortex and hippocampus in order to understand how these regions may interact during the processing of contextual information. There is a wealth of data that demonstrates that the

retrosplenial cortex and hippocampus are anatomically connected, predominantly via the subiculum, but little is known about how these regions interact in awake, behaving animals (Koike et al., 2017; Nitzan et al., 2020). The final aim was to investigate neuronal network activity in J20 mice, and compare any changes to those we have seen in the retrosplenial cortex (Chapter 3), and those previously described in the literature (Palop et al., 2007). Altered neuronal network activity may underlie cognitive impairments seen in Alzheimer's disease, the specific nature of these changes may provide insights into the specific neurophysiological effects of amyloid pathology, revealing novel targets for cognitive-enhancing drugs.

In order to investigate changes in hippocampal network activity during contextual novelty, we recorded LFPs and multi-unit spiking activity from the CA1 region of the hippocampus, while mice freely explored either a novel or familiar environment. As these recordings were made concurrent with our retrosplenial cortex recordings described in Chapter 3, the data in these two chapters are from the same experimental group. To probe the effects of AD-associated amyloid pathology on hippocampal activity we used J20 mice, a widely employed mouse model of amyloidopathy. In this chapter, we demonstrate that in addition to the previously demonstrated novelty-associated beta bursting in the retrosplenial cortex (Chapter 3), novelty-associated beta bursting also occurs in the hippocampus, and that these beta bursts are highly synchronous between these two regions. We also demonstrate a number of additional neurophysiological correlates of contextual memory in the hippocampus, many of which vary dramatically from those in the retrosplenial cortex. These data demonstrate that increased beta power in the hippocampus during novelty conforms well to a

model of discrete beta bursts, and that synchronous beta bursts in the retrosplenial cortex and hippocampus may form temporal windows of effective communication between these regions during contextual information processing. Finally, we observed a range of changes in hippocampal network activity in J20 mice, including aberrant beta bursting and altered oscillatory activity, many of which are different to those in the retrosplenial cortex, and may underlie cognitive dysfunction in these animals (Cheng et al., 2007). Divergent changes in network activity in the retrosplenial cortex and hippocampus of J20 mice highlights the importance of uncovering the specific mechanisms by which amyloid pathology affects neuronal function.

4.2 Methods

4.2.1 Author's Note

As the data in this chapter was collected as part of the same study described in Chapter 3, this methods section will be generally the same as the one in the previous chapter, however there are a number of notable differences that warrant the inclusion of a separate methods section for this chapter.

4.2.2 Animals

8 male J20 mice and 6 wild-type littermates were bred at the University of Exeter and housed on a 12-hour light/dark cycle. All procedures were carried out in accordance with the UK Animal (Scientific Procedures) Act 1986 65 and were approved by the University of Exeter Animal Welfare and Ethical Review Body. Access to food and water was provided ad libitum. All animals were kept on a 12-hour light/dark cycle, with the light/dark cycle matching the normal daylight/night-time cycle, meaning all interactions including handling, surgery and behaviour took place during the light cycle. Mice were group housed prior to surgery, and

single housed post-surgery, in order to prevent damage to the surgical implants. All mice were between 6 to 8 months of age at the time of recordings.

4.2.3 Surgery

Mice were unilaterally implanted with a 16 channel, single shank silicon probe (NeuroNexus Technologies, A1x16-5mm-100-177-CM16LP), in the right retrosplenial cortex (AP –2 mm, ML +0.5 mm, DV +1.75 mm, 0° Pitch, Figure 3.1c). These silicon probes penetrated the entire retrosplenial cortex, and were targeted towards the pyramidal cell layer of the dorsal hippocampal CA1 region. Mice were anaesthetised using isoflurane and fixed into a stereotaxic frame. A small craniotomy was drilled over the desired co-ordinate, and at least one hole was drilled in each of the major skull plates, in which miniature screws were placed to act as supports (Antrin Miniature Specialties). The probe was slowly lowered into the desired location, and fixed in place with dental cement (RelyX Unicem, 3M). The ground wire from the probe was connected to a silver wire, attached to a screw overlying the cerebellum. Throughout surgery, body temperature was monitored with a rectal probe and regulated by a feedback-controlled heat mat. Animals were kept hydrated by subcutaneous injections of Hartmann's solution once per hour of surgery (0.01 ml/g body weight).

4.2.4 Data Analysis

All single-site LFP analyses were performed for a single channel in the stratum oriens of the CA1. The location of our probes was estimated from post-hoc histology, and for those animals where the probe crossed stratum pyramidale, a reversal of theta oscillation phase could be seen in LFP recordings. Due to the thickness of the corpus callosum towards the midline, in some experimental animals, probes did not reach the hippocampus, but stopped short. It is for that

reason that for all analyses, n = 5 for wild-type mice and n = 6 for J20 mice. Eleven mice in total were used in this study, 5 wild-type and 6 J20, with each mouse undergoing a total of ten recording sessions (5 days, 2 sessions per day). Unfortunately, the local field potential data from Day 3 session 1 (i.e. session 3a) was corrupted for a single wild-type mouse, and therefore data for this mouse from this session was omitted from all figure making and statistics.

4.3 Results

In order to investigate neurophysiological correlates of spatial learning and memory in the hippocampus (HC), and compare them to those demonstrated in the retrosplenial cortex in Chapter 3, local field potentials were recorded simultaneously from the CA1 region of the dorsal hippocampus, and the retrosplenial cortex, in the same experimental group as in Chapter 3. In rodents, the dorsal hippocampus can be found directly ventral to the RSC, making concurrent recordings possible using a single, vertical silicon probe. In order to directly compare the activity of the hippocampus to that which we have seen in the retrosplenial cortex in Chapter 3, similar analyses were performed, including spectral analysis, beta burst detection, and multi-unit activity analysis. Furthermore, through simultaneous recordings in different brain regions, it is possible to investigate temporal correlations between these regions, and probe functional connectivity across this network. As such, a number of analyses were performed to determine the extent of oscillatory interactions between the RSC and HC, and also between the subregions of the RSC itself.

4.3.1 Hippocampal Spectral Analysis

In order to investigate any changes in oscillatory activity in HC during environmental novelty, power spectral analysis was performed on the entire 15

minutes of each session (Figure 4.1a). These power spectra were averaged across novel and familiar sessions for wild-type and J20 mice (Figure 4.1b). Significant findings are summarised in Table 3, however a more detailed account of these findings, including descriptive statistics, will be listed here in-text. There was a significant interaction between the effects of genotype and novelty on theta power ($F(1,9) = 20.8$, $p = 0.001$, Mixed ANOVA). Theta power was significantly higher during novel sessions in wild-type mice (Nov: 28.9 ± 0.5 dB; Fam: 28.6 ± 0.5 dB, $p = 0.009$), but significantly lower during novel sessions in J20 mice (Nov: 25.3 ± 0.7 dB; Fam: 25.6 ± 0.7 dB, $p = 0.01$). Theta power was significantly lower in J20 mice than in wild-type mice, during both novel (WT: 28.9 ± 0.5 dB; J20: 25.3 ± 0.7 dB, $p = 0.02$), and familiar sessions (WT: 28.6 ± 0.5 dB; J20: 25.6 ± 0.7 dB, $p = 0.04$). Alpha power was significantly higher overall during familiar sessions (Main Effect Novelty - $F(1,9) = 9.8$, $p = 0.01$, Mixed ANOVA), while beta and gamma power were significantly higher overall during novel sessions (Beta: Main Effect Novelty - $F(1,9) = 25.2$, $p = 7e\text{-}4$, Mixed ANOVA; Gamma: Main Effect Novelty - $F(1,9) = 10.4$, $p = 0.01$, Mixed ANOVA). Alpha power was significantly higher during familiar sessions in wild-type (Nov: 21.5 ± 0.5 dB; Fam: 21.8 ± 0.5 dB, $p = 0.01$), but not J20 mice. Beta power was significantly higher during novel sessions in both wild-type (Nov: 19.5 ± 0.6 dB; Fam: 19.2 ± 0.5 dB, $p = 0.04$) and J20 mice (Nov: 19.3 ± 0.4 dB; Fam: 18.8 ± 0.4 dB, $p = 9e\text{-}4$), while gamma power was only significantly higher during novel sessions in J20 mice (Nov: 13.5 ± 0.5 dB; Fam: 13.3 ± 0.4 dB, $p = 0.03$). Delta and gamma power were significantly lower overall in J20 mice (Delta: Main Effect Genotype - $F(1,9) = 7.7$, $p = 0.02$, Mixed ANOVA; Gamma: Main Effect Genotype - $F(1,9) = 12.6$, $p = 0.006$, Mixed ANOVA).

We previously demonstrated that the retrosplenial cortex was highly active during the first minute upon exposure to a novel environment (Chapter 3). In order to investigate whether this was also the case in the hippocampus, power spectral analysis was performed on the first minute of each session (Figure 4.1d). There was a significant interaction between the effects of genotype and novelty on theta power ($F(1,9) = 12.8$, $p = 0.006$, Mixed ANOVA). Theta power was significantly higher during novel sessions in wild-type mice (Nov: 29.7 ± 0.7 dB; Fam: 28.7 ± 0.6 dB, $p = 0.01$), but not in J20 mice. Theta power was significantly lower in J20 mice than in wild-type mice, during novel sessions (WT: 29.7 ± 0.7 dB; J20: 25.2 ± 0.9 dB, $p = 0.02$), but not familiar sessions. Beta power was significantly higher overall during novel sessions (Main Effect Novelty - $F(1,9) = 13.9$, $p = 0.005$, Mixed ANOVA). Beta power was significantly higher during novel sessions for wild-type (Nov: 21.3 ± 0.9 dB; Fam: 19.6 ± 0.5 dB, $p = 0.008$), but not J20 mice. Delta and gamma power were significantly lower overall in J20 mice (Delta: Main Effect Genotype - $F(1,9) = 11.6$, $p = 0.008$, Mixed ANOVA; Gamma: Main Effect Genotype - $F(1,9) = 10.4$, $p = 0.01$, Mixed ANOVA).

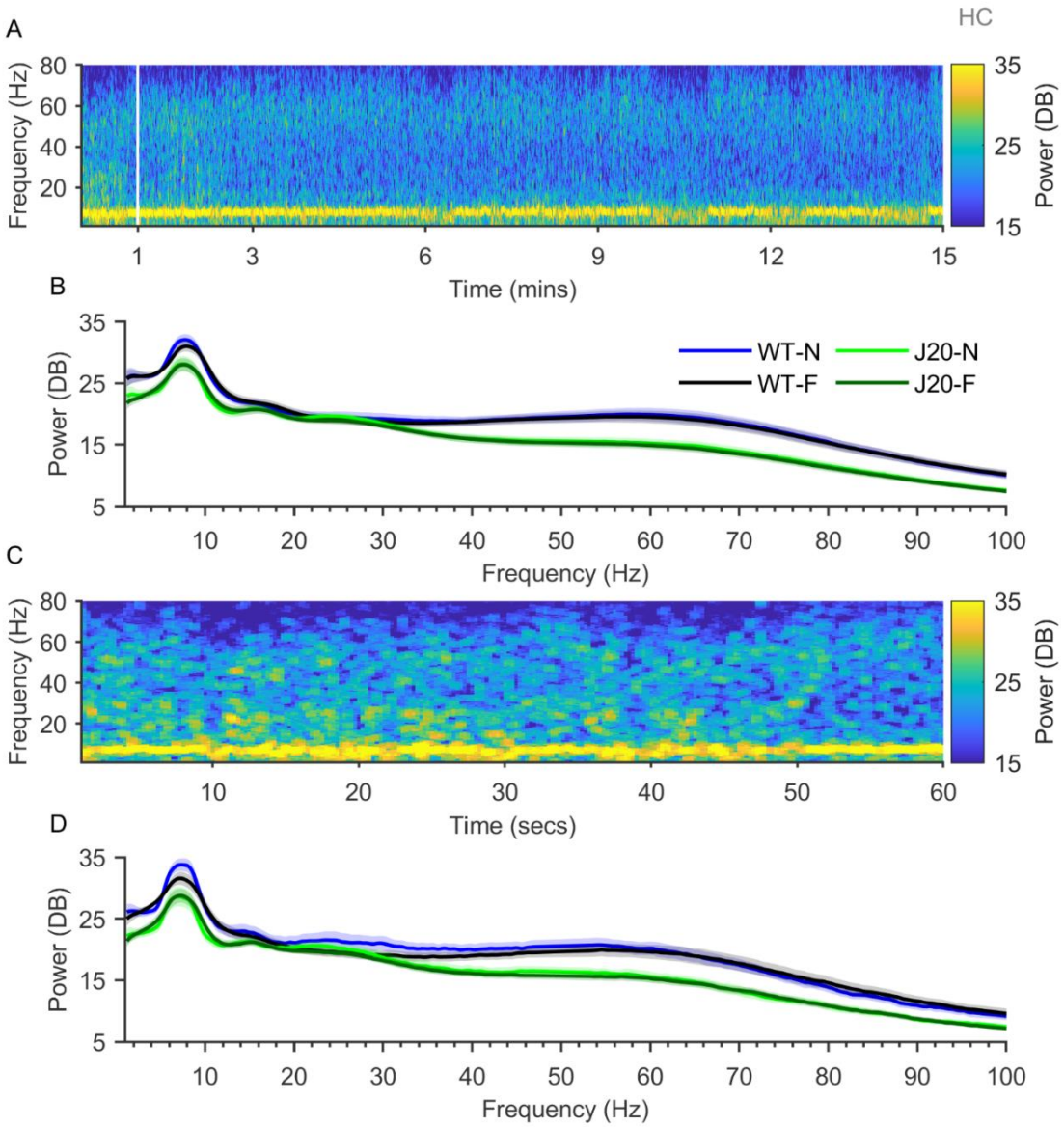

Figure 4.1 Beta (20-30 Hz) power is marginally higher during novelty in the hippocampus.
A. Example power spectrogram for an entire novel session in a wild-type mouse. B. Average power spectra for the entire 15 minutes of all novel and familiar sessions, for wild-type and J20 mice. Beta power was significantly higher during novel sessions in wild-type ($p = 0.04$) and J20 mice ($p = 9e\text{-}4$). Theta power was significantly higher during novel sessions in wild-type mice ($p = 0.009$), but significantly lower during novel sessions in J20 mice ($p = 0.01$). Delta and gamma power were significantly lower overall in J20 mice ($p = 0.02$, $p = 0.006$, respectively). C. Example power spectrogram shown in A, expanded to show the first 60 seconds of the session. D. Average power spectra for the first minute of all novel and familiar sessions, for wild-type and J20 mice. Beta power was significantly higher during novel sessions in wild-type ($p = 0.008$), but not J20 mice. Delta and gamma power were significantly lower overall in J20 mice ($p = 0.008$, $p = 0.01$, respectively). (Data shown as mean ± SEM, WT: $n = 5$, J20: $n = 6$).

Table 3 Hippocampal spectral analysis - Summary of significant results

Analysis Type	Frequency Band	Relationship	p-value
Whole Session	δ	WT > J20	0.02
	θ	N X G	0.001
	θ	$n_{WT} > f_{WT}$	0.009
	θ	$f_{J20} > n_{J20}$	1.00E-02
	θ	$n_{WT} > n_{J20}$	2.00E-02
	θ	$f_{WT} > f_{J20}$	4.00E-02
	α	f > n	1.00E-02
	α	$f_{WT} > n_{WT}$	1.00E-02
	β	n > f	7.00E-04
	β	$n_{WT} > f_{WT}$	0.04
	β	$n_{J20} > f_{J20}$	9.00E-04
	γ	n > f	0.01
	γ	$n_{J20} > f_{J20}$	3.00E-02
	γ	WT > J20	0.006
First Minute	δ	WT > J20	0.008
	θ	N X G	6.00E-03
	θ	$n_{WT} > f_{WT}$	1.00E-02
	θ	$n_{WT} > n_{J20}$	2.00E-02
	β	n > f	5.00E-03
	β	$n_{WT} > f_{WT}$	0.008
	γ	WT > J20	0.01

N, novelty; G, genotype; N X G, interaction between novelty and genotype; n, novel; f, familiar; WT, wild-type; J20, J20; δ, delta; θ, theta; α, alpha; β, beta; γ, gamma

4.3.2 Hippocampal Beta Bursting Activity

Beta bursts can be detected in local field potential recordings from the hippocampus, using the same algorithm as used previously in the RSC (Figure 4.2a). The number of beta bursts detected in the hippocampus was significantly higher overall during novel sessions (Main Effect Novelty - $F(1,9) = 27.3$, $p = 5e\text{-}4$, Mixed ANOVA); there were significantly more beta bursts detected during novel sessions in both wild-type (WT - Nov: 31.9 ± 3.9; Fam: 22.9 ± 1.3, $p = 0.02$) and J20 mice (J20 - Nov: 66.2 ± 2.7; Fam: 51.6 ± 2.7, $p = 0.001$). Moreover, there were significantly more beta bursts detected overall in J20 mice than in wild-type mice (Main Effect Genotype - $F(1,9) = 38.1$, $p = 2e\text{-}4$, Mixed ANOVA).

As shown in (Figure 4.2c, right), in the hippocampus, the rate of beta bursting was reasonably steady throughout familiar sessions, but higher during the first minute of novel sessions, for both genotypes (Figure 4.2c, left). Beta burst rate was significantly higher overall during novel sessions (Main Effect Novelty - $F(1,9) = 14.7$, $p = 0.004$, Mixed ANOVA), and also significantly higher overall during the initial part of recording sessions (Main Effect Time - $F(1,9) = 7.9$, $p = 0.02$, Mixed ANOVA). During novel sessions, initial burst rate was significantly higher than final burst rate in wild-type (WT - Nov Initial: 9.7 ± 3; Final: 1.2 ± 0.3, $p = 0.03$), but not J20 mice (J20 - Nov Initial: 8.7 ± 2.7; Final: 4.2 ± 0.6, $p = 0.2$). Furthermore, while there was no significant difference in initial burst rate during novel sessions between wild-type and J20 mice (Nov Initial - WT: 9.7 ± 3; J20: 8.7 ± 2.7, $p = 0.8$), final burst rate during novel sessions was significantly higher in J20 mice than in wild-type mice (Nov Final - WT: 1.2 ± 0.3; J20: 4.2 ± 0.6, $p = 0.002$). During familiar sessions, there was no significant difference between initial and final burst rate for either wild-type (WT - Fam Initial: 2.6 ± 0.5; Final:

1.4 ± 0.1, p = 0.3) or J20 mice (J20 - Fam Initial: 5.1 ± 0.9; Final: 3.5 ± 0.4, p = 0.1). Furthermore, during familiar sessions, both initial burst rate and final burst rate were significantly higher in J20 mice than in wild-type mice (Fam Initial - WT: 2.6 ± 0.5; J20: 5.1 ± 0.9, p = 0.04; Fam Final - WT: 1.4 ± 0.1; J20: 3.5 ± 0.4, p = 0.002).

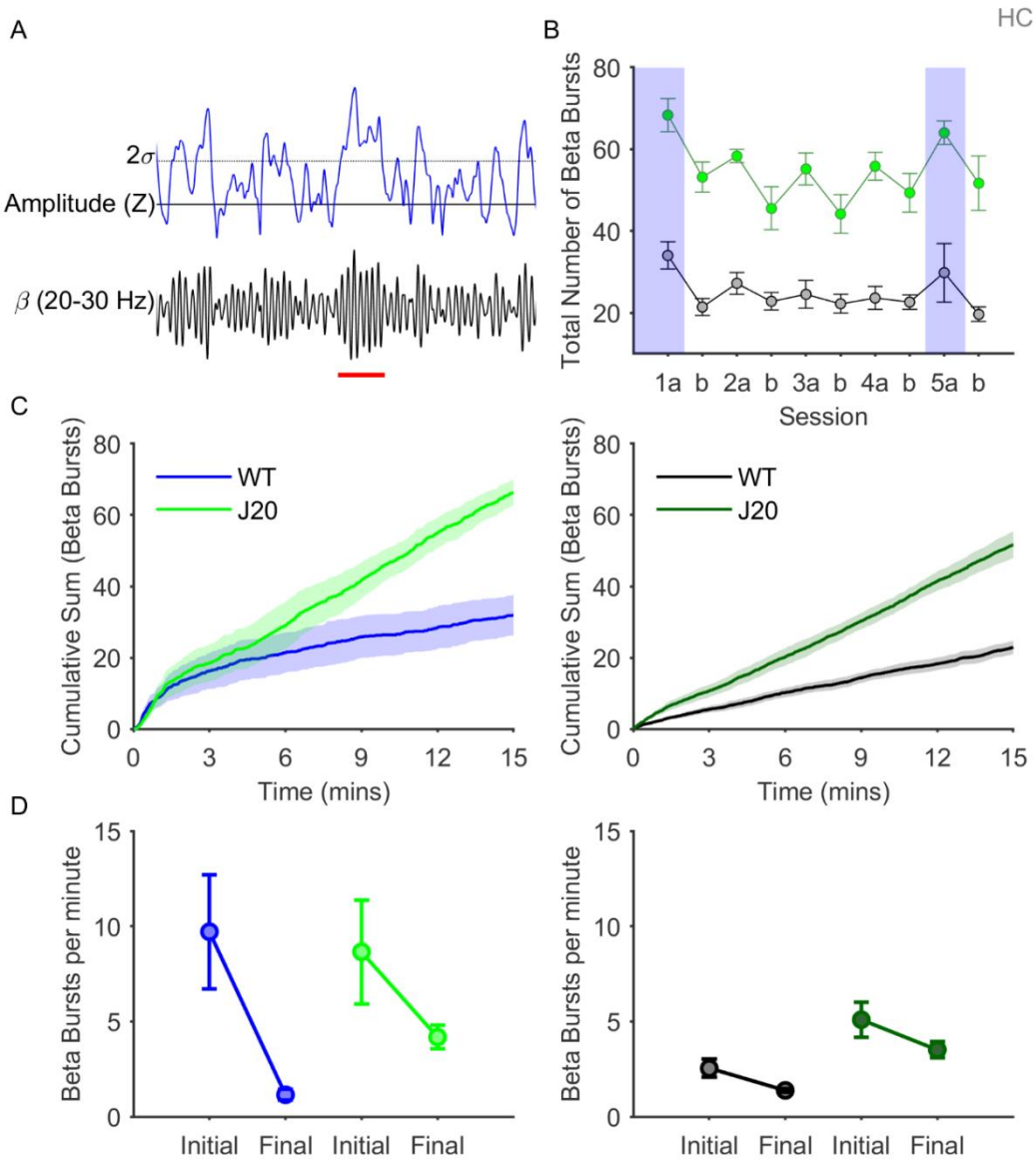

Figure 4.2 Beta bursting activity in the hippocampus.
A. Diagram illustrating how beta bursts were detected. B. Graph showing the average number of beta bursts detected in HC in each session, for wild-type (black) and J20 mice (green). Novel sessions Day1a and Day5a are highlighted in blue for clarity. Significantly more beta bursts were detected during novel sessions as compared to familiar sessions, for both wild-type ($p = 0.04$) and J20 mice ($p = 0.002$). On average, significantly more beta bursts were detected in J20 mice ($p = 3.4e\text{-}4$). C. Cumulative frequency graphs of beta bursts detected in novel (left) and familiar sessions (right), for wild-type and J20 mice. D. Graphs showing beta burst rate during novel (left) and familiar sessions (right), for wild-type and J20 mice. Beta burst rate was significantly higher overall during novel sessions ($p = 0.005$). During novel sessions, initial burst rate was significantly higher than final burst rate in wild-type ($p = 0.03$), but not J20 mice ($p = 0.18$). Final burst rate was significantly higher in J20 mice than in wild-type mice, for both novel ($p = 0.002$), and familiar sessions ($p = 0.002$). (Data shown as mean ± SEM, WT: n = 5, J20: n = 6).

4.3.3 Hippocampal Beta Burst Characteristics

Hippocampal beta burst characteristics were investigated, to determine whether they vary depending on novelty or genotype, and to compare hippocampal beta bursts to their retrosplenial counterparts. Beta burst magnitude was significantly higher overall during novel sessions (Main Effect Novelty - $F(1,9) = 26.1$, $p = 6e\text{-}4$, Mixed ANOVA). As shown in (Figure 4.3a), beta bursts were significantly larger in magnitude during novel sessions in wild-type (WT - Nov: 179 ± 13.7 µV; Fam: 157 ± 9.6 µV, $p = 0.001$) and J20 mice (J20 - Nov: 153 ± 7.2 µV; Fam: 143 ± 6.1 µV, $p = 0.04$). Beta burst duration was also significantly higher overall during novel sessions (Main Effect Novelty - $F(1,9) = 7.2$, $p = 0.03$, Mixed ANOVA). As shown in (Figure 4.3b), beta bursts were significantly longer in duration during novel sessions in wild-type (WT - Nov: 186 ± 3.8 ms; Fam: 175 ± 0.5 ms, $p = 0.02$), but not J20 mice (J20 - Nov: 186 ± 1.2 ms; Fam: 184 ± 0.7 ms, $p = 0.4$).

As before, in order to understand the frequency profile of hippocampal beta bursts, power spectral analysis was performed on individual beta bursts. As a control, these burst spectra were compared to power spectra of epochs of equal length directly prior to each burst. These power spectra were averaged across all bursts and “pre-bursts”, for wild-type and J20 mice (Figure 4.3c). Alpha power was significantly higher overall during beta bursts (Main Effect Burst - $F(1,9) = 20.5$, $p = 0.001$, Mixed ANOVA). There were significant interactions between the effect of genotype and burst on theta, beta and gamma power (Theta: Interaction - $F(1,9) = 16.4$, $p = 0.003$, Mixed ANOVA; Beta: Interaction - $F(1,9) = 9.6$, $p = 0.01$, Mixed ANOVA; Gamma: Interaction - $F(1,9) = 12.9$, $p = 0.006$, Mixed ANOVA). Beta bursts in wild-type mice were associated with significant increases in alpha, beta and gamma power (Alpha: WT – Pre-Burst: 21.1 ± 0.6 dB; Burst:

22.1 ± 0.6 dB, p = 0.003; Beta: WT – Pre-Burst: 18 ± 0.6 dB; Burst: 25.8 ± 0.6 dB, p = 2e-12; Gamma: WT – Pre-Burst: 14.8 ± 0.6 dB; Burst: 15.5 ± 0.6 dB, p = 2e-5). Beta bursts in J20 mice were associated with significant increases in beta and gamma power (Beta: J20 – Pre-Burst: 18 ± 0.4 dB; Burst: 25.1 ± 0.4 dB, p = 2e-12; Gamma: J20 – Pre-Burst: 12 ± 0.4 dB; Burst: 12.3 ± 0.5 dB, p = 0.008), and a significant decrease in theta power (Theta: J20 – Pre-Burst: 24.5 ± 0.7 dB; Burst: 23.7 ± 0.8 dB, p = 0.002).

In order to investigate beta rhythmicity in the hippocampus, the period of beta oscillations was calculated for all beta bursts and all epochs without beta bursts, and the distribution of these beta periods were calculated and averaged across all burst and non-burst epochs, in all sessions, for wild-type and J20 mice (Figure 4.3d). As in the RSC, while the distribution of beta periods during beta bursts was reasonably consistent, peaking around 0.04s, equivalent to a 25 Hz oscillation, the distribution of beta periods in non-burst epochs was skewed heavily towards longer beta periods. These data suggests a loss of beta rhythmicity during non-burst epochs, similar to what was seen in the retrosplenial cortex and supporting a “bursty generator” (van Ede et al., 2018), however due to a number of caveats to this type of analysis (discussed in Chapter 3), interpretation of this data is limited.

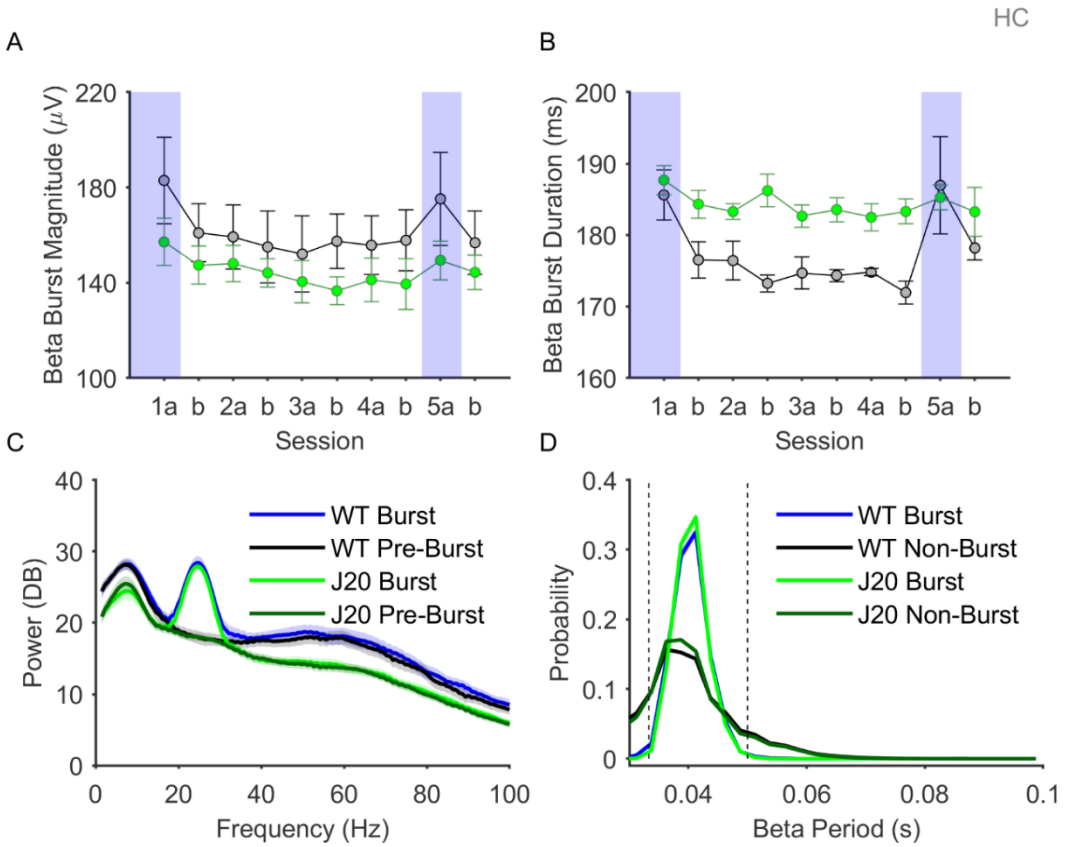

Figure 4.3 Beta burst characteristics in the hippocampus.
A. Graph showing the average beta burst magnitude in HC in each session, for wild-type and J20 mice. Beta bursts were significantly larger in magnitude during novel sessions in wild-type ($p = 0.003$), but not J20 mice ($p = 0.08$). Furthermore, there was no significant overall difference between burst magnitude in wild-type and J20 mice. B. Graph showing the average duration of beta bursts in HC in each session, for wild-type and J20 mice. Beta bursts were significantly longer in duration during novel sessions in wild-type ($p = 0.007$), but not J20 mice ($p = 0.6$). C. Average power spectra for beta burst, and pre-burst epochs. Beta bursts are associated with a large, significant increase in beta power, in both wild-type ($p = 3.4e-12$) and J20 mice ($p = 3.5e-12$). D. Average distributions of beta oscillation period for burst and non-burst epochs, in wild-type and J20 mice. Beta oscillations are tightly rhythmic during beta bursts, but not during non-burst epochs. (Data shown as mean ± SEM, WT: n = 5, J20: n = 6).

4.3.4 Hippocampal Phase-amplitude Coupling

Phase-amplitude coupling efficacy in the hippocampus was calculated for a range of phase and amplitude frequencies, and plotted as comodulograms, as shown in (Figure 4.4a). As in the RSC, there were two large peaks in these comodulograms, in the theta-gamma and theta-alpha/beta frequency ranges. The strength of phase-amplitude coupling was quantified for theta-alpha/beta and theta-gamma coupling for each session (Figure 4.4b). Theta-alpha/beta coupling was significantly higher overall during novel sessions (Main Effect Novelty - $F(1,9) = 9.7$, $p = 0.01$, Mixed ANOVA). Theta-alpha beta coupling was significantly higher during novel sessions in wild-type (WT - Nov: 2.5 ± 0.3; Fam: 1.5 ± 0.1, $p = 0.02$), but not J20 mice (J20 - Nov: 2.4 ± 0.4; Fam: 2 ± 0.2, $p = 0.2$). There was a significant interaction between the effects of genotype and novelty on theta-gamma coupling (Interaction - $F(1,9) = 15.8$, $p = 0.003$, Mixed ANOVA). Theta-gamma coupling was significantly higher during novel sessions in wild-type (WT - Nov: 3.5 ± 0.2; Fam: 2.7 ± 0.2, $p = 0.002$), but not J20 mice (J20 - Nov: 2.2 ± 0.3; Fam: 2.4 ± 0.3, $p = 0.2$). As before, this analysis was performed for the first minute of each session. When the same analysis was performed on the last minute of each session, there was no effect of genotype or novelty on coupling on either theta-alpha/beta coupling (Main Effect Genotype - $F(1,9) = 4.2$, $p = 0.07$, Mixed ANOVA; Main Effect Novelty - $F(1,9) = 1.7$, $p = 0.2$, Mixed ANOVA; Figure 4.5b, left) or theta-gamma coupling (Main Effect Genotype - $F(1,9) = 0.9$, $p = 0.4$, Mixed ANOVA; Main Effect Novelty - $F(1,9) = 2$, $p = 0.2$, Mixed ANOVA; Figure 4.5b, right).

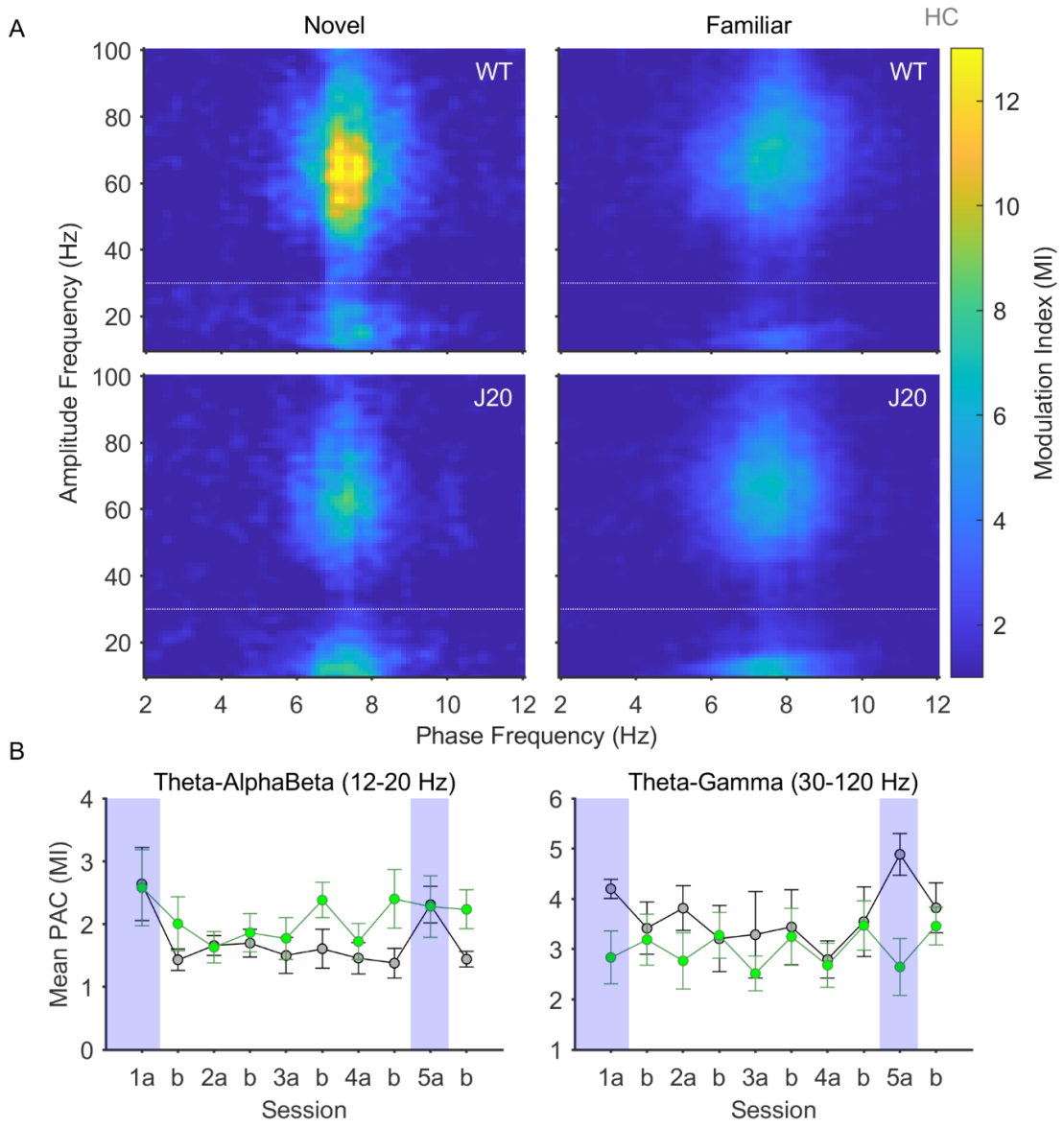

Figure 4.4 Theta-gamma phase-amplitude coupling is increased in the hippocampus during novelty.
A. Average comodulograms showing the strength of cross-frequency phase-amplitude coupling in HC during the first minute of novel and familiar sessions, for wild-type and J20 mice. Note the presence of two peaks in the theta-alpha/beta and theta-gamma ranges (the boundaries of which are denoted by the dotted lines). B. Average MI in the theta-alpha/beta (left) and theta-gamma ranges (right), for each session, for wild-type (black) and J20 mice (green). Novel sessions Day1a and Day5a are highlighted in blue for clarity. Theta-alpha/beta coupling was significantly higher during novel sessions for wild-type ($p = 0.02$), but not J20 mice ($p = 0.2$). Theta-gamma coupling was significantly higher during novel sessions for wild-type ($p = 0.01$), but not J20 mice ($p = 0.8$). (Data shown as mean ± SEM, WT: $n = 5$, J20: $n = 6$).

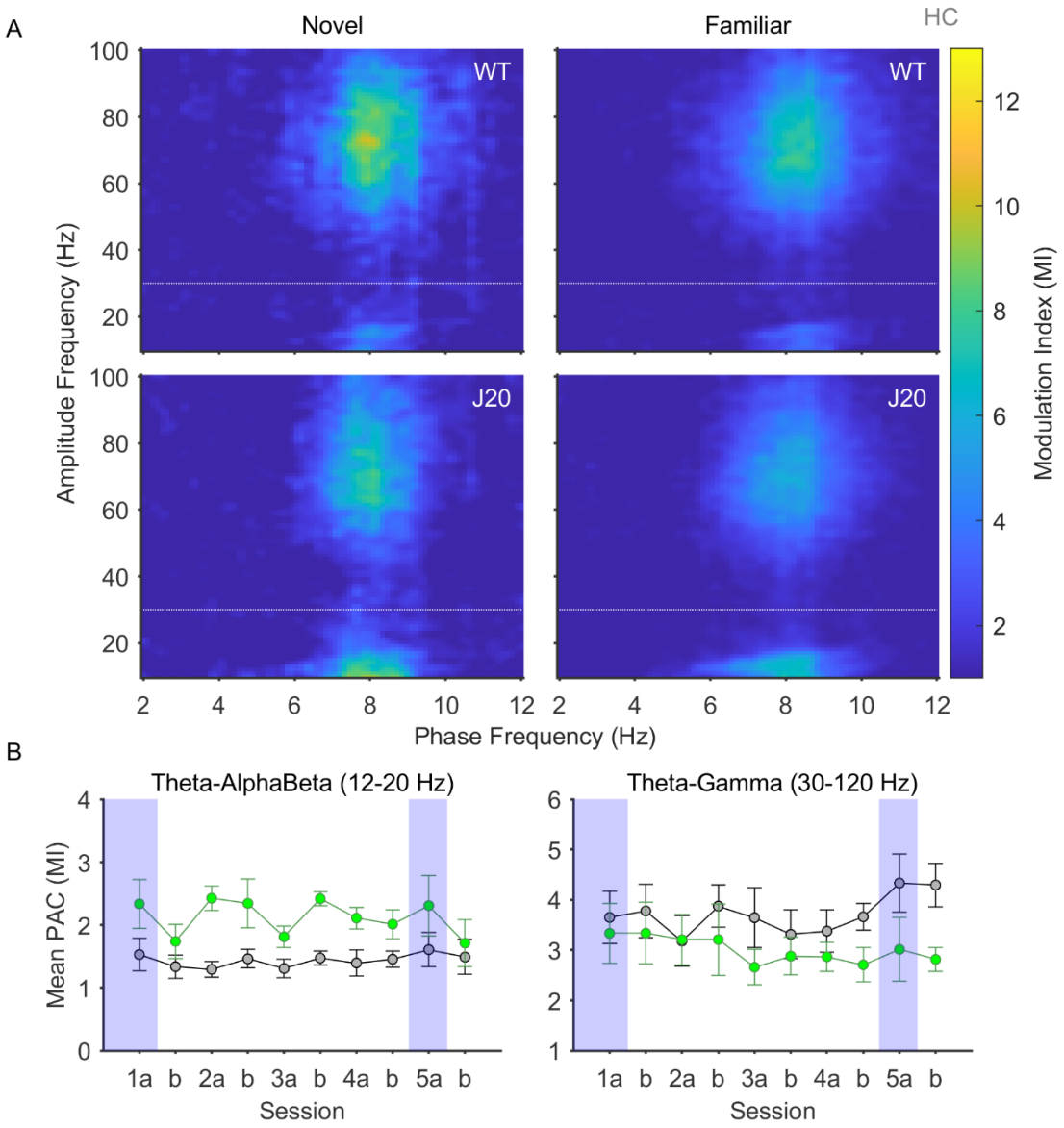

Figure 4.5 Phase-amplitude coupling during the final minute of each session in the granular retrosplenial cortex.

A. Average comodulograms showing the strength of cross-frequency phase-amplitude coupling in HC during the final minute of novel and familiar sessions, for wild-type and J20 mice. Note the presence of two peaks in the theta-alpha/beta and theta-gamma ranges (the boundaries of which are denoted by the dotted lines). B. Average MI in the theta-alpha/beta (left) and theta-gamma ranges (right), for each session, for wild-type (black) and J20 mice (green). Novel sessions Day1a and Day5a are highlighted in blue for clarity. There was no significant effect of genotype or novelty on theta-alpha/beta coupling ($p = 0.07$, $p = 0.2$, respectively). There was no significant effect of genotype or novelty on theta-gamma coupling ($p = 0.4$, $p = 0.2$, respectively). (Data shown as mean ± SEM, WT: $n = 5$, J20: $n = 6$).

4.3.5 Hippocampal Spiking Activity

General neuronal spiking activity, as well as spiking during beta bursts was also investigated in the stratum oriens of the HC. As shown in the left panel of (Figure 4.6a), neuronal spike waveforms had larger amplitudes on average in J20 mice (green), compared to wild-type mice (black) (WT: -68.6 ± 5.2 μV; J20: -95.4 ± 6.3 μV; $t(9) = 3.2$, $p = 0.01$; unpaired t-test). Furthermore, as shown in the right panel of (Figure 4.6a), neuronal firing rate was significantly higher on average in J20 mice (WT: 33 ± 10.4 Hz; J20: 79.2 ± 11.2 Hz; $t(9) = -3$, $p = 0.02$; unpaired t-test). As mentioned in Chapter 3, both the average spike waveform and average firing rate may vary greatly between animals depending on the distance between all detected neurons and the recording channel, which is especially relevant in these hippocampal recordings due to this region's dense laminar structure. The average beta amplitude during beta bursts is shown in (Figure 4.6b), averaged across all bursts with non-overlapping time segments. Beta bursts in both genotypes are associated with a brief, monophasic increase in beta amplitude that lasts no more than 200 ms on average. Finally, (Figure 4.6c) shows peri-event time histograms for spike rate during beta bursts, as a Z score from the pre-burst baseline (left of the dotted line). Beta bursting in the HC was associated with a non-significant trend towards increased spike rate during beta bursts in wild-type mice (Z-scored spike rate from baseline: 1.5 ± 0.5; $t(4) = 2.7$, $p = 0.053$; one-sample t-test; Figure 5c, left), which appeared to be reduced in J20 mice (Z-scored spike rate from baseline: 0.5 ± 0.7; $t(5) = 0.8$, $p = 0.5$; one-sample t-test; Figure 5c right).

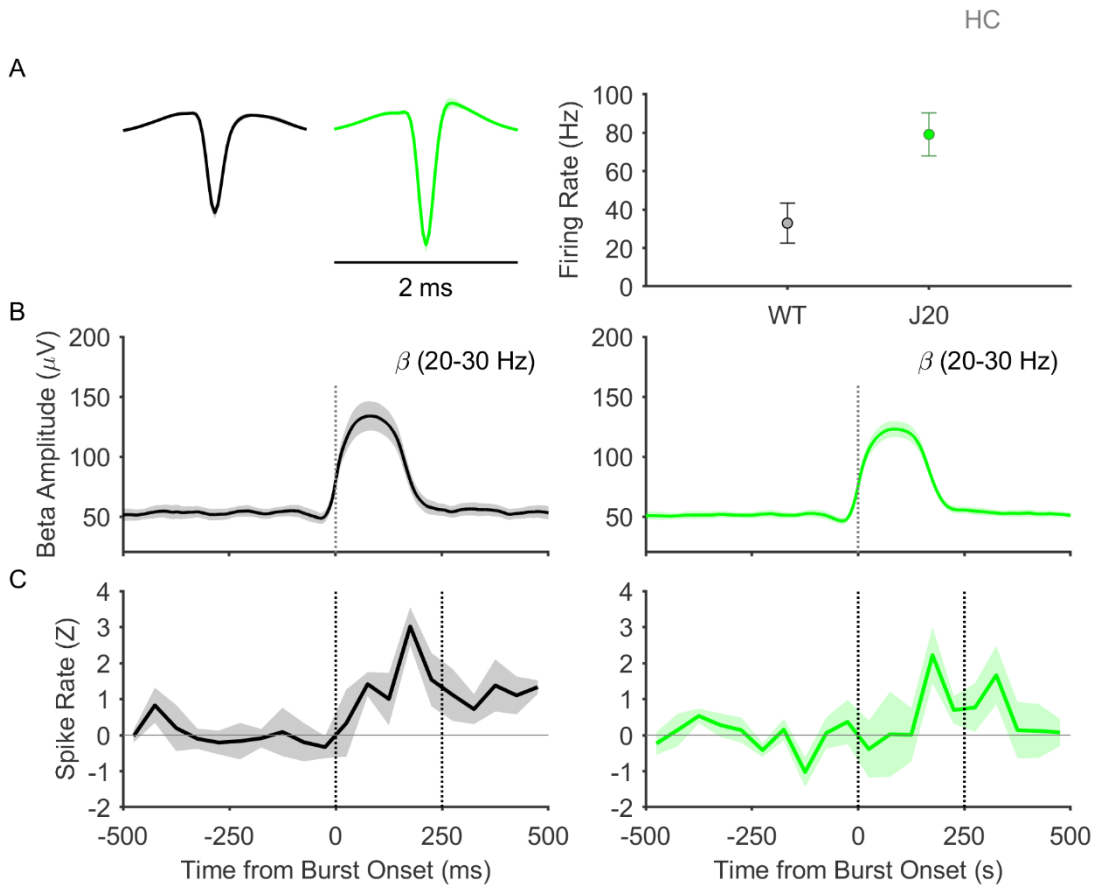

Figure 4.6 The overall firing rate of hippocampal neurons in J20 mice is increased.
A. Average spike waveforms for multi-unit activity in wild-type (black) and J20 (green) mice (left) and graph of average firing rate for detected multi-units across all sessions (right). Spike waveforms had larger amplitudes on average in J20 mice ($p = 0.01$). Furthermore, neuronal firing rate was significantly higher on average in J20 mice ($p = 0.02$). B. Graphs showing beta amplitude over time for beta bursts, time locked to the onset of the burst (dotted line), and averaged across all detected bursts, for wild-type mice (left) and J20 mice (right). Beta bursting was associated with a monophasic increase in beta amplitude that returns to baseline after around 250 ms. C. Peri-event histograms showing multi-unit activity spike rate during beta bursts, for wild-type (left) and J20 mice (right). Data is shown as Z score from baseline (pre-burst epoch), and averaged across all beta bursts with non-overlapping time segments. Solid horizontal line is shown to indicate the baseline of zero, while the vertical lines indicate the time window of interest used to calculate the average spike rate during beta bursts. There was a non-significant trend towards increased spike rate during beta bursts in wild-type mice ($p = 0.053$), which appeared to be reduced in J20 mice ($p = 0.5$). (Data shown as mean ± SEM, WT: $n = 5$, J20: $n = 6$).

4.3.6 Intra-Retrosplenial Coherence

Coherence analysis is a technique used to investigate oscillatory synchrony between electrophysiological signals, to determine how strongly correlated these regions are in terms of oscillatory activity, and thus infer the strength of functional connectivity between them. Coherence values range from 0 to 1; identical signals will have a value of 1, while a coherence of 0 would indicate no similarity of phase or amplitude. Synchrony is a commonly used term in neuroscience and usually refers to phase-synchronisation, defined by Tass et al. (1998) as “the existence of preferred values of phase difference”, between two signals. While zero-lag phase synchrony could be considered as true synchrony, when we refer to synchrony throughout this thesis, we are merely referring to the extent of the similarity of phase between two signals. As with spectral analysis, coherence is quantified in the frequency domain, in order to investigate synchrony across a range of oscillation frequencies. In order to investigate the extent of oscillatory synchrony between the two retrosplenial subregions, coherence was calculated between a single channel in the RSCdg and single channel in the RSCg (the same channels used in chapter 1). Coherograms between RSCdg and RSCg show very high coherence between these two subregions, with a clear peak at theta frequency (5-12 Hz), and another peak at gamma frequency (60 Hz), that persisted throughout the session (Figure 4.7a). As in our power spectral analysis, these coherence spectra were averaged across novel and familiar sessions for wild-type and J20 mice (Figure 4.7b). Significant findings are summarised in Table 4, however a more detailed account of these findings, including descriptive statistics, will be listed here in-text. Delta and alpha coherence were significantly higher overall during familiar sessions (Delta: Main Effect Novelty - $F(1,11) = 5.4$, $p = 0.04$, Mixed ANOVA; Alpha: Main Effect Novelty - $F(1,11) = 8.6$, $p = 0.01$,

Mixed ANOVA). Delta coherence was significantly higher during familiar sessions in wild-type (Nov: 0.88 ± 0.03; Fam: 0.9 ± 0.02, p = 0.03), but not J20 mice (Nov: 0.91 ± 0.01; Fam: 0.92 ± 0.01, p = 0.5), while alpha coherence was significantly higher during familiar sessions in J20 mice (Nov: 0.91 ± 0.01; Fam: 0.92 ± 0.01, p = 0.01), but not wild-type mice (Nov: 0.92 ± 0.01; Fam: 0.93 ± 0.01, p = 0.2). Gamma coherence was significantly higher overall during novel sessions (Main Effect Novelty - F(1,11) = 7.2, p = 0.02, Mixed ANOVA). Gamma coherence was significantly higher during novel sessions in J20 mice (Nov: 0.88 ± 0.01; Fam: 0.87 ± 0.01, p = 0.01), but not wild-type mice (Nov: 0.88 ± 0.01; Fam: 0.88 ± 0.01, p = 0.3). As we have consistently shown, the greatest neurophysiological responses to contextual novelty are seen during the first minute after exposure to the environment. Therefore, we investigated coherence again, but averaging across only the first minute of each session (Figure 4.7c, d). Delta, theta and alpha coherence were significantly higher overall during familiar sessions (Delta: Main Effect Novelty - F(1,11) = 6.8, p = 0.02, Mixed ANOVA; Theta: Main Effect Novelty - F(1,11) = 9.7, p = 0.01, Mixed ANOVA; Alpha: Main Effect Novelty - F(1,11) = 8.7, p = 0.01, Mixed ANOVA). Delta coherence was significantly higher during familiar sessions in wild-type (Nov: 0.85 ± 0.03; Fam: 0.88 ± 0.03, p = 0.03), but not J20 mice (Nov: 0.9 ± 0.02; Fam: 0.91 ± 0.01, p = 0.4). Theta and alpha coherence were significantly higher during familiar sessions in J20 mice (Theta: Nov: 0.95 ± 0.01; Fam: 0.97 ± 0.003, p = 0.01; Alpha: Nov: 0.9 ± 0.01; Fam: 0.92 ± 0.01, p = 0.02), but not wild-type mice (Theta: Nov: 0.95 ± 0.01; Fam: 0.96 ± 0.01, p = 0.1; Alpha: Nov: 0.9 ± 0.01; Fam: 0.91 ± 0.01, p = 0.1). Gamma coherence was significantly higher overall during novel sessions (Main Effect Novelty - F(1,11) = 9.3, p = 0.01, Mixed ANOVA). Gamma coherence was significantly higher during novel sessions in J20 mice (Nov: 0.88 ± 0.01; Fam:

0.87 ± 0.01, p = 0.01), but not wild-type mice (Nov: 0.88 ± 0.008; Fam: 0.88 ± 0.009, p = 0.2).

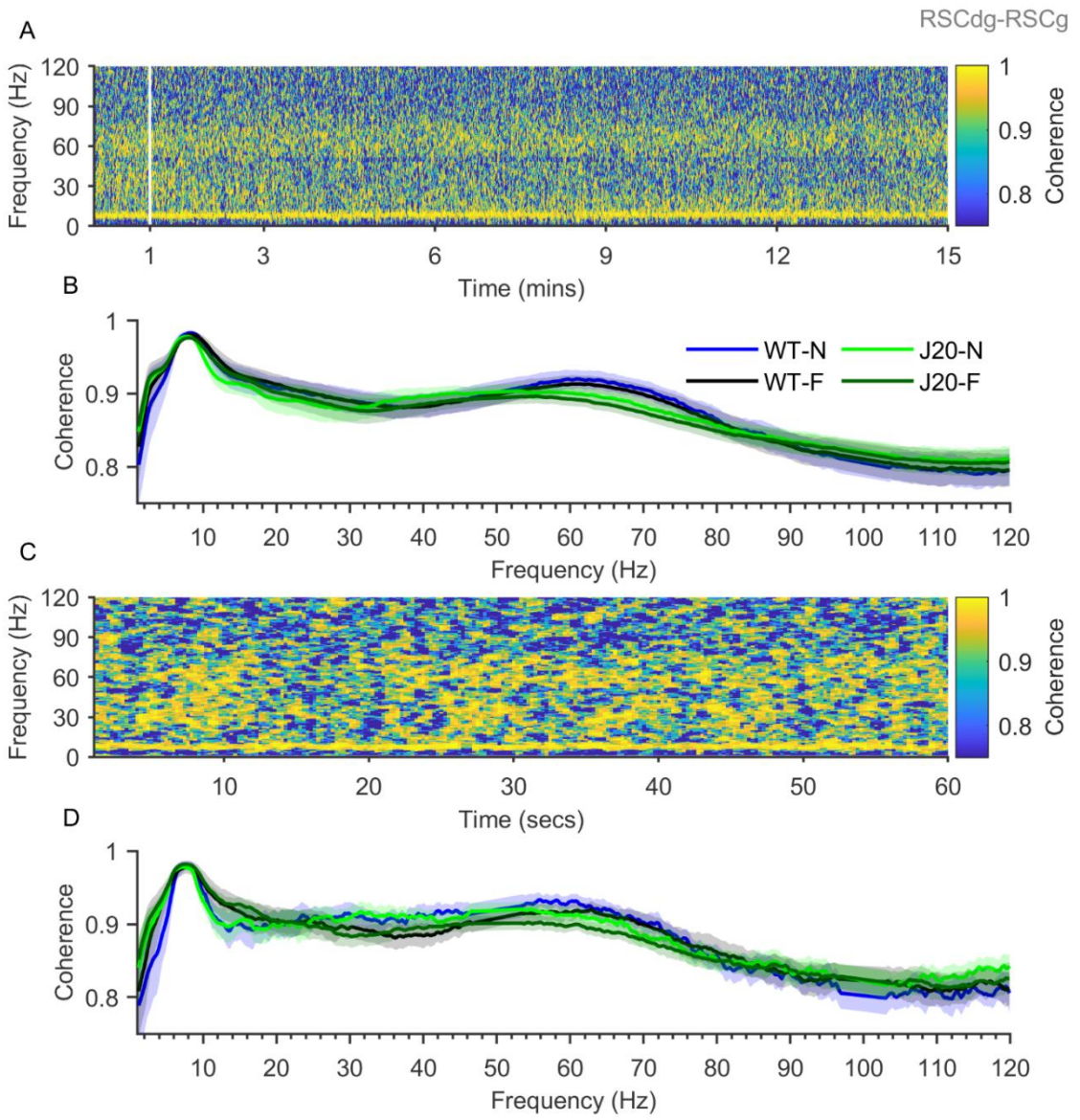

Figure 4.7 Intra-retrosplenial coherence varies depending on novelty.
A. Example coherogram showing coherence between RSCdg and RSCg across an entire novel session in a wild-type mouse. B. Average coherence between RSCdg and RSCg for the entire 15 minutes of all novel and familiar sessions, for wild-type and J20 mice. Delta coherence was significantly higher during familiar sessions in wild-type ($p = 0.03$), but not J20 mice ($p = 0.5$), while alpha coherence was significantly higher during familiar sessions in J20 mice ($p = 0.01$), but not wild-type mice ($p = 0.2$). Gamma coherence was significantly higher during novel sessions in J20 mice ($p = 0.01$), but not wild-type mice ($p = 0.3$). C. Example coherogram shown in A, expanded to show the first 60 seconds of the session. D. Average coherence between RSCdg and RSCg for the first minute of all novel and familiar sessions, for wild-type and J20 mice. Theta and alpha coherence were significantly higher during familiar sessions in J20 mice ($p = 0.01$, $p = 0.02$, respectively), but not wild-type mice ($p = 0.14$, $p = 0.13$, respectively). Gamma coherence was significantly higher during novel sessions in J20 mice ($p = 0.009$), but not wild-type mice ($p = 0.18$). (Data shown as mean ± SEM, WT: $n = 5$, J20: $n = 8$).

Table 4 Intra-Retrosplenial Coherence - Summary of significant results

Analysis Type	Frequency Band	Relationship	p-value
Whole Session	δ	$f > n$	0.04
	δ	$f_{WT} > n_{WT}$	0.03
	α	$f > n$	0.01
	α	$f_{J20} > n_{J20}$	0.01
	γ	$n > f$	0.02
	γ	$n_{J20} > f_{J20}$	1.00E-02
First Minute	δ	$f > n$	0.02
	δ	$f_{WT} > n_{WT}$	0.03
	θ	$f > n$	0.01
	θ	$f_{J20} > n_{J20}$	0.01
	α	$f > n$	1.00E-02
	α	$f_{J20} > n_{J20}$	0.02
	γ	$n > f$	0.01
	γ	$n_{J20} > f_{J20}$	0.01

n, novel; f, familiar; WT, wild-type; J20, J20; δ, delta; θ, theta; α, alpha; γ, gamma

4.3.7 Hippocampal-Retrosplenial Coherence

Anatomical studies have demonstrated that the hippocampus and retrosplenial cortex are highly anatomically connected, via the subicular complex (Wyss and Van Groen, 1992), but little is known about functional connectivity between these structures, particularly *in vivo.* A recent study by Nitzan et al. (2020) has demonstrated that sharp wave ripples from the hippocampus propagate through the subiculum to the retrosplenial cortex, revealing a novel source of oscillatory interaction between these regions. In order to investigate extent of oscillatory synchrony between the retrosplenial cortex and the hippocampus, coherence was calculated between a single channel in the RSCg and single channel in the HC (the same hippocampal channel used throughout this chapter). Coherograms between RSCg and HC show high coherence between these two regions. As before, there were clear peaks at theta (5-12 Hz), and gamma frequencies (60 Hz), that persisted throughout the session (Figure 4.8a). As in our power spectral analysis, these coherence spectra were averaged across novel and familiar sessions for wild-type and J20 mice (Figure 4.8b). Significant findings are summarised in Table 5, however a more detailed account of these findings, including descriptive statistics, will be listed here in-text. There was a significant interaction between the effects of genotype and novelty on delta coherence ($F(1,9) = 9.5$, $p = 0.01$, Mixed ANOVA). Delta coherence was significantly higher during novel sessions in wild-type (Nov: 0.83 ± 0.01; Fam: 0.81 ± 0.01, $p = 0.04$), but not J20 mice (Nov: 0.71 ± 0.01; Fam: 0.73 ± 0.01, $p = 0.08$). Furthermore, delta coherence was significantly lower in J20 mice than in wild-type mice, during novel (WT: 0.83 ± 0.01; J20: 0.71 ± 0.01, $p = 0.001$), and familiar sessions (WT: 0.81 ± 0.01; J20: 0.73 ± 0.01, $p = 0.01$). Theta coherence was significantly lower overall in J20 mice than in wild-type mice (Main Effect Genotype - $F(1,9) = 7.1$, p

= 0.03, Mixed ANOVA). Beta coherence was significantly higher overall during novel sessions (Main Effect Novelty - F(1,9) = 6.4, p = 0.03, Mixed ANOVA). Beta coherence was significantly higher during novel sessions in wild-type (Nov: 0.79 ± 0.01; Fam: 0.77 ± 0.01, p = 0.03), but not J20 mice (Nov: 0.77 ± 0.01; Fam: 0.76 ± 0.01, p = 0.4). As before, we investigated coherence again, averaging across only the first minute of each session (Figure 4.8c, d). Delta coherence was significantly lower overall in J20 mice than in wild-type mice (Main Effect Genotype - F(1,9) = 14.8, p = 0.004, Mixed ANOVA). There were significant interactions between the effects of genotype and novelty on theta and beta coherence (Theta: F(1,9) = 5.5, p = 0.04, Mixed ANOVA; Beta: Interaction - F(1,9) = 9.2, p = 0.01, Mixed ANOVA). Theta coherence was significantly lower in J20 mice than in wild-type mice during novel sessions (WT: 0.93 ± 0.01; J20: 0.86 ± 0.01, p = 0.01), but not familiar sessions (WT: 0.92 ± 0.01; J20: 0.88 ± 0.01, p = 0.2).

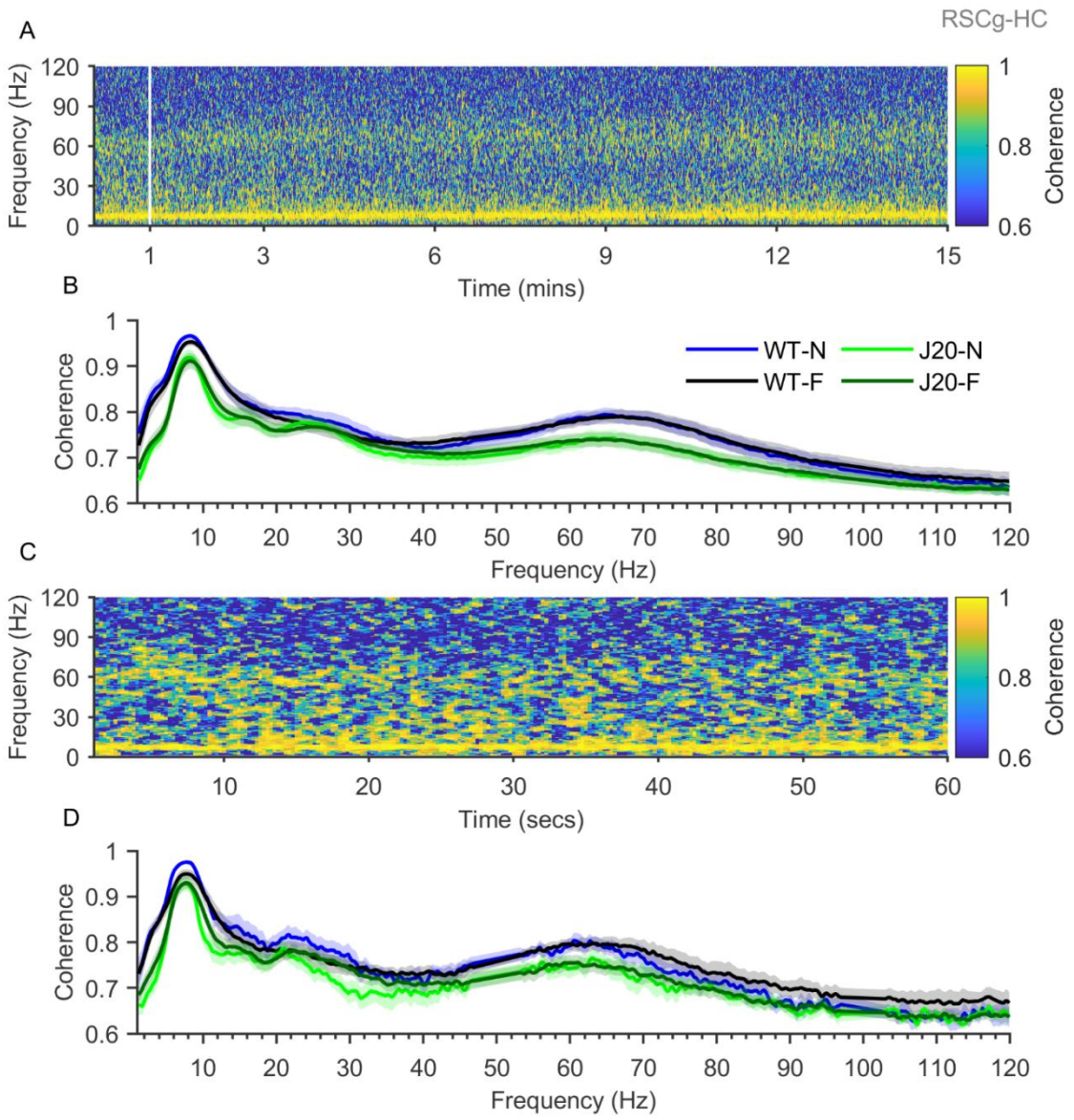

Figure 4.8 Hippocampal-retrosplenial coherence is generally unaffected by novelty.
A. Example coherogram showing coherence between RSCg and HC across an entire novel session in a wild-type mouse. B. Average coherence between RSCg and HC for the entire 15 minutes of all novel and familiar sessions, for wild-type and J20 mice. Delta coherence was significantly higher during novel sessions in wild-type ($p = 0.04$), but not J20 mice ($p = 0.08$). Delta coherence was significantly lower in J20 mice, during novel ($p = 0.001$) and familiar sessions ($p = 0.01$). Beta coherence was significantly higher during novel sessions in wild-type ($p = 0.02$), but not J20 mice ($p = 0.5$). C. Example coherogram shown in A, expanded to show the first 60 seconds of the session. D. Average coherence between RSCg and HC for the first minute of all novel and familiar sessions, for wild-type and J20 mice. Delta coherence was significantly lower overall in J20 mice than in wild-type mice ($p = 0.004$). Theta coherence was significantly lower in J20 mice than in wild-type mice during novel sessions ($p = 0.01$), but not familiar sessions ($p = 0.17$). (Data shown as mean ± SEM, WT: $n = 5$, J20: $n = 6$).

Table 5 Hippocampal-Retrosplenial Coherence - Summary of significant results

Analysis Type	Frequency Band	Relationship	p-value
Whole	δ	N X G	0.01
	δ	$n_{WT} > f_{WT}$	0.04
	δ	$n_{WT} > n_{J20}$	1.00E-03
	δ	$f_{WT} > f_{J20}$	1.00E-02
	θ	WT > J20	3.00E-02
	β	n > f	3.00E-02
	β	$n_{WT} > f_{WT}$	0.03
First	δ	WT > J20	0.004
	θ	N X G	4.00E-02
	θ	$n_{WT} > n_{J20}$	0.01
	β	N X G	0.01

N, novelty; G, genotype; N X G, interaction between novelty and genotype; n, novel; f, familiar; WT, wild-type; J20, J20; δ, delta; θ, theta; β, beta

4.3.8 Intra-Retrosplenial Granger Causality

Granger causality is an analytical technique used to investigate statistical causality between two time series (Granger, 1969). If past values of one signal can predict future values of another signal, then this is an indicator of Granger causality. In electrophysiology, this technique is often used to whether there is directionality in the functional connectivity between two brain regions, which could indicate what influence they have on each other (Seth et al., 2015). It is important to note that this “causality” is statistical, and not indicative of true causality. While coherence analysis is symmetrical, and provides no insight into directionality, Granger causality can provide valuable information about potential directionality of oscillations in a neuronal network. Furthermore, the passive spread of electrical fields through tissue, known as volume conduction, can lead to spurious coherence due to the instantaneous passive spread of oscillations from a common source (Cohen, 2015). In this regard, Granger causality is a superior measure to coherence, in that it is far less sensitive to indirect connectivity (Bastos and Schoffelen, 2016). We investigated Granger causality between both retrosplenial cortex subregions, in order to determine whether there is any directionality in oscillatory activity within this brain region. As shown in (Figure 4.9a), in order to visualise the balance of Granger causality in the retrosplenial cortex, we calculated Granger causality in 15 second time bins across the entire 15-minute session, and subtracted Granger causality in the RSCg to RSCdg direction from Granger causality in the RSCdg to RSCg direction. As shown in these “Grangerograms”, Granger causality from the RSCg to the RSCdg is highly dominant, throughout recording sessions, suggesting a potential unidirectional flow of oscillatory activity. Average Granger causality spectra were calculated for the first minute of each session for wild-type and J20 mice, and shown in (Figure

4.9b). Significant findings are summarised in Table 6, however a more detailed account of these findings, including descriptive statistics, will be listed here in-text. There was a significant 3-way interaction between genotype, novelty and direction on Granger causality in all frequency bands (Delta: 3 Way Interaction - $F(1,11) = 30.5$, $p = 2e\text{-}4$, Mixed ANOVA; Theta: 3 Way Interaction - $F(1,11) = 23$, $p = 6e\text{-}4$, Mixed ANOVA; Alpha: 3 Way Interaction - $F(1,11) = 14.3$, $p = 0.003$, Mixed ANOVA; Beta: 3 Way Interaction - $F(1,11) = 7.8$, $p = 0.02$, Mixed ANOVA; Gamma: 3 Way Interaction - $F(1,11) = 7$, $p = 0.02$, Mixed ANOVA). In wild-type mice, Granger causality in the theta, alpha, beta and gamma bands were significantly higher overall in the granular to dysgranular direction (Theta: WT - Dg>G: 0.04 ± 0.02; G>Dg: 0.19 ± 0.05, $p = 0.02$; Alpha: WT - Dg>G: 0.02 ± 0.004; G>Dg: 0.13 ± 0.04, $p = 0.01$; Beta: WT - Dg>G: 0.01 ± 0.002; G>Dg: 0.1 ± 0.03, $p = 0.02$; Gamma: WT - Dg>G: 0.01 ± 0.004; G>Dg: 0.1 ± 0.03, $p = 0.004$). Furthermore, in wild-type mice, gamma Granger causality was significantly higher during novel sessions in the granular to dysgranular direction (WT - G>Dg Nov: 0.13 ± 0.04; Fam: 0.09 ± 0.03, $p = 0.03$). In J20 mice, Granger causality in the alpha band was significantly higher overall in the granular to dysgranular direction (J20 - Dg>G: 0.03 ± 0.01; G>Dg: 0.1 ± 0.03, $p = 0.04$). Furthermore, in J20 mice, delta, theta and alpha Granger causality were significantly lower during familiar sessions in the dysgranular to granular direction (Delta: J20 - Dg>G Nov: 0.14 ± 0.05; Fam: 0.08 ± 0.03, $p = 0.007$; Theta: J20 - Dg>G Nov: 0.07 ± 0.02; Fam: 0.04 ± 0.004, $p = 0.005$; Alpha: J20 - Dg>G Nov: 0.05 ± 0.01; Fam: 0.03 ± 0.01, $p = 0.02$), while in the granular to dysgranular direction, delta, theta, alpha and beta Granger causality were significantly lower during novel sessions (Delta: J20 - G>Dg Nov: 0.07 ± 0.02; Fam: 0.18 ± 0.04, $p = 2e\text{-}4$; Theta: J20 - G>Dg Nov: 0.07 ± 0.02; Fam: 0.16 ± 0.03, $p = 1e\text{-}4$; Alpha: J20 - G>Dg Nov: 0.08 ± 0.02;

Fam: 0.14 ± 0.03, p = 3e-4; Beta: J20 - G>Dg Nov: 0.07 ± 0.02; Fam: 0.1 ± 0.03, p = 0.002).

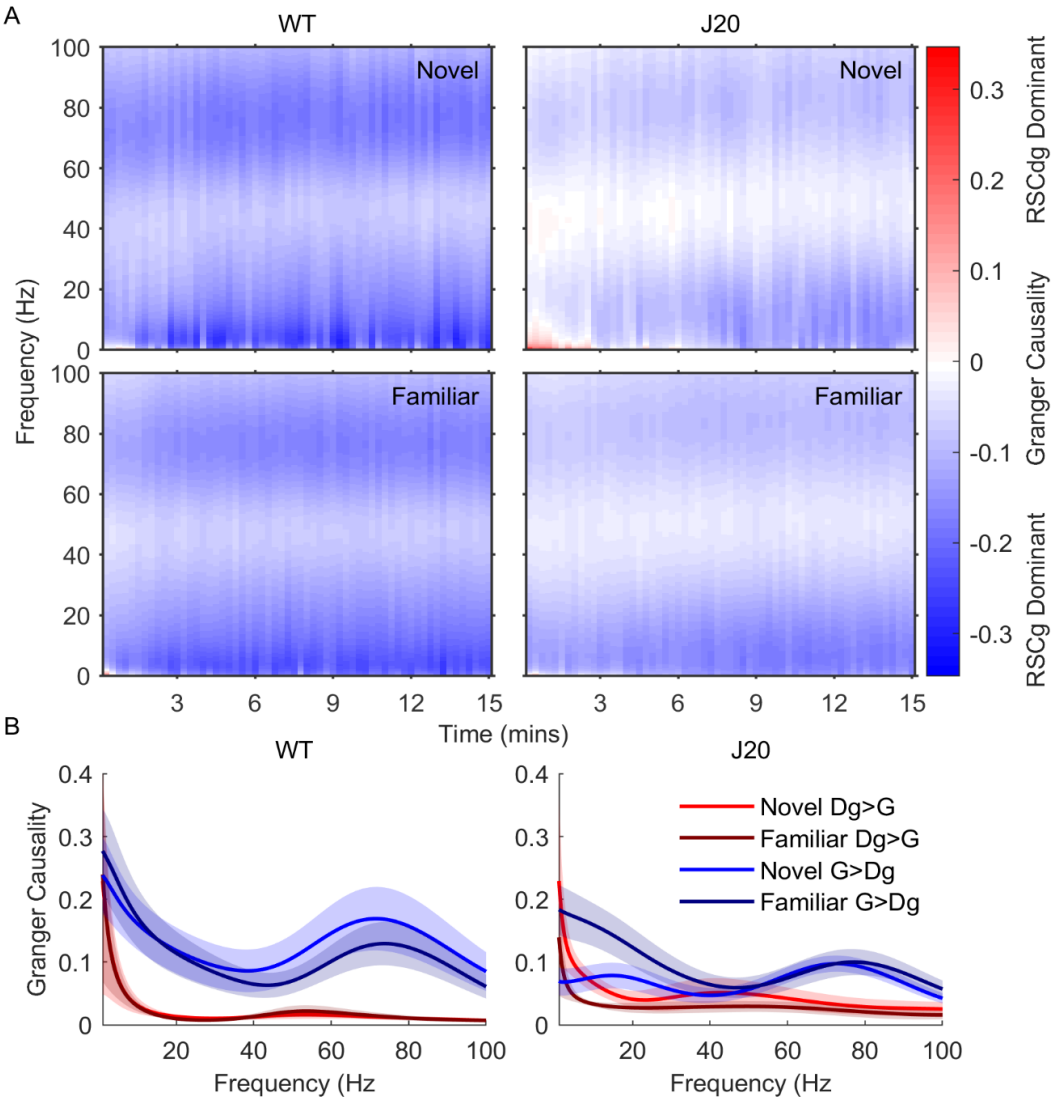

Figure 4.9 Granger Causality is higher from the RSCg to the RSCdg.
A. Average Grangerograms, illustrating the balance of Granger causality between RSCdg (Dg) and RSCg (G), averaged across novel (top) and familiar sessions (bottom), for wild-type (left) and J20 mice (right). Data shown is the Granger causality in the RSCg to RSCdg direction, subtracted from the Granger causality in the RSCdg to RSCg direction. Darker colors indicate a directional imbalance in Granger causality. B. Average Granger causality spectra for the first minute of novel and familiar sessions, in both directions, for wild-type (left), and J20 mice (right). In wild-type mice, Granger causality in the theta, alpha, beta and gamma bands was significantly higher overall in the RSCg to RSCdg direction ($p = 0.02$, $p = 0.01$, $p = 0.02$, $p = 0.004$, respectively). Furthermore, in wild-type mice, gamma Granger causality was significantly higher overall during novel sessions in the RSCg to RSCdg direction ($p = 0.03$). In J20 mice, Granger causality in the alpha band was significantly higher overall in the RSCg to RSCdg direction ($p = 0.04$). Furthermore, in J20 mice, delta, theta and alpha Granger causality were significantly lower during familiar sessions in the RSCdg to RSCg direction ($p = 0.007$, $p = 0.005$, $p = 0.02$, respectively), while in the RSCg to RSCdg direction, delta, theta, alpha and beta Granger causality were significantly lower during novel sessions ($p = 2e\text{-}4$, $p = 1e\text{-}4$, $p = 3e\text{-}4$, $p = 0.002$, respectively). (Data shown as mean ± SEM, WT: n = 5, J20: n = 8).

Table 6 Intra-Retrosplenial Granger Causality - Summary of significant results

Genotype	Frequency Band	Relationship	p-value
N/A	δ	N X G X D	2.00E-04
	θ	N X G X D	6.00E-04
	α	N X G X D	0.003
	β	N X G X D	0.02
	γ	N X G X D	0.02
WT	θ	G2D > D2G	2.00E-02
	α	G2D > D2G	0.01
	β	G2D > D2G	0.02
	γ	G2D > D2G	0.004
	γ	$G2D_n > G2D_f$	0.03
J20	α	G2D > D2G	4.00E-02
	δ	$D2G_n > D2G_f$	0.007
	θ	$D2G_n > D2G_f$	0.005
	α	$D2G_n > D2G_f$	0.02
	δ	$G2D_f > G2D_n$	2.00E-04
	θ	$G2D_f > G2D_n$	1.00E-04
	α	$G2D_f > G2D_n$	3.00E-04
	β	$G2D_f > G2D_n$	0.002

N, novelty; G, genotype; D, direction; N X G X D, interaction between novelty, genotype and direction; D2G, RSCdg to RSCg; G2D, RSCg to RSCdg; n, novel; f, familiar; δ, delta; θ, theta; α, alpha; β, beta; γ, gamma

4.3.9 Hippocampal-Retrosplenial Granger Causality

We investigated Granger causality between the RSCg and hippocampus, in order to determine the extent of directionality in oscillatory activity between these brain regions. As shown in (Figure 4.10a), in order to visualise the balance of Granger causality in the retrosplenial cortex, we calculated Granger causality in 15 second time bins across the entire 15-minute session, and subtracted Granger causality in the HC to RSCg direction from Granger causality in the RSCg to HC direction. As shown in these “Grangerograms”, there is a high degree of Granger causality from both RSCg to HC, and from HC to RSCg, suggesting bidirectional flow of oscillatory activity. Interestingly, Granger causality in the gamma band appears to be hippocampal dominant at around 70 Hz, and retrosplenial dominant at around 50 Hz. Average Granger causality spectra were calculated for the first minute of each session for wild-type and J20 mice, and shown in (Figure 4.10b). Significant findings are summarised in Table 7, however a more detailed account of these findings, including descriptive statistics, will be listed here in-text. There was a significant 3-way interaction between genotype, novelty and direction on Granger causality in all frequency bands (Delta: 3 Way Interaction - $F(1,9) = 11.9$, $p = 0.007$, Mixed ANOVA; Theta: 3 Way Interaction - $F(1,9) = 9.7$, $p = 0.01$, Mixed ANOVA; Alpha: 3 Way Interaction - $F(1,9) = 8.9$, $p = 0.02$, Mixed ANOVA; Beta: 3 Way Interaction - $F(1,9) = 7$, $p = 0.03$, Mixed ANOVA; Gamma: 3 Way Interaction - $F(1,9) = 20.8$, $p = 0.001$, Mixed ANOVA). In wild-type mice, Granger causality in the delta, theta and alpha bands was significantly higher overall in the hippocampus to granular RSC direction (Delta: WT - G>HC: 0.4 ± 0.08; HC>G: 0.5 ± 0.05, $p = 0.02$; Theta: WT - G>HC: 0.16 ± 0.04; HC>G: 0.29 ± 0.04, $p = 0.005$; Alpha: WT - G>HC: 0.06 ± 0.02; HC>G: 0.15 ± 0.03, $p = 0.007$). Furthermore, in wild-type mice, delta, theta and gamma Granger causality were

significantly higher during familiar sessions in the granular RSC to hippocampus direction (Delta: WT - G>HC Nov: 0.2 ± 0.1; Fam: 0.4 ± 0.1, p = 0.006; Theta: WT - G>HC Nov: 0.08 ± 0.02; Fam: 0.2 ± 0.05, p = 0.03; Gamma: WT - G>HC Nov: 0.09 ± 0.03; Fam: 0.13 ± 0.04, p = 0.002). In J20 mice, Granger causality in the delta, theta, alpha and beta bands were significantly higher overall in the hippocampus to granular RSC direction (Delta: J20 - G>HC: 0.18 ± 0.05; HC>G: 0.4 ± 0.05, p = 0.04; Theta: J20 - G>HC: 0.09 ± 0.02; HC>G: 0.29 ± 0.03, p = 0.004; Alpha: J20 - G>HC: 0.04 ± 0.01; HC>G: 0.19 ± 0.02, p = 0.002; Beta: J20 - G>HC: 0.02 ± 0.006; HC>G: 0.12 ± 0.02, p = 0.009). Furthermore, in J20 mice, delta, theta, alpha and beta Granger causality were significantly lower during novel sessions in the hippocampus to granular RSC direction (Delta: J20 - HC>G Nov: 0.2 ± 0.05; Fam: 0.4 ± 0.06, p = 8e-5; Theta: J20 - HC>G Nov: 0.16 ± 0.03; Fam: 0.3 ± 0.04, p = 8e-4; Alpha: J20 - HC>G Nov: 0.12 ± 0.01; Fam: 0.2 ± 0.02, p = 0.004; Beta: J20 - HC>G Nov: 0.08 ± 0.01; Fam: 0.13 ± 0.02, p = 0.009).

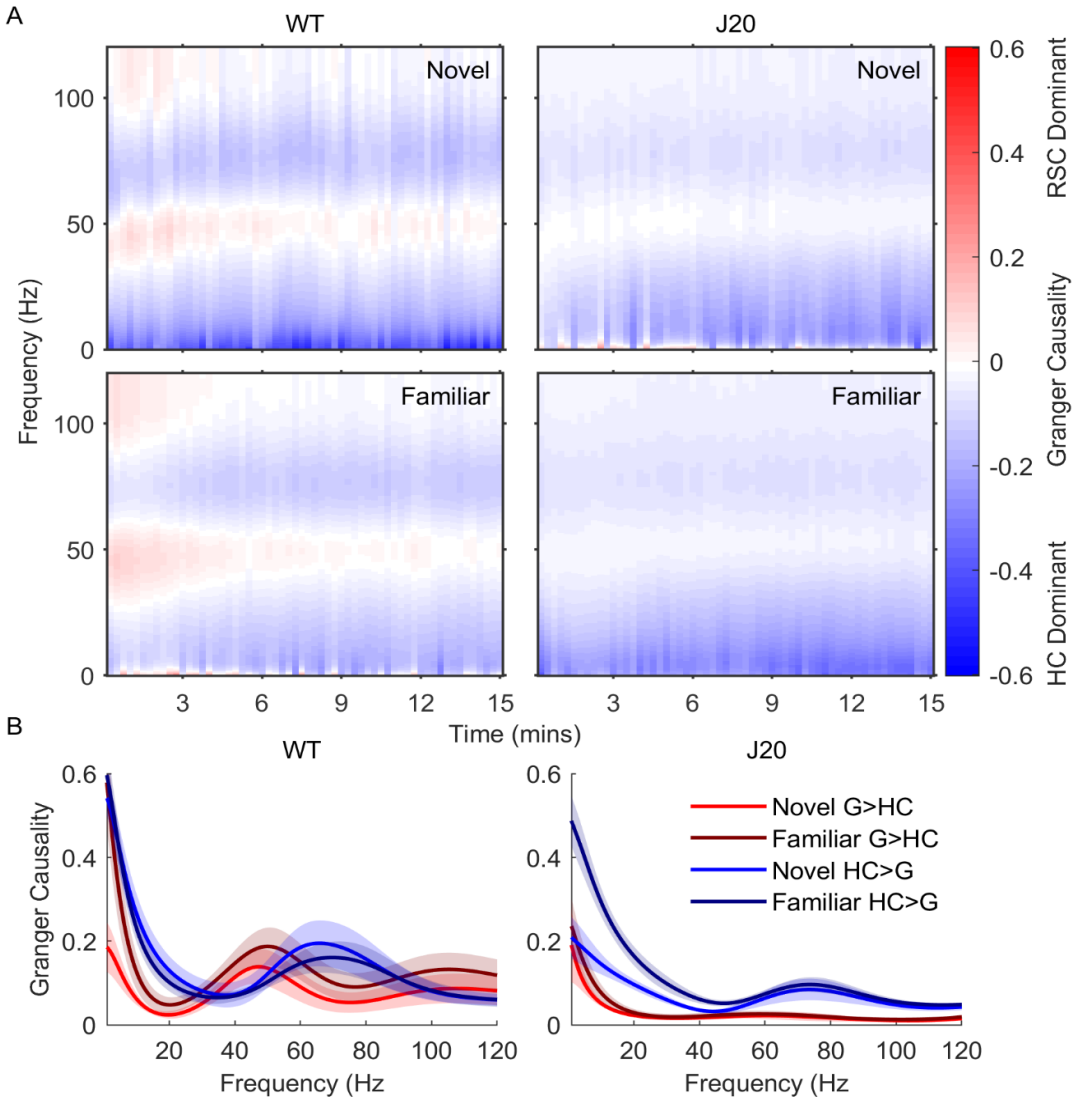

Figure 4.10 Granger causality from the RSCg to the hippocampus is increased during familiar sessions.
A. Average Grangerograms, illustrating the balance of Granger causality between RSCg (G) and HC, averaged across novel (top) and familiar sessions (bottom), for wild-type (left) and J20 mice (right). Data shown is the Granger causality in the HC to RSCg direction, subtracted from the Granger causality in the RSCg to HC direction. Darker colors indicate a directional imbalance in Granger causality. B. Average Granger causality spectra for the first minute of novel and familiar sessions, in both directions, for wild-type (left), and J20 mice (right). In wild-type mice, Granger causality in the delta, theta and alpha bands were significantly higher overall in the hippocampus to RSCg direction ($p = 0.02$, $p = 0.005$, $p = 0.007$, respectively). Furthermore, in wild-type mice, delta, theta and gamma Granger causality were significantly higher during familiar sessions in the RSCg to hippocampus direction ($p = 0.006$, $p = 0.03$, $p = 0.002$, respectively). In J20 mice, Granger causality in the delta, theta, alpha and beta bands were significantly higher overall in the hippocampus to RSCg direction ($p = 0.04$, $p = 0.004$, $p = 0.002$, $p = 0.009$, respectively). Furthermore, in J20 mice, delta, theta, alpha and beta Granger causality were significantly lower during novel sessions in the hippocampus to RSCg direction ($p = 8e\text{-}5$, $p = 8e\text{-}4$, $p = 0.004$, $p = 0.009$, respectively). (Data shown as mean ± SEM, WT: n = 4, J20: n

Table 7 Hippocampal-Retrosplenial Granger Causality - Summary of significant results

Genotype	Frequency Band	Relationship	p-value
N/A	δ	N X G X D	7.00E-03
	θ	N X G X D	1.00E-02
	α	N X G X D	0.02
	β	N X G X D	0.03
	γ	N X G X D	0.001
WT	δ	H2G > G2H	2.00E-02
	θ	H2G > G2H	0.005
	α	H2G > G2H	0.007
	δ	$G2H_f > G2H_n$	0.006
	θ	$G2H_f > G2H_n$	0.03
	γ	$G2H_f > G2H_n$	2.00E-03
J20	δ	H2G > G2H	0.04
	θ	H2G > G2H	0.004
	α	H2G > G2H	0.002
	β	H2G > G2H	9.00E-03
	δ	$H2G_f > H2G_n$	8.00E-05
	θ	$H2G_f > H2G_n$	8.00E-04
	α	$H2G_f > H2G_n$	0.004
	β	$H2G_f > H2G_n$	0.009

N, novelty; G, genotype; D, direction; N X G X D, interaction between novelty, genotype and direction; H2G, Hippocampus to RSCg; G2H, RSCg to Hippocampus; n, novel; f, familiar; δ, delta; θ, theta; α, alpha; β, beta; γ, gamma

4.3.10 Burst Cross-Correlation

We have demonstrated throughout this study that beta bursts can be reliably detected in both subregions of the retrosplenial cortex, and the hippocampus. So far, we have considered beta bursting in these regions as independent, and analysed their temporal profile, and characteristics accordingly. However, we have shown that oscillations within this network are highly correlated, and as such, beta bursts may also be temporally correlated as well. Cross-correlation analysis allows investigation into correlations between signals with at varying time lags. The strength of correlation, as well as the time lag at which the correlation is maximal, can provide insight into temporal correlations between oscillations and make suggestions about potential directionality (Figure 4.11a). The use of multi-site silicon probes in this study allows additional insight into how burst cross-correlation changes across the length of the probe (Figure 4.11b).

Cross-correlation analysis is commonly used in electrophysiology to investigate relationships between the timing of spikes from different neurons, in order to investigate potential functional interactions between them (Ostojic et al., 2009). For these types of data, cross correlation analysis is performed on the time stamps of the spikes, and not the spike waveforms, as the point of interest is the temporal relationship between the timing of the spikes, and not correlations between the spike waveforms themselves. Conversely, the focus of our analysis was the extent of correlation between beta bursts in one area of the brain and beta oscillations in another area of the brain, with regards to waveform shape and phase synchrony, and as such our analysis was performed on time-locked beta-filtered local field potentials, and not on the time stamps of these beta bursts. Beta bursts were detected in the RSCdg and cross-correlation analysis was

performed on a burst-by-burst basis between this burst signal, and time-locked signals from all other channels. The peak cross-correlation and peak lag were calculated across all channels, and averaged across all beta bursts in novel, and familiar sessions, for both wild-type and J20 mice. During beta bursts in the RSCdg, beta oscillations are highly correlated between RSCdg and RSCg (correlation coefficient > 0.9), in both novel (Figure 4.11c, top) and familiar sessions (Figure 4.11c, bottom). There was no significant effect of genotype or novelty on burst cross correlation between RSCdg and RSCg (Main Effect Novelty - $F(1,8) = 5.3$, $p = 0.051$, Mixed ANOVA; Main Effect Genotype - $F(1,8) = 0.9$, $p = 0.4$, Mixed ANOVA). During beta bursts in the RSCdg, beta oscillations were also highly correlated between RSCdg and hippocampus (correlation coefficient > 0.8), during both novel (Figure 4.11c, top) and familiar sessions (Figure 4.11c, bottom). Burst cross correlation between RSCdg and hippocampus was significantly lower overall during novel sessions (Main Effect Novelty - $F(1,8) = 7.1$, $p = 0.03$, Mixed ANOVA). Burst cross correlation was significantly lower during novel sessions in J20 mice (J20 - Nov: 0.8 ± 0.02; Fam: 0.9 ± 0.01, $p = 0.007$), but not wild-type mice. As shown in (Figure 4.11d), beta oscillations are highly synchronous across the retrosplenial-hippocampal network during beta bursts. Burst cross correlation lags were statistically analysed using one-sample t-tests, to determine whether their peak lag was significantly non-zero, and whether beta oscillations were synchronous. During novel sessions, beta bursts in RSCdg and RSCg were synchronous in both wild-type (-0.07 ± 0.09 ms, $t(3) = -0.48$, $p = 0.7$; one-sample t-test) and J20 mice (0.2 ± 0.1 ms, $t(5) = 1.6$, $p = 0.18$; one-sample t-test). Conversely, during familiar sessions, beta bursts in RSCdg and RSCg were significantly asynchronous in both wild-type (-0.19 ± 0.02 ms, $t(3) = -6.4$, $p = 0.008$; one-sample t-test) and J20 mice (-0.4 ± 0.1

ms, t(5) = -2.9, p = 0.03; one-sample t-test). During novel sessions, beta bursts in RSCdg and hippocampus were synchronous in both wild-type (-0.3 ± 0.3 ms, t(3) = -0.6, p = 0.6; one-sample t-test) and J20 mice (-2.9 ± 1.2 ms, t(5) = -1.9, p = 0.1; one-sample t-test). Conversely, during familiar sessions, beta bursts in the RSCdg and hippocampus were significantly asynchronous in both wild-type (-1.8 ± 0.3 ms, t(3) = -3.5, p = 0.04; one-sample t-test) and J20 mice (-2.2 ± 0.4 ms, t(5) = -4.1, p = 0.009; one-sample t-test).

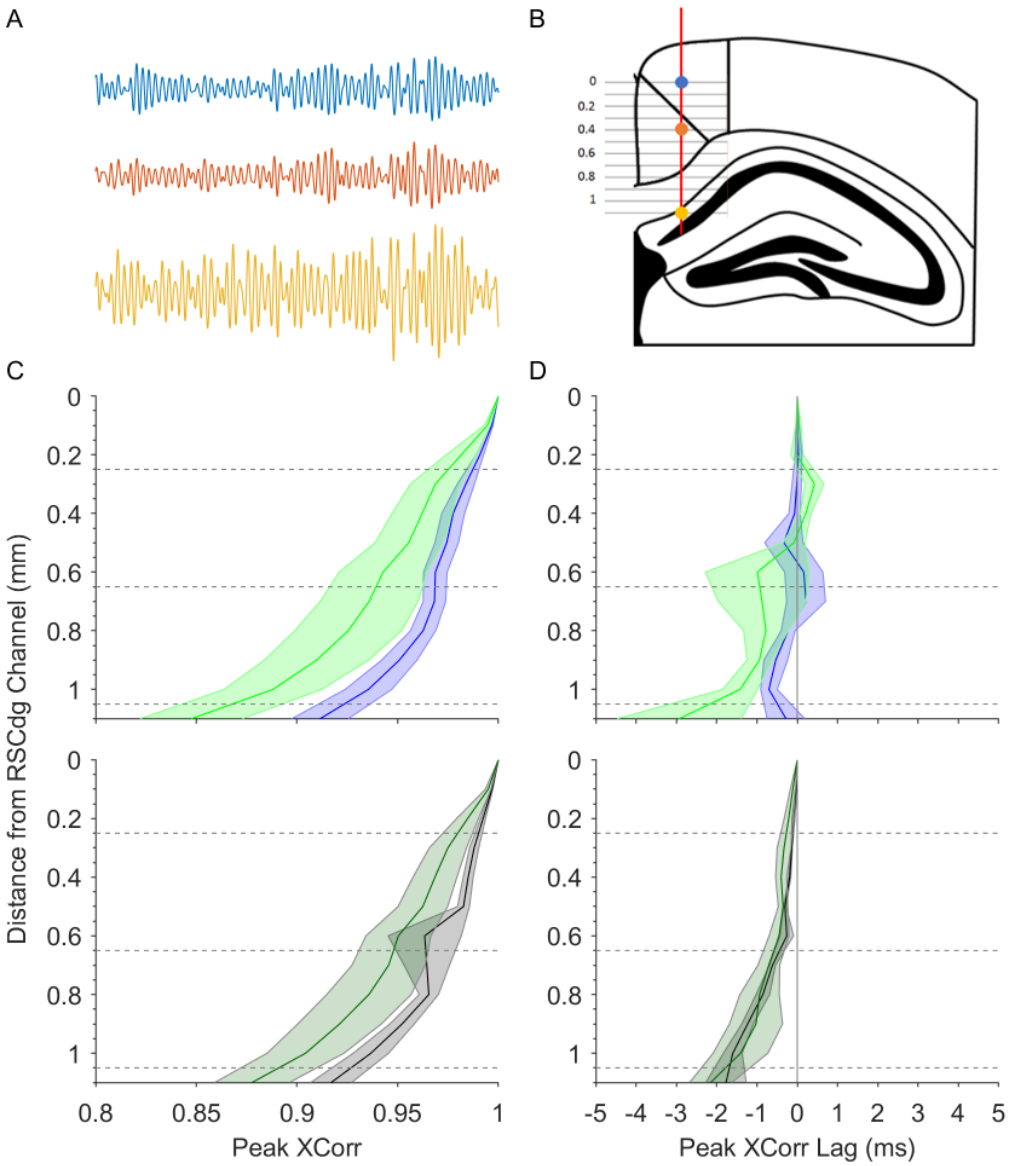

Figure 4.11 Beta bursts in the RSC and hippocampus are highly correlated and synchronous.

A. Example beta oscillations in the RSCdg (blue), RSCg (orange) and hippocampus (yellow). B. Diagram showing the probe location, as well as the relative locations of the retrosplenial and hippocampal channels. Horizontal lines indicate the depths of channels across the probe, from the RSC channel to the hippocampal channel, with distance from RSCdg channel in millimetres. C. Peak beta burst cross correlation, across the probe. Peak cross correlation was calculated for each beta burst detected in RSCdg, and averaged across all bursts, in novel sessions (above) and familiar sessions (below), for wild-type (blue, black) and J20 mice (green, dark green). Beta bursts were highly correlated across the probe. D. Peak beta burst cross correlation lag, across the probe. Peak lag is calculated as the time at which burst cross-correlation is at its peak. Positive values indicate that beta bursts in the RSCdg precede those detected at each depth, while negative values indicate that beta bursts in the RSCdg lag behind those detected at each depth. Peak lag was calculated for each beta burst detected in RSCdg, and averaged across all bursts, in novel sessions (above) and familiar sessions (below), for wild-type (blue, black) and J20 mice (green, dark green). (Data shown as mean ± SEM, WT: n = 4, J20: n = 6).

4.4 Discussion

4.4.1 Summary

The aim of this study was to investigate hippocampal network activity in response to contextual novelty, in order to compare electrophysiological correlates of novelty in the hippocampus to those described in the retrosplenial cortex in Chapter 3. Furthermore, through concurrent recordings in the retrosplenial cortex and hippocampus, we aimed to determine the extent of functional connectivity between these regions, through investigation into temporally correlated oscillatory activity. Furthermore, the inclusion of J20 mice in this study allowed us to investigate potential changes in hippocampal network activity, and compare them to those demonstrated in the retrosplenial cortex (Chapter 3).

4.4.2 Power Spectral Analysis

Power spectral analysis was performed in order to investigate oscillatory activity in the hippocampus across a range of frequency bands, and compare the effects of novelty and genotype on hippocampal activity. First, we performed power spectral analysis across the entire 15-minute recording sessions, in order to identify general oscillatory changes that occur while animals explore novel environments. During novel sessions, beta power was significantly increased in both genotypes. Furthermore, in wild-type mice, while theta power was significantly higher during novel sessions, alpha power was significantly lower. Increased hippocampal beta power during novelty mirrors the changes shown in the RSC in Chapter 3, and supports previous work by Berke et al. (2008) and França et al. (2020), who have previously demonstrated increased beta power in the hippocampus when mice explore novel environments. Furthermore, increased hippocampal beta power has also been shown during the exploration

of novel objects, or object locations (França et al., 2014, 2020; Iwasaki et al., 2021). Iwasaki et al. (2021) also demonstrated that increased beta power during object memory encoding sessions was associated with improved performance during subsequent memory retrieval. These studies suggest that hippocampal beta oscillations are associated with memory encoding.

We also performed power spectral analysis on the first minute of each session, in order to focus on the times immediately after the animal is exposed to the environment, during which it is thought that memory encoding or retrieval will occur. During novel sessions, theta and beta power were significantly increased in wild-type mice, but there was no effect of novelty on power in any frequency band in J20 mice, which suggests that increased beta power during novelty in J20s is not found during the first minute of the session, but throughout. Hippocampal delta and gamma power were consistently lower overall in J20 mice. Reduced gamma activity has been previously demonstrated in electroencephalographic recordings from J20 mice (Verret et al., 2012), and was associated with inhibitory interneuron dysfunction seen in these mice (Palop et al., 2007), which is thought to result in epileptiform activity, although this was not seen in our mice, potentially due to our use of relatively short recordings. Interestingly, the overall increases in alpha, beta and gamma power seen in the RSC in J20 mice were absent in the hippocampus. Amyloid pathology has been demonstrated in both hippocampus and retrosplenial cortex in J20 mice (Whitesell et al., 2019), suggesting a divergence in the neurophysiological consequences of amyloid pathology between these two brain regions.

As we have demonstrated, hippocampal beta activity is associated with contextual novelty in wild-type mice. Interestingly, the generalised increase in

beta power previously shown in the RSC of J20 mice was absent in the hippocampus (Chapter 3). Furthermore, while novelty-associated beta oscillatory activity was maintained in the RSC in J20 mice, in the hippocampus this relationship was lost. This together suggests that while beta oscillations can be found in both cortex and hippocampus, beta oscillations, and their associations with contextual novelty, are far more pronounced in the cortex.

4.4.3 Beta Bursting Activity

As in the retrosplenial cortex, hippocampal beta activity appears as discrete bursts rather than continuous oscillations, and beta bursts are significantly more frequent during novel sessions. These findings support previous work by (Berke et al., 2008; França et al., 2014). Beta burst rate was significantly higher overall during novel sessions, and while beta bursting was generally stable throughout familiar sessions, during novel sessions beta burst rate was significantly higher during the first minute of the session in wild-type mice. This novelty-associated bursting, and this pattern of novelty associated bursting in the hippocampus is similar to that which we have previously seen in the retrosplenial cortex (Chapter 3). In wild-type mice, the total number of beta bursts detected in the hippocampus was similar to the total number of beta bursts detected in the retrosplenial cortex, however the initial rate of beta bursting during novel sessions appears to be far greater in the retrosplenial cortex. This suggests a more pronounced response to novelty in the retrosplenial cortex, and may explain the attenuated increase in beta power during the first minute of novel sessions in the hippocampus.

In the hippocampus, as in the retrosplenial cortex, significantly more beta bursts were detected overall in J20 mice. It is notable that this increase in burst detection in the hippocampus was the largest of all three areas tested so far. Furthermore,

from plots of total number of bursts detected in J20 mice, a clear “saw-tooth” pattern can be seen (Figure 4.2 Beta bursting activity in the hippocampus., with higher numbers of bursts detected on the first session of every recording day, regardless of novelty. If a high level of beta bursting occurs during perceived novelty (i.e. the animal believes the environment to be novel), then increased beta bursting on the first session of each day could suggest that animals are uncertain whether the environment is familiar or not. While the second session of each day occurs only 15 minutes after the first, there is approximately 24 hours between the second session of one day, and the first session of the next, so disrupted memory encoding during each session or disrupted memory consolidation during this period could result in “forgetting” which could result in this saw-tooth pattern. The relationship between beta bursting and novelty was altered slightly in the hippocampus in J20 mice. While there were significantly more beta bursts detected during novel sessions in J20 mice, there was no significant difference between the beta burst rate during the first minute and final 10 minutes of novel sessions. Furthermore, while there was no significant difference between beta burst rate in the initial minute of novel sessions between wild-type and J20 mice, beta burst rate was significantly higher in J20s during familiar sessions, and the final 10 minutes of novel sessions. These findings mirror those in the RSC, and support our hypothesis that there is either a theoretical regional maximum burst rate, or that different mechanisms underlie novelty-associated beta bursts and familiarity-associated beta bursts. While the rate of novelty-associated beta bursting in the RSCdg is almost double that in the hippocampus, the rate of beta bursting during familiar sessions appears to be remarkably similar, further supporting the idea of a basal beta burst rate, which is greatly increased in J20 mice.

4.4.4 Beta Bursting Characteristics

Beta burst characteristics were investigated in the hippocampus, as before, in order to investigate how hippocampal beta bursts differ from their retrosplenial counterparts, and to determine whether any of these characteristics vary depending on novelty. Beta bursts were significantly larger in magnitude during novelty, in both genotypes, and beta bursts were significantly longer in duration during novelty in wild-type, but not J20 mice. If the function of beta bursts is to transiently activate neurons, then increases in beta burst magnitude or duration during novelty could serve to enhance this activation. In the retrosplenial cortex we noted a significant overall increase in burst magnitude in J20 mice, however this was notably absent in the hippocampus. Due to the nature of our beta burst detection algorithm, we had considered that overall increases in beta burst magnitude or duration during novel sessions could, at least in part, account for an increase in beta burst detection. It is therefore notable that beta burst detection was greatly increased in the hippocampus of J20 mice during novel sessions, in the absence of significant overall increases in beta burst magnitude or duration. This also argues against a simple increase in beta burst magnitude underlying the increased beta burst detection in the hippocampus of J20 mice.

Spectral analyses during and outside of beta bursts allowed us to investigate how oscillatory activity changes during beta bursts, both within, and outside of the beta frequency band. Furthermore, this analysis allows us to determine which novelty-associated spectral changes arise from increased beta bursting, and which do not. As in the retrosplenial cortex, the frequency of beta bursts lies within the 20-30 Hz range, supporting their characterisation as such. Notably, in the hippocampus, beta power outside of beta bursts appeared to be roughly similar

between wild-type and J20 mice. Conversely, in the retrosplenial cortex of J20 mice beta power is increased even outside of burst epochs (Chapter 3), suggesting that increased beta power in this region is independent of beta bursting. In J20 mice, beta bursting was associated with a significant decrease in theta power, suggesting that beta bursting in these animals may require a minor shift in hippocampal network activity.

4.4.5 Phase-Amplitude Coupling

Phase-amplitude coupling has been widely studied in the hippocampus, during a range of behaviours (Colgin et al., 2009; Tort et al., 2009; Lega et al., 2016). In this study, we show two main peaks in hippocampal phase-amplitude coupling comodulograms, which indicate coupling between the phase of theta (6-8 Hz) and the amplitude of alpha/beta (12-30 Hz) and gamma (50-100 Hz) oscillations, respectively. It is of note that the dominant form of phase-amplitude coupling in the hippocampus is theta-gamma coupling, while in the retrosplenial cortex, theta-alpha/beta coupling was greater. Furthermore, in the hippocampus of wild-type mice, theta gamma coupling was significantly higher during novel sessions, while there was no effect of novelty on theta-gamma coupling in the retrosplenial cortex. These data highlight the relevance of theta-gamma coupling in the hippocampus, and suggest that perhaps theta-alpha/beta coupling is the cortical equivalent of theta-gamma coupling. Previous studies have demonstrated strong theta-gamma coupling in the hippocampus, and have also shown that different layers of the CA1 are associated with different frequencies of modulated gamma oscillations (for review, see Zhang et al., 2019a). In this study, our hippocampal channel is located in the stratum oriens, which is associated with 60-120 Hz gamma oscillations, similar to that previously seen in stratum lacunosum-

moleculare (Zhang et al., 2019). Theta-fast gamma coupling has been associated with the encoding of sensory information (Bieri et al., 2014), so taken together, our results suggest that increased hippocampal theta-gamma coupling during contextual novelty supports memory encoding. In J20 mice, there is no effect of novelty on either theta-alpha/beta or theta-gamma coupling in the hippocampus, which therefore may impair memory encoding, and result in cognitive dysfunction previously shown in these animals (Cheng et al., 2007; Wright et al., 2013). Previous studies have demonstrated impaired theta-gamma phase-amplitude coupling in the hippocampus of J20 mice (Mondragón-Rodríguez et al., 2018), and that optogenetically driving medial septal neurons at gamma frequency was sufficient to restore hippocampal gamma power and theta-gamma coupling, and rescue spatial memory deficits in these animals (Etter et al., 2019). These studies demonstrate the importance of theta-gamma coupling to normal hippocampal function, and emphasise the impact of phase-amplitude coupling deficits on cognition.

4.4.6 Neuronal spiking during Beta Bursts

We have previously shown that retrosplenial beta bursts are associated with a significant increase in neuronal spiking rate (Chapter 3), and as such we hypothesised that beta bursts function to transiently activate neuronal ensembles, in order to create and encode cortical representations of environmental information. In our hippocampal data, we also saw a trend towards increased neuronal spiking during beta bursts, although this was not significant. As we have previously noted, due to the nature of this analysis as multi-unit activity, it is highly possible that we captured activity from a number of neurons, which may have different responses to beta bursts, thus causing the high

variability seen in this data. Different neurons may respond differently depending on neuronal subtype or classification, therefore important next steps would be to repeat this experiment with probes with greater channel density, in order to isolate single-units. In the hippocampus, we also noted an overall increase in spike amplitudes, and neuronal firing rates in J20 mice that was absent in the retrosplenial cortex. This data supports previous reports of neuronal hyperexcitability in the hippocampus in this model (Palop et al., 2007). Furthermore, numerous studies have demonstrated that both firing rates and spike waveforms can vary dramatically between different classes of neurons, with inhibitory interneurons generally showing faster firing rates (McCormick et al., 1985; Henze et al., 2000; Nowak et al., 2003). Therefore an overall increase in neuronal firing rate in the hippocampus in J20 mice may be indicative of the compensatory inhibitory remodelling previously shown by Palop et al. (2007). Future studies into single-unit activity may reveal the effects of beta bursting on the spiking of specific neuronal populations *in vivo,* which may provide further insight into their function.

4.4.7 Intra-retrosplenial Coherence

Coherence analysis was performed between the dysgranular and granular retrosplenial cortex, in order to investigate the extent of oscillatory synchrony between these two subregions. As expected for channels within the same brain region, coherence was high across a range of frequencies. When coherence was analysed across the whole 15-minute recording session, delta coherence was significantly higher during familiar sessions in wild-type mice, but not J20 mice. Conversely, in J20 mice, alpha coherence was significantly higher during familiar sessions, while gamma coherence was significantly higher during novel sessions.

When only the first minute was analysed, again, delta coherence was significantly higher during familiar sessions in wild-type mice. In J20 mice, theta and alpha coherence were significantly higher during familiar sessions, while gamma coherence was significantly higher during novel sessions. The increase in delta coherence during familiar sessions was surprising, considering the absence of notable changes to delta power in the retrosplenial cortex. Furthermore, delta oscillations are generally associated with slow-wave sleep, and thus often overlooked in studies in awake, behaving animals. However, work by Nacher et al. (2013) has shown that delta coherence between parietal and frontal cortex is associated with decision making. It is possible that increased delta coherence between the subregions of the retrosplenial cortex may be indicative of memory retrieval or the determination of novelty of familiarity. It is of note that despite dramatic increases in retrosplenial beta power during novel sessions in both genotypes, there was no concurrent increase in beta coherence. Furthermore, any differences in coherence between novel and familiar sessions appear to be negligible, considering the extremely high coherence values across all frequency bands. Moreover, there were no significant overall differences between wild-type and J20 mice in coherence in any frequency band, despite dramatic increases in spectral power in the 12-40 Hz range, as shown in Chapter 3. Due to the strong anatomical connectivity between these subregions, as well as the spatial proximity, oscillations in these subregions are highly synchronous, so it is possible that even dramatic changes in oscillatory activity may have little consequence on coherence across the retrosplenial cortex.

4.4.8 Hippocampal-Retrosplenial Coherence

Numerous studies have investigated the extent of anatomical connectivity between the hippocampus and retrosplenial cortex. Both regions are thought to be heavily involved in navigation, spatial learning and memory and contextual memory (Bird and Burgess, 2008; Todd and Bucci, 2015). While direct anatomical connections from the hippocampal CA1 region to the RSCdg are sparse, the RSCg receives inputs from CA1 and subiculum (Wyss and Van Groen, 1992). Far less is known about the functional connectivity between the RSC and hippocampus, in vivo. Coherence analysis was performed between the RSCg and hippocampus, in order to determine the extent of oscillatory synchrony between them, during environmental novelty. Delta and beta coherence were significantly higher during novel sessions in wild-type mice. This novelty-associated increase in delta coherence between retrosplenial cortex and hippocampus in combination with the novelty-associated decrease in delta coherence between retrosplenial cortex subregions could indicate that changes in delta synchrony in this network may support memory processes through dynamic modulation of cortico-cortical and cortico-hippocampal functional connectivity. Work by Fujisawa and Buzsáki (2011) demonstrated that phase coupling between 4 Hz oscillations in the prefrontal cortex and theta oscillations in the hippocampus facilitated joint modulation of local gamma oscillations and neuronal spiking. Theta coherence has been shown to increase between RSC and HC during contextual novelty, during a fear conditioning paradigm (Corcoran et al., 2016). Furthermore, theta coherence was lower during successful memory retrieval than unsuccessful memory retrieval (Corcoran et al., 2016). While we saw no evidence of novelty-associated changes in theta coherence, these data show that functional connectivity between the retrosplenial cortex and

hippocampus can vary during on contextual memory processing. While we saw no effect of novelty on beta coherence between the subregions of the retrosplenial cortex, beta coherence was increased between the hippocampus and retrosplenial cortex during novelty. This increase in beta coherence could indicate that beta oscillations are synchronous during novelty-associated beta bursting, but independent during spontaneous beta bursting during familiarity. This beta synchrony could develop directly, or by modulation from a common burst generator which drives beta bursting during novelty in both regions. Brief epochs of high beta synchrony have been demonstrated throughout the cortical-basal ganglia network (Leventhal et al., 2012), supporting the idea that beta bursts may form temporal windows of functional connectivity between distant brain regions. If this is the case, then the absence of an increase in beta coherence during novelty in J20 mice would suggest a loss of beta burst synchrony between the hippocampus and retrosplenial cortex during novelty. Finally, decreased delta and theta coherence between these two regions could indicate a reduction in functional connectivity, mirroring the “disconnection” seen in human Alzheimer’s disease (Locatelli et al., 1998). One major caveat to coherence analysis is the influence of volume conduction on these measures. As previously mentioned, volume conduction refers to the passive spread of electrical fields through tissue, and is the process which allows the recording of neural oscillations from distant current sources (Cohen, 2015). High levels of coherence may be detected due to the instantaneous passive spread of oscillations from a common source, and as such are potentially a poor representation of genuine functional connectivity. One potential counter to this limitation is the use of alternative methods such as the weighted phase lag index, which is far less sensitive to the effects of volume conduction.

4.4.9 Intra-retrosplenial Granger Causality

As previously discussed, Granger causality is a mathematical technique that can be used to investigate directional interactions between time series (Granger, 1969), which in neuroscience is sometimes considered to represent the flow of information in neuronal networks (Stokes and Purdon, 2017). The reasoning behind this inference is that numerous aspects of neural oscillations including the power (Osipova et al., 2006), frequency (Colgin et al., 2009) and phase of neural oscillations (Jensen, 2005) can be considered to convey information, therefore directionality of these interactions could be considered to represent directional flow of this information. In this study we used Granger causality in order to investigate directionality in oscillatory activity between brain regions, and how this may be affected by novelty or genotype. Granger causality is generally used on electrophysiological recordings from distant brain regions or sensors (Seth et al., 2015), however we decided to use this technique on local field potentials from the subregions of the retrosplenial cortex, in order to investigate directionality of oscillations within this region. We demonstrated that Granger causality is far greater in the theta, alpha, beta and gamma bands in the RSCg to RSCdg direction, which suggests that the flow of information within the retrosplenial is highly directional (Seth et al., 2015). Such an imbalance could be due to anatomical connectivity, and an imbalance in projections between the subregions. Additionally, as we have previously noted, due to the probe location, the channels in RSCg are in the deep layers of the cortex, while the channels in RSCdg are in more superficial layers, therefore, it is possible that this directionality is as a consequence of laminar projections within the cortex. Gamma Granger causality from the RSCg to the RSCdg was significantly higher overall during familiar sessions, which was of note considering we showed

increases in gamma power in both subregions of the retrosplenial cortex during novelty in Chapter 3, however as with our coherence analysis the effect of novelty on Granger causality within the retrosplenial cortex was minimal, indicating that intra-retrosplenial cortex communication is consistently high and reasonably invariant during health. In J20 mice, however, there were a number of differences. During novelty, Granger causality in the delta, theta and alpha band was decreased in the RSCg to RSCdg direction, but increased in the RSCdg to RSCg direction. These opposing changes could indicate a dramatic change in retrosplenial network activity, potentially arising from amyloid pathology or compensatory mechanisms. These results support the use of Granger causality in order to discover novel insights into directionality of oscillatory activity within brain regions.

4.4.10 Hippocampal-Retrosplenial Granger Causality

Granger causality was also investigated between the hippocampus and RSCg. Previous studies have shown direct and indirect anatomical connectivity from the hippocampus to the retrosplenial cortex and vice versa (Wyss and Van Groen, 1992). It was therefore of interest to investigate the directionality of oscillatory activity between these two regions. As we have shown, coherence between RSC and HC is high, indicating a high degree of temporally correlated activity. In wild-type mice, while Granger causality was significantly higher in the delta, theta and alpha bands in the HC to RSCg direction, this imbalance was far less than that previously shown within the retrosplenial cortex, indicating that oscillatory activity is far less unidirectional between these structures. Interestingly, gamma Granger causality was relatively equal in both directions, but peaked at different frequencies, with gamma Granger causality in the RSCg to HC direction peaking

around 50 Hz, while gamma Granger causality in the HC to RSCg direction peaked around 70 Hz. These two peaks are notable, as there has been a large body of work which has demonstrated that information flow between different structures in the hippocampal formation occurs at different frequencies of gamma (Colgin et al., 2009; Colgin, 2015b; López-Madrona et al., 2020). Our data indicates that the same happens between the retrosplenial cortex and the hippocampus, with two different “channels” potentially allowing for effective communication in both directions, simultaneously. Granger causality in the RSCg to HC direction was significantly higher in the delta, theta and gamma bands during familiar sessions, which may indicate information flow from the RSC to HC for the purpose of memory retrieval.

In J20 mice, while Granger causality in the hippocampus to RSC direction was relatively normal, there appeared to be a large broadband reduction in Granger causality in the RSC to hippocampus direction, so much so that the gamma peak is completely absent. While delta, theta and gamma Granger causality from the RSC to HC are increased during familiarity in wild-type mice, this relationship is completely absent in J20 mice. This aberrant Granger causality that disproportionately affects the retrosplenial cortex to hippocampus direction is suggestive of complex retrosplenial cortex dysfunction that is not apparent in coherence analysis. Furthermore, while Granger causality in the hippocampus to RSC direction was unaffected by novelty in wild-type mice, during novel sessions Granger causality in the delta, theta, alpha and beta bands was decreased in the hippocampus to RSC direction in J20 mice. This difference is of note as it is remarkably similar to the decreased Granger causality in the delta, theta, alpha and beta bands in the RSCg to RSCdg direction in J20 mice. This suggests this

entire pathway from the hippocampus through the RSCg all the way to the RSCdg is hypoactive during novelty, resulting is a functional disconnection of the retrosplenial cortex from the hippocampus. These data provide unique insights into the directionality of oscillatory activity in this specific part of the Papez Circuit, and reveal specific pathways which are disrupted in a mouse model of Alzheimer's disease (Psychiatry and 1937, n.d.).

4.4.11 Burst Cross Correlation

In order to directly test the temporal relationship between beta bursts along the probe, we performed cross-correlation analysis between beta bursts detected in RSCdg, and time-locked beta filtered signals from the other channels. To clarify, our analysis was performed on time-locked beta-filtered local field potentials, and not on the time stamps of these beta bursts. From this data, it was clear that beta bursts across the retrosplenial cortex, and in the hippocampus were highly correlated, with a small decrease in burst cross correlation in J20 mice. Furthermore, beta bursts were highly synchronous during novel sessions, but significantly asynchronous during familiar sessions. It is important to note that this "asynchrony" is merely indicative of a significant non-zero lag between beta oscillations, this peak lag amounted to hippocampal beta oscillations leading retrosplenial beta oscillations by 2 milliseconds on average. Considering that the average duration of beta bursts is around 170 milliseconds, this time difference is minimal, but could provide some insight into the mechanisms underlying beta bursting. As previously mentioned earlier in this chapter, the effects of volume conduction are instantaneous, so the existence of non-zero phase lags between beta oscillations in distant regions indicates that beta oscillations in the retrosplenial cortex are not simply being volume conducted from the

hippocampus (Plonsey and Heppner, 1967; Stinstra and Peters, 1998). Secondly, a 2-millisecond lag during familiarity is within the realms of a bi-synaptic conduction delay (Katz and Miledi, 1965), suggesting that beta oscillations in the retrosplenial cortex are potentially being driven by the hippocampus. These data support previous findings that beta bursts provide transient windows of beta synchrony between different brain regions that may facilitate effective communication over long distances (Leventhal et al., 2012; Lundqvist et al., 2018).

4.4.12 Conclusions

In conclusion, we have demonstrated a number of hippocampal correlates of contextual novelty, many of which are vastly different to those in the retrosplenial cortex. Additionally, we have identified a broad range of neurophysiological changes in the hippocampus of J20 mice, that are different to those seen in the retrosplenial cortex, raising interesting questions about the pathological mechanisms underlying these changes. Finally, we have demonstrated that oscillatory activity within the retrosplenial cortex, and between the retrosplenial cortex and hippocampus, show high temporal correlations and strong functional connectivity that vary dynamically, depending on contextual novelty.

5 Chapter 5

5.1 Introduction

Beta bursting has been previously described in a range of brain regions, and is associated with a wide variety of behaviours. Spontaneous beta bursts have been identified in the somatosensory cortex and frontal cortex in humans, rodents and non-human primates (Sherman et al., 2016), and pre-stimulus beta bursting in the somatosensory cortex of mice and humans is negatively correlated with tactile stimulus detection (Shin et al., 2017). In motor cortex in humans, beta bursts were associated with the termination of movement (Feingold et al., 2015), and in another study the timing of motor cortex beta bursts was associated with the timing of movement initiation, and errors were associated with delayed or reduced beta bursting (Little et al., 2019). Furthermore, pathological beta bursting throughout the striatum and motor cortex during Parkinson's disease is correlated with poor motor performance (Sharott et al., 2005; McCarthy et al., 2011; Tinkhauser et al., 2018; Torrecillos et al., 2018). As we have shown, beta bursting in the retrosplenial cortex and hippocampus is enhanced during contextual novelty, and beta bursts are highly synchronous between these two structures. It was therefore of interest to investigate novelty-associated beta bursting across the cortex, and determine the temporal relationships between cortical beta bursts. As suggested by Feingold et al. (2015), the role of beta bursting may vary dramatically depending on its location within the brain. As shown by Leventhal et al. (2012), beta bursts were synchronous across the cortical-basal ganglia network during a movement task. In whole brain preparations *in vitro*, carbachol-induced beta oscillations spread across the surface of the cortex, indicating that cortical beta synchrony may be high during beta bursts (Kilb and Luhmann,

2003). In order to investigate beta bursting across the cortex, mice were fitted with EEG style multi-electrode arrays (Figure 5.1b), covering the entire dorsal cortical surface (Figure 5.1c), and underwent a single-trial version of the Novel/Familiar environment task (Figure 5.1a). Furthermore, in order to investigate potential mechanisms underlying the aberrant beta bursting we saw in J20 mice in Chapters 3 and 4, we included an additional experimental group of J20 mice in this study. Whole-brain imaging has demonstrated dramatic differences in amyloid plaque density across the cortex in J20 mice, with highest relative plaque in the retrosplenial cortex (Whitesell et al., 2019), making this the ideal model to compare network activity across the cortex. In this Chapter, we demonstrate that spontaneous beta bursting occurs across the cortex, but novelty-associated beta bursting appears localised around the retrosplenial cortex, and that beta oscillations are highly synchronous across the cortex during beta bursts. Finally, excessive beta bursting in J20 mice appears localised above the retrosplenial cortex, suggesting a direct correlation between amyloid pathology and aberrant beta bursting.

5.2 Methods

5.2.1 Animals

3 male J20 mice and 3 wild-type littermates were bred at the University of Exeter and housed on a 12-hour light/dark cycle. All procedures were carried out in accordance with the UK Animal (Scientific Procedures) Act 1986 65 and were approved by the University of Exeter Animal Welfare and Ethical Review Body. Access to food and water was provided ad libitum. All animals were kept on a 12-hour light/dark cycle, with the light/dark cycle matching the normal daylight/night-time cycle, meaning all interactions including handling, surgery and behaviour

took place during the light cycle. Mice were group housed prior to surgery, and single housed post-surgery, in order to prevent damage to the surgical implants. All mice were approximately 3 months of age at the time of recordings.

5.2.2 Surgery

Mice were fitted with 30-channel EEG probes (NeuroNexus Technologies, MouseEEG, Figure 5.1b), which were fixed to the dorsal surface of the skull. Surgery was performed generally the same as for depth electrode implantation. Mice were anaesthetised using isoflurane and fixed into a stereotaxic frame. An incision was made along the midline of the scalp, and the skull was revealed. The EEG probes used cover a large area, so a large area of the skull had to be exposed in order to adhere the array, and affix support screws. In order to attach the probe to the surface of the skull, a small droplet of saline was placed around the centre of the skull, upon which the probe was gently laid. The surface tension of the liquid kept the probe in contact with the skull, and allowed it to be moved in order to align the cross with bregma (see Figure 5.1b). Once in place, dental cement (RelyX Unicem, 3M) was applied to the gaps between the rows of electrodes, and around the outside of the probe to hold it in place while holes were drilled for support screws (Antrin Miniature Specialties). Screws were implanted in the frontal bones, and occipital bones, with the ground wire from the probe attached to a screw overlying the cerebellum using silver wire. The connector for the probe was manipulated and fixed in position above the probe, and the entire implant was covered with dental cement for support. Throughout surgery, body temperature was monitored with a rectal probe and regulated by a feedback-controlled heat mat. Animals were kept hydrated by subcutaneous

injections of Hartmann's solution once per hour of surgery (0.01 ml/g body weight).

5.2.3 Behaviour

During this study, we used a single-trial version of the Novel/Familiar environment task, where animals would only undergo a single novel session, equivalent to either Session 1a in our previous nomenclature. As we have shown in Chapters 3 and 4, the most notable neurophysiological responses to novelty occur in the first couple of minutes after exposure to a novel environment, so by comparing network activity in the first minute of this single trial with network activity in the final 10 minutes of the trial, we could essentially use these as substrates for novelty and familiarity, respectively. For this study we used the square arena with black and white stripes from Chapters 3 and 4 study for continuity (Figure 5.1a). Each animal was places into the area and were allowed to freely explore their environment for 15 minutes, after which, they were returned to their home cage. As before, in order to reduce the stress associated with the recording process, animals were acclimatised to this process during 10-minute test session 3 days prior to the start of the experiment, in which they were tethered and recorded from while in their home cage.

5.2.4 Data Analysis

EEG-style surface probes allow sampling of electrophysiological data from across the entire dorsal surface of the cortex, however due to the spatial filtering properties of the skull, these recordings have far less spatial specificity than depth recordings (Srinivasan et al., 1998). In order to stratify analysis in this study, all channels on the probe were grouped based on the broad cortical areas above which they were located, however without source localisation techniques such as

those commonly used in human EEG or magnetoencephalography (MEG) studies, it is not possible to conclusively ascertain the exact source of oscillatory activity. Of the 30 channels on the probe, 4 regions were excluded from analysis, as they were found at the borders between multiple regions (Figure 5.1c). Analysis was performed as before, however some minor differences were made regarding downsampling of data to preserve memory when analysing data from this number of channels. Signals were downsampled by 30 times for beta burst detection, rather than 10 times, for a sampling rate of 1000 Hz, while signals for burst cross-correlation analysis were downsampled by 3 times, for a sampling rate of 10 kHz. Analysis was performed on each channel individually, and averaged across channels within the same brain region for much of the data. For the construction of heat maps, the built-in MATLAB function scatteredInterpolant was used to assign each value to the coordinate of its channel with relation to bregma, and interpolate between these scattered datapoints. Natural neighbour interpolation was used to interpolate between datapoints within the convex hull, but no extrapolation was performed outside the convex hull using scatteredInterpolant. Nearest neighbour extrapolation using scatteredInterpolant treats the nearest neighbour as the nearest true datapoint, rather than the outside edge of the convex hull, resulting in edge effects. Instead, we performed a “skirt” extrapolation, by which nearest neighbour extrapolation was instead performed on the outside edge of the convex hull, resulting in far superior heat maps. Heat maps were overlaid on images taken from Allen’s Brain Explorer (Wang et al., 2020).

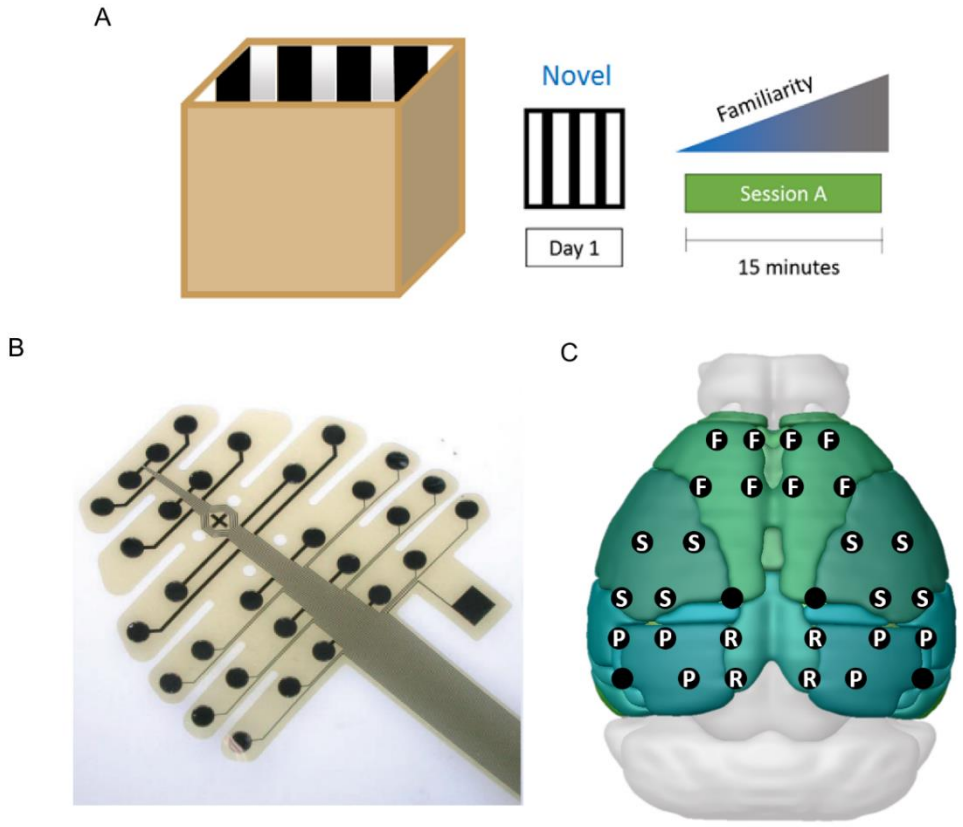

Figure 5.1 Experimental Design.
A. Diagram of the recording arena used for this study, as well as the experimental procedure for the single-trial version of the novel/familiar environment task. The arena used in this study was the same as the one used previously. The mouse was placed in the novel arena for a single recording session and allowed to explore for 15 minutes. B. Photograph showing the type of recording probes used in this study, taken from the 2021 NeuroNexus catalogue. These probes are flexible arrays that are fixed to the skull, and span the entire dorsal cortical surface. C. Diagram showing the approximate locations of all recording sites, superimposed on an image of the mouse brain taken from Allen Brain Explorer. Channels were grouped based on general cortical region, as denoted by the letters (F – Frontal Cortex, S – Somatosensory Cortex, P – Parietal Cortex, R – Retrosplenial Cortex). Blank channels represent those channels not allocated to any group, due to positioning at the border of multiple regions.

5.3 Results

In this study, we sought to investigate the relationship between beta bursts in the retrosplenial cortex, and those found in other cortical regions, mice were fitted with electroencephalography-style electrode arrays, which were directly attached to the dorsal surface of the skull. The high channel count of these probes, as well as the large spacing between adjacent channels allows the recording of electrophysiological signals from across the entire dorsal cortical surface. Furthermore, the ease of implantation of these probes allows for a high level of consistency in the placement of each channel. In addition to the retrosplenial cortex, these EEG probes allowed us to sample from a range of cortical regions where beta bursts have been previously demonstrated: the motor cortex, somatosensory cortex and parietal cortex. For a number of our analyses, we decided to average across channels positioned above these broad cortical areas, however it is important to note that while local field potential recordings from depth electrodes are thought to record from a relatively spatially limited area, EEG recordings have far less spatial specificity, due in part to the distance from the brain, and the spatial filtering properties of the skull (Srinivasan et al., 1998). For the sake of clarity, we have referred to recordings from channels above a certain region as recordings from that region, however this does not preclude the possibility that these channels are sampling from a larger spatial area than this may suggest. In order to determine the effects of contextual novelty on oscillatory activity across the cortex, and compare them to those seen in the retrosplenial cortex in Chapter 3, these mice underwent a novel/familiar environment task, as before. From Chapters 3 and 4, it is clear that the most dramatic changes in oscillatory activity occur soon after exposure to the novel environment, and

persist for around a minute, before returning to normal. It is for this reason that we experimented with a “single-trial” design of the novel/familiar environment task for this study, where animals would only undergo a single recording session in a novel environment. We hypothesised that the first minute, and last 10 minutes of this single novel session could be effectively used as substrates for novelty and familiarity, respectively, although on a shorter time scale than in the multi-session design. We have previously demonstrated numerous examples of network dysfunction in the retrosplenial cortex (Chapter 3) and hippocampus (Chapter 4) in J20 mice, a mouse model of Alzheimer’s disease, and we noted that the changes seen in the hippocampus were often distinct from those in the retrosplenial cortex. It is for this reason that we included a group of J20 mice in this study, in order to determine whether the neurophysiological changes seen in the RSC in J20 were specific to this region, or were indicative of aberrant oscillatory activity across the cortex. We performed a range of analyses, many of which are similar to those used in Chapters 3 and 4, in order to dissect a range of aspects of oscillatory activity across the cortex, and directly compare between these distinct recording modalities.

5.3.1 Cortical Spectral Analysis

In order to investigate any changes in oscillatory activity in across the cortex during environmental novelty, power spectral analysis was performed for all recording channels. As before, oscillatory activity was compared between the first minute of the session (the initial part), and the last ten minutes of the session (the final part). Spectral analysis was performed on the initial and final parts of the session, for all channels, and averaged across cortical regions for wild-type and J20 mice (Figure 5.2). It is of note that retrosplenial power spectra from EEG recordings are similar in shape to retrosplenial power spectra from LFP recordings, despite significant attenuation of spectral power across all frequency bands (Figure 5.2d). Power spectra for each cortical region are shown in (Figure 5.2), while (Figure 5.3) shows spectral power in each frequency band across the entire cortical surface, during novelty and familiarity, for both genotypes. In the frontal cortex (FC), gamma power was significantly higher overall during novelty (Gamma: Main Effect Novelty - $F(1,4) = 13.8$, $p = 0.02$, Mixed ANOVA). Gamma power was significantly higher during novelty in J20 mice (Nov: 8.5 ± 0.8 dB; Fam: 7.4 ± 0.8 dB, $p = 0.03$), but not wild-type mice. Furthermore, beta power was significantly higher overall in J20 mice compared to wild-type mice (Main Effect Genotype - $F(1,4) = 8.8$, $p = 0.04$, Mixed ANOVA). In the somatosensory cortex (SSC), theta, beta and gamma power were significantly higher overall during novelty (Theta: Main Effect Novelty - $F(1,4) = 9.7$, $p = 0.04$, Mixed ANOVA; Beta: Main Effect Novelty - $F(1,4) = 16.4$, $p = 0.02$, Mixed ANOVA; Gamma: Main Effect Novelty - $F(1,4) = 28.1$, $p = 0.006$, Mixed ANOVA). Beta and gamma power were significantly higher during novelty in J20 mice (Beta: Nov: 11 ± 0.4 dB; Fam: 9.7 ± 0.4 dB, $p = 0.02$; Gamma: Nov: 9.1 ± 0.7 dB; Fam: 7.4 ± 0.8 dB, $p = 0.008$), but not wild-type mice. In the parietal cortex (PC), delta power was significantly higher

overall during familiarity (Main Effect Novelty - $F(1,4) = 21.6$, $p = 0.01$, Mixed ANOVA). Delta power was significantly higher during novelty in J20 mice (Nov: 16.2 ± 1.4 dB; Fam: 17.1 ± 1.5 dB, $p = 0.02$), but not wild-type mice. Finally, in the retrosplenial cortex, there was no significant effect of genotype or novelty on power in any frequency band.

In order to investigate whether beta bursting could be detected in EEG recordings, we visually inspected a number of these recordings from channels overlying the retrosplenial cortex in the time and frequency domains (Figure 5.4), similar to our previous approach in Chapter 3 (Figure 3.5). As in local field potential recordings from the retrosplenial cortex (Figure 3.5), increased beta power occurred in brief, discrete epochs, as shown in the expanded power spectrogram in Figure 5.4. As before, this can also be seen clearly in beta-filtered local field potentials, where these periods of high beta amplitude intersperse an otherwise very low amplitude oscillation. In order to better understand the timescale and frequency domains of these events, and compare them to our local field potential recordings, wavelet analysis was used to investigate their time course and frequency profile further. As exemplified in Figure 5.4, these individual events were short in duration, and peaked in the 20-30 Hz, beta band.

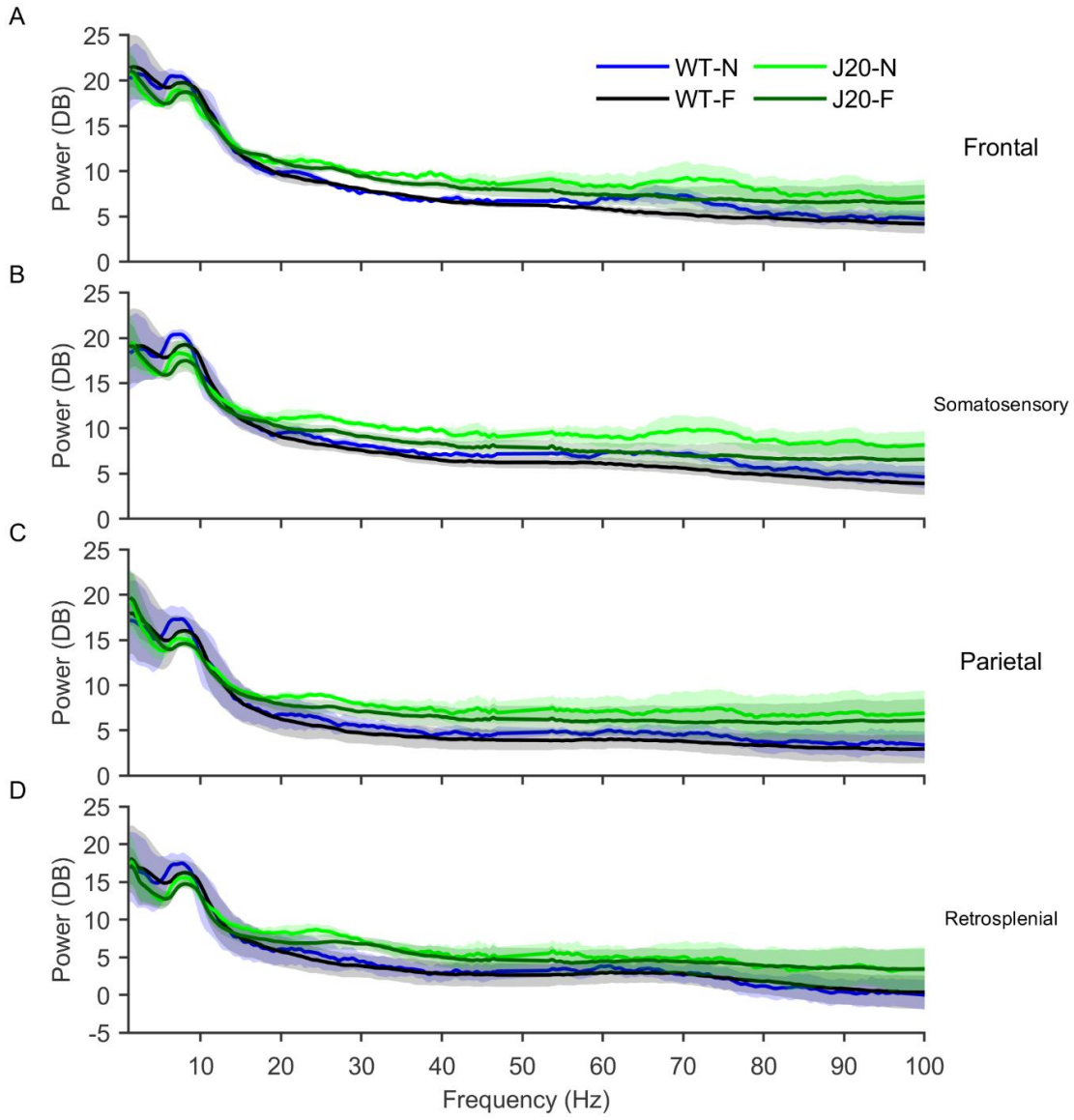

Figure 5.2 Various spectral changes are observed across the cortex in J20 mice.

A. Average frontal cortex power spectra for the first minute of the session (N) and the last 10 minutes of the session (F), for wild-type and J20 mice. Gamma power was significantly higher during novelty in J20 mice ($p = 0.03$), while beta power was significantly higher overall in J20 mice ($p = 0.04$). B. Average somatosensory cortex power spectra for the first minute of the session (N) and the last 10 minutes of the session (F), for wild-type and J20 mice. Beta and gamma power were significantly higher during novelty in J20 mice ($p = 0.02$, $p = 0.008$, respectively). C. Average parietal cortex power spectra for the first minute of the session (N) and the last 10 minutes of the session (F), for wild-type and J20 mice. Delta power was significantly higher during novelty in J20 mice ($p = 0.02$). D. Average retrosplenial cortex power spectra for the first minute of the session (N) and the last 10 minutes of the session (F), for wild-type and J20 mice. There was no significant effect of genotype or novelty on power in any frequency band. (Data shown as mean ± SEM, WT: n = 3, J20: n = 3).

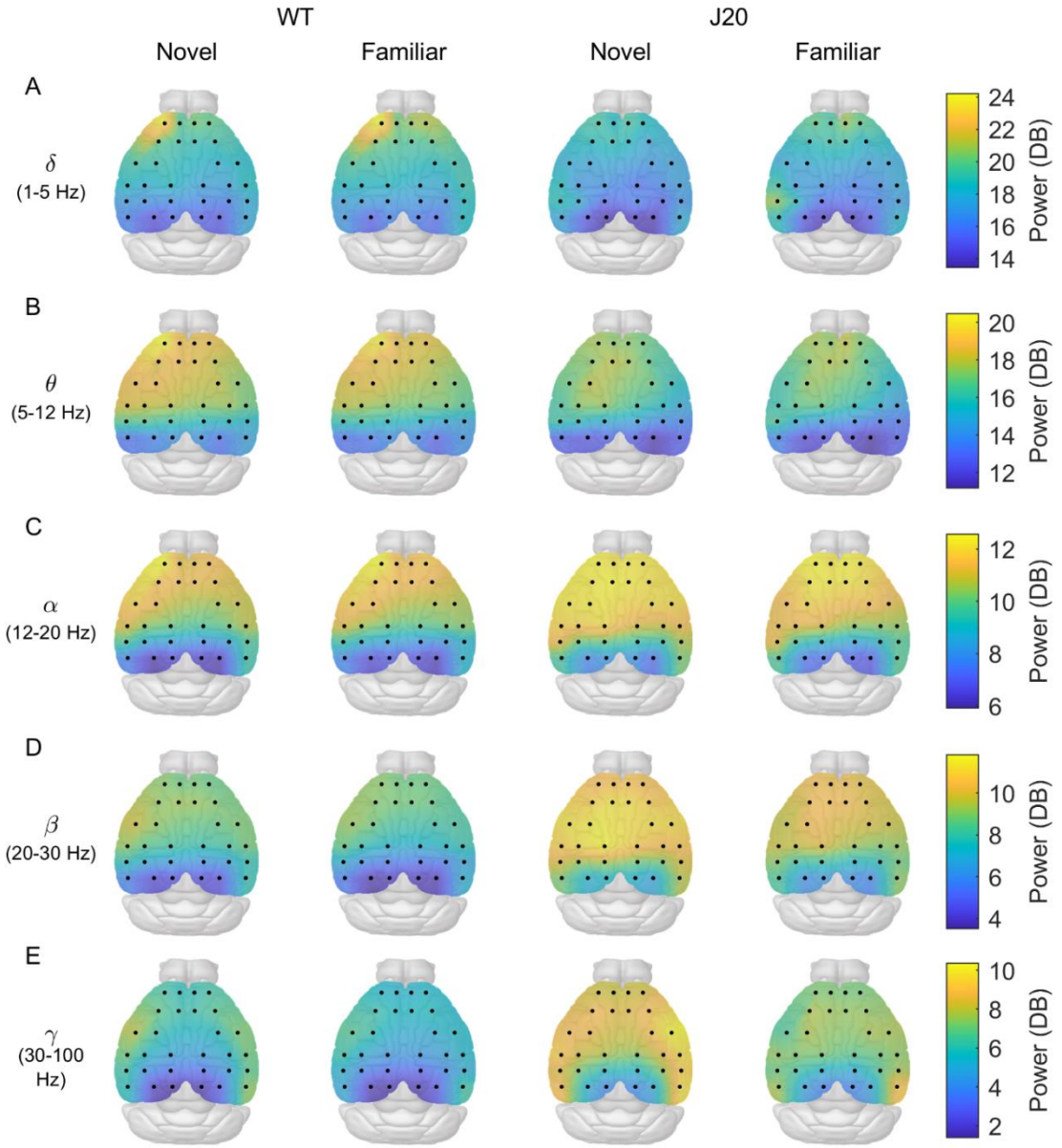

Figure 5.3 Heat maps illustrating the mean power in each frequency band across the entire cortical surface, during the first minute (Novel) and last 10 minutes (Familiar) of the session, in both genotypes.
A. Delta (1-5 Hz) power across the cortex. There appeared to be no effect of genotype or novelty on delta power across the cortex. B. Theta (5-12 Hz) power across the cortex. Theta power appeared to be marginally lower across the cortex in J20 mice. C. Alpha (12-20 Hz) power across the cortex. Alpha power appears to be marginally higher in J20 mice, but only above frontal regions. D. Beta (20-30 Hz) power across the cortex. Beta power appears to be substantially higher in J20 mice in all areas except for central, retrosplenial channels. E. Gamma (30-100 Hz) power across the cortex. Gamma power appears to be substantially higher in J20 mice in all areas except for central, retrosplenial channels. Overall, power in all frequency bands appears lowest in central, retrosplenial channels. (Data shown as mean, WT: n = 3, J20: n = 3).

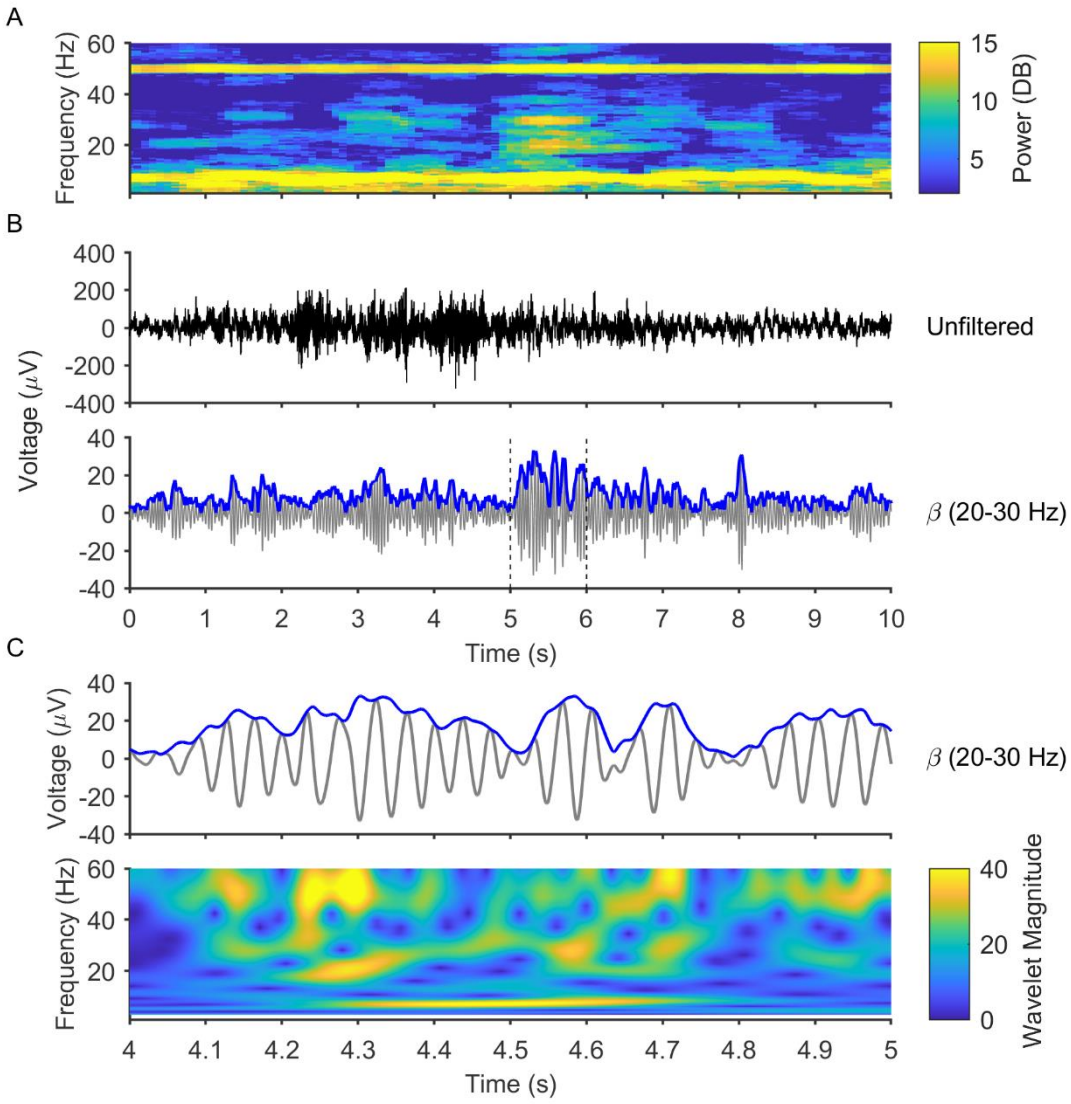

Figure 5.4 Beta bursting can be seen in EEG recordings taken from channels above the retrosplenial cortex.
A. Example power spectrogram showing transient increases in beta power. B. EEG recordings of data shown in A, both unfiltered (top), and filtered in the beta band (bottom), with the envelope amplitude in blue for clarity. The beta-filtered EEG shows clear epochs of high beta amplitude, which intersperse a low amplitude continuous beta oscillation. C. Expanded trace of the dashed area in shown in B (top), and a continuous wavelet spectrogram of this time series (bottom). Due to the high temporal resolution of wavelet-based methods, these periods of high beta amplitude can be seen to be brief in duration, only lasting around 100-200 ms.These beta bursts appear to be similar to those seen in local field potential recordings, although lower in amplitude.

5.3.2 Cortical Beta Bursting Activity

Beta bursts could be recorded in EEG recordings from across the cortex, using the same algorithm used for local field potential recordings in Chapters 3 and 4, despite the low-pass filtering effect the of the skull (Pfurtscheller and Cooper, 1975). In order to investigate the prevalence of beta bursts across the cortex, we compared the total number of beta bursts detected between cortical regions (Figure 5.5). There was a significant overall effect of region on total number of beta bursts detected (Main Effect Region - $F(3,12) = 5.3$, $p = 0.02$, Mixed ANOVA). In wild-type mice, the total number of beta bursts detected appeared to be similar across all regions of the cortex (Figure 5.5b), while in J20 mice there was a non-significant trend towards increased beta burst detection, especially over the retrosplenial cortex (Figure 5.5a, right).

As in Chapter 3, contextual novelty is associated with a significant increase in retrosplenial beta burst rate during the first minute of novel sessions, after which it returns to a lower, baseline rate. Therefore, in order to determine whether beta bursting is associated with contextual novelty across the cortex, we investigated the rate of beta bursting during the initial part and final part of this single novel session, for all animals (Figure 5.5c). These data are shown as heat maps in (Figure 5.5c) and quantified in (Figure 5.6). While the total number of beta bursts detected was relatively consistent across the cortex in wild-type mice (Figure 5.5a), beta burst rate appeared to be higher during novelty, especially over the retrosplenial cortex (Figure 5.5c, left), a pattern mirrored in J20 mice (Figure 5.5c, right). The distributions of beta bursts and beta burst rates shown in (Figure 5.6) show that in wild-type mice, beta burst rate appears to be reasonably steady throughout the session in FC, SSC and PC, while in the RSC the beta burst rate

appears to be substantially higher during the initial part of the session, with an approximate 3-fold increase. In J20 mice, however, beta burst rate appears to be higher during the initial part of the session for all cortical areas (Figure 5.6). Beta burst rate was significantly higher overall during novelty in the somatosensory cortex (Main Effect Novelty - $F(1,4) = 9.2$, $p = 0.04$, Mixed ANOVA), however this difference was only significant for J20 mice (Nov: 6.3 ± 1.3; Fam: 2.1 ± 0.3, $p = 0.05$), and not wild-type mice. There was also a trend towards higher beta burst rates during novelty in the retrosplenial cortex, however this was not significant (Main Effect Novelty - $F(1,4) = 6.8$, $p = 0.059$, Mixed ANOVA).

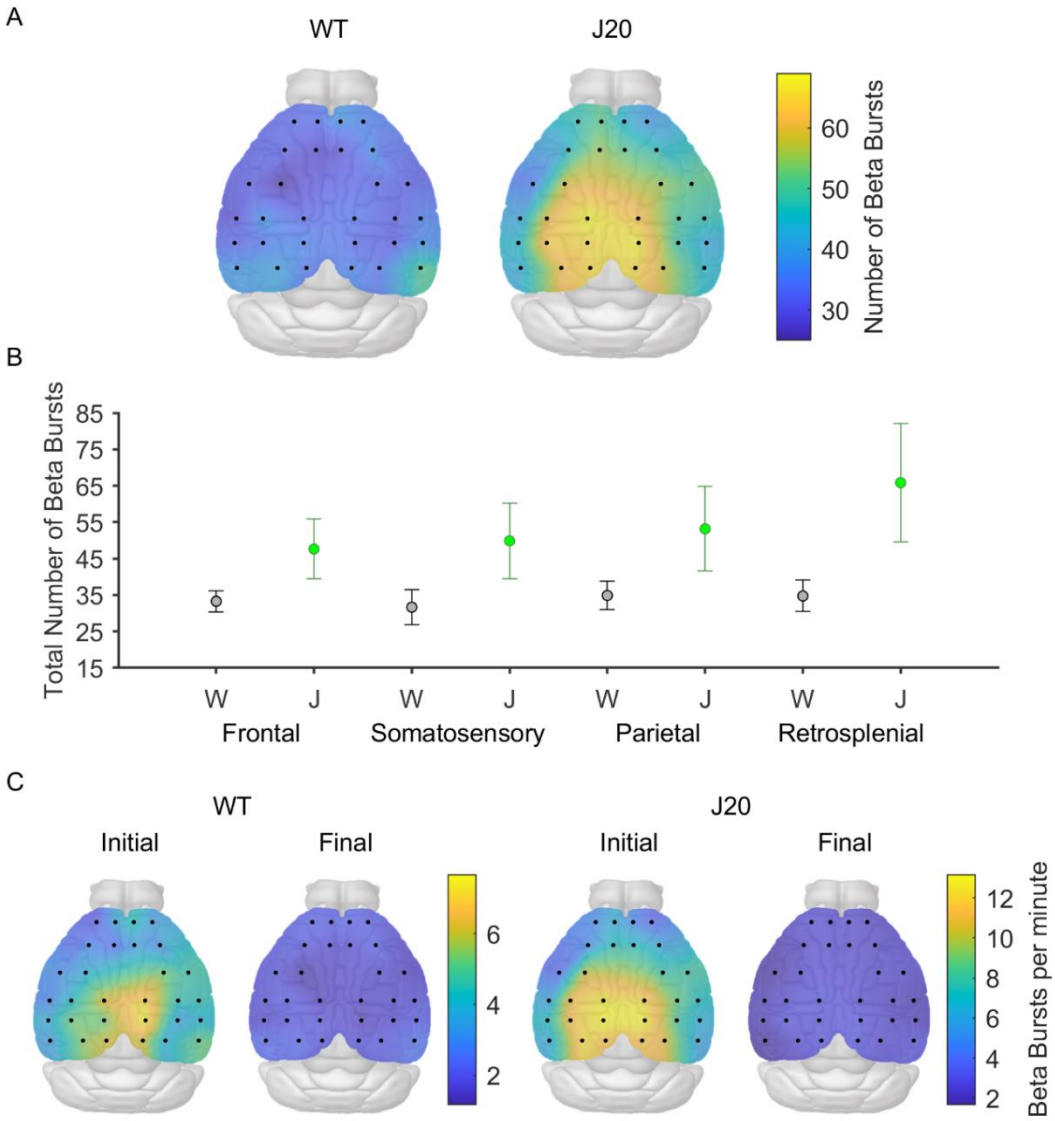

Figure 5.5 Beta bursting activity across the cortex.
A. Heat maps illustrating the total number of beta bursts detected at all channels, averaged across all wild-type (left) and J20 mice (right). In wild-type mice, relatively equal numbers of beta bursts were detected across the cortex. In J20 mice, beta burst detection appeared to be increased across the cortex, in particular above the retrosplenial cortex. B. Graph showing the average number of beta bursts detected in all regions, for wild-type (black) and J20 mice (green). There was a significant effect of region of beta burst detection ($p = 0.02$) and a trend towards increased beta bursting in J20 mice. C. Heat maps illustrating the average beta burst rate during the first minute (initial) and last 10 minutes of the session (final), for wild-type (left) and J20 mice (right). In both wild-type and J20 mice, beta burst rate appears to be far higher during the initial part of the session, particularly in retrosplenial cortex channels. (Data shown as mean ± SEM, WT: $n = 3$, J20: $n = 3$).

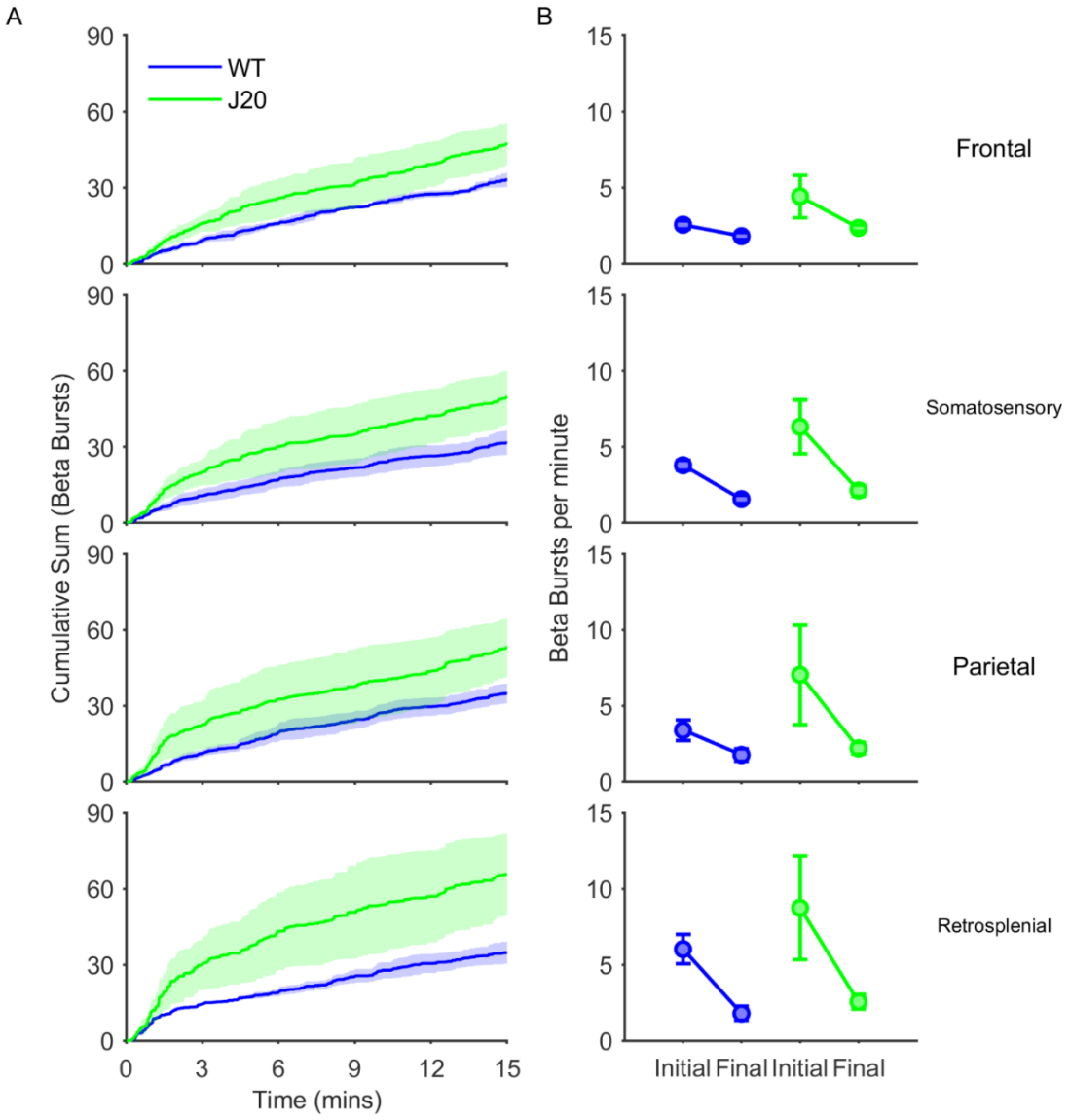

Figure 5.6 Beta burst distribution and rate across the cortex.
A. Cumulative frequency graphs of beta bursts detected in each cortical region during the recording session, for wild-type and J20 mice. In wild-type mice, beta bursting appeared to be reasonably steady across the session in most regions, except for retrosplenial cortex, where there is increased beta bursting during the first minute of the session. In J20 mice, beta bursting appeared to be increased during the first minute of the session in all cortical regions. D. Graphs showing average beta burst rate in each cortical region, during the first minute (initial) and last 10 minutes (final) of the recording session, for wild-type and J20 mice. Beta burst rate was significantly higher overall during novelty in the somatosensory cortex ($p = 0.04$), but this was only significant for J20 mice ($p = 0.05$). There was a trend towards higher beta burst rates during novelty in the retrosplenial cortex, however this was not significant ($p = 0.059$). (Data shown as mean ± SEM, WT: $n = 3$, J20: $n = 3$).

5.3.3 Cortical Beta Burst Characteristics

Beta burst characteristics were investigated across the cortex, in order to compare retrosplenial beta bursts to those in other cortical regions, and to investigate whether these characteristics vary depending on genotype. There was a significant overall effect of region on beta burst magnitude (Main Effect Region - $F(3,12) = 18.3$, $p = 9e\text{-}5$, Mixed ANOVA, Figure 5.7a, b). On average, beta bursts in the retrosplenial cortex were significantly smaller in magnitude than those in the frontal cortex (RSC: 44.6 ± 7.2 µV; FC: 59.4 ± 5.6 µV, $p = 0.008$), and somatosensory cortex (RSC: 44.6 ± 7.2 µV; SSC: 58.5 ± 5.8 µV, $p = 0.009$). There was no significant effect of genotype or region on beta burst duration (Figure 5.7c, d).

As before, in order to understand the frequency profile of beta bursts across the cortex, power spectral analysis was performed on individual beta bursts. As a control, these burst spectra were compared to power spectra of epochs of equal length directly prior to each burst. These power spectra were averaged across all bursts and "pre-bursts", for wild-type and J20 mice (Figure 5.8a). In the frontal cortex, alpha and beta power were significantly higher overall during beta bursts (Alpha: Main Effect Burst - $F(1,4) = 11.9$, $p = 0.03$, Mixed ANOVA; Beta: Main Effect Burst - $F(1,4) = 298.8$, $p = 6.e\text{-}5$, Mixed ANOVA). Beta power was significantly higher during beta bursts in both wild-type (Pre-Burst: 8.28 ± 0.89 dB; Burst: 15.9 ± 0.7 dB, $p = 3e\text{-}4$) and J20 mice (Pre-Burst: 9.4 ± 0.5 dB; Fam: 18.1 ± 0.7 dB, $p = 2e\text{-}4$), while alpha power was only significantly higher during beta bursts in J20 mice (Pre-Burst: 12.1 ± 0.2 dB; Fam: 13.8 ± 0.3 dB, $p = 0.04$). In the somatosensory cortex, alpha, beta and gamma power were significantly higher overall during beta bursts (Alpha: Main Effect Burst - $F(1,4) = 9.8$, $p = 0.03$,

Mixed ANOVA; Beta: Main Effect Burst - F(1,4) = 327.8, p = 5e-5, Mixed ANOVA; Gamma: Main Effect Burst - F(1,4) = 9.6, p = 0.04, Mixed ANOVA). Beta power was significantly higher during beta bursts in both wild-type (Pre-Burst: 7.98 ± 0.9 dB; Burst: 15.8 ± 0.7 dB, p = 3e-4) and J20 mice (Pre-Burst: 9.2 ± 0.5 dB; Fam: 18.1 ± 0.7 dB, p = 2e-4), while alpha and gamma were only significantly higher during beta bursts in J20 mice (Alpha: Pre-Burst: 11.1 ± 0.4 dB; Fam: 13 ± 0.5 dB, p = 0.05; Gamma: Pre-Burst: 7.2 ± 1.2 dB; Fam: 9.3 ± 1.7 dB, p = 0.05). In the parietal cortex, alpha, beta and gamma power were significantly higher overall during beta bursts (Alpha: Main Effect Burst - F(1,4) = 39.9, p = 0.003, Mixed ANOVA; Beta: Main Effect Burst - F(1,4) = 306.7, p = 6e-5, Mixed ANOVA; Gamma: Main Effect Burst - F(1,4) = 22.4, p = 0.009, Mixed ANOVA). Alpha and beta power were significantly higher during beta bursts in both wild-type (Alpha: Pre-Burst: 8.5 ± 1.9 dB; Fam: 10.5 ± 2.1 dB, p = 0.01; Beta: Pre-Burst: 5.7 ± 1.5 dB; Fam: 13.6 ± 1.3 dB, p = 3e-4) and J20 mice (Alpha: Pre-Burst: 9.3 ± 0.4 dB; Burst: 11.4 ± 0.7 dB, p = 0.01; Beta: Pre-Burst: 7.3 ± 0.8 dB; Fam: 16.4 ± 1.1 dB, p = 2e-4), while gamma power was only significantly higher during beta bursts in J20 mice (Gamma: Pre-Burst: 6 ± 1.6 dB; Burst: 8.5 ± 2.2 dB, p = 0.02). Finally, in the retrosplenial cortex, alpha, beta and gamma power were significantly higher overall during beta bursts (Alpha: Main Effect Burst - F(1,4) = 33.2, p = 0.005, Mixed ANOVA; Beta: Main Effect Burst - F(1,4) = 279, p = 8e-5, Mixed ANOVA; Gamma: Main Effect Burst - F(1,4) = 10.4, p = 0.03, Mixed ANOVA). Alpha and beta power were significantly higher during beta bursts in both wild-type (Alpha: Pre-Burst: 8 ± 2.2 dB; Fam: 9.6 ± 2.4 dB, p = 0.02; Beta: Pre-Burst: 4.6 ± 1.9 dB; Fam: 12.2 ± 1.6 dB, p = 4e-4) and J20 mice (Alpha: Pre-Burst: 8.4 ± 0.7 dB; Burst: 10.5 ± 0.5 dB, p = 0.01; Beta: Pre-Burst: 6.7 ± 0.9 dB; Burst: 15.6 ± 1 dB, p = 2e-4).

In order to investigate beta rhythmicity across the cortex, the period of beta oscillations was calculated for all beta bursts and all epochs without beta bursts, and the distribution of these beta periods was calculated and averaged across all burst and non-burst epochs, in all sessions, for wild-type and J20 mice (Figure 5.8b). As before, while the distribution of beta periods during beta bursts was reasonably consistent, peaking around 0.04s, equivalent to a 25 Hz oscillation, the distribution of beta periods in non-burst epochs was far more variable, which is suggestive of a loss of beta rhythmicity during non-burst epochs, however this is inconclusive without further experiments (for discussion of the limitations of this analysis see Chapter 3).

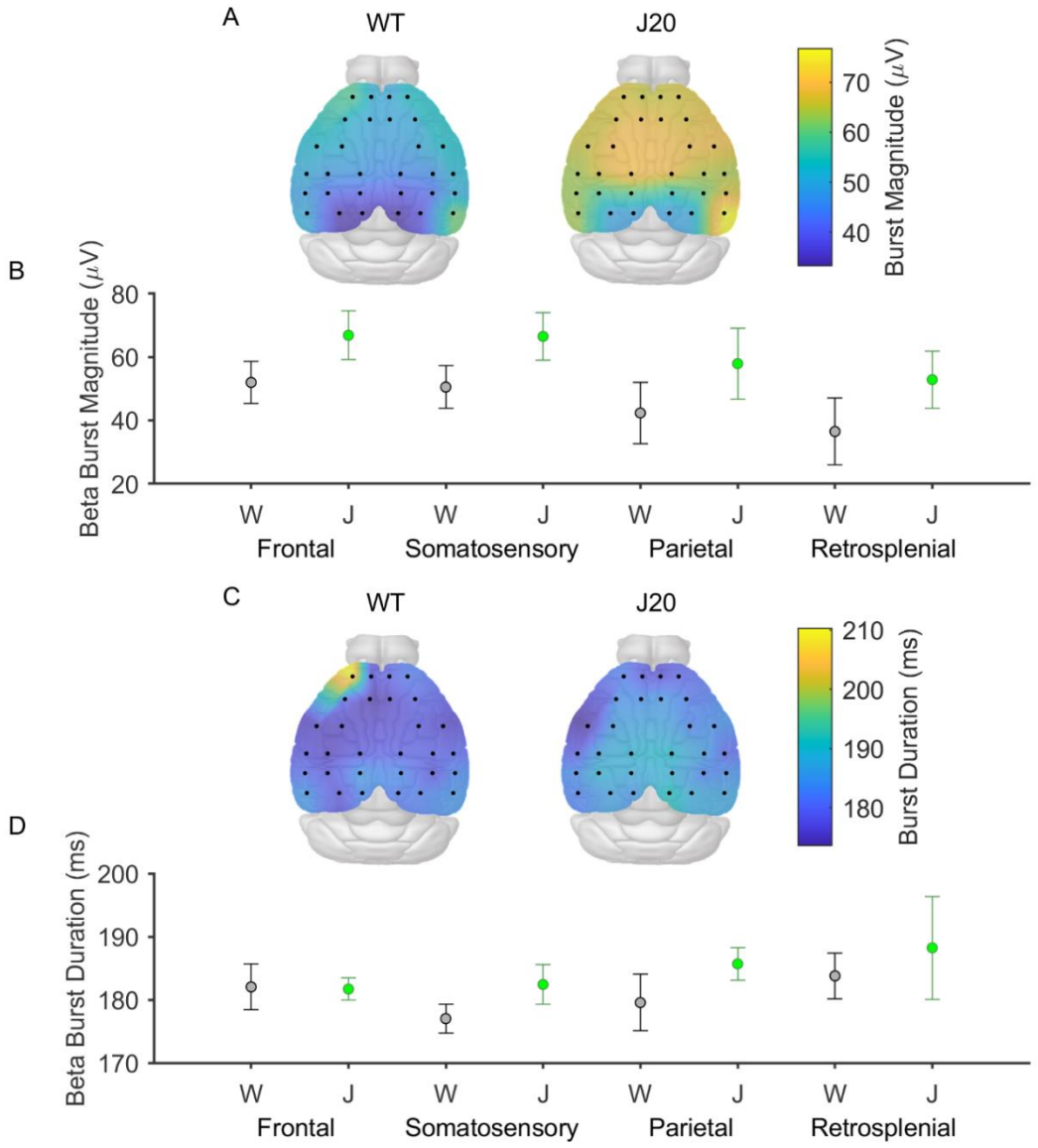

Figure 5.7 Beta burst magnitude and duration across the cortex.
A. Heat maps illustrating the average magnitude of beta bursts detected at all channels, averaged across all wild-type (left) and J20 mice (right). In J20 mice, beta burst magnitude appeared to be higher across the cortex. B. Graph showing the average magnitude of beta bursts detected in all cortical regions, for wild-type (black) and J20 mice (green). There was a significant effect of region on beta burst magnitude ($p = 9e05$). On average, beta bursts in the retrosplenial cortex were significantly smaller in magnitude in the retrosplenial cortex than in the frontal and somatosensory cortices ($p = 0.008$, $p = 0.009$, respectively). C. Heat maps illustrating the average duration of beta bursts detected at all channels, averaged across all wild-type (left) and J20 mice (right). Beta burst duration appeared to be generally unaffected by genotype across the cortex. D. Graph showing the average duration of beta bursts detected in all cortical regions, for wild-type (black) and J20 mice (green). There was no significant effect of genotype or region on beta burst duration. (Data shown as mean ± SEM, WT: $n = 3$, J20: $n = 3$).

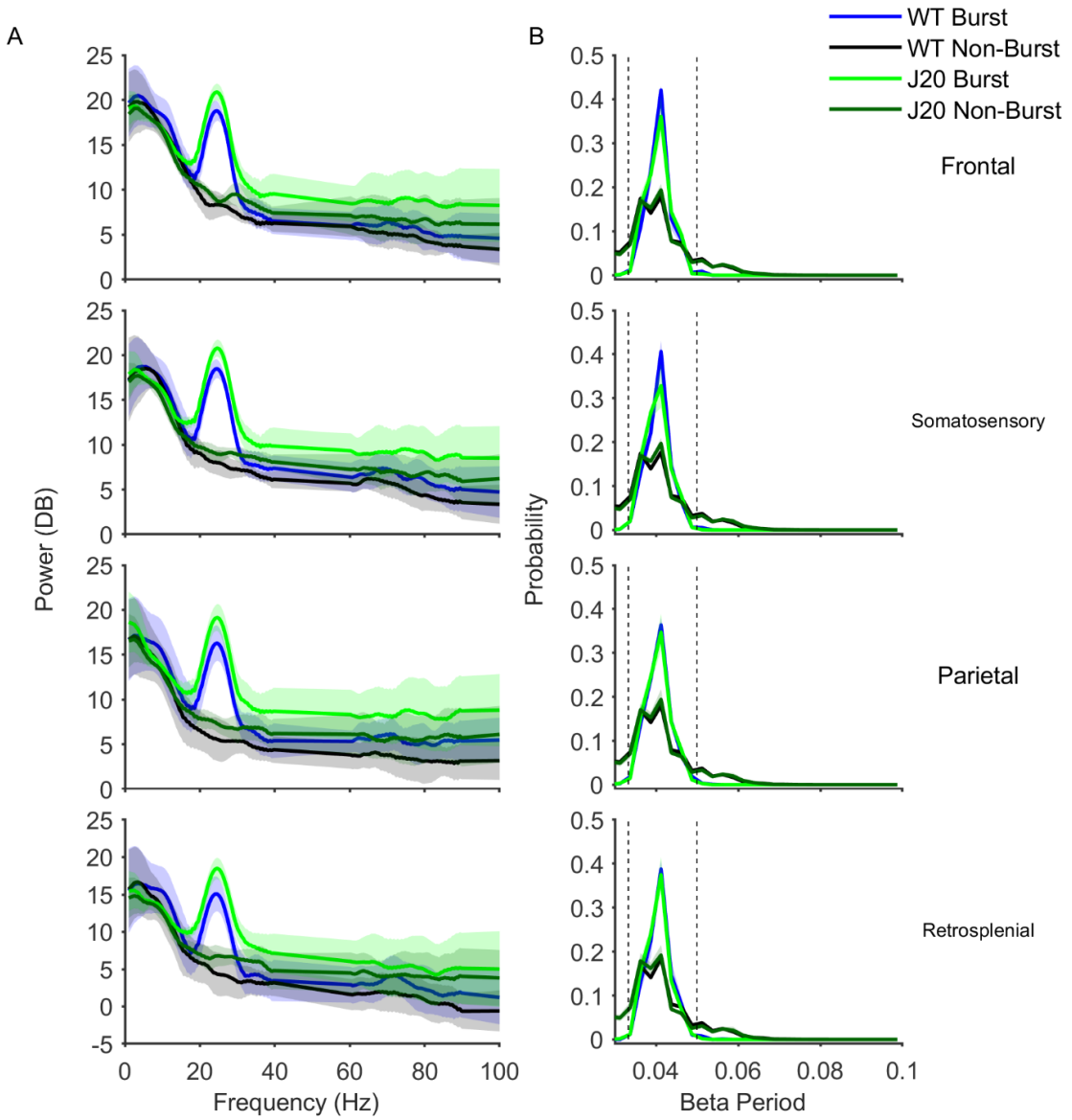

Figure 5.8 Beta burst frequency profile and rhythmicity across the cortex.
A. Average power spectra for beta burst and pre-burst epochs, for all cortical regions, averaged across all wild-type and J20 mice. Beta bursts are associated with a large, significant increase in beta power in all cortical regions, for both wild-type (Frontal: p = 3e-4, Somatosensory: p = 3e-4, Parietal: p = 3e-4, Retrosplenial: p = 4e-4) and J20 mice (Frontal: p = 2e-4, Somatosensory: p = 2e-4, Parietal: p = 3e-4, Retrosplenial: p = 2e-4). B. Average distributions of beta oscillation period for burst and non-burst epochs, for all cortical regions, averaged across all wild-type and J20 mice. Beta oscillations are tightly rhythmic during beta bursts, but not during non-burst epochs. (Data shown as mean ± SEM, WT: n = 3, J20: n = 3).

5.3.4 Burst Cross-Correlation

In order to directly determine the temporal relationship between retrosplenial beta bursts, and beta bursts detected elsewhere in the cortex, we performed cross-correlation analysis as described in Chapter 4. Briefly, beta bursts were detected at a single channel directly above the retrosplenial cortex, and cross-correlation analysis was performed on a burst-by-burst basis between each burst signal, and time-locked signals from all other recording sites. While our previous analysis investigated beta burst cross-correlations across the dorsoventral axis of the retrosplenial cortex (Chapter 3), and dorsal hippocampus (Chapter 4), these EEG-style probes allowed investigation into the spatio-temporal extent of retrosplenial beta bursts across the entire dorsal cortical surface. The peak cross-correlation and peak lag were calculated across all channels, and averaged across all beta bursts, for both wild-type and J20 mice (Figure 5.9). During beta bursts in the retrosplenial cortex of wild-type mice, beta oscillations were highly correlated across the retrosplenial cortex (correlation coefficient > 0.95), and the rest of the cortical surface (correlation coefficient > 0.8) (Figure 5.9a). Furthermore, while beta oscillations appeared to be highly correlated across the retrosplenial cortex during beta bursts in J20 mice (correlation coefficient > 0.95), burst cross-correlation appeared to be reduced across the rest of the cortical surface (correlation coefficient > 0.7). Retrosplenial-somatosensory burst cross-correlation was significantly decreased in J20 mice (WT: 0.92 ± 0.02; J20: 0.81 ± 0.02, $p = 0.04$).

Peak burst cross-correlation lag was also calculated in order to investigate the degree of synchrony between beta bursts detected over the retrosplenial and beta oscillations across the cortex. As shown in (Figure 5.9c, d), beta oscillations

are highly synchronous across the cortical surface during beta bursts. Burst cross correlation lags were statistically compared to zero to determine whether their peak lag was significantly non-zero, and the beta oscillations were synchronous. During retrosplenial beta bursts in wild-type mice, beta oscillations were synchronous between the retrosplenial cortex and all other cortical regions (Frontal: 2.9 ± 1.2 ms, $t(2) = 2.5$, $p = 0.1$; one-sample t-test; Somatosensory: 0.5 ± 0.2 ms, $t(2) = 2.4$, $p = 0.143$; one-sample t-test; Parietal: -0.1 ± 0.3 ms, $t(2) = -0.46$, $p = 0.7$; one-sample t-test; Retrosplenial: 0.02 ± 0.02 ms, $t(2) = 1.3$, $p = 0.3$; one-sample t-test). During retrosplenial beta bursts in J20 mice, beta oscillations were synchronous across the frontal, somatosensory and retrosplenial cortices (Frontal: 1.7 ± 2.5 ms, $t(2) = 0.7$, $p = 0.6$; one-sample t-test; Somatosensory: 0.5 ± 0.4 ms, $t(2) = 1$, $p = 0.4$; one-sample t-test; Retrosplenial: -0.001 ± 0.04 ms, $t(2) = -0.03$, $p = 0.97$; one-sample t-test), however beta oscillations in the parietal cortex were significantly asynchronous (Parietal: 2 ± 0.5 ms, $t(2) = 4.3$, $p = 0.05$; one-sample t-test).

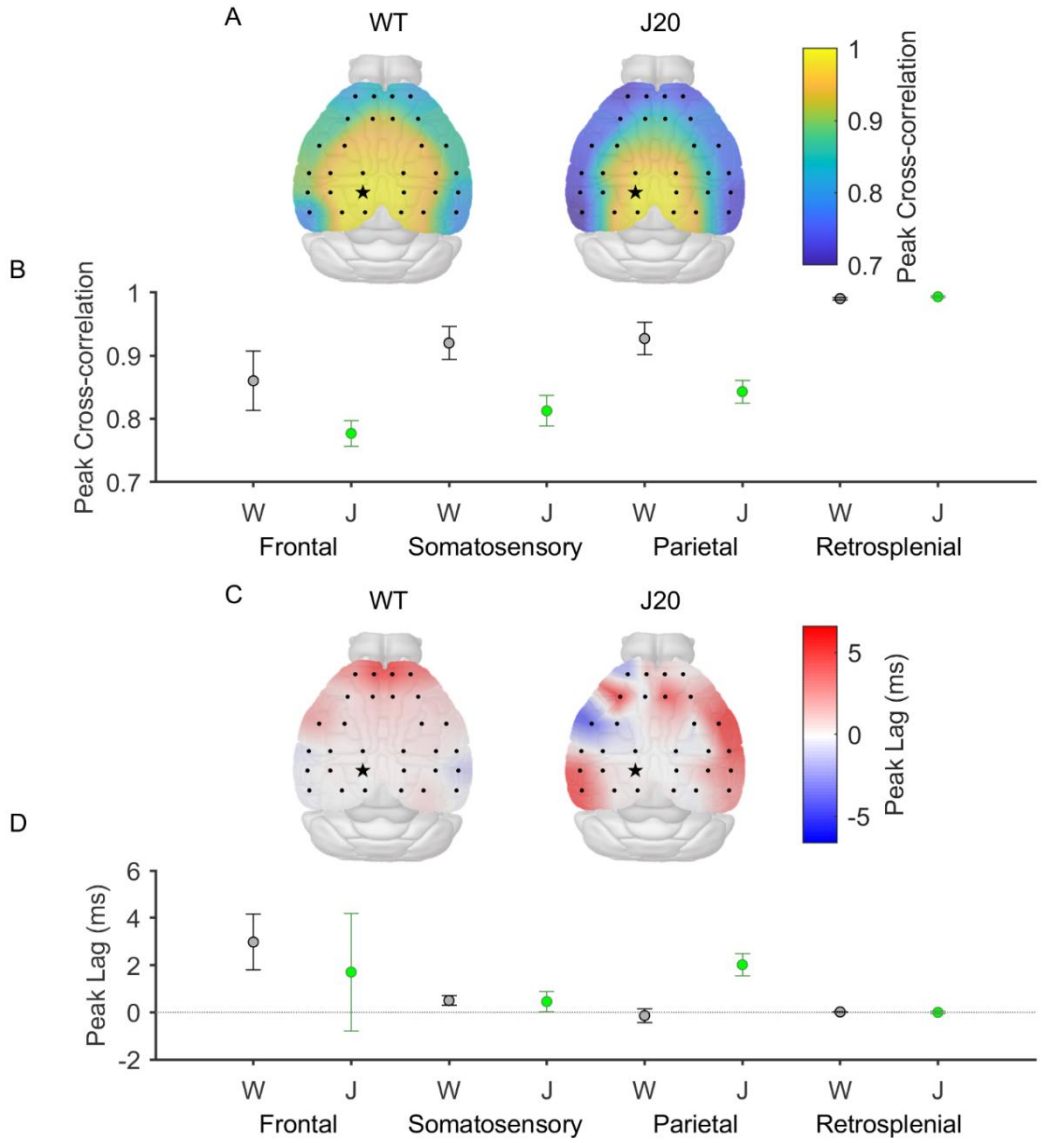

Figure 5.9 Beta bursts are highly correlated and synchronous across the cortex. A. Heat maps illustrating the peak cross-correlation between beta bursts detected in the retrosplenial cortex (RSC) (star), and beta oscillations across the cortex, averaged across all beta bursts in all wild-type (left) and J20 mice (right). Beta oscillations are highly correlated across the entire RSC during beta bursts in both genotypes, however in J20 mice there appears to be a loss of correlation outside the RSC. B. Graph showing the peak cross-correlation between RSC beta bursts and beta oscillations in all cortical regions, averaged across all beta bursts in all wild-type (black) and J20 mice (green). Retrosplenial-somatosensory burst cross-correlation was significantly lower in J20 mice ($p = 0.04$). C. Heat maps illustrating the peak lag between beta bursts detected in the RSC (star), and beta oscillations across the cortex, averaged across all beta bursts in all wild-type (left) and J20 mice (right). Beta oscillations are highly synchronous across the entire RSC during beta bursts in both genotypes, however in J20 mice there appears to be a loss of synchrony outside the RSC. D. Graph showing the peak lag between RSC beta bursts and beta oscillations in all cortical regions, averaged across all beta bursts in all wild-type (black) and J20 mice (green). During retrosplenial beta bursts in wild-type mice, beta oscillations were synchronous across all cortical regions (Frontal: $p = 0.1$; Somatosensory: $p = 0.143$; Parietal: $p = 0.7$; Retrosplenial: $p = 0.3$). During retrosplenial beta bursts in J20 mice, beta oscillations in the parietal cortex were significantly asynchronous ($p = 0.05$). (Data shown as mean ± SEM, WT: n = 3, J20: n = 3).

5.4 Discussion

5.4.1 Summary

The aim of this study was to investigate oscillatory activity in a range of cortical regions in response to contextual novelty, and compare this to the neurophysiological correlates of novelty previously demonstrated in the retrosplenial cortex in Chapter 3. Furthermore, we interrogated beta bursting activity in a number of cortical areas, in order to determine whether beta bursting is ubiquitous across the cortex, or specific to the retrosplenial cortex. Finally, the inclusion of J20 mice in this study allowed us to determine whether the aberrant oscillatory activity in the retrosplenial cortex of these mice described in Chapter 3 is limited to this region, or part of a larger generalised cortical dysfunction.

5.4.2 Power Spectral Analysis

Power spectral analysis was performed in order to investigate oscillatory activity across a range of frequency bands, between wild-type and J20 mice. In order to investigate the effect of novelty, spectral power was compared between the first minute and final 10 minutes of the session because, as we have shown in Chapters 3 and 4, oscillatory responses to contextual novelty peak within the first minute after exposure to the environment and rapidly diminish. Power spectra from these EEG recordings reveal a broadband attenuation of spectral power compared to power spectra from LFP recordings. Furthermore, heat maps of power in each frequency band reveal a gradient in power across the cortex, with higher power at the rostral end of the cortex, and lower power at the caudal end. The cause of this gradient is unclear, and while it is possible that this is due to the design of these probes, and suggestive of weaker adhesion of channels close to the connector, a similar gradient has been shown by Lee et al. (2011) despite

using different probes with the connector at the caudal end. There was no significant effect of novelty on beta power in the retrosplenial cortex, which is at odds with the results from our local field potential study, in which beta power is increased during novelty, and higher overall in J20 mice. There are a number of possible reasons for discrepancies between these two studies, for this analysis and all others. Firstly, Chapters 3 and 4 involved multiple recording sessions, so it is possible that repeated exposure to familiar environments solidifies the experience far more than previously considered. Additionally, the use of multi-trial design allowed averaging across multiple novel and familiar sessions, reducing variability. It is important to note that the group sizes in this study were far smaller in this study, further increasing variability, and reducing statistical power.

Beta power was significantly higher during novelty in the somatosensory cortex in J20 mice, but not wild-type mice, and in the frontal cortex, beta power was significantly higher overall in J20 mice. Beta power has been previously shown to decrease in the somatosensory cortex during tactile stimulus perception (van Ede and Maris, 2013; Shin et al., 2017), however it is important to note that many human EEG studies have demonstrated that somatosensory beta oscillations are closely associated with motor functions, and as such it is difficult to disentangle these two processes (Zhang et al., 2008; Engel and Fries, 2010; van Ede and Maris, 2013). This trend towards increased beta power in J20 mice, as well as a trend towards higher power in the 30-50 Hz range, mirrors the results seen in the Chapter 3 and suggests that this may be a broadly cortical phenomenon. Previous work by Palop et al. (2007) and Verret et al. (2012) has shown aberrant neuronal network activity across the neocortex in J20 mice, however these

appeared to be epileptiform in nature, while we found no evidence of overt epileptiform activity in these mice.

5.4.3 Beta Bursting Activity

We were able to detect beta bursts across the whole cortex, and in wild-type mice the total number of beta bursts detected was generally consistent across all cortical regions. This result supports previous studies demonstrating transient beta oscillations in a range of cortical areas, and supports the idea that beta oscillations are a broad cortical phenomenon which underlie a variety of functions depending on their location (Leventhal et al., 2012; Feingold et al., 2015; Shin et al., 2017). In J20 mice, beta burst detection appeared to be increased across the cortex, but especially over the retrosplenial cortex, which is consistent with our findings in Chapter 3 showing overall increased beta burst detection in the retrosplenial cortex in J20 mice. This pattern of increased beta bursting specifically around the retrosplenial cortex seems to mirror the pattern of amyloid plaque density in J20 mice demonstrated by Whitesell et al. (2019), where relative plaque density was highest in the retrosplenial cortex and adjacent areas.

In order to investigate the relationship between contextual novelty and beta bursting across the cortex, we compared the beta burst rate during the first minute and last 10 minutes of the session. In wild-type mice, the rate of beta bursting appeared to be higher during the novel part of the session compared to the familiar part of the session, especially in the retrosplenial cortex, with an approximate 3-fold increase in retrosplenial beta burst rate during novelty, however this difference was not significant. While this result could be attributed to low statistical power due to small sample sizes in this study, it is important to note that while similar numbers of beta bursts were detected overall in the

retrosplenial cortex in this study and in Chapter 3, the difference between initial and final burst rate was far more pronounced in the previous chapter. During novel sessions, initial burst rate was around 18 times higher than final burst rate in the dysgranular retrosplenial cortex, and around 12 times higher than final burst rate in the granular retrosplenial cortex.

These results support the assertation by us, and others (Shin et al., 2017), that cortical beta oscillations appear as transient bursts, which may not be apparent in averaged data. This data indicates that beta bursts can be detected ubiquitously across the cortex, but that contextual novelty-associated beta bursting is relatively specific to the retrosplenial cortex, suggesting that the role of beta bursts in this brain region is related to the processing of contextual information.

5.4.4 Beta Bursting Characteristics

As we have shown, beta bursts can be detected across the cortex. It was therefore of interest to investigate the characteristics of these beta bursts, to determine the degree of similarity between beta bursts in the retrosplenial cortex, and those in other cortical regions. There was a significant effect of region on beta burst magnitude, with beta bursts in the retrosplenial cortex being significantly smaller in magnitude than their frontal counterparts. This decrease in beta burst magnitude from rostral to caudal channels perfectly mirrored the gradient in spectral power seen earlier in this chapter, and as before, it is unclear whether the cause of this is a true biological gradient, or a technical anomaly resulting from poor channel adhesion. Due to the nature of burst detection algorithm, it is possible that reduced beta burst magnitude may result in a decreased signal-to-noise ratio in the beta band, thus decreasing overall beta

burst detection. It is also of note that there appeared to be a trend towards increased beta burst magnitude across the cortex in J20 mice, mirroring the increased retrosplenial beta burst magnitude seen in Chapter 3. There was no significant effect of genotype on beta burst duration, again mirroring the results from the retrosplenial cortex in Chapter 3.

As before, spectral analysis was performed on beta burst and pre-burst epochs, in order to investigate the frequency profile of beta bursts, and determine whether this is consistent across the cortex. Beta bursts across the cortex were associated with a significant increase in beta power, that peaked around 25 Hz. Furthermore, this sharp increase in power was generally limited to the 20-30 Hz beta band, therefore supporting these frequencies as the beta band, and also supporting the naming of these transient oscillations as beta bursts.

The striking consistency of beta burst characteristics across the cortex suggests that the mechanisms underlying the generation of beta bursts are generally similar between different cortical areas, despite vast differences in anatomical connectivity between these regions. This supports the idea that beta bursts are generated locally within the cortex, and suggests that it is changes in the rate of beta bursting that supports their varying functions within different cortical regions (Shin et al., 2017).

5.4.5 Burst Cross Correlation

Beta bursts can be detected throughout the cortex, and beta burst characteristics are generally consistent between different cortical areas, however the temporal relationship between beta oscillations in these different regions has yet to be shown. In order to investigate the extent of spatio-temporal correlations between retrosplenial beta bursts and beta oscillations throughout the cortex, we

performed cross-correlation analysis between beta bursts detected in the retrosplenial cortex, and time-locked beta filtered signals from all other recording sites. In wild-type mice, beta oscillations were highly correlated across the cortex during retrosplenial beta bursts, with average peak correlation coefficients greater than 0.8 throughout the cortex. Furthermore, during retrosplenial beta bursts, beta oscillations were synchronous throughout the cortex. In J20 mice, beta oscillations appeared to be less correlated across the cortex during beta bursts, with a significant decrease in retrosplenial-somatosensory burst cross-correlation compared to wild-type mice, and beta oscillations were less synchronous, with significant asynchrony in the parietal cortex. These results mirror those seen between the retrosplenial cortex and hippocampus in Chapter 4, with a trend towards reduced correlation and reduced synchrony between beta oscillations in the retrosplenial cortex and hippocampus during retrosplenial beta bursts and may underlie the reduced beta functional connectivity that has been demonstrated in human EEG studies of individuals with Alzheimer's disease (Stam et al., 2007; Briels et al., 2020).

Taken together, beta bursts are transient epochs of high beta amplitude and rhythmicity, and facilitate brief periods of high beta synchrony throughout the cortex. We have previously demonstrated that beta bursts are associated with increased neuronal spiking in the retrosplenial cortex (Chapter 4). The retrosplenial cortex has been shown to encode contextual information, so beta bursts may serve to transiently activate these same neuronal ensembles in order to form cortical representations (Czajkowski et al., 2014). Synchronous beta oscillations between cortical areas could facilitate the formation of cortical representations, through simultaneous activation of disparate neuronal

populations, and by providing temporal windows of high functional connectivity between distant brain regions.

5.4.6 Experimental Design

It is worth noting that combination of the low sample sizes in this study, in combination with the single-trial design of the novel/familiar environment task greatly reduced the statistical power of this study. These were the unfortunate consequences of issues we had with the stability of implants in a couple of our mice, which necessitated termination of these animals, and early termination of these experiments, after only a single recording session had been completed. While we were still able to obtain a great deal of valuable data from this study despite these issues, future experiments would entail larger sample sizes, and the same multi-trial version of the novel/familiar environment task used in Chapters 3 and 4.

5.4.7 Conclusions

In conclusion, we have demonstrated that beta bursts can be detected across the cortex, that beta burst characteristics are highly consistent between cortical regions, and that beta oscillations are highly correlated and highly synchronous across the cortex during in the retrosplenial beta bursts. These results provide valuable insight into the potential mechanisms underlying beta burst generation and support our hypothesised role of beta bursting throughout the cortex during contextual novelty. Finally, we have demonstrated that neurophysiological changes seen in the retrosplenial cortex of J20 mice in Chapter 3 can be found throughout the cortex, suggesting a broader cortical dysfunction in this strain, and that reduced beta cross-correlation and synchrony across the cortex during beta

bursts may underlie reduced beta functional connectivity in human Alzheimer's disease (Stam et al., 2007; Briels et al., 2020).

6 Chapter 6

6.1 Introduction

Throughout this thesis, we have demonstrated that beta bursts occur across the brain, with a high degree of similarity regarding features such as duration and frequency profile. Many previous studies have demonstrated bursts of beta oscillations within the brain (Leventhal et al., 2012; Feingold et al., 2015; Shin et al., 2017), and even more have described that beta oscillations appear transient (Berke et al., 2008; França et al., 2014). The mechanisms underlying beta bursting are unclear, although numerous mathematical modelling and in vitro studies have provided a number of insights. Mechanisms underlying beta oscillations have been suggested to be similar to those underlying gamma oscillations, with a reliance on networks of interneurons to generate such high-frequency oscillations , with a variable involvement of excitatory neurons depending on brain region (for review, see Bartos et al., 2007; Spitzer and Haegens, 2017). Spontaneous beta oscillations in the CA3 in hippocampal slices were shown to be insensitive to the NMDA receptor antagonist (2R)-amino-5-phosphonovaleric acid (APV), but blocked by antagonists at GABA receptors (Treviño et al., 2007). A mathematical model of networks of GABAergic interneurons of the striatum, known as medium spiny neurons, suggested that interactions between GABA currents and M-currents promotes beta oscillations, which is enhanced by cholinergic signalling and suppressed by dopamine (McCarthy et al., 2011). Infusion of the cholinergic agonist carbachol into the striatum of awake mice was sufficient to induce beta oscillations, supporting these claims, and reduced dopamine signalling in Parkinson's Disease has been shown to underlie pathological beta bursting in this disease (Sharott et al., 2005), likely

due to the disinhibition of striatal acetylcholine release (DeBoer et al., 1996). Cholinergic agonists have been shown to induce beta oscillations in the cortex (Kilb and Luhmann, 2003), and hippocampus *in vitro* (Shimono et al., 2000; Arai and Natsume, 2006). Furthermore the beta oscillations shown by Arai and Natsume (2006) were transient in nature, similar to our findings *in vivo.* These results suggest that acetylcholine signalling can induce beta bursting in the hippocampus and retrosplenial cortex, and microdialysis studies have demonstrated that acetylcholine release is increased in both the hippocampus and frontal cortex during contextual novelty (Aloisi et al., 1997; Giovannini et al., 2001), further supporting this hypothesis. In this study, we aimed to pharmacologically induce beta bursting in the retrosplenial cortex *in vitro*, in order to further understand the mechanisms underlying beta bursting in the retrosplenial cortex. Furthermore, in order to attempt to elucidate the mechanisms underlying aberrant beta bursting in the retrosplenial cortex and hippocamps of J20 mice, we compared pharmacologically-induced beta bursting in brain slices from wild-type and J20 mice. In this Chapter, we demonstrate that continuous application of the cholinergic agonist carbachol is sufficient to induce rhythmic bursts of beta oscillations in the retrosplenial cortex that are strikingly similar to those seen *in vivo* in Chapter 3. Moreover, carbachol-induced beta bursting in slices from J20 mice was indistinguishable from beta bursting in slices from wild-type mice, indicating that external factors are responsible for aberrant beta bursting in these mice. These data demonstrate that carbachol-induced beta bursting is a valuable *in vitro* assay for further investigations into mechanisms underlying beta bursting.

6.2 Methods

6.2.1 Slice Preparation

Mice were killed by cervical dislocation and their brains were immediately removed and transferred to ice-cold sucrose solution (~4 °C). The cerebellum and frontal cortex were removed and 400 µm thick coronal slices were cut in the same ice-cold sucrose solution, using a Leica VT1200 vibratome (Leica). With reference to (Paxinos and Franklin, 2012), four consecutive slices were chosen that spanned the region 1.3 to 2.4 mm posterior from bregma (Figure 6.1b). Slices were transferred to oxygenated artificial cerebrospinal fluid (aCSF), hemisected, before being transferred to a Haas Top incubation chamber (Warner Instruments), where slices were continuously perfused with the same aCSF at approximately 37 °C for a minimum of 30 minutes until ready for use. Each slice was transferred to the recording interface chamber and left to equilibrate for a minimum of 30 minutes before use. All mice were between 8 to 10 months of age at the time of termination.

6.2.2 Data Collection

Continuous extracellular recordings were made using a single glass pipette filled with aCSF, and the experimental protocol was kept consistent from experiment to experiment (Figure 6.1c). Data was amplified using an AxoClamp-2A (Axon Instruments), amplified and bandpass filtered between 1 Hz and 1.3 kHz by a LHBF-48X (npi Electronic Instruments), and line noise was removed using a HumBug Noise Eliminator (Quest Scientific). Finally, the signal was digitised at 2 kHz by using a PCIe6341 (National Instruments) and acquired and visualised on MATLAB using the WaveSurfer application (Adam, 2021). Data was stored and analysed offline.

6.2.3 Experimental Protocol

After the slice had equilibrated, the electrode was placed in the deep layers of the granular retrosplenial cortex and a 10-minute baseline was recorded. After this, 25 µM carbachol was continuously applied to the bath, which usually took around 5 minutes to begin to take effect. The recording was then continued for 35 minutes, post administration of carbachol, during which time the network effects had plateaued. The recording was then stopped and the electrode transferred to the superficial layers of the granular retrosplenial cortex (Figure 6.1b) and 10 minutes of data was recorded. This protocol allowed us to record from the deep and shallow layers of the retrosplenial cortex within the same slice, but precluded baseline recordings from the superficial layers of the retrosplenial cortex.

6.2.4 Solutions

Sucrose solution was composed of: 189 mM sucrose, 26 mM $NaHCO_3$, 10 mM D-glucose, 5 mM $MgSO_4$, 3 mM KCl, 1.25 mM NaH_2PO_4 and 0.1 mM $CaCl_2$. aCSF was composed of 124 mM NaCl, 24 mM $NaHCO_3$, 10 mM D-glucose, 3 mM KCl, 1.2 mM $CaCl_2$ and 1 mM $MgSO_4$.

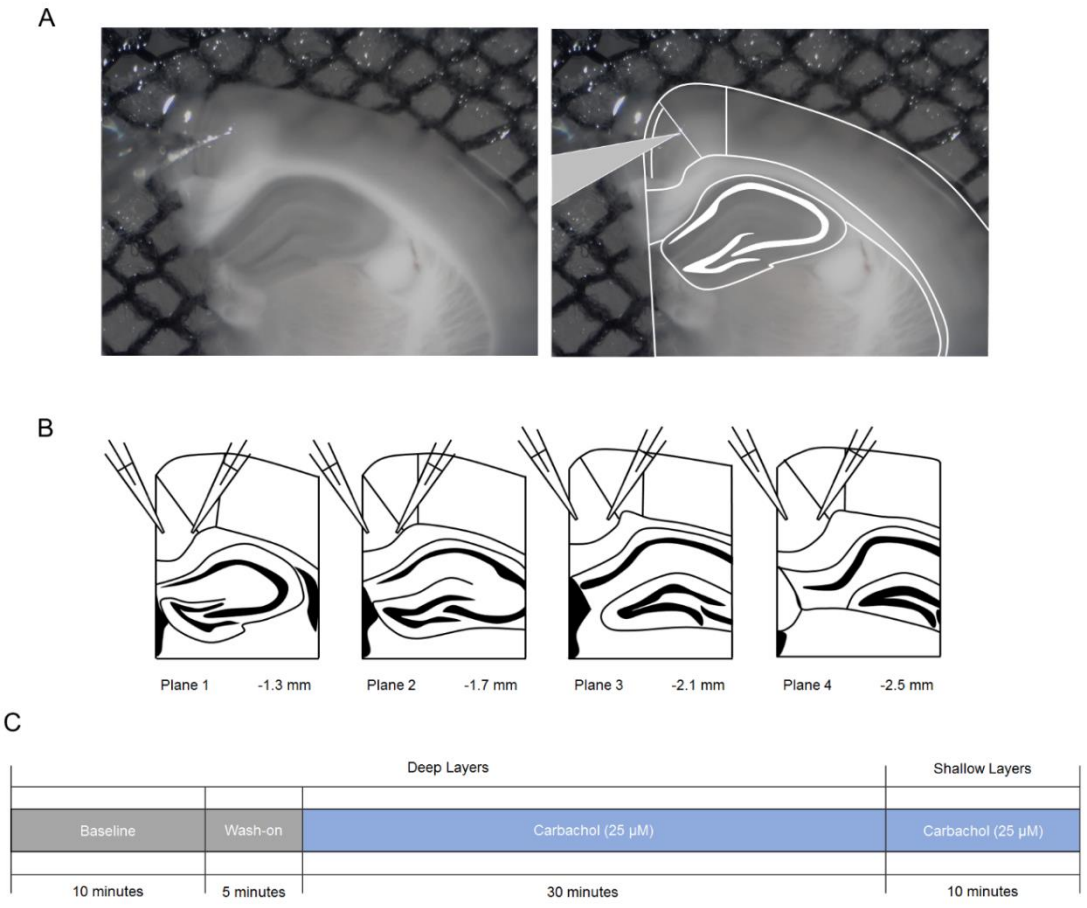

Figure 6.1 Experimental Design.
A. Example photomicrograph of the recording setup (left), and the same photogram with key features highlighted (right). A single glass recording electrode was placed in the deep layers (shown) or shallow layers of the granular retrosplenial cortex. Layer 2/3 is clearly visible in the granular retrosplenial cortex, making consistent electrode placement possible. In order to record from the deep layers, electrodes were placed near the edge of the cingulum bundle, as indicated by the light patch above the corpus callosum. B. Four consecutive slices were chosen, in order to investigate potential changes in network activity across the rostro-caudal axis of the retrosplenial cortex. The approximate distances from bregma are given, and the electrode locations are shown for each plane. C. The general recording protocol consisted of a 10-minute baseline, with the slice in aCSF and the electrode in the deep layers of the granular retrosplenial cortex, following which 25 µM carbachol was washed on. This wash-on period lasted around 5 minutes, after which the effect of the carbachol on the activity of the slice became clear. Carbachol was washed on for 30 minutes, by which time the network activity would generally plateau, and then the electrode was moved to the shallow layers for another 10-minute recording. This design allows us to record from both deep and shallow layers within the same slice, but does not provide us a baseline recording for shallow layers of the retrosplenial cortex.

6.3 Results

In this study, we aimed to find a means of pharmacologically induce beta bursting in the retrosplenial cortex *in vitro*, in order to develop an assay which could be used to probe the potential mechanisms underlying the generation of beta bursts. To this end, we performed a number of brain slice electrophysiology experiments, where we took continuous extracellular recordings from the retrosplenial cortex, in the presence, and absence of different pharmacological compounds. The region of the retrosplenial cortex chosen was used as it encompassed the region 2 mm posterior from bregma where our *in vivo* local field potential recordings were performed in Chapter 3. Furthermore, the benefit of keeping slicing planes consistent between experiments was twofold. Firstly, we aimed to reduce variability which could arise from differences in recording location, and secondly, this allowed us to investigate whether there were differences in oscillatory activity across this rostro-caudal axis. As we have shown in Chapter 3, our EEG recordings show a gradient of decreasing spectral power from the rostral end of the retrosplenial cortex to the caudal end. As previously mentioned, we were unable to determine whether this was biological, or an experimental artefact due to poor adhesion of these electrodes to the skull. By investigating oscillatory activity across multiple rostro-caudal planes, we hoped to answer this question, and others. We chose to record from the granular retrosplenial cortex as the location of this subregion deep within the longitudinal fissure between hemispheres meant that the superficial layers of this region were likely to be better preserved during the removal and slicing of the brain. In each slice we also recorded from both the deep, and shallow layers of the retrosplenial cortex, around layer 2/3 and layer 5/6 respectively, in order to compare oscillatory activity

between these layers. In Chapter 3, we recorded from the deep layers of the granular retrosplenial cortex, and due to the vertical placement of our recording probes, these probes were likely running parallel to the layers of this subregion, allowing us to only sample from around layer 5/6. By recording from across the layers of the granular retrosplenial cortex, we were able to compare our findings to our *in vivo* findings from Chapter 3, and investigate network activity in the superficial layers of the retrosplenial cortex for the first time. As we have shown throughout this thesis, we have noted significant increases in the rate and magnitude of beta bursts in the retrosplenial cortex of J20 mice, compared to their wild-type counterparts. In order to attempt to understand the underlying cause of this aberrant oscillatory activity, be they structural or otherwise, we performed these experiments in J20 mice, and wild-type controls.

We performed a range of analyses, to investigate whether beta oscillations could be pharmacologically induced in vitro, including spectral analysis and beta burst detection. We aimed to keep these analyses as similar as possible to those used *in vivo*, in order to directly compare the results of these studies and to maintain consistency. This was made possible by careful design of our analysis functions, such as beta burst detection algorithms with variable thresholding.

6.3.1 Retrosplenial Spectral Activity *In Vitro*

A number of previous studies have demonstrated that the muscarinic acetylcholine receptor agonist carbachol is sufficient to induce beta oscillations in the hippocampus and across the cortex (Shimono et al., 2000; Kilb and Luhmann, 2003; Arai and Natsume, 2006). In order to investigate the effects of carbachol on oscillatory activity in the retrosplenial cortex in brain slices, power spectral analysis was performed for both deep, and shallow electrode sites. For

deep layers, spectral analysis was performed on the entire 10-minute baseline period, and the final 10 minutes of the 30-minute drug period, in order to capture the oscillatory activity at the point by which this had plateaued. As shallow layer drug recordings were performed immediately after deep layer drug recordings, the activity in the slice would already have plateaued, so 10-minute recordings were sufficient to capture peak oscillatory activity. Therefore, for shallow layers, spectral analysis was performed on the entire 10-minute drug period. For all depths and planes, power spectra were averaged across all experiments, for both wild-type and J20 mice (Figure 6.2).

As expected, in the absence of carbachol, local field potentials from the deep layers of the retrosplenial cortex showed no notable oscillatory activity in any plane, as indicated by almost perfectly flat power spectra (Figure 6.2a). In the presence of carbachol, there appeared to be a substantial increase in power across all frequency bands, peaking at around 7 Hz, for all depths and planes (Figure 6.2). We investigated the effect of slice plane and genotype on carbachol-induced oscillatory power in a range of frequency bands, for both deep and shallow recordings, separately. In deep layers, there was a significant overall effect of plane on theta power (Main Effect Plane - $F(3,75) = 2.8$, $p = 0.05$, Two-Way ANOVA). In J20 slices, theta power was significantly higher in Plane 2 than in Planes 1 and 3 (Plane 2: 24.3 ± 2.2 dB, Plane 1: 15.1 ± 3 dB, $p = 0.01$; Plane 2: 24.3 ± 2.2 dB, Plane 3: 14.9 ± 2 dB, $p = 0.002$). Power in every frequency band was significantly higher overall in J20 slices than in wild-type slices (Delta: Main Effect Genotype - $F(1,75) = 19$, $p = 4e\text{-}5$, Two-Way ANOVA; Theta: Main Effect Genotype - $F(1,75) = 13$, $p = 5e\text{-}4$, Two-Way ANOVA; Alpha: Main Effect Genotype - $F(1,75) = 67$, $p = 0.01$, Two-Way ANOVA; Beta: Main Effect Genotype

- F(1,75) = 6.5, p = 0.01, Two-Way ANOVA; Gamma: Main Effect Genotype - F(1,75) = 7.4, p = 0.008, Two-Way ANOVA). In shallow layers, there was no significant effect of genotype or plane on power in any frequency band.

These power spectra demonstrate that carbachol induces a broadband increase in spectral power in the retrosplenial cortex *in* vitro, that peaks in the theta range (5-12 Hz). While beta power appears to increase upon exposure to carbachol, there does not appear to be a specific peak in the beta frequency range, which could clearly indicate the induction of beta bursting. However, as we have previously shown from *in vivo* hippocampal LFP and cortical EEG data (Chapter 3 and Chapter 4), beta bursting can appear in the absence of overt changes to beta power in averaged power spectra, due to their sparse, phasic nature. As shown in (Figure 6.3b), in the absence of carbachol beta oscillations in the deep layers of the retrosplenial cortex appear low in amplitude, and with variable rhythmicity, similar to beta oscillations during non-burst epochs *in vivo*. However, upon administration of carbachol, brief epochs of high beta amplitude and high beta rhythmicity can be seen (Figure 6.3c). Wavelet analysis of the data shown in (Figure 6.3d), demonstrated that this transient high amplitude epoch of beta oscillations appeared similar to beta bursts detected *in vivo*, with high power in the beta band (20-30 Hz) that lasted around 150 milliseconds. This data indicates that administration of carbachol is sufficient to induce beta bursts in the retrosplenial cortex, and allows us to further investigate this phenomenon *in vitro*.

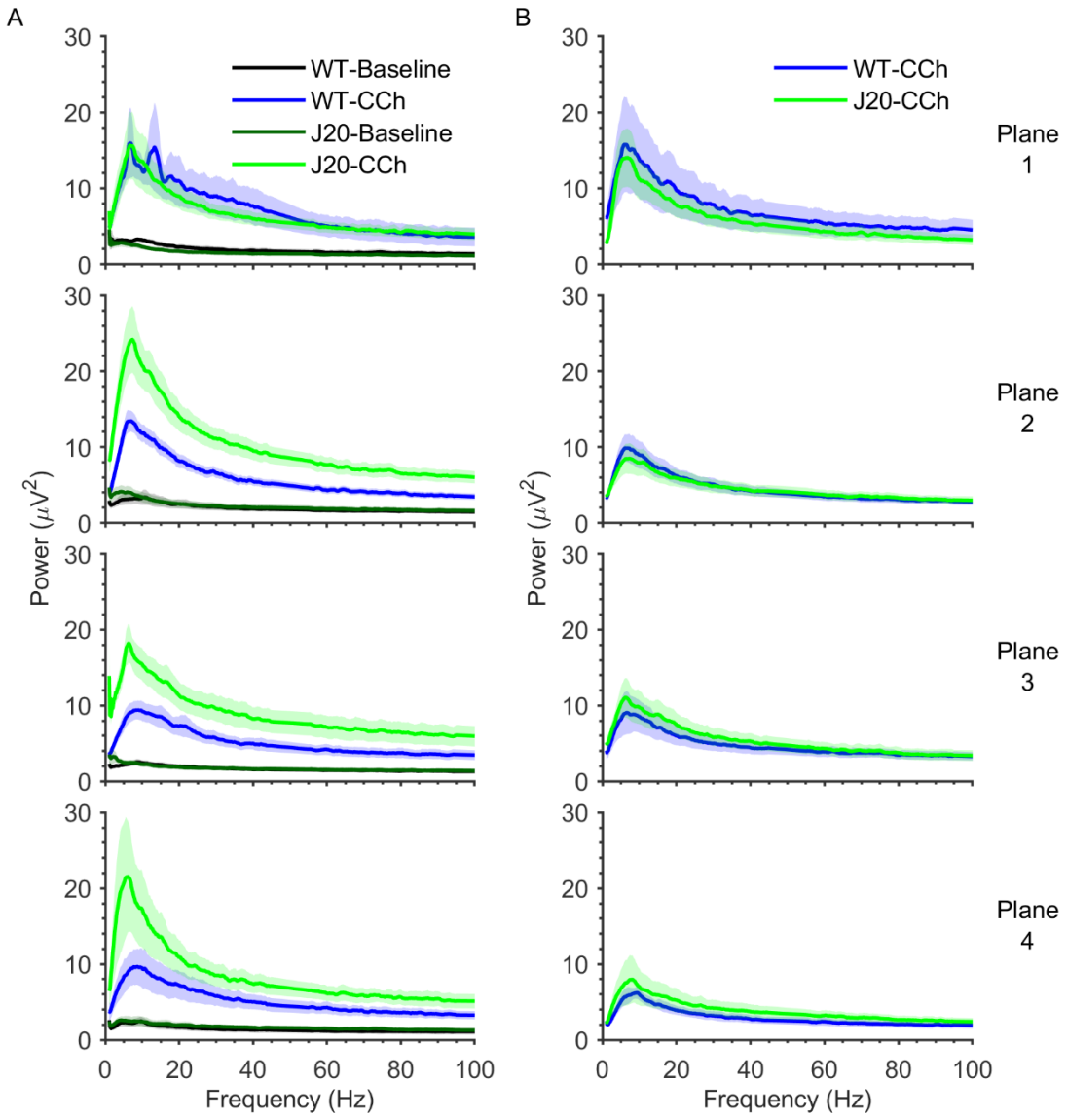

Figure 6.2 Carbachol induced a broadband increase in spectral power that peaked around 7 Hz.

A. Average baseline and carbachol-induced power spectra for deep layer recordings, across all planes, for both wild-type and J20 slices. In J20 slices, theta power was significantly higher in Plane 2 than in Planes 1 and 3 ($p = 0.01$, $p = 0.002$, respectively). Furthermore, power in every frequency band was significantly higher overall in J20 slices than in wild-type slices (Delta: $p = 4e\text{-}5$; Theta: $p = 5e\text{-}4$; Alpha: $p = 0.01$; Beta: $p = 0.01$; Gamma: $p = 0.008$). B. Average carbachol-induced power spectra for shallow layer recordings, across all planes, for both wild-type and J20 slices. There was no significant effect of genotype or plane on power in any frequency band. (Data shown as mean ± SEM; Deep-WT: Plane 1: n = 5, Plane 2: n = 14, Plane 3: n = 9, Plane 4: n = 4; Deep-J20: Plane 1: n = 6, Plane 2: n = 10, Plane 3: n = 11, Plane 4: n = 5; Shallow-WT: Plane 1: n = 4, Plane 2: n = 9, Plane 3: n = 9, Plane 4: n = 4; Shallow-J20: Plane 1: n = 7, Plane 2: n = 10, Plane 3: n = 8, Plane 4: n = 6).

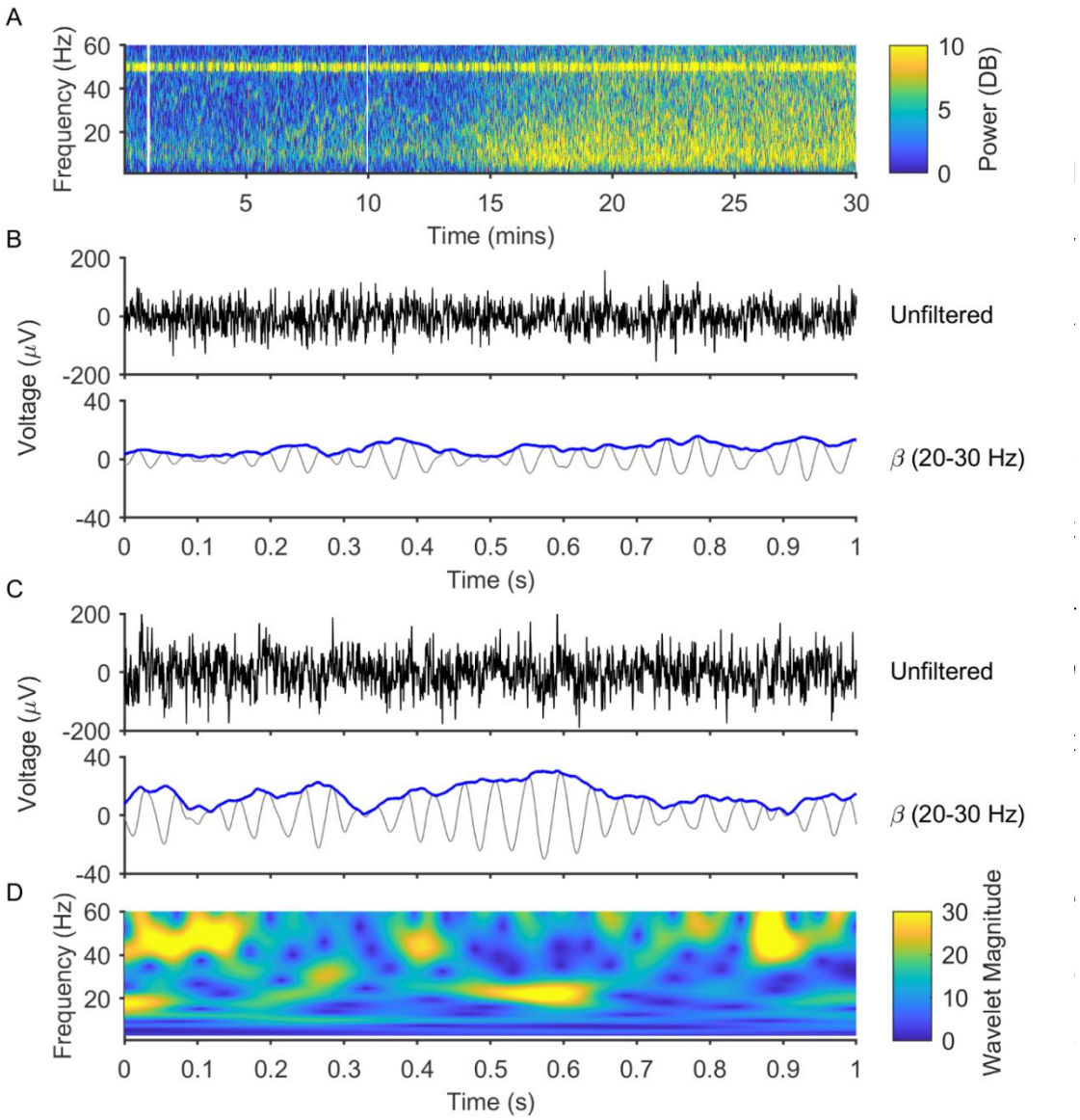

Figure 6.3 Carbachol induces transient epochs of high beta power and beta rhythmicity in the retrosplenial cortex in vitro, that are reminiscent of beta bursts.

A. Example power spectrogram for an entire recording session, from deep layers of granular retrosplenial cortex in a wild-type brain (slice plane 1). Administration of carbachol (at 10 minutes, denoted by the white line) induces a broadband increase in spectral power that peaks around 7 Hz. B. Local field potential recordings from the baseline period of the data shown in A, both unfiltered (top), and filtered in the beta band (bottom), with the envelope amplitude in blue for clarity. Beta amplitude and rhythmicity are low in the absence of carbachol. C. Local field potential recordings from the carbachol-on period of the data shown in A, both unfiltered (top), and filtered in the beta band (bottom), with the envelope amplitude shown in blue for clarity. In the presence of carbachol, transient increases in beta amplitude and rhythmicity appear in the local field potential. D. Wavelet spectrogram of the data shown in C, demonstrating the phasic nature of these beta oscillations, that persist for approximately 100-200 ms.

cortex in J20 mice. In order to determine the effect of carbachol on beta bursting *in vitro*, we investigated the rate of beta bursting in the absence and presence of carbachol, in both wild-type and J20 mice (Figure 6.4 and Figure 6.5). In both deep, and shallow layers of the retrosplenial cortex, carbachol induces a relatively steady rate of beta bursting, as shown by the relatively linear cumulative frequency plots shown in (Figure 6.4 and Figure 6.5, respectively). In the deep layers of the retrosplenial cortex, carbachol significantly increased the rate of beta bursting, compared to baseline (Main Effect Condition - $F(1,131) = 169$, $p = 2e\text{-}25$, 3-Way ANOVA), however there was no significant effect of genotype or plane on beta burst rate (Figure 6.4). In the shallow layers of the retrosplenial cortex, carbachol induced a significant rate of beta bursting (Main Effect Condition - $F(1,96) = 358$, $p = 3e\text{-}34$, 3-Way ANOVA), however there was no significant effect of genotype or plane on beta burst rate (Figure 6.5).

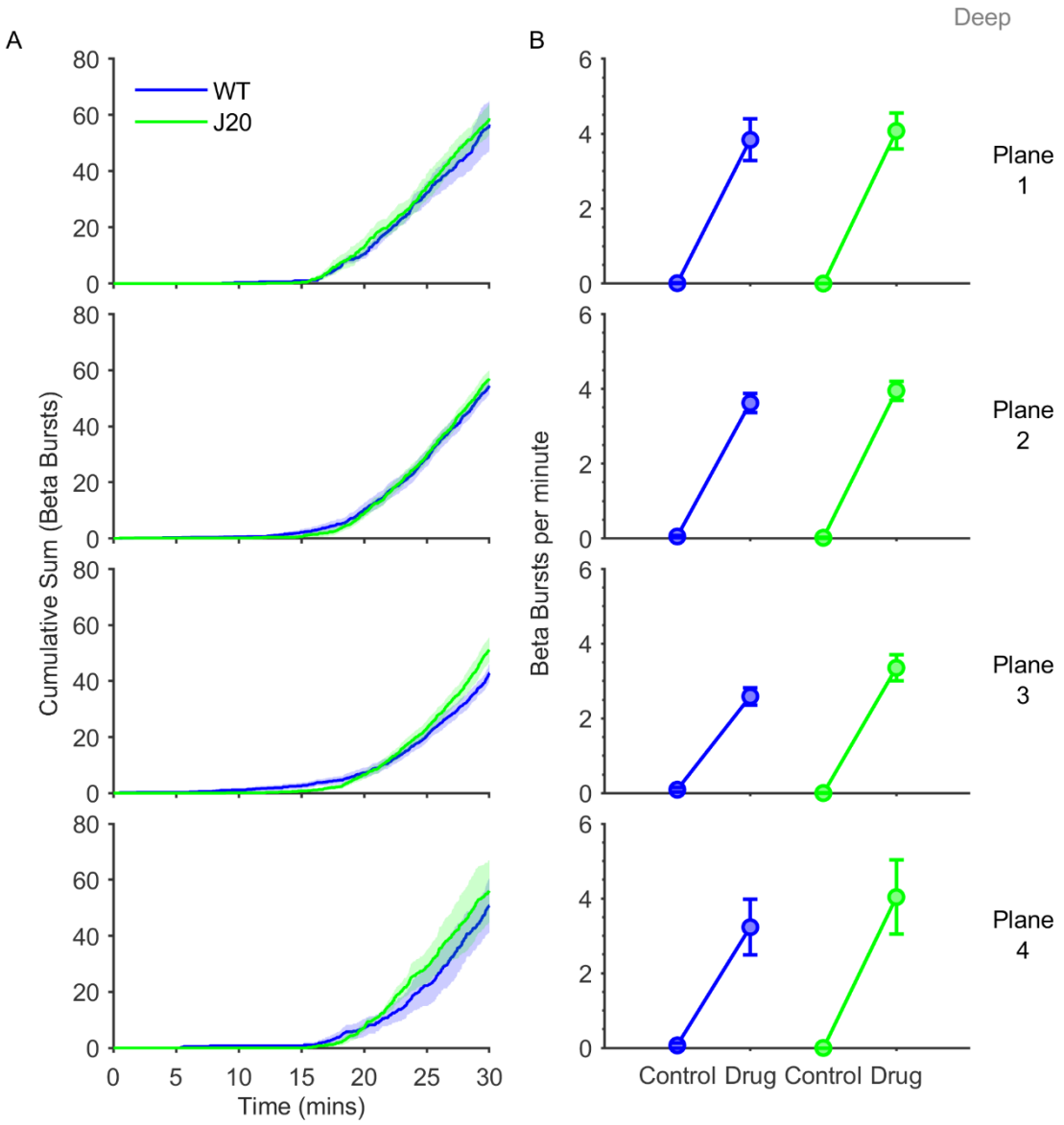

Figure 6.4 Beta burst distribution and rate in the deep layers of the retrosplenial cortex in vitro.
A. Cumulative frequency graphs of beta bursts detected during the recording session in the deep layers of the retrosplenial cortex, for each slice plane, averaged across all experiments for both wild-type and J20 slices. Carbachol induces a steady rate of beta bursting that persists for the entire session, in all slice planes, for both wild-type and J20 slices. In the absence of carbachol, beta bursts do not spontaneously occur. B. Graphs showing the average beta burst rate in the deep layers of the retrosplenial cortex, in the absence and presence of carbachol (control and drug respectively), for all slice planes, for wild-type and J20 slices. Carbachol significantly increased the rate of beta bursting ($p = 2e\text{-}25$), however there was no significant effect of genotype or plane on beta burst rate. (Data shown as mean ± SEM; Deep-WT: Plane 1: n = 5, Plane 2: n = 17, Plane 3: n = 15, Plane 4: n = 5; Deep-J20: Plane 1: n = 7, Plane 2: n = 13, Plane 3: n = 15, Plane 4: n = 6).

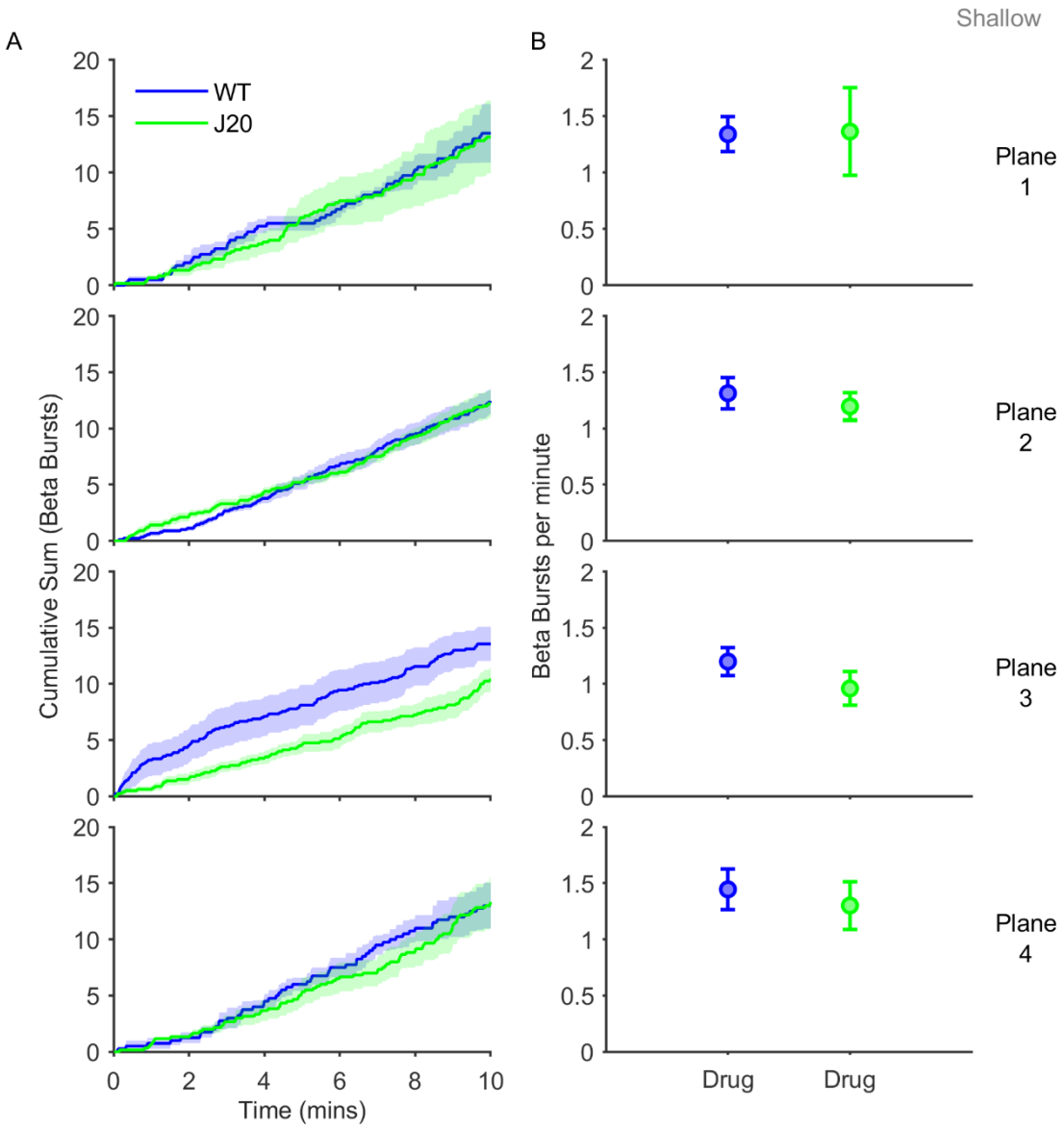

Figure 6.5 Beta burst distribution and rate in the shallow layers of the retrosplenial cortex in vitro.
A. Cumulative frequency graphs of beta bursts detected during the recording session in the shallow layers of the retrosplenial cortex, for each slice plane, averaged across all experiments for both wild-type and J20 slices. In the presence of carbachol (the entire 10 minutes shown), there is a steady rate of beta bursting in all slice planes, for both wild-type and J20 slices. B. Graphs showing the average beta burst rate in the shallow layers of the retrosplenial cortex, in the absence and presence of carbachol (control and drug respectively), for all slice planes, for wild-type and J20 slices. Carbachol significantly increased the rate of beta bursting compared to zero ($p = 3e-34$), however there was no significant effect of genotype or plane on beta burst rate. (Data shown as mean ± SEM, Shallow-WT: Plane 1: n = 4, Plane 2: n = 9, Plane 3: n = 9, Plane 4: n = 4; Shallow-J20: Plane 1: n = 6, Plane 2: n = 10, Plane 3: n = 8, Plane 4: n = 6).

6.3.3 Retrosplenial Beta Burst Characteristics *In Vitro*

In order to compare carbachol-induced beta bursts *in vitro* to spontaneous beta bursts *in vivo*, a number of beta burst characteristics were investigated in the deep (Figure 6.6) and shallow layers of the retrosplenial cortex (Figure 6.7). Moreover, as we have previously shown in Chapter 3, specific beta burst characteristics vary between wild-type and J20 mice. By investigating beta burst characteristics in the retrosplenial cortex in brain slices from J20 mice, and comparing them to the changes we see *in vivo*, we may better understand the source of aberrant beta bursting in these animals. There was no significant effect of genotype or plane on total number of beta bursts detected in either the deep (Figure 6.6a), or shallow layers of the retrosplenial cortex (Figure 6.7a). Beta bursts were significantly larger in magnitude overall in J20 slices in the deep layers of the retrosplenial cortex (Main Effect Genotype - $F(1,75) = 6$, $p = 0.01$, Two-Way ANOVA, Figure 6.6b), but not in the shallow layers (Figure 6.7b). There was no significant effect of genotype or plane on beta burst duration in either the deep (Figure 6.6c), or the shallow layers of the retrosplenial cortex (Figure 6.7c).

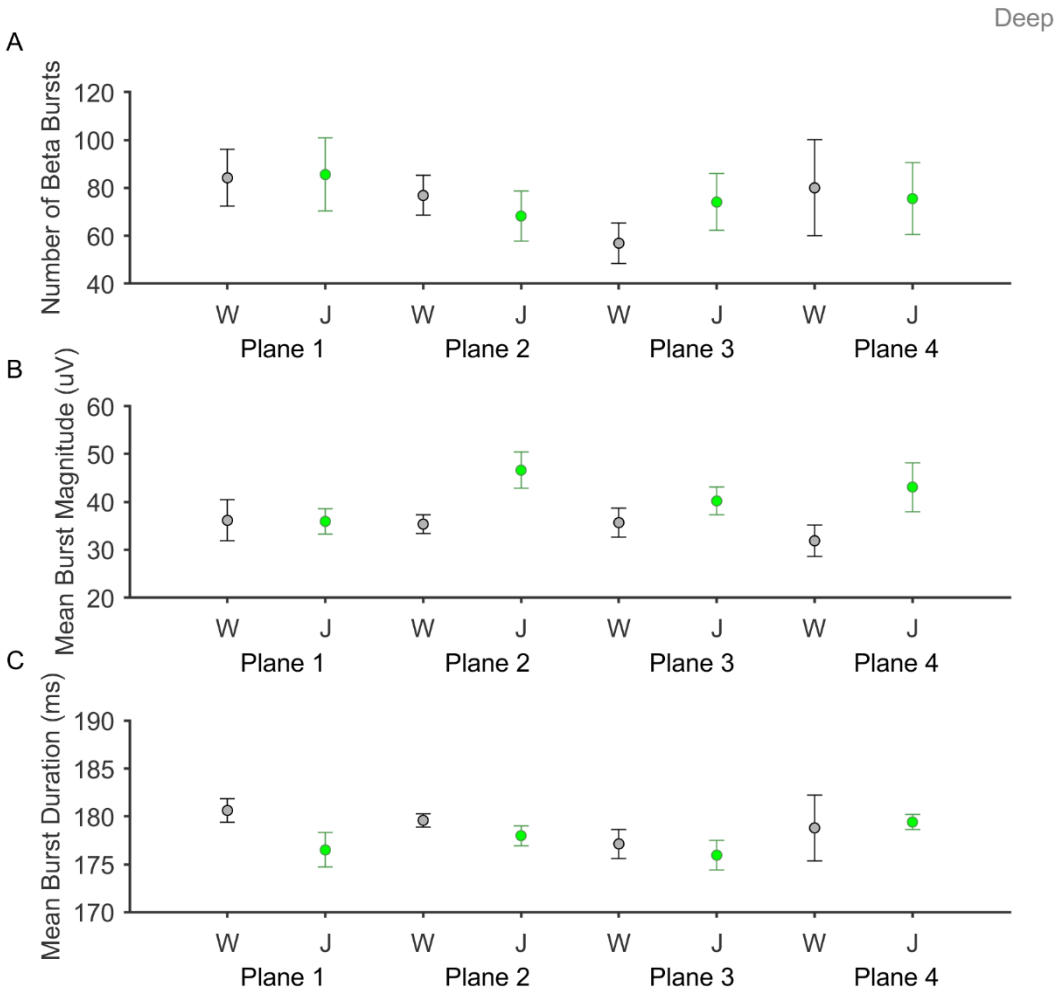

Figure 6.6 Beta burst number, magnitude and duration in the deep layers of the retrosplenial cortex in vitro.
A. Graph showing the average number of beta bursts detected in the deep layers of the retrosplenial cortex, in all slice planes for wild-type (black) and J20 slices (green). There was no significant effect of genotype or plane on the total number of beta bursts detected. B. Graph showing the average magnitude of beta bursts detected in the deep layers of the retrosplenial cortex, in all slice planes for wild-type (black) and J20 slices (green). Overall, beta bursts were significantly larger in magnitude in J20 slices ($p = 0.01$). C. Graph showing the average duration of beta bursts detected in the deep layers of the retrosplenial cortex, in all slice planes for wild-type (black) and J20 slices (green). There was no significant effect of genotype or plane on beta burst duration. (Data shown as mean ± SEM; Deep-WT: Plane 1: n = 5, Plane 2: n = 17, Plane 3: n = 15, Plane 4: n = 5; Deep-J20: Plane 1: n = 7, Plane 2: n = 13, Plane 3: n = 15, Plane 4: n = 6).

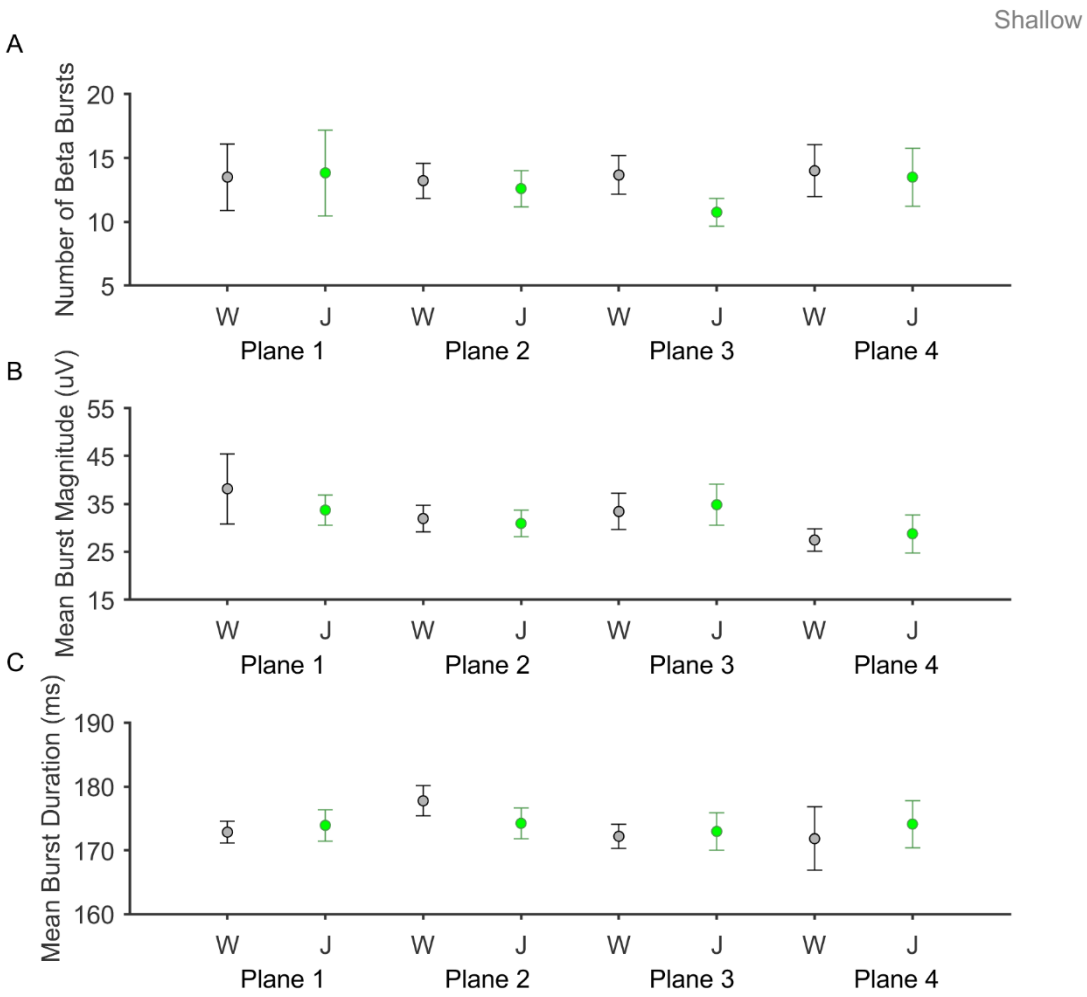

Figure 6.7 Beta burst number, magnitude and duration in the shallow layers of the retrosplenial cortex in vitro.
A. Graph showing the average number of beta bursts detected in the shallow layers of the retrosplenial cortex, in all slice planes for wild-type (black) and J20 slices (green). There was no significant effect of genotype or plane on the total number of beta bursts detected. B. Graph showing the average magnitude of beta bursts detected in the shallow layers of the retrosplenial cortex, in all slice planes for wild-type (black) and J20 slices (green). There was no significant effect of genotype or plane on the beta burst magnitude. C. Graph showing the average duration of beta bursts detected in the shallow layers of the retrosplenial cortex, in all slice planes for wild-type (black) and J20 slices (green). There was no significant effect of genotype or plane on beta burst duration. (Data shown as mean ± SEM, Shallow-WT: Plane 1: n = 4, Plane 2: n = 9, Plane 3: n = 9, Plane 4: n = 4; Shallow-J20: Plane 1: n = 6, Plane 2: n = 10, Plane 3: n = 8, Plane 4: n = 6)

In order to investigate the frequency profile of beta bursts *in vitro*, and compare it to the frequency profile of beta bursts *in vivo*, power spectral analysis was performed on individual beta bursts, and compared to epochs of equal length prior to immediately prior to each burst. As before, these power spectra were averaged across all bursts and "pre-burst" epochs, for each depth and plane, for both wild-type and J20 mice (Figure 6.8a and Figure 6.9a). In the deep layers of the retrosplenial cortex (Figure 6.8), beta bursts were associated with a significant increase in beta power for all slice planes (Plane 1: Main Effect Burst - $F(1,10) = 738$, $p = 1e\text{-}10$, Mixed ANOVA; Plane 2: Main Effect Burst - $F(1,28) = 1282$, $p = 6e\text{-}25$, Mixed ANOVA; Plane 3: Main Effect Burst - $F(1,28) = 2576$, $p = 4\ e\text{-}29$, Mixed ANOVA; Plane 4: Main Effect Burst - $F(1,9) = 458$, $p = 5e\text{-}9$, Mixed ANOVA). Additionally, in the deep layers of Plane 2 there was a significant interaction between the effects of genotype and burst on alpha power (Interaction - $F(1,28) = 6$, $p = 0.02$, Mixed ANOVA), and a significant increase in gamma power during beta bursts (Main Effect Novelty - $F(1,28) = 4.9$, $p = 0.03$, Mixed ANOVA). Furthermore, in the deep layers of Plane 2, delta, theta, beta and gamma power were significantly higher overall in J20 mice (Delta: Main Effect Genotype - $F(1,28) = 9.6$, $p = 0.004$, Mixed ANOVA; Theta: Main Effect Genotype - $F(1,28) = 7.3$, $p = 0.01$, Mixed ANOVA; Beta: Main Effect Genotype - $F(1,28) = 9.3$, $p = 0.005$, Mixed ANOVA; Gamma: Main Effect Genotype - $F(1,28) = 8.1$, $p = 0.008$, Mixed ANOVA). In the shallow layers of the retrosplenial cortex (Figure 6.9), beta bursts were associated with a significant increase in beta power for all slice planes (Plane 1: Main Effect Burst - $F(1,8) = 243$, $p = 3e\text{-}7$, Mixed ANOVA; Plane 2: Main Effect Burst - $F(1,17) = 1010$, $p = 1e\text{-}16$, Mixed ANOVA; Plane 3: Main Effect Burst - $F(1,15) = 607$, $p = 2e\text{-}13$, Mixed ANOVA; Plane 4: Main Effect Burst - $F(1,8) = 606$, $p = 8e\text{-}9$, Mixed ANOVA). Additionally, beta bursts in the

shallow layers of Planes 2 and 4 were associated with significantly higher delta power (Plane 2: Main Effect Burst - $F(1,17) = 4.8$, $p = 0.04$, Mixed ANOVA; Plane 4: Main Effect Burst - $F(1,8) = 5.4$, $p = 0.05$, Mixed ANOVA), while beta bursts in the shallow layers of Plane 3 were associated with a significant decrease in gamma power (Main Effect Novelty - $F(1,15) = 6.9$, $p = 0.02$, Mixed ANOVA). There were significant interactions between genotype and burst on alpha power in Plane 1 (Interaction - $F(1,8) = 5.6$, $p = 0.05$, Mixed ANOVA) and theta power in Plane 3 (Interaction - $F(1,15) = 5.4$, $p = 0.04$, Mixed ANOVA). Finally, there was no significant effect of genotype on power in any frequency band.

As before, in order to verify that beta bursts *in vitro* were associated with increased beta rhythmicity, the period of beta oscillations was calculated for all beta bursts and all epochs without beta bursts, and the distribution of these beta periods was calculated and averaged across all burst and non-burst epochs, for each depth and plane, for both wild-type and J20 mice (Figure 6.8b and Figure 6.9b). As before, while the distribution of beta periods during beta bursts was reasonably consistent, generally peaking around 0.04s, equivalent to a 25 Hz oscillation, the distribution of beta periods in non-burst epochs was far more variable, which is suggestive of reduced beta rhythmicity during non-burst epochs, although interpretation of this analysis is limited (for limitations of this analysis see Chapter 3).

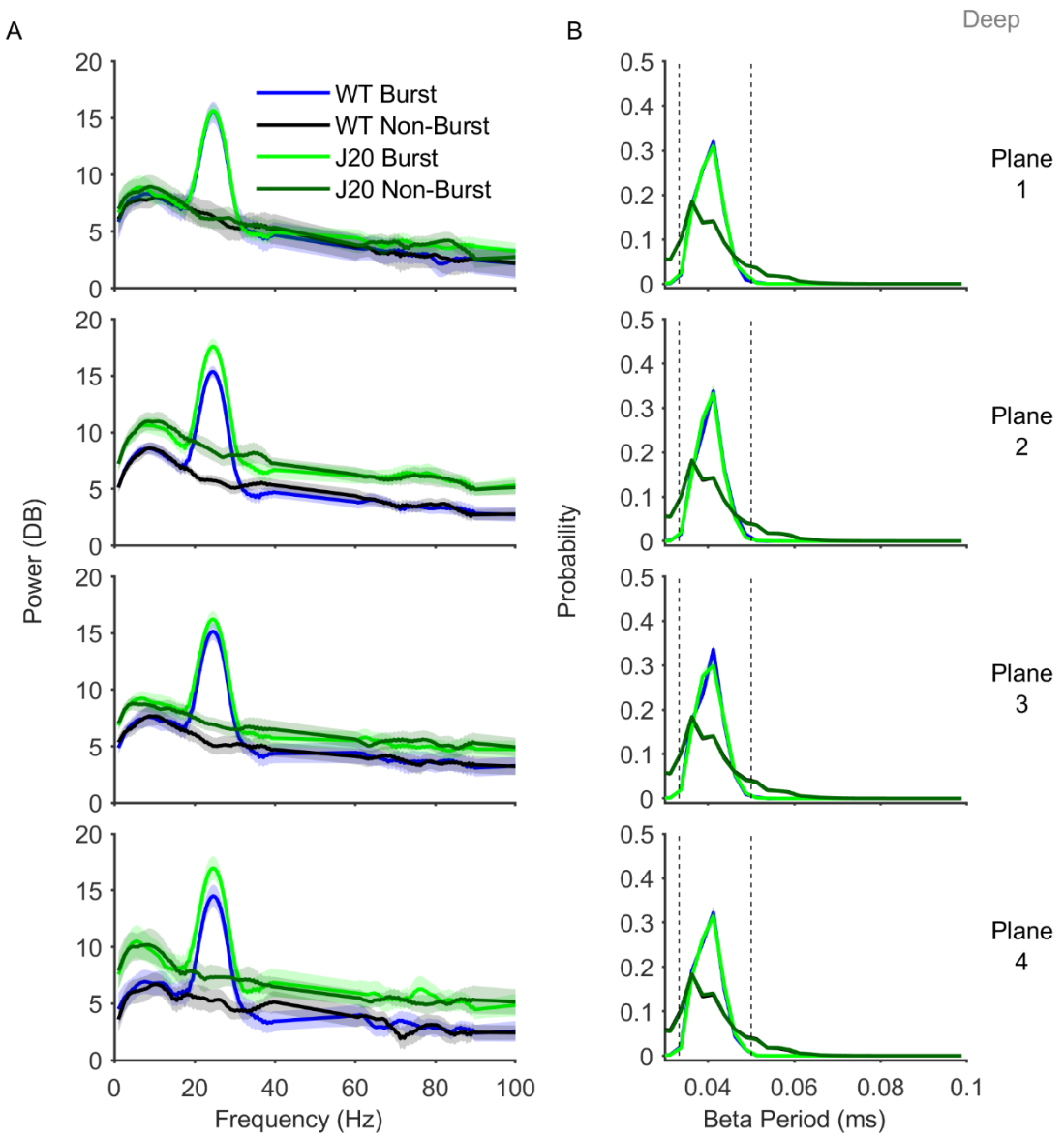

Figure 6.8 Beta burst frequency profile and rhythmicity in the deep layers of the retrosplenial cortex in vitro.
A. Average power spectra for beta burst and pre-burst epochs, in all slice planes, averaged across all wild-type and J20 slices. Beta bursts in the deep layers of the retrosplenial cortex are associated with a large, significant increase in beta power in all slice planes (Plane 1: p = 1e-10; Plane 2: p = 6e-25; Plane 3: p = 4 e-29; Plane 4: p = 5e-9). B. Average distributions of beta oscillation period for burst and non-burst epochs in the deep layers of the retrosplenial cortex, for all slice planes, averaged across all wild-type and J20 slices. Beta oscillations are tightly rhythmic during beta bursts, but not during non-burst epochs. (Data shown as mean ± SEM; Deep-WT: Plane 1: n = 5, Plane 2: n = 17, Plane 3: n = 15, Plane 4: n = 5; Deep-J20: Plane 1: n = 7, Plane 2: n = 13, Plane 3: n = 15, Plane 4: n = 6).

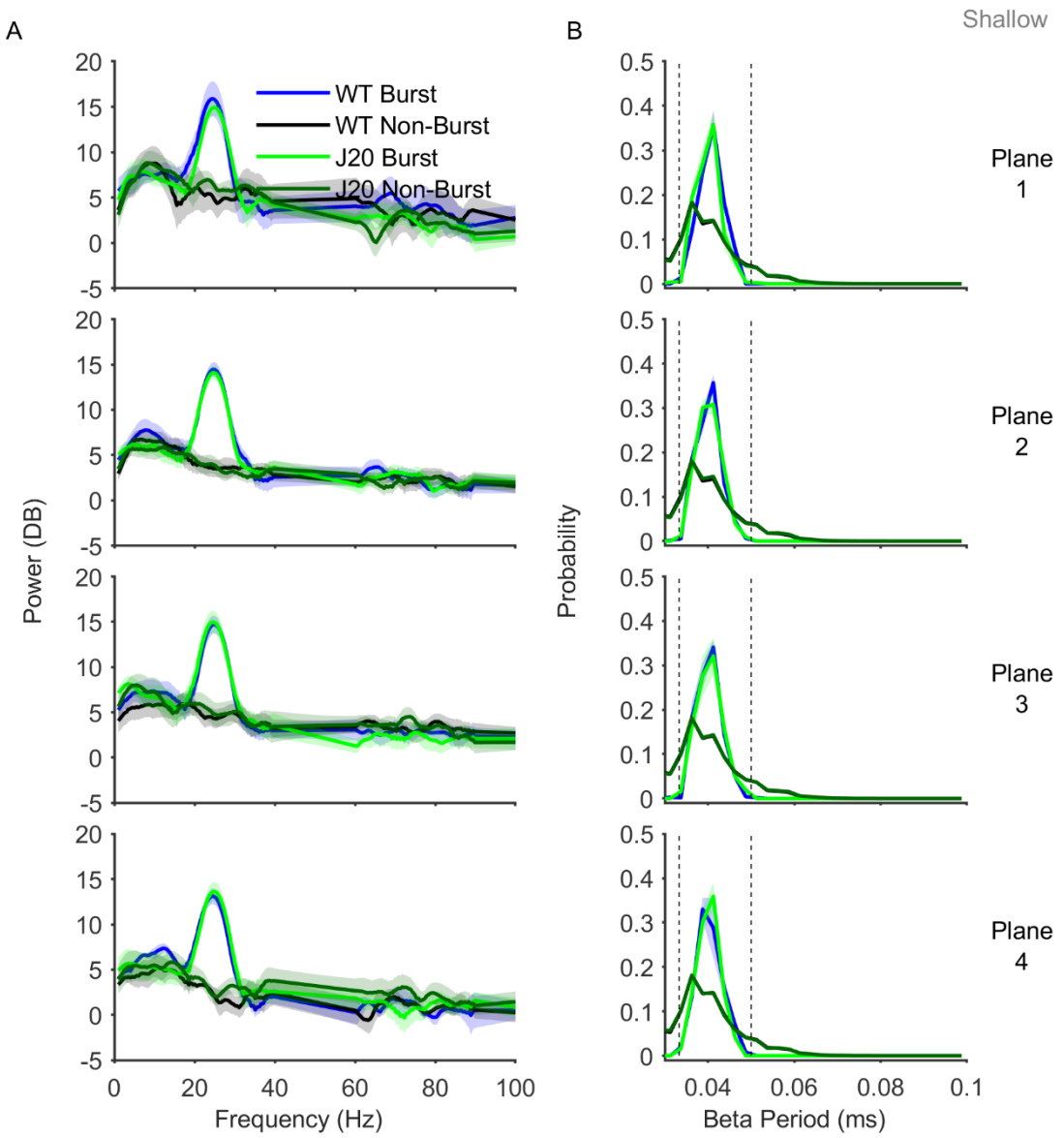

Figure 6.9 Beta burst frequency profile and rhythmicity in the shallow layers of the retrosplenial cortex in vitro.
A. Average power spectra for beta burst and pre-burst epochs, in all slice planes, averaged across all wild-type and J20 slices. Beta bursts in the shallow layers of the retrosplenial cortex are associated with a large, significant increase in beta power in all slice planes (Plane 1: p = 3e-7; Plane 2: p = 1e-16; Plane 3: p = 2e-13; Plane 4: p = 8e-9). B. Average distributions of beta oscillation period for burst and non-burst epochs in the shallow layers of the retrosplenial cortex, for all slice planes, averaged across all wild-type and J20 slices. Beta oscillations are tightly rhythmic during beta bursts, but not during non-burst epochs. (Data shown as mean ± SEM, Shallow-WT: Plane 1: n = 4, Plane 2: n = 9, Plane 3: n = 9, Plane 4: n = 4; Shallow-J20: Plane 1: n = 6, Plane 2: n = 10, Plane 3: n = 8, Plane 4: n = 6).

6.4 Discussion

6.4.1 Summary

The aim of this study was to attempt to pharmacologically induce beta oscillations in the retrosplenial cortex *in vitro*, in order to gain some insight into the potential mechanisms that underlie this oscillatory activity, including potential neurotransmitters or neuronal populations. By comparing oscillatory activity across the rostro-caudal axis of the retrosplenial cortex, and between deep and shallow layers, we aimed to interrogate the spatial patterns of beta bursting we have previously demonstrated in this region. Finally, we investigated oscillatory activity in J20 mice, in order to determine whether the aberrant neuronal network activity seen in the cortex and hippocampus of these mice *in vivo* is recapitulated *in vitro*, so that we could better understand the potential causes of this dysfunction.

6.4.2 Power Spectral Analysis

Power spectral analysis was performed in order to investigate oscillatory activity in the deep and shallow layers of the retrosplenial cortex *in vitro*. Additionally, spectral analysis was performed during each experiment, in order to verify that slices were viable and healthy and ensure that noise was at a minimum. In the absence of carbachol, there was no noticeable oscillatory activity in the retrosplenial cortex. Administration of carbachol resulted in a broadband increase in spectral power, peaking at theta frequency (7 Hz), which was consistent across all slice planes and probe depths, in both wild-type and J20 slices. It is well established that carbachol and other cholinergic agonists are able to induce theta oscillations in the hippocampus and cortex *in vitro*, and that this theta oscillation is similar to theta oscillations seen *in vivo* (Konopacki et al., 1987; Lévesque et

al., 2017). Furthermore, direct infusion of carbachol to the stratum oriens of the hippocampus of rats under urethane anaesthesia elicits theta oscillations (Rowntree and Bland, 1986). Lesions of the medial septum and diagonal band of Broca have been shown to completely abolish theta oscillations in both the hippocampus and cortex (Petsche et al., 1962; Kolb and Whishaw, 1977; Rawlins et al., 1979). These data together support our finding that cholinergic agonism alone is sufficient to generate theta oscillations in vitro, although it is important to note that the theta peak in the retrosplenial cortex *in vitro* is far broader than we have seen *in vivo*. In the deep layers of the retrosplenial cortex, there was a significant increase in power in every frequency band in slices from J20 mice, compared to slices from wild-type mice. Similar increases in power were seen in the retrosplenial cortex of J20 mice *in vivo* in Chapter 3, although this increase was limited to alpha and beta frequency bands, as opposed to a large increase across all frequency bands. Increased spectral power in the retrosplenial *in vivo* could result from a number of causes, and could be driven by changes in the activity of any number of regions that project to the retrosplenial cortex, however *in vitro*, many of these connections have been severed, which raise the possibility that the cause of cortical hyperexcitability in these mice may be local. Previous work in this strain has demonstrated that aberrant cortical network activity in this strain is associated with interneuron dysfunction in the parietal cortex, due to reduced expression of the voltage-gated sodium channel Nav1.1 (Verret et al., 2012). Furthermore, application of nanomolar concentrations of soluble amyloid-β to mouse brain slices is sufficient to induce hyperexcitability of pyramidal cells in the cingulate cortex by reducing inhibition by fast-spiking interneurons (Ren et al., 2018). It is therefore possible that increased broadband activity in the retrosplenial cortex in J20 mice may be indicative of cortical hyperexcitability,

arising from disinhibition due to interneuron dysfunction. Interestingly, in the shallow layers of the retrosplenial cortex there was no such increased power.

6.4.3 Beta Bursting Activity

The main aim of this study was to investigate whether it was possible to pharmacologically induce beta bursting in the retrosplenial cortex *in vitro*. While power spectral analysis indicated a significant increase in beta power upon administration of carbachol, power spectra failed to consistently show a peak in the beta frequency range similar to what is seen *in vivo* (Chapters 3 and 5). However, as we have shown in the hippocampus and in EEG recordings, sparse, transient beta bursting can have little to no effect on power spectra averaged across long time periods. As such, we detected carbachol-induced beta bursting throughout the retrosplenial cortex *in vitro*. In intact cerebral cortex preparations from new-born rats, carbachol has been shown to induce transient beta oscillations which propagate across the cortex (Kilb and Luhmann, 2003). Carbachol has also been shown to induce beta oscillations in hippocampal slices (Shimono et al., 2000). The amplitude of these oscillations was largest in the apical dendrites of the CA1 and CA3, where the medial septum cholinergic projections have been shown to terminate (Houser et al., 1983). Furthermore, work by Arai and Natsume (2006) built on these findings, by demonstrating that carbachol-induced beta oscillations in the CA3 region of the hippocampus appears as rhythmic bursts, with consistent duration and inter-burst interval. These data suggest that cholinergic signalling may underlie the generation of beta oscillations in the cortex and hippocampus. Additionally, the appearance of beta oscillations in the cortex in brain slices, where subcortical inputs have been severed, argues against theories that cortical beta oscillations originate in the

basal ganglia or striatum (Holgado et al., 2010; McCarthy et al., 2011). The retrosplenial cortex receives cholinergic projections from a number of basal forebrain nuclei including the medial septum and diagonal band of Broca (Shute and Lewis, 1967; Eckenstein et al., 1988; Gage et al., 1994). These projections, along with numerous other subcortical projections, form the cingulum bundle, which travels along the length of the brain to supply the cingulate cortex, and subsequently the retrosplenial cortex (for review, see Bubb et al., 2018). As shown in (Figure 6.1a), the cingulum bundle is visible in coronal slices, as a light-coloured area found close to the deep layers of the retrosplenial cortex, directly above the corpus callosum. Some cholinergic projections to the retrosplenial cortex travel through the fornix, which is also known to be the pathway by which cholinergic medial septum neurons project to the hippocampus, with dense axon terminals in stratum oriens (Houser et al., 1983; Gage et al., 1994). It is of key importance that in this study, and in previous work in slices, beta oscillations appear as rhythmic bursts, despite carbachol being administered continuously, which provides a number of insights into the mechanisms underlying beta bursting (Shimono et al., 2000; Kilb and Luhmann, 2003; Arai and Natsume, 2006). Firstly, that beta oscillations occur as spontaneous and rhythmic “bursts”, even in brain slices, suggests that beta oscillations naturally occur as bursts, and that there is no central pacemaker for the timing of beta bursts. Previous work has suggested that beta bursts may arise from synchronous bursts of excitatory activity at the proximal and distal dendrites of pyramidal neurons, and in a computational model, continuous proximal and distal drive at 10 Hz was sufficient to produce beta bursts (Sherman et al., 2016). This second finding could explain the strong phase-amplitude coupling we have seen between theta (5-12 Hz) and beta oscillations in the retrosplenial cortex (Chapter 3).

One notable finding in our data was that there was no significant difference between the rate of beta bursting in slices from the brains of wild-type and J20 mice. This was reasonably surprising given the substantial increases in beta burst rate in the granular retrosplenial cortex of J20 mice that we have previously shown. In Chapter 3, we demonstrated that beta burst rate in the granular retrosplenial cortex increases dramatically during environmental novelty, and was only significantly higher in J20 mice during familiar sessions, and the final parts of novel sessions. This led us to suggest that perhaps there is a theoretical "maximum beta burst rate" that is being reached during periods of intense beta bursting in novelty, or that there are different mechanisms underlying the different rates of beta bursting during novelty and familiarity. Similar rates of carbachol-induced beta bursting in the retrosplenial cortex between wild-type and J20 slice *in vitro* could therefore indicate that carbachol-induced beta bursting is equivalent to the novelty-associated beta bursting seen *in vivo*. Acetylcholine release has been shown to increase significantly in the hippocampus and cortex in rats during exploration of a novel environment, so it is possible that carbachol in this experiment is mimicking the natural increase in cholinergic signalling during contextual novelty (Giovannini et al., 2001).

6.4.4 Beta Bursting Characteristics

We have demonstrated that carbachol induces beta bursting in the retrosplenial cortex *in vitro*, however it was of interest to determine how similar these beta bursts were to those detected *in vivo*, and whether these beta burst characteristics varied depending on genotype or location. Beta bursts were significantly larger in magnitude overall in J20 slices compared to wild-type slices, but only in the deep layers of the retrosplenial cortex. This result recapitulates the

increased beta burst magnitude seen in J20 mice *in vivo* in Chapter 3, and suggests that the underlying cause of this change is located in the retrosplenial cortex. It is of note that the broadband increase in spectral power in the retrosplenial cortex in J20 mice was also limited to the deep layers of the retrosplenial cortex, indicating some layer specificity of this cortical hyperexcitability phenotype. The underlying cause of this is uncertain, but may arise from the inhibitory interneuron dysfunction previously demonstrated in this line (Palop et al., 2007; Verret et al., 2012). Another alternative hypothesis could be related to cholinergic signalling in the retrosplenial cortex. As we have previously mentioned, the cingulum bundle is a significant source of cholinergic projections to the retrosplenial cortex (Bubb et al., 2018), so it is possible that increased densities of acetylcholine receptors in the deep layers of the retrosplenial cortex could make this region more sensitive to the effects of carbachol. The magnitude of beta bursts *in vitro* (~40 µV) was far lower than *in vivo* (~80 µV). This is to be expected, as previous work has demonstrated that carbachol-induced beta oscillations were far smaller in amplitude and far lower in frequency in coronal slices than in *in vitro* whole-brain preparations, suggesting that beta oscillations involve large cortical networks, and that the loss of cortico-cortical connectivity in brain slices attenuates these oscillations (Kilb and Luhmann, 2003).

On average, the duration of beta bursts *in vitro* (~180 ms) was strikingly similar to the duration of beta bursts *in vivo* (~180 ms), as was the frequency profile. This suggests that carbachol-induced beta bursts are characteristically similar to beta bursts *in vivo* and are therefore a valid model for beta bursting, but also supports our previous assertions that beta oscillations naturally occur as bursts within the

cortex, and that the mechanism underlying the time course of these beta bursts is maintained *in vitro*.

6.4.5 Conclusions

In conclusion, we have demonstrated that beta bursts can be induced in the retrosplenial cortex *in vivo* upon administration of carbachol, an agonist at acetylcholine receptors, shown, for the first time, that these beta bursts are strikingly similar to those seen *in vivo,* with regards to temporal dynamics and features. These data provide a number of key insights into the mechanisms underlying beta bursting in the cortex and hippocampus and provides a valuable assay for further studying beta bursts across the brain in a model system. One such area of research is the effect of difference neurotransmitters of beta bursting activity. Work by Kondabolu et al. (2016) has suggested that pathological beta bursting seen in the motor cortex and basal ganglia in Parkinson's disease is merely an aberration from normal cortico-striatal network activity, arising from the loss of dopamine signalling (Kondabolu et al., 2016; Tinkhauser et al., 2018). Dopamine has been shown to suppress the release of acetylcholine in the striatum, so a loss of dopamine signalling could result in excessive cholinergic signalling, which may enhance beta oscillatory activity (DeBoer et al., 1996; Ikarashi et al., 1997). Accordingly, dopamine depletion in rats results in increased beta power in the frontal cortex and basal forebrain, and increased beta coherence between these regions (Sharott, 2005). This assay provides a means to test the acute effects of different neurotransmitters such as dopamine, and learn more about that pathophysiology of Parkinson's disease.

7 General Discussion

7.1 Key Findings

Throughout this thesis, we have described numerous discoveries which provide valuable insight into how a number of areas of the brain respond to contextual novelty. Furthermore, the findings in this study may be highly relevant to future research into Alzheimer's Disease and Parkinson's Disease, while providing functional assays for the testing of potential cognitive enhancing or disease modifying therapies. In this section, we will detail some of these findings, and discuss their potential implications.

7.2 Beta Bursting across the Brain

Throughout this thesis we have demonstrated that discrete "bursts" of beta oscillations, termed beta bursts, can be detected across the rodent cortex, and the hippocampus *in vivo*. In Chapters 3, 4 and 5, we demonstrated that beta bursts occur spontaneously throughout the brain during active waking in mice, and that this spontaneous beta bursting generally occurs at a steady rate. These beta bursts lasted between 170 and 180 milliseconds on average, which was consistent across all brain areas, even in the EEG recordings in Chapter 5. It is important to note that our beta burst detection algorithm had a minimum duration threshold of 150 milliseconds, so it is possible that beta bursts can be shorter than 150 milliseconds, and the beta bursts detected throughout these studies are on the longer end of this spectrum, although the low variability of beta burst duration in this study argues otherwise. The magnitude of beta bursts differed between the retrosplenial cortex and the hippocampus, although this is to be expected given the tight laminar structure of the hippocampal CA1 region, and

the looser laminar structure of the retrosplenial cortex. Notably, in EEG recordings, beta burst magnitude appeared to be consistent across the cortex. The consistency of these beta burst characteristics across the brain indicates that the beta bursts previously discovered across the cortex, and subcortical regions are one in the same, and that similar mechanisms underly beta bursting throughout the brain (Berke et al., 2008; Leventhal et al., 2012).

Beta bursts were associated with a significant increase in neuronal spiking in the dysgranular retrosplenial cortex, but not the granular retrosplenial cortex. Additionally, while there was a trend towards increased neuronal spiking during beta bursts in the hippocampus, this was not significant. Our analysis of neuronal spiking throughout this study was multi-unit activity, as due to the geometry of our probes we would be unable to reliably separate spikes from individual neurons, known as single units, using traditional spatiotemporal clustering methods (Quiroga et al., 2004). The putative multi-units in this study may include spiking from multiple different classes of neurons, which could have vastly different responses to beta bursts, which would greatly dilute the results. During sharp wave ripples, for example, spiking of neurons in the retrosplenial cortex varies dramatically between different neuronal subtypes or neurons in different cortical layers (Nitzan et al., 2020; Opalka et al., 2020). In order to better compare the effects of beta bursting on neuronal spiking across the retrosplenial cortex, it would therefore be optimal to record from neurons in the same cortical area in both subregions, and also to detect single units rather than multi-units.

The most notable aspect of beta bursting in this study was the dramatic effects of contextual novelty on beta bursting activity. During novel recording sessions, beta burst detection was significantly increased in the retrosplenial cortex and

hippocampus. Furthermore, while beta bursting occurred in the retrosplenial cortex and hippocampus at a steady rate during familiar sessions, during novel sessions, the rate of beta bursting was significantly higher during the first minute after exposure to the environment, resulting in the increased overall beta burst detection during novel sessions. This increase in beta bursting was considerable, with an approximate 10-fold increase in beta burst rate in the retrosplenial cortex and hippocampus during this initial part of the session. In Chapter 5, we demonstrate that while beta bursts could be detected across the cortex, this novelty-associated increase in beta bursting was absent, suggesting that this process is specific to brain regions involved in contextual learning and memory. Additionally, during novel sessions beta bursts were significantly larger in magnitude in both the retrosplenial cortex and the hippocampus, and significantly longer in duration in the retrosplenial cortex. Considering our findings that beta bursts are associated with increases in neuronal spiking, increases in beta burst magnitude could strengthen this modulation, or modulate a larger number of neurons. Furthermore, increases in beta burst duration could provide longer temporal windows for increased beta bursting, or longer windows for synchronous beta oscillations between distant brain regions, facilitating transient epochs of effective communication (Kilb and Luhmann, 2003).

Finally, through our beta burst cross-correlation analysis in Chapters 4 and 5, we demonstrated that during beta bursts in the retrosplenial cortex, beta oscillations are highly correlated and synchronous between the retrosplenial cortex and the hippocampus, and across the entire cortex. These results mirror previous findings which demonstrated that transient beta bursts occur synchronously across the cortex-basal ganglia network (Leventhal et al., 2012), and that extensive cortico-

cortical connections allow beta oscillations to propagate across the entire cortex (Kilb and Luhmann, 2003). One theory in cognitive neuroscience is that communication within the brain can occur through oscillatory synchrony. This “communication through coherence” would mean that transient epochs of high beta synchrony across the brain could therefore provide temporal windows of effective communication across large scale brain networks (Kopell et al., 2000; Varela et al., 2001; Fries, 2005, 2015).

7.3 Additional Functional Correlates of contextual novelty

In addition to the previously discussed findings regarding beta bursting, we also demonstrated a number of functional correlates of contextual novelty that were seemingly independent of, or unrelated to, beta bursting. In the retrosplenial cortex, we noted increases in gamma power during novelty. Power spectra reveal that this increased gamma power is generally in the 30 to 50 Hz frequency range. As this frequency range is adjacent to the beta band (20-30 Hz), at first glance this may appear as a result of frequency spill over from increased beta power due to increased beta bursting activity during novelty, however power spectral analysis revealed only marginal increases in gamma power during beta bursting. Numerous studies have demonstrated increases in cortical gamma power during memory encoding, and was predictive of successful memory encoding (Sederberg et al., 2003, 2007; Kahana, 2006; Jun et al., 2021). This suggests that the increased gamma power during novelty shown in this study, in particular during the first minute of novel sessions, may be indicative of contextual memory encoding in the retrosplenial cortex. While we have demonstrated throughout this thesis that beta oscillations conform to a model of discrete burst, the nature of gamma oscillations in this study was not investigated. Previous studies have

demonstrated that gamma oscillations appear as transient bursts as well, and that these gamma bursts have been associated with encoding and reactivation of sensory information (Lundqvist et al., 2016), however the amplitude of gamma oscillations can vary dramatically, especially when coupled to the phase of lower frequency oscillations such as theta (Canolty and Knight, 2010). This dynamic amplitude modulation could result in gamma oscillations appearing as discrete bursts (van Ede et al., 2018), so care should be taken to characterise these "gamma bursts" with the same rigour as we have characterised beta bursts in this study. In Chapters 3 and 5, we investigated phase-amplitude coupling across a range of frequencies, to investigate the extent of this cross-frequency coupling in the retrosplenial cortex and hippocampus, and to compare between the two. In this study, we identified two types of phase-amplitude coupling in the retrosplenial cortex and hippocampus: theta-alpha/beta and theta-gamma. Furthermore, while both forms were present in both areas, theta-alpha/beta coupling was dominant in the retrosplenial cortex, while theta-gamma coupling was dominant in the hippocampus. Theta-gamma coupling has been well extensively studied, and in the hippocampus, theta-gamma coupling is thought to support both memory encoding and retrieval (Colgin et al., 2009; Axmacher et al., 2010; Newman et al., 2013; Lega et al., 2016). As such, theta-gamma coupling was significantly higher during novel sessions in the hippocampus, but there was no effect of novelty on theta-gamma coupling in the retrosplenial cortex. Theta-alpha/beta coupling was significantly higher during novelty in both the retrosplenial cortex and the hippocampus. While theta-beta coupling is far less established within the field, theta-beta phase amplitude coupling has been demonstrated in the hippocampus and inferior temporal cortex during working memory and object novelty, respectively (Axmacher et al., 2010; Daume et al., 2017). Whether theta-

beta coupling has any connection to beta bursting is uncertain: our beta rhythmicity data indicate that beta bursts do not conform to a dynamic amplitude modulation model like gamma oscillations (Shin et al., 2017; van Ede et al., 2018), so it is unlikely that beta bursts are solely a product of theta-beta coupling. However one distinct possibility is that theta-beta phase amplitude coupling allows synchronous theta oscillations across large brain networks to modulate local beta oscillations, which could support the long distance beta synchrony demonstrated here and in previous studies (Canolty and Knight, 2010; Canolty et al., 2010; Leventhal et al., 2012).

Finally, in Chapter 4 coherence analysis and Granger causality analysis allowed us to investigate oscillatory interactions between the subregions of the retrosplenial cortex, and between the retrosplenial cortex and the hippocampus. Coherence between the retrosplenial cortex and the hippocampus was high, indicating high functional connectivity between these two brain regions. Furthermore, while retrosplenial-hippocampal delta coherence was increased during novel sessions, intra-retrosplenial delta coherence was increased during familiar sessions. While delta oscillations are generally associated with slow-wave sleep, these data suggest that they may be relevant during active wake than previously considered, and that dynamic changes in delta coherence may support different contextual memory processes within the cortex and hippocampus (Fries et al., 2008; Fujisawa and Buzsáki, 2011; Nacher et al., 2013). Interestingly, beta coherence between the retrosplenial cortex and hippocampus was significantly higher during novelty, while intra-retrosplenial beta coherence was unchanged. In combination with the burst cross-correlation analysis in Chapters 4 and 5, this suggests that while beta synchrony is a

persistent feature across the cortex, likely due to extensive cortico-cortical connectivity, beta synchrony can vary between the retrosplenial cortex and the hippocampus, potentially allowing gating of beta bursts.

7.4 Aberrant beta bursting in J20 mice

In order to probe the specific neurophysiological consequences of amyloid pathology on cortical and hippocampal network activity, we included J20 mice in all of the studies previously mentioned. In Chapters 3, 4 and 5, we demonstrated that neuronal network activity in J20 mice was altered in a number of different ways, including a variety of dramatic changes to beta bursting activity. Firstly, beta burst detection was significantly higher overall in the retrosplenial cortex and the hippocampus, and EEG data demonstrated a trend towards increased beta bursting across the entire cortex, with the largest increase centred over the retrosplenial cortex. In the hippocampus in J20 mice, plots of total beta burst detection revealed a “saw-tooth” pattern, with increased beta bursting during the first session of each day, in familiar days as well as novel days. If increased beta bursting in the retrosplenial cortex and hippocampus is indicative of perceived novelty, then increased beta bursting during upon first exposure to an already familiar environment could indicate uncertainty towards the novelty of the environment, due to contextual memory deficits in these mice. A notable feature of increased beta bursting in J20 mice is that this increase in beta burst detection arose from a significant increase in beta bursting during familiarity, but not novelty. In fact, while the rate of beta bursting during familiar sessions was more than doubled in J20 mice, there was no significant difference between the rate of beta bursting during the first minute of novel sessions, where the rate beta bursting is highest. As previously mentioned during Chapters 3 and 4, this could

have a number of implications for the mechanisms underlying beta bursting. Firstly, this could indicate a “maximum beta burst rate” which is already reached during novelty-associated beta bursting, and acts as a ceiling which cannot be exceeded even during aberrant beta bursting in J20 mice. This maximum beta burst rate may be set by a pacemaker or could be intrinsic, similar to how the refractory period of action potentials sets the maximal spontaneous firing rate of the neuron (Barrett and Barret, 1976). Beta bursts are high amplitude oscillatory events so it is highly possible that such an intense depolarisation could be followed by a period of hyperpolarisation.

In order to verify that beta bursts in J20 mice were the same as beta bursts in wild-types, and not the emergence of a different pathological phenomenon, we compared the frequency profiles and rhythmicity distributions of beta bursts in both genotypes. As in wild-type mice, beta bursts in J20 mice were associated with a large increase in beta power that peaked around 25 Hz, and an increase in beta oscillatory rhythmicity compared to non-burst epochs. These features were almost identical in both genotypes, which confirmed that we were most likely measuring the same phenomenon in J20 mice that we had identified in wild-type mice. We also compared beta burst magnitude and duration between genotypes. Due to the design of our beta burst detection algorithm, increases in beta burst magnitude or duration could, at least in part, account for increased beta burst detection. In J20 mice, beta bursts were significantly larger overall in magnitude in the retrosplenial cortex but not the hippocampus. Furthermore, beta burst duration was significantly higher during novelty in wild-type mice, but not J20 mice. This divergence is notable considering that amyloid pathology in J20 mice at this age is thought to be widespread in both the hippocampus and retrosplenial

cortex (Mucke et al., 2000; Whitesell et al., 2019), so this cannot simply be explained by differential amyloid pathology in these two regions. A cortical hyperexcitability phenotype has been previously demonstrated in this mouse line and is thought to underlie the increased risk of epilepsy in people with Alzheimer's disease (Hauser et al., 1986; Minkeviciene et al., 2009), and while compensatory inhibitory modelling has been demonstrated in the hippocampus (Palop et al., 2007), no such changes have been demonstrated in the cortex. This compensatory inhibitory modelling in the hippocampus may account for the non-significant trend towards reduced beta burst magnitude we see in the hippocampus in J20 mice. These results point towards excessive beta bursting as a neurophysiological phenotype of amyloid pathology in J20 mice, and considering the significant increases in neuronal spiking during beta bursting in wild-type mice, this aberrant beta bursting in these animals could be expected to result in excessive neuronal activation in. However, this is not the case, and one of the most notable changes to beta bursting in J20 mice is that neuronal spiking is not modulated by beta bursting in the retrosplenial cortex. If the hypothesised function of beta bursting in the retrosplenial cortex is to activate neurons to create cortical representations of environments (or objects, as shown by França et al. (2014)), then uncoupling of beta bursting from neuronal spiking would render beta bursts ineffectual. The cause of this uncoupling is uncertain, and it is possible that this is actually a compensatory mechanism in order to prevent aberrant neuronal activation due to excessive beta bursting, similar to other inhibitory compensation within the brain (Palop et al., 2007; Pan et al., 2018).

7.5 Altered network activity in J20 mice

Alongside the aberrant beta bursting activity, we found a number other of examples of altered network activity in J20 mice. Beta power was higher overall in J20 mice across the retrosplenial cortex, and while at first glance this may appear to result from increased beta bursting in these mice, power spectral analysis of burst and non-burst epochs reveals that this increased beta power occurs independent of beta bursting. Increased beta power could result in a lower threshold for beta burst generation, resulting in the increased rate of spontaneous familiarity-associated beta bursting seen in J20 mice. Moreover, gamma power in the retrosplenial cortex was significantly higher overall in J20 mice, and was centred around the 30-60 Hz frequency range, while in the hippocampus, gamma power was significantly lower overall in J20 mice. This decrease in gamma power in the hippocampus has been previously shown in this mouse line (Mondragón-Rodríguez et al., 2018; Etter et al., 2019), and was associated with increased epileptiform activity (Verret et al., 2012), although epileptiform activity was not noted in our animals. Phase-amplitude coupling was also altered in J20 mice, in both the retrosplenial cortex, and hippocampus. In wild-type mice, we demonstrated novelty-associated increases in theta-gamma coupling in the hippocampus, and theta-alpha/beta coupling in the retrosplenial cortex, yet these relationships were completely lost in J20 mice. While the relevance of theta-alpha/beta coupling is unclear, previous studies have demonstrated reduced theta-gamma coupling in the hippocampus of J20 mice, resulting from impairments in gamma oscillations, not theta oscillations (Mondragón-Rodríguez et al., 2018; Etter et al., 2019). Restoring hippocampal gamma oscillations restored theta-gamma coupling and rescued spatial memory in these animals,

highlighting the importance of these oscillations and indicating a potential avenue for rescuing cognitive impairments in Alzheimer's disease. Finally, we noted numerous reductions in coherence and Granger causality in J20 mice that were suggestive of disintegration of cortico-hippocampal networks. Delta and theta coherence were reduced between the hippocampus and retrosplenial cortex, indicating a loss of functional connectivity between these two structures, while disproportionate reductions in broadband Granger causality from the granular retrosplenial cortex to the hippocampus suggested impaired oscillatory activity flow in this specific edge of the cortico-hippocampal network. Impaired communication between the hippocampus and the cortex in Alzheimer's disease is thought to have a number of detrimental effects to cognition in Alzheimer's disease (Stoub et al., 2006; Allen et al., 2007).

7.6 Potential mechanisms underlying beta bursting

Through our investigations into beta bursting activity we came up with a number of suggestions for the generation of beta bursting activity across the brain. Numerous previous studies have aimed to elucidate the mechanisms underlying beta oscillations, including the brain regions and neurotransmitters involved (Shimono et al., 2000; Kilb and Luhmann, 2003; Arai and Natsume, 2006; Holgado et al., 2010; McCarthy et al., 2011). As described in Chapter 6, in order to investigate potential mechanisms underlying beta bursting in the retrosplenial cortex, we attempted to pharmacologically induce beta bursting *in vitro.* We found that administration of the cholinergic agonist carbachol was sufficient to induce beta bursts in the retrosplenial cortex that were strikingly similar to those we have found *in vivo.* This supported previous findings that application of carbachol to a whole-brain preparation *in vitro* was able to induce transient beta oscillations

which propagate across the cortical surface (Kilb and Luhmann, 2003), and application of carbachol to hippocampal slices is sufficient to induce beta oscillations (Shimono et al., 2000). Our findings indicate that cholinergic inputs to the cortex and hippocampus and generate beta oscillations which naturally appear as transient bursts in the absence of subcortical inputs. This *in vitro* model of beta bursting provides a valuable assay by which mechanisms underlying beta bursting can be further investigated.

7.7 Animal models of Alzheimer's disease

A number of considerations have to be taken into account when producing animal models of disease. The Three R's: Replacement, Refinement and Reduction, were set out by Russell and Burch (1959) to be a set of principles for humane animal research. Replacement refers to replacing *in vivo* experiments on living animals, with *in vitro* experiments, Reduction refers to reducing the number of animals to the minimum necessary for appropriate statistical power, and Refinement refers to the lessening of severity of necessary *in vivo* procedures. The use of rodents in animal research provides numerous practical advantages, and provides a means to study complex aspects of mammalian physiology on one of the lower order mammals. Alzheimer's disease does not occur naturally in mice and rats, but numerous other mammals show a variety of the pathological hallmarks of Alzheimer's disease, including canines and a variety of non-human primates (Walker et al., 2009; Fast et al., 2013; Prpar Mihevc and Majdič, 2019). Alzheimer's disease is thought to develop over a period of decades, while the typical lifespan for a mouse is between 1.3 to 3 years, so it is thought that this short lifespan may not provide the time necessary for the slow aggregation of neuropathology seen in Alzheimer's disease (Comfort, 1959). However, in non-

human primates, amyloid beta deposition has been shown to begin proportional to these species lifespans, generally around middle age even in species such as squirrel monkeys, whose lifespans are far shorter than ours, at around 30 years (Walker et al., 2009). As previously mentioned, Alzheimer's disease pathology also appears in canines, as does an age-relative cognitive disorder known as canine cognitive dysfunction (CCD) (Fast et al., 2013; Prpar Mihevc and Majdič, 2019). This data suggests that non-human primates and dogs would be superior models to rodents for sporadic Alzheimer's disease, however there are numerous ethical concerns with the use of higher order animals in research, especially non-human primates, which greatly limit their use.

Transgenic mouse models of Alzheimer's disease have come under a great deal of criticism of late, in part due to a number of late-stage clinical trials for amyloid β-targeted therapeutics. These compounds were able to demonstrate beneficial effects in transgenic mouse models of amyloid pathology, but these results were unable to be replicated in humans, bringing into question the validity of these models. Numerous transgenic mouse models of Alzheimer's disease, including the J20 mouse model used in this study, induce amyloid pathology by overexpression of APP with one or many mutations found in the familial variant of the disease. This means of modelling Alzheimer's disease has a variety of limitations. Firstly, the overexpression of APP can cause a variety of physiological disturbances unrelated to amyloid-β pathology, and could result in confounding phenotypes that are a poor representation of Alzheimer's disease (for review see Sasaguri et al., 2017). In order to avoid these issues, a number of newer "knock-in" transgenic lines were developed in which the endogenous mouse amyloid β gene is humanised and different mutations are added, resulting in

neuropathology without overexpression of APP (Saito et al., 2014). Secondly, while a small proportion of Alzheimer's disease cases are associated with autosomal dominant mutations in APP or presenilin (approximately 1%), the vast majority of cases are sporadic, with unknown aetiology (Bekris et al., 2010; R Cacace, 2016). This means that these transgenic mouse lines are effectively modelling the familial form of Alzheimer's disease, and attempting to extend these findings to the sporadic form of the disease. Finally, most of the commonly used amyloid mouse models fail to show any tau pathology, another key pathological hallmark of Alzheimer's disease (Games et al., 1995; Hsiao et al., 1996; Sturchler-Pierrat et al., 1997). Amyloid β has been shown in accelerate the development of tau pathology (Götz et al., 2001; Lewis et al., 2001), and depletion of endogenous tau in J20 mice resulted in improved cognition and prolonged survival (Roberson et al., 2007). Many mouse models of amyloidopathy fail to show any considerable neurodegeneration, which is often considered to be as a consequence of tau pathology (Hardy and Higgins, 1992; Walsh et al., 2017). In conclusion, mouse models which fail to replicate key aspects of Alzheimer's disease-related neuropathology may provide an incomplete or inaccurate representation of the neurophysiological dysfunction caused by Alzheimer's disease.

7.8 Implications for Future Study

The findings detailed in this thesis have a number of broader implications for electrophysiology. Firstly, we have demonstrated that beta oscillations across the brain conform to a model of discrete bursts of high beta amplitude, and high beta rhythmicity. While other patterns of oscillatory activity such as sleep spindles and sharp-wave ripples are well established as discrete events (Loomis et al., 1935;

Vanderwolf, 1969; O'Keefe, 1976), the classification of beta oscillations varies, with some studies considering it as a continuous oscillation, and others considering it as discrete bursts. Whether oscillations are classified as continuous or transient can reveal a great deal of information about their mechanisms, and direct appropriate analysis. There has been a great deal of discussion in recent years regarding the transient nature of a number of oscillations (Jones, 2016; van Ede et al., 2018). Averaging across trials or long behavioural epochs can cause transient oscillations to smear and appear as continuous oscillations, potentially precluding the identification of a range of behaviourally relevant oscillatory events (Shin et al., 2017). As such, some studies identified the transient nature of beta oscillations, but averaged the data across long epochs (relative to event duration), potentially diluting important rate information (Berke et al., 2008; França et al., 2014). A number of recent studies have demonstrated that even theta oscillations demonstrate substantial heterogeneity, such as varying levels of cross-frequency coupling, on a cycle-by-cycle basis (Colgin et al., 2009; Lopes-dos-Santos et al., 2018; López-Madrona et al., 2020). These data demonstrate that there is a great deal of insight that can be gained from investigating oscillatory activity over short timescales.

It is important to note that there are a number of methodological considerations to be taken into account when analysing transient neural oscillations. Firstly, as we have previously mentioned, continuous oscillations which vary dramatically in their amplitude over time may appear as transient events in the time or frequency domain (Shin et al., 2017; van Ede et al., 2018). It was for this reason that we took care to investigate the rhythmicity of beta oscillations during burst and non-burst epochs. Our results demonstrated that beta oscillations are highly

arrhythmic outside of burst epochs, which supported their classification as burst-like events. However, recent studies into putative gamma bursts during working memory seem do not take into account potential rhythmic changes in gamma amplitude, such as those that occur during theta-gamma phase-amplitude coupling, so it is possible that these events are not “true bursts” (Lundqvist et al., 2016, 2018). Furthermore, as demonstrated by Jones (2016), oscillatory events which appear to be similar in the frequency domain can result from completely different waveforms. It is for this reason that careful removal of recording artefacts is a particularly important processing step for this kind of analysis, which must occur before automated detection of transient oscillatory events.

Another key methodological consideration regarding neural oscillations is the importance of focusing on behaviourally relevant epochs for analysis. This is relevant not only for the analysis of transient oscillations, as discussed above, but also for other oscillatory activity. We demonstrated that novelty-associated increases in beta power were highest during the first minute of novel sessions, which led us to investigate the nature of this beta activity further. Novelty-associated beta bursting generally occurred during the first minute of the session, after which beta bursting was far lower. Phase-amplitude coupling analysis revealed notable differences when performed on either the first minute, or final minute of recording sessions. Across the retrosplenial cortex and in the hippocampus, theta-alpha/beta coupling was significantly higher during novel sessions in wild-type mice, but only during the first minute of the recording session, and the same was seen for theta-gamma coupling in the hippocampus. While assessment of behaviourally relevant epochs is straightforward in event-related potential tasks or other tasks with clear phases and requirements, such

as delayed alternation tasks, these results demonstrate the value of finding behaviourally relevant epochs in tasks or paradigms with less clear-cut sections.

7.9 Future Directions

As we have mentioned, these results open up a number of possible avenues for future experimentation, and while our findings have provided numerous insights into contextual memory processing in the brain, there are a multitude of questions yet to be answered.

- As repeatedly stated throughout this thesis, beta bursting in the retrosplenial cortex and hippocampus is a functional correlate of contextual novelty. This means that while we have shown that beta bursting is correlated with contextual novelty, we have not demonstrated a causal link between the two. Firstly, as the novel/familiar environment task is a behavioural paradigm and not a behavioural task, per se, we are unable to determine the success of contextual memory encoding. The use of a contextual memory task with a measurable behavioural outcome, such as freezing during contextual fear conditioning, would allow investigation into the strength of correlations between beta bursting and successful memory encoding. Furthermore, by investigating the behavioural effects of either suppressing beta bursting during contextual novelty, or inducing beta bursting during contextual familiarity, a casual role for beta bursting may be revealed. Through the use of techniques such as optogenetics, it is possible to elicit or suppress oscillatory activity either acutely or chronically with great success (Iaccarino et al., 2016; Etter et al., 2019).

- An additional benefit to using a contextual memory task with a measurable behavioural outcome would be the ability to investigate the extent of cognitive dysfunction in mouse models of Alzheimer's disease, such as J20 mice, and therefore determine whether memory deficits in these animals' correlate with neuronal network dysfunction. This may reveal novel sources of cognitive impairment in Alzheimer's disease, and provide novel insights into how learning and memory are processed within the brain.
- As previously discussed, there are a number of limitations to mouse models of Alzheimer's disease, including the J20 line used throughout this project. It is therefore unclear whether aberrant beta bursting seen in these animals is seen in other mouse models of Alzheimer's disease, or human Alzheimer's disease. While aberrant beta bursting is a well-established pathological hallmark of Parkinson's disease (McCarthy et al., 2011), to the authors knowledge, this has not been demonstrated in Alzheimer's disease. It is therefore important to clarify whether this occurs in other animal models of Alzheimer's disease, or ideally in human Alzheimer's disease itself. As we have demonstrated, beta bursts can be detected in EEG recordings despite spatial filtering by the scalp and skull (Srinivasan et al., 1998). Understanding the cause of aberrant beta bursting in J20 mice may provide novel insights into the mechanisms underlying pathological beta bursting in Parkinson's disease.
- Another valuable avenue of research would be confirmation of novelty-associated beta bursting in humans or non-human primates. Due to the size and anatomical position of the retrosplenial cortex in rodents, we were

able to non-intrusively investigate retrosplenial beta bursting using rodent EEG, however in humans and non-human primates, the retrosplenial cortex is far deeper in the brain, machining non-intrusive recordings far more difficult. Analytical techniques such as source localisation of EEG or MEG signals could allow recording of oscillatory activity from the retrosplenial cortex or hippocampus in order to investigate beta bursting activity during contextual novelty. The use of virtual reality technology allows human subjects to explore virtual environments while in spatially restricted laboratory environments, while brain activity is recorded using techniques such as EEG or MRI (Tremmel et al., 2019). These technologies make it possible to further delve into the role of beta bursting in humans.

- Finally, we have demonstrated that it is possible to pharmacologically induce beta bursting *in vitro*, and that these beta bursts are similar to those seen *in vivo*. While our experiments were fairly limited, there are numerous applications for this assay. Firstly, the effects of numerous other pharmacological agents on beta bursting could be tested, such as the effect of glutamatergic or GABAergic compounds, which may reveal the specific cell types underlying the generation of beta bursts. Alternatively, other modulatory neurotransmitters such as dopaminergic agonists may reveal how beta bursting is modulated within the brain. This *in vitro* assay provides a versatile platform to test a variety of hypotheses surrounding beta bursting in both health and disease.

7.10 Final Conclusions

Throughout this thesis we have described a number of novel neurophysiological correlates of contextual memory across a range of brain regions. We have demonstrated that transient bursts of beta oscillations are highly upregulated during contextual novelty in both the cortex and hippocampus, and that these beta bursts are highly synchronous across distant brain regions. Neurophysiological correlates of behaviour such as those described throughout this thesis can provide novel insights into how the brain performs its various functions. Through our work in J20 mice, we have identified numerous examples of altered neuronal work activity, including aberrant beta bursting activity, which may underlie cognitive impairments seen in these animals. By furthering our understanding of the specific neurophysiological alterations that occur as a result of Alzheimer's disease pathology, we may better understand this disease and potentially discover invaluable methods of restoring cognitive function in dementia.

8 References

Adam (2021) WaveSurfer.

Ahmed OJ, Mehta MR (2012) Running speed alters the frequency of hippocampal gamma oscillations. J Neurosci 32:7373–7383.

Alexander AS, Rangel LM, Tingley D, Nitz DA (2018) Neurophysiological signatures of temporal coordination between retrosplenial cortex and the hippocampal formation. Behav Neurosci 132:453–468.

Allen G, Barnard H, McColl R, Hester A., Fields J., Weiner M., Ringe W., Lipton A., Brooker M, McDonald E, Rubin C., Cullum C. (2007) Reduced hippocampal functional connectivity in Alzheimer disease. Arch Neurol 64:1482–1487.

Aloisi AM, Casamenti F, Scali C, Pepeu G, Carli G (1997) Effects of novelty, pain and stress on hippocampal extracellular acetylcholine levels in male rats. Brain Res 748:219–226.

Alzheimer's Association (2015) 2015 Alzheimer's disease facts and figures. Alzheimer's Dement 11:332–384.

Alzheimer A (1907) Uber eine eigenartige Erkrankung der Hirnrinde. Allg Zeits Psychiatry Psych Y Gerichtl Med 64:146–148.

Andersen P, Bliss TVP, Skrede KK (1971) Lamellar organization of hippocampal excitatory pathways. Exp Brain Res 1971 132 13:222–238.

Arai J, Natsume K (2006) The properties of carbachol-induced beta oscillation in rat hippocampal slices. Neurosci Res 54:95–103.

Arriagada P V., Growdon JH, Hedley-Whyte ET, Hyman BT (1992) Neurofibrillary tangles but not senile plaques parallel duration and severity of Alzheimer's disease. Neurology 42:631–639.

Axmacher N, Henseler MM, Jensen O, Weinreich I, Elger CE, Fell J (2010) Cross-frequency coupling supports multi-item working memory in the human hippocampus. Proc Natl Acad Sci 107:3228–3233.

Barnett L, Seth AK (2014) The MVGC multivariate Granger causality toolbox: A new approach to Granger-causal inference. J Neurosci Methods 223:50–68.

Barrett EF, Barret JN (1976) Separation of two voltage-sensitive potassium currents, and demonstration of a tetrodotoxin-resistant calcium current in frog motoneurones. J Physiol 255:737–774.

Bartos M, Vida I, Jonas P (2007) Synaptic mechanisms of synchronized gamma oscillations in inhibitory interneuron networks. Nat Rev Neurosci 2007 81 8:45–56.

Bartus RT, Dean RL, Beer B, Lippa A (1982) The cholinergic hypothesis of geriatric memory dysfunction. Science 217:408–414.

Bastos AM, Schoffelen JM (2016) A tutorial review of functional connectivity analysis methods and their interpretational pitfalls. Front Syst Neurosci 9.

Bekris LM, Yu C-E, Bird TD, Tsuang DW (2010) Genetics of Alzheimer Disease. J Geriatr Psychiatry Neurol 23:213.

Belluscio MA, Mizuseki K, Schmidt R, Kempter R, Buzsáki G (2012) Cross-Frequency Phase–Phase Coupling between Theta and Gamma Oscillations in the Hippocampus. J Neurosci 32:423.

Berchtold N., Cotman C. (1998) Evolution in the conceptualization of dementia and Alzheimer's disease: Greco-Roman period to the 1960s. Neurobiol Aging 19:173–189.

Berger H (1934) Über das Elektrenkephalogramm des Menschen. Dtsch Medizinische Wochenschrift 60:1947–1949.

Berke JD, Hetrick V, Breck J, Greene RW (2008) Transient 23-30 Hz oscillations in mouse hippocampus during exploration of novel environments. Hippocampus 18:519–529.

Bieri KW, Bobbitt KN, Colgin LL (2014) Slow and fast gamma rhythms coordinate different spatial coding modes in hippocampal place cells. Neuron 82:670.

Bigl V, Woolf NJ, Butcher LL (1982) Cholinergic projections from the basal forebrain to frontal, parietal, temporal, occipital, and cingulate cortices: A combined fluorescent tracer and acetylcholinesterase analysis. Brain Res Bull 8:727–749.

Binder LI, Frankfurter A, Rebhun LI (1985) The distribution of tau in the mammalian central nervous system. J Cell Biol 101:1371–1378.

Bird CM, Burgess N (2008) The hippocampus and memory: insights from spatial processing. Nat Rev Neurosci 9:182–194.

Boccara CN, Sargolini F, Thoresen VH, Solstad T, Witter MP, Moser EI, Moser MB (2010) Grid cells in pre-and parasubiculum. Nat Neurosci 13:987–994.

Booth CA, Ridler T, Murray TK, Ward MA, de Groot E, Goodfellow M, Phillips KG, Randall AD, Brown JT (2016) Electrical and network neuronal properties are preferentially disrupted in dorsal, but not ventral, medial entorhinal cortex in a mouse model of tauopathy. J Neurosci 36:312–324.

Braak H, Braak E (1991) Neuropathological stageing of Alzheimer-related changes. Acta Neuropathol 1991 824 82:239–259.

Braak H, Braak E (1995) Staging of alzheimer's disease-related neurofibrillary changes. Neurobiol Aging 16:271–278.

Briels CT, Schoonhoven DN, Stam CJ, de Waal H, Scheltens P, Gouw AA (2020) Reproducibility of EEG functional connectivity in Alzheimer's disease. Alzheimer's Res Ther 12.

Brittain JS, Sharott A, Brown P (2014) The highs and lows of beta activity in cortico-basal ganglia loops. Eur J Neurosci 39:1951–1959.

Brodmann K (1909) Vergleichende Lokalisationslehre der Grosshirnrinde inihren Prinzipien dargestellt auf Grund des Zellenbaues. Leipzig: Barth.

Brown P, Oliviero A, Mazzone P, Insola A, Tonali P, Di Lazzaro V (2001) Dopamine dependency of oscillations between subthalamic nucleus and pallidum in Parkinson's disease. J Neurosci 21:1033–1038.

Bubb EJ, Metzler-Baddeley C, Aggleton JP (2018) The cingulum bundle: Anatomy, function, and dysfunction. Neurosci Biobehav Rev 92:104–127.

Burgess N, Maguire EA, O'Keefe J (2002) The Human Hippocampus and Spatial and Episodic Memory. Neuron 35:625–641.

Busche MA, Eichhoff G, Adelsberger H, Abramowski D, Wiederhold KH, Haass C, Staufenbiel M, Konnerth A, Garaschuk O (2008) Clusters of hyperactive neurons near amyloid plaques in a mouse model of Alzheimer's disease. Science (80-) 321:1686–1689.

Buzsáki G (2002) Theta oscillations in the hippocampus. Cell Press.

Buzsáki G, Anastassiou CA, Koch C (2012) The origin of extracellular fields and currents-EEG, ECoG, LFP and spikes. Nat Rev Neurosci 13:407–420.

Buzsáki G, Buhl DL, Harris KD, Csicsvari J, Czéh B, Morozov A (2003) Hippocampal network patterns of activity in the mouse. Neuroscience 116:201–211.

Buzsáki G, Draguhn A (2004) Neuronal oscillations in cortical networks. Science (80-) 304:1926–1929.

Buzsáki G, Leung L., Vanderwolf C. (1983) Cellular bases of hippocampal EEG in the behaving rat. Brain Res 287:139–171.

Buzśaki G, Wang XJ (2012) Mechanisms of gamma oscillations. Annu Rev Neurosci 35:203–225.

Campbell R (2021) raacampbell/shadedErrorBar.

Canolty RT, Edwards E, Dalal SS, Soltani M, Nagarajan SS, Kirsch HE, Berger MS, Barbare NM, Knight RT (2006) High gamma power is phase-locked to theta oscillations in human neocortex. Science (80-) 313:1626–1628.

Canolty RT, Ganguly K, Kennerley SW, Cadieu CF, Koepsell K, Wallis JD, Carmena JM (2010) Oscillatory phase coupling coordinates anatomically dispersed functional cell assemblies. Proc Natl Acad Sci U S A 107:17356–17361.

Canolty RT, Knight RT (2010) The functional role of cross-frequency coupling. Trends Cogn Sci 14:506–515.

Caro-Martín CR, Delgado-García JM, Gruart A, Sánchez-Campusano R (2018) Spike sorting based on shape, phase, and distribution features, and K-TOPS clustering with validity and error indices. Sci Reports 2018 81 8:1–28.

Carr MF, Karlsson MP, Frank LM (2012) Transient Slow Gamma Synchrony Underlies Hippocampal Memory Replay. Neuron 75:700–713.

Chartier-Harlin M-C, Crawford F, Houlden H, Warren A, Hughes D, Fidani L, Goate A, Rossor M, Roques P, Hardy J, Mullan M (1991) Early-onset Alzheimer’s disease caused by mutations at codon 717 of the β-amyloid

precursor protein gene. Nat 1991 3536347 353:844–846.

Chen Z, Resnik E, McFarland JM, Sakmann B, Mehta MR (2011) Speed controls the amplitude and timing of the Hippocampal Gamma rhythm. PLoS One 6.

Cheng IH, Scearce-Levie K, Legleiter J, Palop JJ, Gerstein H, Bien-Ly N, Puoliväli J, Lesné S, Ashe KH, Muchowski PJ, Mucke L (2007) Accelerating amyloid-β fibrillization reduces oligomer levels and functional deficits in Alzheimer disease mouse models. J Biol Chem 282:23818–23828.

Choo IH, Lee DY, Oh JS, Lee JS, Lee DS, Song IC, Youn JC, Kim SG, Kim KW, Jhoo JH, Woo JI (2010) Posterior cingulate cortex atrophy and regional cingulum disruption in mild cognitive impairment and Alzheimer's disease. Neurobiol Aging 31:772–779.

Chrobak JJ, Buzsáki G (1998) Gamma oscillations in the entorhinal cortex of the freely behaving rat. J Neurosci 18:388–398.

Citron M, Oltersdorf T, Haass C, McConlogue L, Hung AY, Seubert P, Vigo-Pelfrey C, Lieberburg I, Selkoe DJ (1992) Mutation of the β-amyloid precursor protein in familial Alzheimer's disease increases β-protein production. Nat 1992 3606405 360:672–674.

Cohen MX (2015) Effects of time lag and frequency matching on phase-based connectivity. J Neurosci Methods 250:137–146.

Colgin LL (2015a) Theta-gamma coupling in the entorhinal-hippocampal system. Curr Opin Neurobiol 31:45–50.

Colgin LL (2015b) Do slow and fast gamma rhythms correspond to distinct functional states in the hippocampal network? Brain Res 1621:309.

Colgin LL, Denninger T, Fyhn M, Hafting T, Bonnevie T, Jensen O, Moser M-B, Moser EI (2009) Frequency of gamma oscillations routes flow of information in the hippocampus. Nat 2009 4627271 462:353–357.

Comfort A (1959) Natural Aging and the Effects of Radiation. Radiat Res Suppl 1:216.

Corcoran K., Frick B., Radulovic J, Kay L. (2016) Analysis of coherent activity between retrosplenial cortex, hippocampus, thalamus, and anterior cingulate cortex during retrieval of recent and remote context fear memory. Neurobiol

Learn Mem 127:93–101.

Cowansage KK, Shuman T, Dillingham BC, Chang A, Golshani P, Mayford M (2014) Direct Reactivation of a Coherent Neocortical Memory of Context. Neuron 84:432–441.

Cummings JL, Morstorf T, Zhong K (2014) Alzheimer's disease drug-development pipeline: few candidates, frequent failures. Alzheimers Res Ther 6:37.

Czajkowski R, Jayaprakash B, Wiltgen B, Rogerson T, Guzman-Karlsson MC, Barth AL, Trachtenberg JT, Silva AJ (2014) Encoding and storage of spatial information in the retrosplenial cortex. Proc Natl Acad Sci 111:8661–8666.

Daume J, Gruber T, Engel AK, Friese U (2017) Phase-amplitude coupling and long-range phase synchronization reveal frontotemporal interactions during visual working memory. J Neurosci 37:313–322.

de Cheveigné A, Nelken I (2019) Filters: When, Why, and How (Not) to Use Them. Neuron 102:280–293.

De Sousa AF, Cowansage KK, Zutshi I, Cardozo LM, Yoo EJ, Leutgeb S, Mayford M (2019) Optogenetic reactivation of memory ensembles in the retrosplenial cortex induces systems consolidation. Proc Natl Acad Sci U S A 116:8576–8581.

De Strooper B, Saftig P, Craessaerts K, Vanderstichele H, Guhde G, Annaert W, Von Figura K, Van Leuven F (1998) Deficiency of presenilin-1 inhibits the normal cleavage of amyloid precursor protein. Nat 1998 3916665 391:387–390.

DeBoer P, Heeringa MJ, Abercrombie ED (1996) Spontaneous release of acetylcholine in striatum is preferentially regulated by inhibitory dopamine D2 receptors. Eur J Pharmacol 317:257–262.

DeKosky S, Scheff S (1990) Synapse loss in frontal cortex biopsies in Alzheimer's disease: correlation with cognitive severity. Ann Neurol 27:457–464.

DeKosky ST, Scheff SW, Styren SD (1996) Structural correlates of cognition in dementia: Quantification and assessment of synapse change. Neurodegeneration 5:417–421.

DeMattos RB, Bales KR, Cummins DJ, Dodart JC, Paul SM, Holtzman DM (2001) Peripheral anti-Aβ antibody alters CNS and plasma Aβ clearance and decreases brain Aβ burden in a mouse model of Alzheimer's disease. Proc Natl Acad Sci U S A 98:8850–8855.

DeMattos RB, Bales KR, Parsadanian M, O'Dell MA, Foss EM, Paul SM, Holtzman DM (2002) Plaque-associated disruption of CSF and plasma amyloid-β (Aβ) equilibrium in a mouse model of Alzheimer's disease. J Neurochem 81:229–236.

Dodart JC, Meziane H, Mathis C, Ungerer A, Bales KR, Paul SM (1999) Behavioral disturbances in transgenic mice overexpressing the V717F β-amyloid precursor protein. Behav Neurosci 113:982–990.

Donoho DL, Johnstone IM (1994) Ideal spatial adaptation by wavelet shrinkage. Biometrika 81:425–455.

Dudek SM, Alexander GM, Farris S (2016) Rediscovering area CA2: unique properties and functions. Nat Rev Neurosci 17:89.

Eckenstein FP, Baughman RW, Quinn J (1988) An anatomical study of cholinergic innervation in rat cerebral cortex. Neurosci 25:457–474.

Engel A., König P, Kreiter A., Singer W (1991) Interhemispheric synchronization of oscillatory neuronal responses in cat visual cortex. Science 252:1177–1179.

Engel AK, Fries P (2010) Beta-band oscillations-signalling the status quo? Curr Opin Neurobiol 20:156–165.

Etter G, van der Veldt S, Manseau F, Zarrinkoub I, Trillaud-Doppia E, Williams S (2019) Optogenetic gamma stimulation rescues memory impairments in an Alzheimer's disease mouse model. Nat Commun 2019 101 10:1–11.

Fast R, Schütt T, Toft N, Møller A, Berendt M (2013) An Observational Study with Long-Term Follow-Up of Canine Cognitive Dysfunction: Clinical Characteristics, Survival, and Risk Factors. J Vet Intern Med 27:822–829.

Faulkner HJ, Traub RD, Whittington MA (1999) Anaesthetic/amnesic agents disrupt beta frequency oscillations associated with potentiation of excitatory synaptic potentials in the rat hippocampal slice. Br J Pharmacol 128:1813–

1825.

Feingold J, Gibson DJ, DePasquale B, Graybiel AM (2015) Bursts of beta oscillation differentiate postperformance activity in the striatum and motor cortex of monkeys performing movement tasks. Proc Natl Acad Sci 112:13687–13692.

França ASC, Borgegius N, Cohen MX (2020) Beta2 oscillations in the hippocampal-cortical novelty detection circuit. Cold Spring Harbor Laboratory.

França ASC, do Nascimento GC, Lopes-dos-Santos V, Muratori L, Ribeiro S, Lobão-Soares B, Tort ABL (2014) Beta2 oscillations (23-30 Hz) in the mouse hippocampus during novel object recognition. Eur J Neurosci 40:3693–3703.

Frank LM, Brown EN, Wilson MA (2001) A Comparison of the Firing Properties of Putative Excitatory and Inhibitory Neurons From CA1 and the Entorhinal Cortex. J Neurophysiol 86:2029–2040.

Fried K (1959) Somatic Chromosomes in Mongolism. Lancet 274:98.

Fries P (2005) A mechanism for cognitive dynamics: Neuronal communication through neuronal coherence. Trends Cogn Sci 9:474–480.

Fries P (2015) Rhythms For Cognition: Communication Through Coherence. Neuron 88:220.

Fries P, Womelsdorf T, Oostenveld R, Desimone R (2008) The Effects of Visual Stimulation and Selective Visual Attention on Rhythmic Neuronal Synchronization in Macaque Area V4. J Neurosci 28:4823–4835.

Fujisawa S, Buzsáki G (2011) A 4-Hz oscillation adaptively synchronizes prefrontal, VTA and hippocampal activities. Neuron 72:153.

Gage SL, Keim SR, Simon JR, Low WC (1994) Cholinergic innervation of the retrosplenial cortex via the fornix pathway as determined by high affinity choline uptake, choline acetyltransferase activity, and muscarinic receptor binding in the rat. Neurochem Res 1994 1911 19:1379–1386.

Games D et al. (1995) Alzheimer-type neuropathology in transgenic mice overexpressing V717F β-amyloid precursor protein. Nature 373:523–527.

Garner AR, Rowland DC, Hwang SY, Baumgaertel K, Roth BL, Kentros C, Mayford M (2012) Generation of a synthetic memory trace. Science (80-) 335:1513–1516.

Giovannini M., Rakovska A, Benton R., Pazzagli M, Bianchi L, Pepeu G (2001) Effects of novelty and habituation on acetylcholine, GABA, and glutamate release from the frontal cortex and hippocampus of freely moving rats. Neuroscience 106:43–53.

Glenner GG, Wong CW (1984) Alzheimer's disease: Initial report of the purification and characterization of a novel cerebrovascular amyloid protein. Biochem Biophys Res Commun 120:885–890.

Goedert M, Spillantini MG, Jakes R, Rutherford D, Crowther RA (1989) Multiple isoforms of human microtubule-associated protein tau: sequences and localization in neurofibrillary tangles of Alzheimer's disease. Neuron 3:519–526.

Götz J, Chen F, Van Dorpe J, Nitsch RM (2001) Formation of neurofibrillary tangles in P301L tau transgenic mice induced by Aβ42 fibrils. Science (80-) 293:1491–1495.

Goutagny R, Jackson J, Williams S (2009) Self-generated theta oscillations in the hippocampus. Nat Neurosci 2009 1212 12:1491–1493.

Granger CWJ (1969) Investigating Causal Relations by Econometric Models and Cross-spectral Methods. Econometrica 37:424.

Groen T van, Wyss JM (1990) Connections of the retrosplenial granular a cortex in the rat. J Comp Neurol 300:593–606.

Haijima A, Ichitani Y (2008) Anterograde and retrograde amnesia of place discrimination in retrosplenial cortex and hippocampal lesioned rats. Learn Mem 15:477–482.

Hanson JE et al. (2020) GluN2A NMDA Receptor Enhancement Improves Brain Oscillations, Synchrony, and Cognitive Functions in Dravet Syndrome and Alzheimer's Disease Models. Cell Rep 30:381–396.

Hardy J (2009) The amyloid hypothesis for Alzheimer's disease: a critical reappraisal. J Neurochem 110:1129–1134.

Hardy JA, Higgins GA (1992) Alzheimer's disease: The amyloid cascade hypothesis. Science (80-) 256:184–185.

Harris K, Henze D, Csicsvari J, Hirase H, Buzsáki G (2000) Accuracy of tetrode spike separation as determined by simultaneous intracellular and extracellular measurements. J Neurophysiol 84:401–414.

Hasselmo ME, Bodelón C, Wyble BP (2002) A Proposed Function for Hippocampal Theta Rhythm: Separate Phases of Encoding and Retrieval Enhance Reversal of Prior Learning. Neural Comput 14:793–817.

Hauser W., Morris M., Heston L., Anderson V. (1986) Seizures and myoclonus in patients with Alzheimer's disease. Neurology 36:1226–1230.

Hayden EY, Teplow DB (2013) Amyloid β-protein oligomers and Alzheimer's disease. Alzheimer's Res Ther 2013 56 5:1–11.

Henze DA, Borhegyi Z, Csicsvari J, Mamiya A, Harris KD, Buzsáki G (2000) Intracellular Features Predicted by Extracellular Recordings in the Hippocampus In Vivo. https://doi.org/101152/jn2000841390 84:390–400.

Hirsh R (1974) The hippocampus and contextual retrieval of information from memory: A theory. Behav Biol 12:421–444.

Holcomb L, Gordon MN, Mcgowan E, Yu X, Benkovic S, Jantzen P, Wright K, Saad I, Mueller R, Morgan D, Sanders S, Zehr C, O'Campo K, Hardy J, Prada CM, Eckman C, Younkin S, Hsiao K, Duff K (1998) Accelerated Alzheimer-type phenotype in transgenic mice carrying both mutant amyloid precursor protein and presenilin 1 transgenes. Nat Med 4:97–100.

Holgado AJN, Terry JR, Bogacz R (2010) Conditions for the Generation of Beta Oscillations in the Subthalamic Nucleus–Globus Pallidus Network. J Neurosci 30:12340.

Houser C., Crawford G., Barber R., Salvaterra P., Vaughn J. (1983) Organization and morphological characteristics of cholinergic neurons: an immunocytochemical study with a monoclonal antibody to choline acetyltransferase. Brain Res 266:97–119.

Hsiao K, Chapman P, Nilsen S, Eckman C, Harigaya Y, Younkin S, Yang F, Cole G (1996) Correlative memory deficits, Aβ elevation, and amyloid plaques in

transgenic mice. Science (80-) 274:99–102.

Hutton M et al. (1998) Association of missense and 5’-splice-site mutations in tau with the inherited dementia FTDP-17. Nature 393:702–704.

Hyslop PA, May PC, Audia JE, Calligaro DO, McMillian CL, Garner CO, Cramer JW, Gitter BD, Porter WJ, Nissen JS, Mabry TE, Bender MH (2004) P1-180 Reduction in a-beta(1-40) and A-beta(1-42) in CSF and plasma in the beagle dog following acute oral dosing of the gamma secretase inhibitor, LY450139. Neurobiol Aging 25:S147.

Iaccarino HF, Singer AC, Martorell AJ, Rudenko A, Gao F, Gillingham TZ, Mathys H, Seo J, Kritskiy O, Abdurrob F, Adaikkan C, Canter RG, Rueda R, Brown EN, Boyden ES, Tsai LH (2016) Gamma frequency entrainment attenuates amyloid load and modifies microglia. Nature 540:230–235.

Iaria G, Chen JK, Guariglia C, Ptito A, Petrides M (2007) Retrosplenial and hippocampal brain regions in human navigation: Complementary functional contributions to the formation and use of cognitive maps. Eur J Neurosci 25:890–899.

Ikarashi Y, Takahashi A, Ishimaru H, Arai T, Maruyama Y (1997) Regulation of dopamine D1 and D2 receptors on striatal acetylcholine release in rats. Brain Res Bull 43:107–115.

Ishizuka N, Weber J, Amaral DG (1990) Organization of intrahippocampal projections originating from CA3 pyramidal cells in the rat. J Comp Neurol 295:580–623.

Itskov PM, Vinnik E, Honey C, Schnupp J, Diamond ME (2012) Sound sensitivity of neurons in rat hippocampus during performance of a sound-guided task. J Neurophysiol 107:1822–1834.

Iwasaki S, Sasaki T, Ikegaya Y (2021) Hippocampal beta oscillations predict mouse object-location associative memory performance. Hippocampus 31:503–511.

Iwatsubo T, Odaka A, Suzuki N, Mizusawa H, Nukina N, Ihara Y (1994) Visualization of Aβ42(43) and Aβ40 in senile plaques with end-specific Aβ monoclonals: Evidence that an initially deposited species is Aβ42(43).

Neuron 13:45–53.

Jack CR, Jr., Petersen RC, Xu Y, O'Brien PC, Smith GE, Ivnik RJ, Tangalos EG, Kokmen E (1998) The Rate of Medial Temporal Lobe Atrophy in Typical Aging and Alzheimer's Disease. Neurology 51:993.

Jack CR, Jr., Petersen RC, Xu YC, Waring SC, O'Brien PC, Tangalos EG, Smith GE, Ivnik RJ, Kokmen E (1997) Medial Temporal Atrophy on MRI in Normal Aging and Very Mild Alzheimer's Disease. Neurology 49:786.

Jacobs J (2014) Hippocampal theta oscillations are slower in humans than in rodents: implications for models of spatial navigation and memory. Philos Trans R Soc B Biol Sci 369.

Jacobsen JS, Wu C-C, Redwine JM, Comery TA, Arias R, Bowlby M, Martone R, Morrison JH, Pangalos MN, Reinhart PH, Bloom FE (2006) Early-onset behavioral and synaptic deficits in a mouse model of Alzheimer's disease. Proc Natl Acad Sci 103:5161–5166.

Jarrett J., Berger E., Lansbury P. (1993) The carboxy terminus of the beta amyloid protein is critical for the seeding of amyloid formation: implications for the pathogenesis of Alzheimer's disease. Biochemistry 32:4693–4697.

Jensen O (2005) Reading the hippocampal code by theta phase-locking. Trends Cogn Sci 9:551–553.

Jensen O, Lisman J. (2000) Position reconstruction from an ensemble of hippocampal place cells: contribution of theta phase coding. J Neurophysiol 83:2602–2609.

Joho RH, Ho CS, Marks GA (1999) Increased gamma- and decreased delta-oscillations in a mouse deficient for a potassium channel expressed in fast-spiking interneurons. J Neurophysiol 82:1855–1864.

Jones SR (2016) When brain rhythms aren't "rhythmic": implication for their mechanisms and meaning. Curr Opin Neurobiol 40:72.

Jonsson T et al. (2012) A mutation in APP protects against Alzheimer's disease and age-related cognitive decline. Nat 2012 4887409 488:96–99.

Jouvet M (1969) Biogenic amines and the states of sleep. Science (80-) 163:32–41.

Jucker M, Walker LC (2013) Self-propagation of pathogenic protein aggregates in neurodegenerative diseases. Nat 2013 5017465 501:45–51.

Jun JJ et al. (2017) Fully integrated silicon probes for high-density recording of neural activity. Nat 2017 5517679 551:232–236.

Jun S, Kim JS, Chung CK (2021) Prediction of Successful Memory Encoding Based on Lateral Temporal Cortical Gamma Power. Front Neurosci 0:464.

Kahana MJ (2006) The Cognitive Correlates of Human Brain Oscillations. J Neurosci 26:1669.

Karran E, De Strooper B (2016) The amyloid cascade hypothesis: are we poised for success or failure? J Neurochem 139:237–252.

Karvat G, Schneider A, Alyahyay M, Steenbergen F, Tangermann M, Diester I (2020) Real-time detection of neural oscillation bursts allows behaviourally relevant neurofeedback. Commun Biol 3.

Katz B, Miledi R (1965) The measurement of synaptic delay, and the time course of acetylcholine release at the neuromuscular junction. Proc R Soc B 161:483–495.

Keene CS, Bucci DJ (2008) Contributions of the Retrosplenial and Posterior Parietal Cortices to Cue-Specific and Contextual Fear Conditioning. Behav Neurosci 122:89–97.

Kilb W, Luhmann HJ (2003) Carbachol-induced Network Oscillations in the Intact Cerebral Cortex of the Newborn Rat. Cereb Cortex 13:409–421.

Kim JJ, Fanselow MS (1992) Modality-specific retrograde amnesia of fear. Science (80-) 256:675–677.

Klausberger T, Somogyi P (2008) Neuronal diversity and temporal dynamics: the unity of hippocampal circuit operations. Science 321:53–57.

Kobayashi Y, Amaral DG (2003) Macaque monkey retrosplenial cortex: II. Cortical afferents. J Comp Neurol 466:48–79.

Kobayashi Y, Amaral DG (2007) Macaque monkey retrosplenial cortex: III. Cortical efferents. J Comp Neurol 502:810–833.

Koike BDV, Farias KS, Billwiller F, Almeida-Filho D, Libourel PA, Tiran-Cappello

A, Parmentier R, Blanco W, Ribeiro S, Luppi PH, Queiroz CM (2017) Electrophysiological evidence that the retrosplenial cortex displays a strong and specific activation phased with hippocampal theta during paradoxical (REM) sleep. J Neurosci 37:8003–8013.

Kolb B, Whishaw IQ (1977) Effects of brain lesions and atropine on hippocampal and neocortical electroencephalograms in the rat. Exp Neurol 56:1–22.

Kondabolu K, Roberts EA, Bucklin M, McCarthy MM, Kopell N, Han X (2016) Striatal cholinergic interneurons generate beta and gamma oscillations in the corticostriatal circuit and produce motor deficits. Proc Natl Acad Sci 113:E3159–E3168.

Konopacki J, Bruce MacIver M, Bland BH, Roth SH (1987) Carbachol-induced EEG “theta” activity in hippocampal brain slices. Brain Res 405:196–198.

Kopan R, Ilagan MXG (2004) γ-Secretase: Proteasome of the membrane? Nat Rev Mol Cell Biol 5:499–504.

Kopell N, Ermentrout GB, Whittington MA, Traub RD (2000) Gamma rhythms and beta rhythms have different synchronization properties. Proc Natl Acad Sci U S A 97:1867–1872.

Kosik K, Joachim C, Selkoe D (1987) Microtubule-associated protein tau (?) is a major antigenic component of paired helical filaments in Alzheimer disease. Alzheimer Dis Assoc Disord 1:203.

Kragel JE, Vanhaerents S, Templer JW, Schuele S, Rosenow JM, Nilakantan AS, Bridge DJ (2020) Hippocampal theta coordinates memory processing during visual exploration. Elife 9.

Kullback S, Leibler R. (1951) On Information and Sufficiency. Ann Math Stat 22:79–86.

Kwapis JL, Jarome TJ, Lee JL, Helmstetter FJ (2015) The retrosplenial cortex is involved in the formation of memory for context and trace fear conditioning. Neurobiol Learn Mem 123:110–116.

Laczó J, Vlček K, Vyhnálek M, Vajnerová O, Ort M, Holmerová I, Tolar M, Andel R, Bojar M, Hort J (2009) Spatial navigation testing discriminates two types of amnestic mild cognitive impairment. 202:252–259.

Lee M, Kim D, Shin H-S, Sung H-G, Choi JH (2011) High-density EEG Recordings of the Freely Moving Mice using Polyimide-based Microelectrode. J Vis Exp.

Lega B, Burke J, Jacobs J, Kahana M. (2016) Slow-Theta-to-Gamma Phase-Amplitude Coupling in Human Hippocampus Supports the Formation of New Episodic Memories. Cereb Cortex 26:268–278.

Lejeune J, Gauthier M, Turpin R (1959) Les chromosomes humains en culture de tissus. C R Hebd Seances Acad Sci 248:602–603.

Lesné S, Kotilinek L, Ashe KH (2008) Plaque-bearing mice with reduced levels of oligomeric amyloid-β assemblies have intact memory function. Neuroscience 151:745–749.

Leung LWS, Borst JGG (1987) Electrical activity of the cingulate cortex. I. Generating mechanisms and relations to behavior. Brain Res 407:68–80.

Leventhal DK, Gage GJ, Schmidt R, Pettibone JR, Case AC, Berke JD (2012) Basal Ganglia Beta Oscillations Accompany Cue Utilization. Neuron 73:523–536.

Lever C, Burton S, Jeewajee A, O'Keefe J, Burgess N (2009) Boundary Vector Cells in the Subiculum of the Hippocampal Formation. J Neurosci 29:9771–9777.

Lévesque M, Cataldi M, Chen LY, Hamidi S, Avoli M (2017) Carbachol-induced network oscillations in an in vitro limbic system brain slice. Neuroscience 348:153–164.

Lewis J, Dickson DW, Lin W-L, Chisholm L, Corral A, Jones G (2001) Enhanced Neurofibrillary Degeneration in Transgenic Mice Expressing Mutant Tau and APP. J Chem Inf Model 293:1487–1491.

Lewis J, McGowan E, Rockwood J, Melrose H, Nacharaju P, Van Slegtenhorst M, Gwinn-Hardy K, Murphy MP, Baker M, Yu X, Duff K, Hardy J, Corral A, Lin WL, Yen SH, Dickson DW, Davies P, Hutton M (2000) Neurofibrillary tangles, amyotrophy and progressive motor disturbance in mice expressing mutant (P301L)tau protein. Nat Genet 25:402–405.

Lindwall G, Cole RD (1984) Phosphorylation affects the ability of tau protein to

promote microtubule assembly. J Biol Chem 259:5301–5305.

Lisman J (2010) Working Memory: The Importance of Theta and Gamma Oscillations. Curr Biol 20:R490–R492.

Lisman JE, Jensen O (2013) The Theta-Gamma Neural Code. Neuron 77:1002–1016.

Little S, Bonaiuto J, Barnes G, Bestmann S (2019) Human motor cortical beta bursts relate to movement planning and response errors. PLOS Biol 17:e3000479.

Liu X, Ramirez S, Pang PT, Puryear CB, Govindarajan A, Deisseroth K, Tonegawa S (2012) Optogenetic stimulation of a hippocampal engram activates fear memory recall. Nat 2012 4847394 484:381–385.

Locatelli T, Cursi M, Liberati D, Franceschi M, Comi G (1998) EEG coherence in Alzheimer's disease. Electroencephalogr Clin Neurophysiol 106:229–237.

Loomis AL, Harvey EN, Hobart G (1935) Potential rhythms of the cerebral cortex during sleep. Science (80-) 81:597–598.

Lopes-dos-Santos V, van de Ven GM, Morley A, Trouche S, Campo-Urriza N, Dupret D (2018) Parsing Hippocampal Theta Oscillations by Nested Spectral Components during Spatial Exploration and Memory-Guided Behavior. Neuron 100:940-952.e7.

López-Madrona VJ, Pérez-Montoyo E, Álvarez-Salvado E, Moratal D, Herreras O, Pereda E, Mirasso CR, Canals S (2020) Different theta frameworks coexist in the rat hippocampus and are coordinated during memory-guided and novelty tasks. Elife 9:1–35.

Lorente de Nó R (1934) Studies on the structure of the cerebral cortex. II. Continuation of the study of the ammonic system. J Psychol Neurol:113–177.

Lowet E, Roberts MJ, Bonizzi P, Karel J, De Weerd P (2016) Quantifying Neural Oscillatory Synchronization: A Comparison between Spectral Coherence and Phase-Locking Value Approaches. PLoS One 11.

Lundqvist M, Herman P, Warden MR, Brincat SL, Miller EK (2018) Gamma and beta bursts during working memory readout suggest roles in its volitional

control. Nat Commun 2018 91 9:1–12.

Lundqvist M, Rose J, Herman P, Brincat SLL, Buschman TJJ, Miller EKK (2016) Gamma and Beta Bursts Underlie Working Memory. Neuron 90:152–164.

Marr D (1971) Simple memory: a theory for archicortex. Philos Trans R Soc London B, Biol Sci 262:23–81.

McCarthy M, Moore-Kochlacs C, Gu X, Boyden E, Han X, Kopell N (2011) Striatal origin of the pathologic beta oscillations in Parkinson's disease. Proc Natl Acad Sci U S A 108:11620–11625.

McCormick DA, Connors BW, Lighthall JW, Prince DA (1985) Comparative electrophysiology of pyramidal and sparsely spiny stellate neurons of the neocortex. https://doi.org/101152/jn1985544782 54:782–806.

Mikofski M (2021) polyfitZero - File Exchange - MATLAB Central.

Minkeviciene R, Rheims S, Dobszay MB, Zilberter M, Hartikainen J, Fülöp L, Penke B, Zilberter Y, Harkany T, Pitkänen AA, Tanila H (2009) Amyloid β-induced neuronal hyperexcitability triggers progressive epilepsy. J Neurosci 29:3453–3462.

Minoshima S, Giordani B, Berent S, Frey KA, Foster NL, Kuhl DE (1997) Metabolic reduction in the posterior cingulate cortex in very early Alzheimer's disease. Ann Neurol 42:85–94.

Mitchell AS, Czajkowski R, Zhang N, Jeffery K, Nelson AJD (2018) Retrosplenial cortex and its role in spatial cognition. Brain Neurosci Adv 2:239821281875709.

Mitchell SJ, Ranck JB (1980) Generation of theta rhythm in medial entorhinal cortex of freely moving rats. Brain Res 189:49–66.

Mitra P, Bokil H (2008) Observed Brain Dynamics.

Moca V V., Bârzan H, Nagy-Dăbâcan A, Mureșan RC (2021) Time-frequency super-resolution with superlets. Nat Commun 12:1–18.

Molchan SE, Martinez RA, Hill JL, Weingartner HJ, Thompson K, Vitiello B, Sunderland T (1992) Increased cognitive sensitivity to scopolamine with age and a perspective on the scopolamine model. Brain Res Rev 17:215–226.

Mondragón-Rodríguez S, Gu N, Manseau F, Williams S (2018) Alzheimer's Transgenic Model Is Characterized by Very Early Brain Network Alterations and β-CTF Fragment Accumulation: Reversal by β-Secretase Inhibition. Front Cell Neurosci 12.

Montgomery S., Buzsáki G (2007) Gamma oscillations dynamically couple hippocampal CA3 and CA1 regions during memory task performance. Proc Natl Acad Sci U S A 104:14495–14500.

Morganti F, Stefanini S, Riva G (2013) From allo- to egocentric spatial ability in early Alzheimer's disease: A study with virtual reality spatial tasks. Cogn Neurosci 4:171–180.

Morris RE, Pandya DN, Petrides M (1999) Fiber System Linking the Mid-Dorsolateral Frontal Cortex With the Retrosplenial/Presubicular Region in the Rhesus Monkey. J Comp Neurol 407:183–192.

Morris RE, Paxinos G, Petrides M (2000) Architectonic Analysis of the Human Retrosplenial Cortex. J Comp Neurol 421:14–28.

Mucke L, Masliah E, Yu G-Q, Mallory M, Rockenstein EM, Tatsuno G, Hu K, Kholodenko D, Johnson-Wood K, McConlogue L (2000) High-Level Neuronal Expression of Aβ1–42 in Wild-Type Human Amyloid Protein Precursor Transgenic Mice: Synaptotoxicity without Plaque Formation. J Neurosci 20:4050–4058.

Mufson EJ, Pandya DN (1984) Some observations on the course and composition of the cingulum bundle in the rhesus monkey. J Comp Neurol 225:31–43.

Mullan M, Crawford F, Axelman K, Houlden H, Lilius L, Winblad B, Lannfelt L (1992) A pathogenic mutation for probable Alzheimer's disease in the APP gene at the N–terminus of β–amyloid. Nat Genet 1:345–347.

Murrell J, Farlow M, Ghetti B, Benson MD (1991) A mutation in the amyloid precursor protein associated with hereditary Alzheimer's disease. Science (80-) 254:97–99.

Nacher V, Ledberg A, Deco G, Romo R (2013) Coherent delta-band oscillations between cortical areas correlate with decision making. Proc Natl Acad Sci

110:15085–15090.

Nelson PT, Head E, Schmitt FA, Davis PR, Neltner JH, Jicha GA, Abner EL, Smith CD, Van Eldik LJ, Kryscio RJ, Scheff SW (2011) Alzheimer's disease is not "brain aging": neuropathological, genetic, and epidemiological human studies. Acta Neuropathol 2011 1215 121:571–587.

Newman EL, Gillet SN, Climer JR, Hasselmo ME (2013) Cholinergic blockade reduces theta-gamma phase amplitude coupling and speed modulation of theta frequency consistent with behavioral effects on encoding. J Neurosci 33:19635–19646.

Nitzan N, McKenzie S, Beed P, Fine English D, Oldani S, Tukker JJ, Buzsáki G, Schmitz D (2020) Propagation of hippocampal ripples to the neocortex by way of a subiculum-retrosplenial pathway. Nat Commun 11.

Nowak LG, Azouz R, Sanchez-Vives M V., Gray CM, McCormick DA (2003) Electrophysiological Classes of Cat Primary Visual Cortical Neurons In Vivo as Revealed by Quantitative Analyses. https://doi.org/101152/jn005802002 89:1541–1566.

Nunan J, Small D. (2000) Regulation of APP cleavage by alpha-, beta- and gamma-secretases. FEBS Lett 483:6–10.

O'Keefe J (1976) Place units in the hippocampus of the freely moving rat. Exp Neurol 51:78–109.

O'Keefe J, Dostrovsky J (1971) The hippocampus as a spatial map. Preliminary evidence from unit activity in the freely-moving rat. Brain Res 34:171–175.

O'Keefe J, Recce M. (1993) Phase relationship between hippocampal place units and the EEG theta rhythm. Hippocampus 3:317–330.

O'Reilly RC, Rudy JW (2001) Conjunctive representations in learning and memory: Principles of cortical and hippocampal function. Psychol Rev 108:311–345.

Oakley H, Cole SL, Logan S, Maus E, Shao P, Craft J, Guillozet-Bongaarts A, Ohno M, Disterhoft J, Van Eldik L, Berry R, Vassar R (2006) Intraneuronal β-Amyloid Aggregates, Neurodegeneration, and Neuron Loss in Transgenic Mice with Five Familial Alzheimer's Disease Mutations: Potential Factors in

Amyloid Plaque Formation. J Neurosci 26:10129–10140.

Oddo S, Caccamo A, Shepherd JD, Murphy MP, Golde TE, Kayed R, Metherate R, Mattson MP, Akbari Y, LaFerla FM (2003) Triple-transgenic model of Alzheimer's Disease with plaques and tangles: Intracellular Aβ and synaptic dysfunction. Neuron 39:409–421.

Onslow ACE, Bogacz R, Jones MW (2011) Quantifying phase-amplitude coupling in neuronal network oscillations. Prog Biophys Mol Biol 105:49–57.

Opalka AN, Huang W-Q, Liu J, Liang HL, Wang D V. (2020) Hippocampal Ripple Coordinates Retrosplenial Inhibitory Neurons during Slow-Wave Sleep. Cell Rep 30:432–441.

Osipova D, Takashima A, Oostenveld R, Fernández G, Maris E, Jensen O (2006) Theta and Gamma Oscillations Predict Encoding and Retrieval of Declarative Memory. J Neurosci 26.

Ostojic S, Brunel N, Hakim V (2009) How Connectivity, Background Activity, and Synaptic Properties Shape the Cross-Correlation between Spike Trains. J Neurosci 29:10234–10253.

Ouimet CC, Baerwald KD, Gandy SE, Greengard P (1994) Immunocytochemical localization of amyloid precursor protein in rat brain. J Comp Neurol 348:244–260.

Palop JJ, Chin J, Roberson ED, Wang J, Thwin MT, Bien-Ly N, Yoo J, Ho KO, Yu GQ, Kreitzer A, Finkbeiner S, Noebels JL, Mucke L (2007) Aberrant Excitatory Neuronal Activity and Compensatory Remodeling of Inhibitory Hippocampal Circuits in Mouse Models of Alzheimer's Disease. Neuron 55:697–711.

Palop JJ, Mucke L (2009) Epilepsy and cognitive impairments in alzheimer disease. Arch Neurol 66:435–440.

Pan G, Chen Z, Zheng H, Zhang Y, Xu H, Bu G, Zheng H, Li Y (2018) Compensatory Mechanisms Modulate the Neuronal Excitability in a Kainic Acid-Induced Epilepsy Mouse Model. Front Neural Circuits 12.

Papez J. (1937) A proposed mechanism of emotion. Arch Neurol Psychiatry 38:725–743.

Paxinos G, Franklin K (2012) Paxinos and Franklin's the Mouse Brain in Stereotaxic Coordinates. Amsterdam, Acad Press:360 p.

Per A, Richard M, David A, Tim B, John OK (2009) The Hippocampal Formation. Hippocampus B.

Petsche H, Stumpf C, Gogolak G (1962) The significance of the rabbit's septum as a relay station between the midbrain and the hippocampus I. The control of hippocampus arousal activity by the septum cells. Electroencephalogr Clin Neurophysiol 14:202–211.

Pfurtscheller G, Cooper R (1975) Frequency dependence of the transmission of the EEG from cortex to scalp. Electroencephalogr Clin Neurophysiol 38:93–96.

Philipson O, Lord A, Gumucio A, O'Callaghan P, Lannfelt L, Nilsson LNG (2010) Animal models of amyloid-??-related pathologies in Alzheimer's disease. FEBS J 277:1389–1409.

Phillips RG, LeDoux JE (1992) Differential Contribution of Amygdala and Hippocampus to Cued and Contextual Fear Conditioning. Behav Neurosci 106:274–285.

Plonsey R, Heppner DB (1967) Considerations of quasi-stationarity in electrophysiological systems. Bull Math Biophys 1967 294 29:657–664.

Prince M, Knapp M, Guerchet M, McCrone P, Prina M, Comas-Herrera A, Wittenberg R, Adelaja B, Hu B, King D, Rehill A, Salimkumar D (2014) Dementia UK: Update, Second Edition.

Prpar Mihevc S, Majdič G (2019) Canine Cognitive Dysfunction and Alzheimer's Disease – Two Facets of the Same Disease? Front Neurosci 0:604.

Psychiatry JP-A of N&, 1937 undefined (n.d.) A proposed mechanism of emotion. jamanetwork.com.

Quiroga RQ, Nadasdy Z, Ben-Shaul Y (2004) Unsupervised spike detection and sorting with wavelets and superparamagnetic clustering. Neural Comput 16:1661–1687.

R Cacace KSCB (2016) Molecular genetics of early-onset Alzheimer's disease revisited. Alzheimers Dement 12:733–748.

Ramirez S, Liu X, Lin PA, Suh J, Pignatelli M, Redondo RL, Ryan TJ, Tonegawa S (2013) Creating a false memory in the hippocampus. Science (80-) 341:387–391.

Rawlins J., Feldon J, Gray J. (1979) Septo-hippocampal connections and the hippocampal theta rhythm. Exp brain Res 37:49–63.

Remondes M, Wilson MA (2015) Slow-γ Rhythms Coordinate Cingulate Cortical Responses to Hippocampal Sharp-Wave Ripples during Wakefulness. Cell Rep 13:1327–1335.

Ren S-Q, Yao W, Yan J-Z, Jin C, Yin J-J, Yuan J, Yu S, Cheng Z (2018) Amyloid β causes excitation/inhibition imbalance through dopamine receptor 1-dependent disruption of fast-spiking GABAergic input in anterior cingulate cortex. Sci Reports 2017 81 8:1–10.

Rinne JO, Brooks DJ, Rossor MN, Fox NC, Bullock R, Klunk WE, Mathis CA, Blennow K, Barakos J, Okello AA, de LIano SRM, Liu E, Koller M, Gregg KM, Schenk D, Black R, Grundman M (2010) 11C-PiB PET assessment of change in fibrillar amyloid-β load in patients with Alzheimer's disease treated with bapineuzumab: a phase 2, double-blind, placebo-controlled, ascending-dose study. Lancet Neurol 9:363–372.

Roberson ED, Scearce-Levie K, Palop JJ, Yan F, Cheng IH, Wu T, Gerstein H, Yu GQ, Mucke L (2007) Reducing endogenous tau ameliorates amyloid β-induced deficits in an Alzheimer's disease mouse model. Science (80-) 316:750–754.

Rose NS, LaRocque JJ, Riggall AC, Gosseries O, Starrett MJ, Meyering EE, Postle BR (2016) Reactivation of latent working memories with transcranial magnetic stimulation. Science (80-) 354:1136–1139.

Rossant C, Kadir SN, Goodman DFM, Schulman J, Hunter MLD, Saleem AB, Grosmark A, Belluscio M, Denfield GH, Ecker AS, Tolias AS, Solomon S, Buzsáki G, Carandini M, Harris KD (2016) Spike sorting for large, dense electrode arrays. Nat Neurosci 2016 194 19:634–641.

Rowntree C., Bland B. (1986) An analysis of cholinoceptive neurons in the hippocampal formation by direct microinfusion. Brain Res 362:98–113.

Rule ME, Vargas-Irwin CE, Donoghue JP, Truccolo W (2017) Dissociation between sustained single-neuron spiking and transient β-LFP oscillations in primate motor cortex. J Neurophysiol 117:1524–1543.

Russell W, Burch R (1959) The Principles of Humane Experimental Technique. London: Methuen & Co.

Saito T, Matsuba Y, Mihira N, Takano J, Nilsson P, Itohara S, Iwata N, Saido T. (2014) Single App knock-in mouse models of Alzheimer's disease. Nat Neurosci 17:661–663.

Santacruz K, Lewis J, Spires T, Paulson J, Kotilinek L, Ingelsson M, Guimaraes A, DeTure M, Ramsden M, McGowan E, Forster C, Yue M, Orne J, Janus C, Mariash A, Kuskowski M, Hyman B, Hutton M, Ashe KH (2005) Tau suppression in a neurodegenerative mouse model improves memory function. Science 309:476–481.

Sargolini F, Fyhn M, Hafting T, McNaughton BL, Witter MP, Moser MB, Moser EI (2006) Conjunctive representation of position, direction, and velocity in entorhinal cortex. Science (80-) 312:758–762.

Sasaguri H, Nilsson P, Hashimoto S, Nagata K, Saito T, Strooper B De, Hardy J, Vassar R, Winblad B, Saido TC (2017) APP mouse models for Alzheimer's disease preclinical studies. EMBO J 36:2473.

Save E, Nerad L, Poucet B (2000) Contribution of Multiple Sensory Information to Place Field Stability in Hippocampal Place Cells. Hippocampus 10:64–76.

Scheff SW, Price DA, Schmitt FA, Mufson EJ (2006) Hippocampal synaptic loss in early Alzheimer's disease and mild cognitive impairment. Neurobiol Aging 27:1372–1384.

Schenk D et al. (1999) Immunization with amyloid-β attenuates Alzheimer disease-like pathology in the PDAPP mouse. Nature 400:173–177.

Scheuner D et al. (1996) Secreted amyloid β-protein similar to that in the senile plaques of Alzheimer's disease is increased in vivo by the presenilin 1 and 2 and APP mutations linked to familial Alzheimer's disease. Nat Med 2:864–870.

Schmued L, Raymick J, Tolleson W, Sarkar S, Zhang YH, Bell-Cohn A (2012)

Introducing Amylo-Glo, a novel fluorescent amyloid specific histochemical tracer especially suited for multiple labeling and large scale quantification studies. J Neurosci Methods 209:120–126.

Schultz C, Engelhardt M (2014) Anatomy of the Hippocampal Formation. Hippocampus Clin Neurosci 34:6–17.

Sederberg P., Schulze-Bonhage A, Madsen J., Bromfield E., McCarthy D., Brandt A, MS T, MJ K (2007) Hippocampal and neocortical gamma oscillations predict memory formation in humans. Cereb Cortex 17:1190–1196.

Sederberg P, Kahana M, … MH-J of, 2003 undefined (2003) Theta and gamma oscillations during encoding predict subsequent recall. Soc Neurosci.

Seth AK, Barrett AB, Barnett L (2015) Granger Causality Analysis in Neuroscience and Neuroimaging. J Neurosci 35:3293–3297.

Shankar GM, Bloodgood BL, Townsend M, Walsh DM, Selkoe DJ, Sabatini BL (2007) Natural Oligomers of the Alzheimer Amyloid-β Protein Induce Reversible Synapse Loss by Modulating an NMDA-Type Glutamate Receptor-Dependent Signaling Pathway. J Neurosci 27:2866–2875.

Sharma K (2019) Cholinesterase inhibitors as Alzheimer's therapeutics. Mol Med Rep 20:1479.

Sharott A (2005) Dopamine depletion increases the power and coherence of beta-oscillations in the cerebral cortex and subthalamic nucleus of the awake rat. Eur J Neurosci 21:1413–1422.

Sharott A, Magill PJ, Harnack D, Kupsch A, Meissner W, Brown P (2005) Dopamine depletion increases the power and coherence of β-oscillations in the cerebral cortex and subthalamic nucleus of the awake rat. Eur J Neurosci 21:1413–1422.

Shen J, Kelleher RJ (2007) The presenilin hypothesis of Alzheimer's disease: Evidence for a loss-of-function pathogenic mechanism. Proc Natl Acad Sci 104:403–409.

Sherman MA, Lee S, Law R, Haegens S, Thorn CA, Hämäläinen MS, Moore CI, Jones SR (2016) Neural mechanisms of transient neocortical beta rhythms: Converging evidence from humans, computational modeling, monkeys, and

mice. Proc Natl Acad Sci U S A 113:E4885.

Shimono K, Brucher F, Granger R, Lynch G, Taketani M (2000) Origins and Distribution of Cholinergically Induced β Rhythms in Hippocampal Slices. J Neurosci 20:8462–8473.

Shin H, Law R, Tsutsui S, Moore CI, Jones SR (2017) The rate of transient beta frequency events predicts behavior across tasks and species. Elife 6.

Shute CC., Lewis P. (1967) The asending cholinergic reticular system: neocortical, olfactory and subcortical projections. Brain 90:497–520.

Siapas AG, Lubenov E V., Wilson MA (2005) Prefrontal Phase Locking to Hippocampal Theta Oscillations. Neuron 46:141–151.

Sirota A, Montgomery S, Fujisawa S, Isomura Y, Zugaro M, Buzsáki G (2008) Entrainment of Neocortical Neurons and Gamma Oscillations by the Hippocampal Theta Rhythm. Neuron 60:683–697.

Smith DM, Bulkin DA (2014) The Form and Function of Hippocampal Context Representations. Neurosci Biobehav Rev 0:52.

Snyder E., Nong Y, Almeida C., Paul S, Moran T, Choi E., Nairn A., Salter M., Lombroso P., Gouras G., Greengard P (2005) Regulation of NMDA receptor trafficking by amyloid-beta. Nat Neurosci 8:1051–1058.

Solstad T, Boccara CN, Kropff E, Moser MB, Moser EI (2008) Representation of geometric borders in the entorhinal cortex. Science (80-) 322:1865–1868.

Spillantini MG, Murrell JR, Goedert M, Farlow MR, Klug A, Ghetti B (1998) Mutation in the tau gene in familial multiple system tauopathy with presenile dementia. Proc Natl Acad Sci 95:7737–7741.

Spitzer B, Haegens S (2017) Beyond the status quo: A role for beta oscillations in endogenous content (RE)activation. eNeuro 4.

Srinivasan R, Tucker DM, Murias M (1998) Estimating the spatial Nyquist of the human EEG. Behav Res Methods, Instruments Comput 30:8–19.

Stackman RW, Clark AS, Taube JS (2002) Hippocampal spatial representations require vestibular input. Hippocampus 12:291–303.

Stam CJ, Nolte G, Daffertshofer A (2007) Phase lag index: assessment of

functional connectivity from multi channel EEG and MEG with diminished bias from common sources. Hum Brain Mapp 28:1178–1193.

Stark E, Abeles M (2007) Predicting Movement from Multiunit Activity. J Neurosci 27:8387–8394.

Stinstra JG, Peters MJ (1998) The volume conductor may act as a temporal filter on the ECG and EEG. Med Biol Eng Comput 36:711–716.

Stokes PA, Purdon PL (2017) A study of problems encountered in Granger causality analysis from a neuroscience perspective. Proc Natl Acad Sci U S A 114.

Stoub T., DeToledo-Morrell L, Stebbins G., Leurgans S, Bennett D., Shah R. (2006) Hippocampal disconnection contributes to memory dysfunction in individuals at risk for Alzheimer's disease. Proc Natl Acad Sci U S A 103:10041–10045.

Sturchler-Pierrat C, Abramowski D, Duke M, Wiederhold KH, Mistl C, Rothacher S, Ledermann B, Bürki K, Frey P, Paganetti PA, Waridel C, Calhoun ME, Jucker M, Probst A, Staufenbiel M, Sommer B (1997) Two amyloid precursor protein transgenic mouse models with Alzheimer disease-like pathology. Proc Natl Acad Sci U S A 94:13287–13292.

Tamaoka A, Odaka A, Ishibashi Y, Usami M, Sahara N, Suzuki N, Nukina N, Mizusawa H, Shoji S, Kanazawa I (1994) APP717 missense mutation affects the ratio of amyloid beta protein species (A beta 1-42/43 and a beta 1-40) in familial Alzheimer's disease brain. J Biol Chem 269:32721–32724.

Tass P, Rosenblum MG, Weule J, Kurths J, Pikovsky A, Volkmann J, Schnitzler A, Freund HJ (1998) Detection of n:m phase locking from noisy data: application to magnetoencephalography. Phys Rev Lett 81.

Taube J, Muller R, Ranck J (1990) Head-direction cells recorded from the postsubiculum in freely moving rats. I. Description and quantitative analysis. J Neurosci 10:420–435.

TCW J, Goate AM (2017) Genetics of β-Amyloid Precursor Protein in Alzheimer's Disease. Cold Spring Harb Perspect Med 7:a024539.

Terry RD, Masliah E, Salmon DP, Butters N, DeTeresa R, Hill R, Hansen LA,

Katzman R (1991) Physical basis of cognitive alterations in alzheimer's disease: Synapse loss is the major correlate of cognitive impairment. Ann Neurol 30:572–580.

Thal DR, Rüb U, Orantes M, Braak H (2002) Phases of Aβ-deposition in the human brain and its relevance for the development of AD. Neurology 58:1791–1800.

Tinkhauser G, Torrecillos F, Duclos Y, Tan H, Pogosyan A, Fischer P, Carron R, Welter ML, Karachi C, Vandenberghe W, Nuttin B, Witjas T, Régis J, Azulay JP, Eusebio A, Brown P (2018) Beta burst coupling across the motor circuit in Parkinson's disease. Neurobiol Dis 117:217–225.

Todd TP, Bucci DJ (2015) Retrosplenial Cortex and Long-Term Memory: Molecules to Behavior. Neural Plast 2015.

Torrecillos F, Tinkhauser G, Fischer P, Green AL, Aziz TZ, Foltynie T, Limousin P, Zrinzo L, Ashkan K, Brown P, Tan H (2018) Modulation of beta bursts in the subthalamic nucleus predicts motor performance. J Neurosci 38:8905–8917.

Tort ABL, Komorowski R, Eichenbaum H, Kopell N (2010) Measuring Phase-Amplitude Coupling Between Neuronal Oscillations of Different Frequencies. J Neurophysiol 104:1195.

Tort ABL, Komorowski RW, Manns JR, Kopell NJ, Eichenbaum H (2009) Theta-gamma coupling increases during the learning of item-context associations. Proc Natl Acad Sci U S A 106:20942–20947.

Traub RD, Whittington MA, Buhl EH, Jefferys JGR, Faulkner HJ (1999) On the Mechanism of the γ → β Frequency Shift in Neuronal Oscillations Induced in Rat Hippocampal Slices by Tetanic Stimulation. J Neurosci 19:1088–1105.

Tremmel C, Herff C, Sato T, Rechowicz K, Yamani Y, Krusienski DJ (2019) Estimating Cognitive Workload in an Interactive Virtual Reality Environment Using EEG. Front Hum Neurosci 0:401.

Treviño M, Vivar C, Gutiérrez R (2007) β/γ Oscillatory Activity in the CA3 Hippocampal Area is Depressed by Aberrant GABAergic Transmission from the Dentate Gyrus after Seizures. J Neurosci 27:251–259.

Trojanowski JQ, Lee VM-Y (2005) Pathological tau: a loss of normal function or a gain in toxicity? Nat Neurosci 2005 89 8:1136–1137.

United Nations, Department of Economic and Social Affairs PD (2015) World Population Ageing 2015.

van Ede F, Maris E (2013) Somatosensory Demands Modulate Muscular Beta Oscillations, Independent of Motor Demands. J Neurosci 33:10849–10857.

van Ede F, Quinn AJ, Woolrich MW, Nobre AC (2018) Neural Oscillations: Sustained Rhythms or Transient Burst-Events? Trends Neurosci 41:415–417.

van Groen T, Wyss JM (1992) Connections of the retrosplenial dysgranular cortex in the rat. J Comp Neurol 315:200–216.

Van Groen T, Wyss JM (2003) Connections of the retrosplenial granular b cortex in the rat. J Comp Neurol 463:249–263.

Vanderwolf C. (1969) Hippocampal electrical activity and voluntary movement in the rat. Electroencephalogr Clin Neurophysiol 26:407–418.

Vanderwolf CH, Leung LS (1982) Effects of entorhinal, cingulate and neocortical lesions on atropine resistant hippocampal RSA. Neurosci Lett:S501.

Vann SD, Aggleton JP (2002) Extensive cytotoxic lesions of the rat retrosplenial cortex reveal consistent deficits on tasks that tax allocentric spatial memory. Behav Neurosci 116:85–94.

Vann SD, Aggleton JP, Maguire EA (2009) What does the retrosplenial cortex do? Nat Rev Neurosci 10:792–802.

Varela F, Lachaux J., Rodriguez E, Martinerie J (2001) The brainweb: phase synchronization and large-scale integration. Nat Rev Neurosci 2:229–239.

Vedder LC, Miller AMP, Harrison MB, Smith DM (2017) Retrosplenial Cortical Neurons Encode Navigational Cues, Trajectories and Reward Locations during Goal Directed Navigation. Cereb Cortex 27:3713–3723.

Verret L, Mann EO, Hang GB, Barth AMI, Cobos I, Ho K, Devidze N, Masliah E, Kreitzer AC, Mody I, Mucke L, Palop JJ (2012) Inhibitory interneuron deficit links altered network activity and cognitive dysfunction in alzheimer model.

Cell 149:708–721.

Vogt BA (1976) Retrosplenial cortex in the rhesus monkey: A cytoarchitectonic and golgi study. J Comp Neurol 169:63–97.

Vogt BA, Miller MW (1983) Cortical connections between rat cingulate cortex and visual, motor, and postsubicular cortices. J Comp Neurol 216:192–210.

Vogt BA, Vogt L, Farber NF (2004) Chapter 22 - Cingulate Cortex and Disease Models. In: The Rat Nervous System (Third Edition), pp 705–727.

Von Stein A, Sarnthein J (2000) Different frequencies for different scales of cortical integration: From local gamma to long range alpha/theta synchronization. Int J Psychophysiol 38:301–313.

Walker ML, Anderson DC, Herndon JG, Walker LC (2009) Ovarian aging in squirrel monkeys (Saimiri sciureus). Reproduction 138:793–799.

Walsh C, Drinkenburg WHIMHIM, Ahnaou A (2017) Neurophysiological assessment of neural network plasticity and connectivity: Progress towards early functional biomarkers for disease interception therapies in Alzheimer's disease. Neurosci Biobehav Rev 73:340–358.

Walsh C, Ridler T, Garrido MG, Witton J, Randall AD, Brown JT (2021) Beta bursting in the retrosplenial cortex is a neurophysiological correlate of environmental novelty which is disrupted in a mouse model of Alzheimer's disease. bioRxiv:2021.04.26.441462.

Wang P, Yang G, Mosier DR, Chang P, Zaidi T, Gong Y-D, Zhao N-M, Dominguez B, Lee K-F, Gan W-B, Zheng H (2005) Defective Neuromuscular Synapses in Mice Lacking Amyloid Precursor Protein (APP) and APP-Like Protein 2. J Neurosci 25:1219–1225.

Wang Q et al. (2020) The Allen Mouse Brain Common Coordinate Framework: A 3D Reference Atlas. Cell 181:936-953.e20.

Wang X., Buzsáki G (1996) Gamma oscillation by synaptic inhibition in a hippocampal interneuronal network model. J Neurosci 16:6402–6413.

Weingarten MD, Lockwood AH, Hwo SY, Kirschner MW (1975) A protein factor essential for microtubule assembly. Proc Natl Acad Sci U S A 72:1858–1862.

Westerman MA, Cooper-Blacketer D, Mariash A, Kotilinek L, Kawarabayashi T, Younkin LH, Carlson GA, Younkin SG, Ashe KH (2002) The Relationship between Aβ and Memory in the Tg2576 Mouse Model of Alzheimer's Disease. J Neurosci 22:1858–1867.

Whitesell JD, Buckley AR, Knox JE, Kuan L, Graddis N, Pelos A, Mukora A, Wakeman W, Bohn P, Ho A, Hirokawa KE, Harris JA (2019) Whole brain imaging reveals distinct spatial patterns of amyloid beta deposition in three mouse models of Alzheimer's disease. J Comp Neurol 527:2122–2145.

Whittington M., Traub R., Jefferys J. (1995) Synchronized oscillations in interneuron networks driven by metabotropic glutamate receptor activation. Nature 373:612–615.

Whittington MA, Traub RD, Kopell N, Ermentrout B, Buhl EH (2000) Inhibition-based rhythms: experimental and mathematical observations on network dynamics. Int J Psychophysiol 38:315–336.

Williams DR (2006) Tauopathies: Classification and clinical update on neurodegenerative diseases associated with microtubule-associated protein tau. Intern Med J 36:652–660.

Wittenberg R, Knapp M, Hu B, Comas-Herrera A, King D, Rehill A, Shi C, Banerjee S, Patel A, Jagger C, Kingston A (2019) The costs of dementia in England. Int J Geriatr Psychiatry 34:1095.

Witter MP, Amaral DG (1991) Entorhinal cortex of the monkey: V. Projections to the dentate gyrus, hippocampus, and subicular complex. J Comp Neurol 307:437–459.

Witter MP, Groenewegen HJ (1990) Chapter 4 The subiculum: cytoarchitectonically a simple structure, but hodologically complex. In: Progress in Brain Research, pp 47–58. Elsevier.

Wright AL, Zinn R, Hohensinn B, Konen LM, Beynon SB, Tan RP, Clark IA, Abdipranoto A, Vissel B (2013) Neuroinflammation and Neuronal Loss Precede Aβ Plaque Deposition in the hAPP-J20 Mouse Model of Alzheimer's Disease. PLoS One 8.

Wyss JM, Van Groen T (1992) Connections between the retrosplenial cortex and

the hippocampal formation in the rat: a review. Hippocampus 2:1–11.

Zhang L, Lee J, Rozell C, Singer AC (2019) Sub-second dynamics of theta-gamma coupling in hippocampal CA1. Elife 8.

Zhang Y, Chen Y, Bressler SL, Ding M (2008) Response preparation and inhibition: The role of the corticalsensorimotor beta rhythm. Neuroscience 156:238–246.

9 Appendix 1

9.1 Power Spectral Analysis - SpectraWYW (While-You-Work)

```
function [SpectraStructure] = SpectraWYW(Folder,Channel)

%First selects the folder with the data, and locates all the LFP data
folder = Folder;
folder = dir(folder);
foldername = folder.folder;
subfolders = {folder.name};
subfolders = subfolders(contains(subfolders,'Day'));
subfolders = strcat(foldername,'\',subfolders);
sessionnames =
["Day1a","Day1b","Day2a","Day2b","Day3a","Day3b","Day4a","Day4b","Day5a","Day5b"];
cd(foldername);

%Starts a megaloop to analyse and cycle through each session in an animals
%folder.
for ind0 = 1:length(subfolders)

    files = dir(subfolders{ind0});
    files = files(arrayfun(@(x) ~strcmp(x.name(1),'.'),files));
    channels = {files.name};
    channels = channels(contains(channels,Channel));
    channels = strcat(subfolders{ind0},'\',channels);
    channelname = string(channels{1}(end-14:end-11));

    animalnumber = foldername(end-1:end);
    animal = strcat('Mouse',animalnumber);
    session = files.folder;
    session = session(end-4:end);

    [~,~,extension] = fileparts(channels{1});
    signals = [];

    for indch = 1
        if strcmp(extension,'.continuous')
            %Performs tracking, calculates speed and total distance travelled in m
            [x,y,~,speed_out,distance] =
TrackingNovelFamiliar(subfolders{ind0},1,'two');
            tsf = fillmissing(speed_out.ts,'linear');
            speed = speed_out.speed;
            %Imports the .continuous data into MatLab
            [signals(:,indch),~,info] = load_open_ephys_data_faster(channels{indch});
        elseif strcmp(extension,'.mat')
            [x,y,ts,speed_out,distance] =
TrackingNovelFamiliarSplitSession(subfolders{ind0});
            tsf = fillmissing(speed_out.ts,'linear');
            speed = speed_out.speed;
            %Imports the .continuous data into MatLab
            load(channels{indch});
            signals(:,indch) = sig;
            info.header.sampleRate = 30000;
        end
```

```
    end

    %Cuts the signals to the experiment duration ie 15minutes in this case
    ExpDurationMinutes = 15;
    Fs = info.header.sampleRate;
    ExpDurationFrames = (ExpDurationMinutes*60)*Fs;
    ExpDurationSeconds = ExpDurationMinutes*60;
    signals = signals(1:ExpDurationFrames,:);

    %Downsamples the signals and timestamps, to reduce computation time,
    %and detrends to remove any baseline fluctuations
    downsampleX = 30;
    signalsds = downsample(signals,downsampleX);
    signaldsdt = detrend(signalsds);

    %Set the parameters for Chronux analysis
    Fs = Fs/downsampleX;
    params.Fs = Fs;
    params.pad = 2;
    params.tapers = [2 3];
    params.err = 0;
    params.trialave = 0;
    params.segave = 0;

    %Performs multi-taper spectral analysis, firstly, for the unbinned
    %signal (ie the whole session) then for the binned signal, for each
    %frequency band. As it is not possible to manually set the bandwidth,
    %this allows us to cut off each band at the exact start and end.
    params.fpass = [1 120];
    [SpecgFull,t,fF] = mtspecgramc(signaldsdt,[1 1],params);
    SpecgFull = 10*log10(SpecgFull);

    MeanSpec = mean(SpecgFull,1);

    MeanSpec(fF>47 & fF<53) = NaN;
    MeanSpec(fF>97 & fF<103) = NaN;
    MeanSpec = fillmissing(MeanSpec,'linear');
%     params.smoothfactorlow = length(fF(fF>=3 & fF<30))/9;
%     MeanCoh(fF>=3 & fF<30) = smoothdata(MeanCoh(fF>=3 &
fF<30),'gaussian',params.smoothfactorlow);
%     params.smoothfactorhigh = length(fF(fF>=30 & fF<=120))/6;
%     MeanCoh(fF>=30 & fF<=120) = smoothdata(MeanCoh(fF>=30 &
fF<=120),'gaussian',params.smoothfactorhigh);

    fD = fF(fF>=1 & fF<5);
    fT = fF(fF>=5 & fF<12);
    fA = fF(fF>=12 & fF<20);
    fB = fF(fF>=20 & fF<30);
    fG = fF(fF>=30 & fF<=100);
    fLG = fF(fF>=30 & fF<65);
    fHG = fF(fF>=65 & fF<=120);
    MeanDelta = MeanSpec(fF>=1 & fF<5);
    MeanTheta = MeanSpec(fF>=5 & fF<12);
    MeanAlpha = MeanSpec(fF>=12 & fF<20);
    MeanBeta = MeanSpec(fF>=20 & fF<30);
    MeanGamma = MeanSpec(fF>=30 & fF<=100);
    MeanLowGamma = MeanSpec(fF>=30 & fF<65);
    MeanHighGamma = MeanSpec(fF>=65 & fF<=120);
```

```
clearvars PowerD PowerT PowerA PowerB PowerG PowerLG PowerHG
clearvars FreqD FreqT FreqA FreqB FreqG FreqLG FreqHG

%Calculates the raw power of each speed bin as the mean power in each
%frequency band, and the freqency, as the frequency at which the power
%is maximal.
PowerD = mean(MeanDelta);
PowerT = mean(MeanTheta);
PowerA = mean(MeanAlpha);
PowerB = mean(MeanBeta);
PowerG = mean(MeanGamma);
PowerLG = mean(MeanLowGamma);
PowerHG = mean(MeanHighGamma);

PeakDC = max(MeanDelta,[],2);
PeaksDC = find(MeanDelta==PeakDC);
FreqD = median(fD(PeaksDC));
PeakTC = max(MeanTheta,[],2);
PeaksTC = find(MeanTheta==PeakTC);
FreqT = median(fT(PeaksTC));
PeakAC = max(MeanAlpha,[],2);
PeaksAC = find(MeanAlpha==PeakAC);
FreqA = median(fA(PeaksAC));
PeakBC = max(MeanBeta,[],2);
PeaksBC = find(MeanBeta==PeakBC);
FreqB = median(fB(PeaksBC));
PeakGC = max(MeanGamma,[],2);
PeaksGC = find(MeanGamma==PeakGC);
FreqG = median(fG(PeaksGC));
PeakLGC = max(MeanLowGamma,[],2);
PeaksLGC = find(MeanLowGamma==PeakLGC);
FreqLG = median(fLG(PeaksLGC));
PeakHGC = max(MeanHighGamma,[],2);
PeaksHGC = find(MeanHighGamma==PeakHGC);
FreqHG = median(fHG(PeaksHGC));

%Stores all data of interest as a non-scalar structure, making it easy
%to look at and compare data from different sessions.
SpectraStructure(ind0).Session = session;
SpectraStructure(ind0).Parameters = params;
SpectraStructure(ind0).fF = fF;
SpectraStructure(ind0).MeanSpectrum = MeanSpec;
SpectraStructure(ind0).SpecgFull = SpecgFull;
SpectraStructure(ind0).X = x;
SpectraStructure(ind0).Y = y;
SpectraStructure(ind0).Distance = distance;
SpectraStructure(ind0).Speed = speed;
SpectraStructure(ind0).DeltaPower = PowerD;
SpectraStructure(ind0).ThetaPower = PowerT;
SpectraStructure(ind0).AlphaPower = PowerA;
SpectraStructure(ind0).BetaPower = PowerB;
SpectraStructure(ind0).GammaPower = PowerG;
SpectraStructure(ind0).LowGammaPower = PowerLG;
SpectraStructure(ind0).HighGammaPower = PowerHG;
SpectraStructure(ind0).DeltaFrequency = FreqD;
SpectraStructure(ind0).ThetaFrequency = FreqT;
SpectraStructure(ind0).AlphaFrequency = FreqA;
```

```
    SpectraStructure(ind0).BetaFrequency = FreqB;
    SpectraStructure(ind0).GammaFrequency = FreqG;
    SpectraStructure(ind0).LowGammaFrequency = FreqLG;
    SpectraStructure(ind0).HighGammaFrequency = FreqHG;

end

%Session Analysis
MeanSpec = cell2mat({SpectraStructure.MeanSpectrum}');
NovelSpecs = MeanSpec(1:8:9,:);
FamiliarSpecs = MeanSpec([2 3 4 5 6 7 8 10],:);
MeanNovelSpec = mean(NovelSpecs);
MeanFamiliarSpec = mean(FamiliarSpecs);
NovelStd = std(NovelSpecs,0,1);
FamiliarStd = std(FamiliarSpecs,0,1);
NovelSEM = NovelStd/sqrt(size(NovelSpecs,1));
FamiliarSEM = FamiliarStd/sqrt(size(FamiliarSpecs,1));

% %Creates the mean spectrums for Novel and Familiar with SEM.
Spectrums = strcat(foldername,'\','Spectrums');
mkdir(Spectrums);
cd(Spectrums);
figure2name = strcat(animal,'-',Channel,'-','SpectrumFamiliarity');
figure('Name',figure2name);
NovelSpec = shadedErrorBar(fF,MeanNovelSpec,NovelSEM);
set(NovelSpec.edge,'LineStyle','none')
NovelSpec.mainLine.LineWidth = 1.5;
NovelSpec.mainLine.Color = [1 0 0];
NovelSpec.patch.FaceColor = [0.6 0 0];
hold on;
FamiliarSpec = shadedErrorBar(fF,MeanFamiliarSpec,FamiliarSEM);
set(FamiliarSpec.edge,'LineStyle','none')
FamiliarSpec.mainLine.LineWidth = 1.5;
FamiliarSpec.mainLine.Color = [0 0 1];
FamiliarSpec.patch.FaceColor = [0 0 0.6];
alpha(0.3);
set(gca,'LineWidth',1.5);
set(gca,'FontSize',12)
xlabel('Frequency (Hz)','fontsize',14);
ylabel('Power (DB)','fontsize',14);
legend({'Novel','Familiar'});
legend boxoff
set(gca,'box','off');
hgsave(figure2name)

%Save the finished data structure as a .mat file for later use
SpectraFolder = strcat(foldername(1:end-2),'Analysed\','Spectra');
mkdir(SpectraFolder);
cd(SpectraFolder);
save(strcat('Spectra','-',(animal),'-',Channel,'.mat'),'SpectraStructure');

end
```

Published with MATLAB® R2019b

9.2 Beta Burst Detection - BurstDetectionWYW (While-You-Work)

```
function [EventData] = BurstDetectionWYW(Folder,Channel)

%First selects the folder with the data, and locates all the LFP data
folder = Folder;
folder = dir(folder);
foldername = folder.folder;
subfolders = {folder.name};
subfolders = subfolders(contains(subfolders,'Day'));
subfolders = strcat(foldername,'\',subfolders);
sessionnames =
["Day1a","Day1b","Day2a","Day2b","Day3a","Day3b","Day4a","Day4b","Day5a","Day5b"];
cd(foldername);

%Starts a megaloop to analyse and cycle through each session in an animals
%folder.
for ind0 = 1:length(subfolders)

    files = dir(subfolders{ind0});
    files = files(arrayfun(@(x) ~strcmp(x.name(1),'.'),files));
    channels = {files.name};
    channels = channels(contains(channels,Channel));
    channels = strcat(subfolders{ind0},'\',channels);
    channelname = string(channels{1}(end-14:end-11));

    if sum(contains(["CH13","CH14","CH19","CH20"],channelname)) == 1
        location = "RSA";
    elseif sum(contains(["CH45","CH46","CH51","CH52"],channelname)) == 1
        location = "MEC";
    end

    animalnumber = Folder(end-1:end);
    animal = strcat('Mouse',animalnumber);
    session = files.folder;
    session = session(end-4:end);

    [~,~,extension] = fileparts(channels{1});

    if strcmp(extension,'.continuous')
        %Performs tracking, calculates speed and total distance travelled in m
        [x,y,~,speed_out,distance] = TrackingNovelFamiliar(subfolders{ind0},1,'two');
        tsf = fillmissing(speed_out.ts,'linear');
        speed = speed_out.speed;
        %Imports the .continuous data into MatLab
        signals = [];
        [signals(:,1),~,info] = load_open_ephys_data_faster(channels{1});
    elseif strcmp(extension,'.mat')
        [x,y,ts,speed_out,distance] =
TrackingNovelFamiliarSplitSession(subfolders{ind0});
        tsf = fillmissing(speed_out.ts,'linear');
        speed = speed_out.speed;
        %Imports the .continuous data into MatLab
        load(channels{1});
        signals(:,1) = sig;
        info.header.sampleRate = 30000;
    end
```

```
    %Cuts the signals to the experiment duration ie 15minutes in this case
    ExpDurationMinutes = 15;
    Fs = info.header.sampleRate;
    ExpDurationFrames = (ExpDurationMinutes*60)*Fs;
    ExpDurationSeconds = ExpDurationMinutes*60;
    signals = signals(1:ExpDurationFrames,:);

    %Downsamples the signals and timestamps, to reduce computation time,
    %and detrends to remove any baseline fluctuations
    downsampleX = 10;
    Fs = Fs/downsampleX;
    ExpDurationFrames = ExpDurationFrames/downsampleX;
    signalsds = downsample(signals,downsampleX);
    signalsdsdt = detrend(signalsds);
    signalmagnitude = abs(hilbert(signalsdsdt));
    %     noisethreshold = prctile(signalmagnitude,99.99);
    %     noisyframes = signalmagnitude > noisethreshold;
    %     noisysecs = reshape(noisyframes,[Fs,ExpDurationSeconds]);
    %     noisysecs = sum(noisysecs,1);
    %     noiseindex = noisysecs>0;
    %     signalmatrix = reshape(signalsdsdt,[Fs,ExpDurationSeconds]);
    %     signalmatrix(:,noiseindex) = [];
    %     signalsdsdt = signalmatrix(:);

    %Set the parameters for Chronux analysis
    params.Fs = Fs;
    params.pad = 2;
    params.tapers = [1 1];
    params.fpass = [1 120];
    params.err = 0;
    params.trialave = 0;
    params.segave = 0;

    % Creates a filter in the beta frequency band (20-30Hz) and applies
    %it to the signal. Then uses a hilbert transform to find the envelope
    %amplitude of the signal, and the instantaneous phase.
    betafilter =
designfilt('bandpassiir','FilterOrder',2,'HalfPowerFrequency1',20,'HalfPowerFrequency2',
30,'DesignMethod','butter','SampleRate',Fs);
    betasignal = filtfilt(betafilter,signalsdsdt);
    betasignalmagnitude = abs(hilbert(betasignal));
    noisethreshold = median(betasignalmagnitude)+10*mad(betasignalmagnitude,1);
    betasignalmagnitude(betasignalmagnitude>noisethreshold) = 0;
    zscorebetasignalmagnitude = zscore(betasignalmagnitude);
    betasignalphase = rad2deg(angle(hilbert(betasignal)));

    %Sets the beta burst detection parameters. The burst must cross 3 standard
    %deviations from the mean for at least 150ms, to be classified.
    burststdthreshold = 2;
    minbetaburstdurationms = 150;
    minbetaburstsamples = Fs*(minbetaburstdurationms/1000);
    minburstcycles = 3;

    %The amplitude detection parameter is applied to the beta signal, in order
    %to find indexes of when the burst reaches the detection threshold. A second
threshold of half the detection threshold
    % is also used to find the starts and stops of each putative burst, in
```

```
    % order to include the sides of each burst.
    burstdetectionthreshold = zscorebetasignalmagnitude>=burststdthreshold;
    burstsidethreshold = zscorebetasignalmagnitude>=burststdthreshold/2;

    %The two thresholds are combined so that a burst would show as 01210,
    %ie below threshold 1, above threshold 1, above thresholds 1+2, and
    %then back down.
    BdtBst = burstdetectionthreshold + burstsidethreshold;
    difBdtBst = diff(BdtBst);
    %Find is used to find where these changes between threshold levels
    %occur in the signal.
    [blocations,~,bchanges] = find(difBdtBst);
    revblocations = flipud(blocations);
    %strfind is used to find the starts of sequences with the change
    %+1+1-1-1, ie 01210, and also the starts of sequences with the change
    %-1-1+1+1, ie the reverse, to find the stops of these 01210 sequences.
    bpatternseek = strfind(bchanges',[1 1 -1 -1]);
    revbpatternseek = strfind(flipud(bchanges)',[-1 -1 1 1]);
    betaburststarts = blocations(bpatternseek);
    betaburststops = flipud(revblocations(revbpatternseek));
    %These stretches are then removed from the data, to turn it into 01110,
    %so that bursts that don't return to 0, such as 0121210, can be
    %detected without redetecting the previously discovered bursts. These
    %bursts that don't return to 0 are referred to as "waves" for now.
    for idy = 1:length(betaburststarts)
        burstdetectionthreshold(betaburststarts(idy):betaburststops(idy)) = 0;
    end
    %Bursts that started before recording are discarded, as are those that stopped after
recording.
    if betaburststops(1)<betaburststarts(1)
        betaburststops = betaburststops(2:end);
    end
    if betaburststarts(end)>betaburststops(end)
        betaburststarts = betaburststarts(1:end-1);
    end
    %In order to detect "waves", we can just look at the detection
    %threshold and only pick out the 2's of 0121's, rather than 121's. This
    %method prevents excessive combination of adjacent waves into extra long
    %events.
    difBdt = diff(burstdetectionthreshold);
    [wlocations,~,wchanges] = find(difBdt);
    revwlocations = flipud(wlocations);
    wpatternseek = strfind(wchanges',[1 -1]);
    revwpatternseek = strfind(flipud(wchanges)',[-1 1]);
    wavestarts = wlocations(wpatternseek);
    wavestops = flipud(revwlocations(revwpatternseek)+1);

    %"Waves" that started before recording are discarded, as are those that stopped
after recording.
    if length(wavestops)>1
        if wavestops(1)<wavestarts(1)
            wavestops = wavestops(2:end);
        end
        if wavestarts(end)>wavestops(end)
            wavestarts = wavestarts(1:end-1);
        end

        wavelength = wavestops-wavestarts;
```

```
        wavestarts = wavestarts(wavelength>minbetaburstsamples);
        wavestops = wavestops(wavelength>minbetaburstsamples);
    else
    end

    %A previosly assigned MINIMUM DURATION parameter is applied to find bursts with
    %sufficient duration to be classified, while all shorter events are removed.
    betaburstlength = betaburststops-betaburststarts;
    betaburststarts = betaburststarts(betaburstlength>minbetaburstsamples);
    betaburststops = betaburststops(betaburstlength>minbetaburstsamples);

    %The burst starts and "wave" starts are combined and put in
    %ascending order, as are the stops. These starts and stops are now the indexes of
all putative bursts.
    ratiob2w = length(betaburststarts)/length(wavestarts);
    betaburststarts = [betaburststarts;wavestarts];
    betaburststops = [betaburststops;wavestops];
    [betaburststarts,sortI] = sort(betaburststarts);
    betaburststops = betaburststops(sortI);
    betaburstlength = betaburststops-betaburststarts;

    %     burstphase = cell(length(betaburststarts),1);
    %     burstcycles = zeros(length(betaburststarts),1);
    %     for indbcycles = 1:length(betaburststarts)
    %         burstphase{indbcycles} =
betasignalphase(betaburststarts(indbcycles):betaburststops(indbcycles),:);
    %         minBValue1 = min(burstphase{indbcycles});
    %         paddedBSignal1 = [minBValue1;burstphase{indbcycles};minBValue1];
    %         %As the phase signal is constantly increasing, findpeaks picks up
    %         %where each cycle ends. As there is no built in "findtroughs"
    %         %function, in order to find the start of each cycle, this is all
    %         %repeated for the -ve of the phase signal.
    %         [bcyclestart,bcyclestartloc] = findpeaks(paddedBSignal1);
    %         minBValue2 = min(-burstphase{indbcycles});
    %         paddedBSignal2 = [minBValue2;-burstphase{indbcycles};minBValue2];
    %         [bcyclestop,bcyclestoploc] = findpeaks(paddedBSignal2);
    %         bcyclestop = -bcyclestop;
    %         if bcyclestoploc(1)<bcyclestartloc(1)
    %             bcyclestop = bcyclestop(2:end);
    %         end
    %         if bcyclestartloc(end)>bcyclestoploc(end)
    %             bcyclestart = bcyclestart(1:end-1);
    %         end
    %         %The length of each cycle is calculated, and then the total length
    %         %of all these cycles is calculated, and then divided by 360degrees
    %         %(a full cycle phase), and rounded down to get the number of
    %         %complete burst cycles.
    %         bcyclelength = bcyclestart-bcyclestop;
    %         totalbcycles = sum(bcyclelength);
    %         burstcycles(indbcycles) = floor(totalbcycles/360);
    %     end

    %Artefact removal on a burst by burst basis, by detecting large almost
    %instantaneous changes in the unfiltered LFP.
    for ib = 1:length(betaburststarts)
        pbm(ib) = max(betasignalmagnitude(betaburststarts(ib):betaburststops(ib),:));
    end
    discard = isoutlier(pbm);
```

```
    params.discardrate = sum(discard)/length(betaburststarts);
    betaburststarts(discard) = [];
    betaburststops(discard) = [];
    betaburstlength(discard) = [];

    %Now the burst start and stop indexes of all putative bursts that do
    %not meet these 2 criteria have been removed, all remaining can
    %be counted as bursts, so we can calculate the total number of bursts
    %in this session, as well as the duration of each burst in
    %milliseconds.
    betaburstnumber = length(betaburstlength);
    burstduration = (betaburstlength/Fs)*1000;
    meanburstduration = mean(burstduration);
    stdburstduration = std(burstduration);
    semburstduration = stdburstduration/sqrt(length(burstduration));
    betaburststartsds = ceil(betaburststarts./Fs);
    betaburststopsds = ceil(betaburststops./Fs);

    %Finally the burst start and stop indexes are used to isolate the
    %filtered and unfiltered bursts, and the peak magnitude of each burst
    %is ascertained. These are averaged, and SEM calculated to gain an
    %idea of the burst dynamics for the session.
    betabursts = cell(betaburstnumber,1);
    betaburstsunfiltered = cell(betaburstnumber,1);
    peakburstmagnitude = zeros(betaburstnumber,1);
    if betaburstnumber>0
        for ind6 = 1:betaburstnumber
            betabursts{ind6} = betasignal(betaburststarts(ind6):betaburststops(ind6),:);
            betaburstsunfiltered{ind6} =
signalsdsdt(betaburststarts(ind6):betaburststops(ind6),:);
            peakburstmagnitude(ind6) =
max(betasignalmagnitude(betaburststarts(ind6):betaburststops(ind6),:));
            burstphase{ind6} =
betasignalphase(betaburststarts(ind6):betaburststops(ind6),:);
            burstspeed(ind6) =
mean(speed(:,betaburststartsds(ind6):betaburststopsds(ind6)));
            %         burstx(ind6) =
nanmean(x(betaburststartscds(ind6):betaburststopscds(ind6)));
            %         bursty(ind6) =
nanmean(y(betaburststartscds(ind6):betaburststopscds(ind6)));

            burstmiddle = length(betabursts{ind6})/2;
            [~,locs] = findpeaks(betabursts{ind6},'MinPeakDistance',100);
            [~,closestpeak] = min(abs(locs-burstmiddle));
            middlepeak(ind6) = locs(closestpeak);
        end
        meanburstmagnitude = mean(peakburstmagnitude);
        stdburstmagnitude = std(peakburstmagnitude);
        semburstmagnitude = stdburstmagnitude/sqrt(length(peakburstmagnitude));
        biggestburstleftlength = middlepeak(find(betaburstlength ==
max(betaburstlength)));
        biggestburstrightlength = max(betaburstlength)-biggestburstleftlength;

        %As in (Shin et al 2017), to attempt to determine the mechanism
        %underlying beta bursts (bursty vs dynamic amplitude modulation),
        %calculate the time lag modulus for the burst and non-burst segments.
        [ifq] = instfreq(betasignal,Fs);
        medianbf = median(ifq);
```

```
        for indb = 1:betaburstnumber
            [~,locs] = findpeaks(betabursts{indb},'MinPeakDistance',100);
            tla(indb) = locs(end)-locs(1);
            %Also calculate average burst frequency
            burstfreq(indb) = Fs/((locs(end)-locs(1))/(length(locs)-1));
        end
        tlmb = (tla - medianbf.*round(tla./medianbf))/medianbf;
        tlmbh = histcounts(tlmb,-0.5:0.1:0.5,'Normalization','probability');
        for indb = 1:betaburstnumber
            if indb == 1
                nonburstsignal = betasignal(1:betaburststarts(indb),:);
            else
                nonburstsignal = betasignal(betaburststops(indb-
1):betaburststarts(indb),:);
            end
            if length(nonburstsignal)>=200
                [~,locs] = findpeaks(nonburstsignal,'MinPeakDistance',100);
                tlb(indb) = locs(end)-locs(1);
                %Also calculate average burst frequency
                nonburstfreq(indb) = Fs/((locs(end)-locs(1))/(length(locs)-1));
            else
                tlb(indb) = NaN;
            end
        end
        tlmn = (tlb - medianbf.*round(tlb./medianbf))/medianbf;
        tlmnh = histcounts(tlmn,-0.5:0.1:0.5,'Normalization','probability');

        % Alternate Method

        MinPeakDist = Fs/40;
        for indb = 1:betaburstnumber
            [~,locsb] = findpeaks(betabursts{indb},'MinPeakDistance',MinPeakDist);
            bperiod{indb} = diff(locsb)./Fs;
            %Also calculate average burst frequency
            burstfreq(indb) = Fs/((locs(end)-locs(1))/(length(locs)-1));
            if indb == 1
                nonburstsignal = betasignal(1:betaburststarts(indb),:);
            else
                nonburstsignal = betasignal(betaburststops(indb-
1):betaburststarts(indb),:);
            end
            if length(nonburstsignal)>=2*(Fs/30)
                [~,locsn] = findpeaks(nonburstsignal,'MinPeakDistance',MinPeakDist);
                %Also calculate average burst frequency
                nonburstfreq(indb) = Fs/((locs(end)-locs(1))/(length(locs)-1));
                nbperiod{indb} = diff(locsn)./Fs;
            end
        end
        bperiodh =
histcounts(cell2mat(bperiod'),0.025:0.0025:0.1,'Normalization','probability');
        nbperiodh =
histcounts(cell2mat(nbperiod'),0.025:0.0025:0.1,'Normalization','probability');

        meanburstfreq = mean(burstfreq);
        stdburstfreq = std(burstfreq);
        semburstfreq = stdburstfreq/sqrt(length(burstfreq));
        meannonburstfreq = mean(nonburstfreq);
        stdnonburstfreq = std(nonburstfreq);
```

```
        semnonburstfreq = stdnonburstfreq/sqrt(length(nonburstfreq));

        %As bursts vary in length, in order to compare them time locked to
        %eachother, they are padded with varying numbers of NaNs on either side
        %to center them all.
        burstsegpad = cell(1,betaburstnumber);
        burstrawsegpad = cell(1,betaburstnumber);
        for ind7 = 1:betaburstnumber
            burstprepadsize = floor(biggestburstleftlength - middlepeak(ind7));
            burstpostpadsize = round(biggestburstrightlength - (betaburstlength(ind7)-
middlepeak(ind7)));
            if any([burstprepadsize burstpostpadsize] < 0)
                burstsegpad{ind7}(max(betaburstlength)+1,1) = NaN;
                burstrawsegpad{ind7}(max(betaburstlength)+1,1) = NaN;
            else
                burstsegpad{ind7} =
padarray(betabursts{ind7},burstprepadsize,NaN,'pre');
                burstsegpad{ind7} =
padarray(burstsegpad{ind7},burstpostpadsize,NaN,'post');
                burstrawsegpad{ind7} =
padarray(betaburstsunfiltered{ind7},burstprepadsize,NaN,'pre');
                burstrawsegpad{ind7} =
padarray(burstrawsegpad{ind7},burstpostpadsize,NaN,'post');
            end
        end
        burstsegpad = cell2mat(burstsegpad);
        burstrawsegpad = cell2mat(burstrawsegpad);
        meanburstseg = nanmean(burstsegpad,2)';
        burstvar = nanstd(burstsegpad,1,2)';
        burstvarlow = meanburstseg-burstvar;
        burstvarhigh = meanburstseg+burstvar;
        [~,meanburstpeaks] = findpeaks(meanburstseg,'MinPeakDistance',100);
        meanburstpeaks = meanburstpeaks./(Fs/1000);

        %In order to investigate oscillatory dynamics before, during and after
        %bursts, power spectra of each burst segment, as well as equal length
        %segments before and after the burst are generated and averaged across
        %bursts. Any bursts that less than a bursts length from the start or
        %end of the session are discarded from this particular analysis.
        fFinterp = linspace(1,120,238);
        bbstarts = betaburststarts(betaburststarts > betaburstlength);
        bblength = betaburstlength(betaburststarts > betaburstlength);
        bbstops = betaburststops(betaburststarts > betaburstlength);
        %The start of a burst is called its start, the start of the whole
        %segment, including the pre-burst, is called the beginning. The same
        %applies to its stop, and its end, respectively.
        bbbegin = bbstarts-bblength;
        bbstarts(bbbegin<=0) = [];
        bblength(bbbegin<=0) = [];
        bbstops(bbbegin<=0) = [];
        bbend = bbstops+bblength;
        bbstarts(bbend>length(signalsdsdt)) = [];
        bblength(bbend>length(signalsdsdt)) = [];
        bbstops(bbend>length(signalsdsdt)) = [];
        newbetaburstnumber = length(bbstarts);

        %The signal segments are indexed and then undergo spectral analysis.
        %Each burst spectrum has 50Hz and 100Hz removed and linearly
```

```
        %interpolated, then it is logged.
        signalbeforebursts = cell(newbetaburstnumber,1);
        signalduringbursts = cell(newbetaburstnumber,1);
        signalafterbursts = cell(newbetaburstnumber,1);
        spectrumbeforebursts = cell(newbetaburstnumber,1);
        spectrumduringbursts = cell(newbetaburstnumber,1);
        spectrumafterbursts = cell(newbetaburstnumber,1);
        for ind8 = 1:newbetaburstnumber
            signalbeforebursts{ind8} = signalsdsdt(bbstarts(ind8)-
bblength(ind8):bbstarts(ind8),:);
            signalduringbursts{ind8} = signalsdsdt(bbstarts(ind8):bbstops(ind8),:);
            signalafterbursts{ind8} =
signalsdsdt(bbstops(ind8):bbstops(ind8)+bblength(ind8),:);
            fullsignal{ind8} = signalsdsdt(bbstarts(ind8)-
bblength(ind8):bbstops(ind8)+bblength(ind8));
            filtsignal{ind8} = betasignal(bbstarts(ind8)-
bblength(ind8):bbstops(ind8)+bblength(ind8));
            [spectrumbeforebursts{ind8},fF{ind8}] =
mtspectrumc(signalbeforebursts{ind8},params);
            [spectrumduringbursts{ind8}] = mtspectrumc(signalduringbursts{ind8},params);
            [spectrumafterbursts{ind8}] = mtspectrumc(signalafterbursts{ind8},params);
            spectrumbeforeburstsi(:,ind8) =
interp1(fF{ind8},spectrumbeforebursts{ind8},fFinterp);
            spectrumbeforeburstsi(:,ind8) = 10*log10(spectrumbeforeburstsi(:,ind8));
            %         spectrumbeforeburstsi(fFinterp>40 & fFinterp<60,ind8) = NaN;
            %         spectrumbeforeburstsi(fFinterp>90 & fFinterp<110,ind8) = NaN;
            %         spectrumbeforeburstsi(:,ind8) =
fillmissing(spectrumbeforeburstsi(:,ind8),'linear');
            spectrumduringburstsi(:,ind8) =
interp1(fF{ind8},spectrumduringbursts{ind8},fFinterp);
            spectrumduringburstsi(:,ind8) = 10*log10(spectrumduringburstsi(:,ind8));
            %         spectrumduringburstsi(fFinterp>40 & fFinterp<60,ind8) = NaN;
            %         spectrumduringburstsi(fFinterp>90 & fFinterp<110,ind8) = NaN;
            %         spectrumduringburstsi(:,ind8) =
fillmissing(spectrumduringburstsi(:,ind8),'linear');
            spectrumafterburstsi(:,ind8) =
interp1(fF{ind8},spectrumafterbursts{ind8},fFinterp);
            spectrumafterburstsi(:,ind8) = 10*log10(spectrumafterburstsi(:,ind8));
            %         spectrumafterburstsi(fFinterp>40 & fFinterp<60,ind8) = NaN;
            %         spectrumafterburstsi(fFinterp>90 & fFinterp<110,ind8) = NaN;
            %         spectrumafterburstsi(:,ind8) =
fillmissing(spectrumafterburstsi(:,ind8),'linear');
        end
        %These burst spectra are then averaged across all bursts.
        meansbb = mean(spectrumbeforeburstsi,2);
        meansdb = mean(spectrumduringburstsi,2);
        meansab = mean(spectrumafterburstsi,2);

    else
    end

    %Stores all data of interest as a non-scalar structure, making it easy
    %to look at and compare data from different sessions.
    %First the parameters and settings.
    EventData(ind0).Session = session;
    EventData(ind0).Parameters = params;
    EventData(ind0).Parameters.MinimumBurstDurationms = minbetaburstdurationms;
    EventData(ind0).Parameters.MinimumBurstCycles = minburstcycles;
```

```
    EventData(ind0).Parameters.BurstThreshold = burststdthreshold;

    %Then Burst Data
    EventData(ind0).NumberOfBetaBursts = betaburstnumber;
    if betaburstnumber>0
        EventData(ind0).BurstStarts = betaburststarts;
        EventData(ind0).BurstStops = betaburststops;
        EventData(ind0).BurstMagnitude = peakburstmagnitude;
        EventData(ind0).BurstLength = betaburstlength;
        EventData(ind0).BurstDuration = burstduration;
        EventData(ind0).BurstFreq = burstfreq;
        EventData(ind0).BurstTimeLagModulusHist = tlmbh;
        EventData(ind0).NonBurstTimeLagModulusHist = tlmnh;
        EventData(ind0).BurstPeriodH = bperiodh;
        EventData(ind0).NonBurstPeriodH = nbperiodh;
        EventData(ind0).AllBurstSegments = burstsegpad;
        EventData(ind0).AllBurstRawSegments = burstrawsegpad;
        EventData(ind0).BurstRS = burstspeed;
        EventData(ind0).FullBurstSignal = fullsignal;
        EventData(ind0).FiltBurstSignal = filtsignal;
        EventData(ind0).SignalBeforeBursts = signalbeforebursts;
        EventData(ind0).SignalDuringBursts = signalduringbursts;
        EventData(ind0).SignalAfterBursts = signalafterbursts;
        EventData(ind0).SpectrumBeforeBursts = meansbb;
        EventData(ind0).SpectrumDuringBursts = meansdb;
        EventData(ind0).SpectrumAfterBursts = meansab;
        EventData(ind0).Frequency = fFinterp;
        EventData(ind0).Signal = signalsdsdt;
    else
    end

    clearvars -except Folder Channel folder foldername subfolders sessionnames ind0
animal channelname EventData

end



RipplesAndBursts = strcat(foldername,'\','RipplesAndBursts');
mkdir(RipplesAndBursts);
cd(RipplesAndBursts);

NumberOfBetaBursts = [EventData(:).NumberOfBetaBursts];
figure2name = strcat(animal,'-',channelname,'-','NumberOfBetaBursts');
figure('Name',figure2name);
subplot(2,2,[1,3])
bar(NumberOfBetaBursts,'b');
set(gca,'LineWidth',1.5);
set(gca,'FontSize',12);
xlabel('Session','fontsize',12);
ylabel('Number Of Beta Bursts','fontsize',14);
set(gca,'box','off');
BurstDuration = vertcat(EventData(:).BurstDuration);
subplot(2,2,2);
histogram(BurstDuration,'FaceColor','b');
set(gca,'LineWidth',1.5);
set(gca,'FontSize',12);
set(gca,'TickLength',[0.02,0.02]);
```

```
xlabel('Burst Length (ms)','fontsize',12);
set(gca,'box','off');
BurstMagnitude = vertcat(EventData(:).BurstMagnitude);
subplot(2,2,4);
histogram(BurstMagnitude,'FaceColor','b');
set(gca,'LineWidth',1.5);
set(gca,'FontSize',12);
set(gca,'TickLength',[0.02,0.02]);
xlabel('Burst Magnitude (μV)','fontsize',12);
set(gca,'box','off');
set(gcf, 'Position',  [250, 100, 750, 500])
hgsave(figure2name)

for indz2 = 1:10
    Fs = EventData(indz2).Parameters.Fs;
    BetaBurstStarts{indz2} = (EventData(indz2).BurstStarts/(Fs*60));
    BurstDist{indz2} = cumsum(histcounts(BetaBurstStarts{indz2},0:(1/60):15)');
    EventData(indz2).BurstDistribution = BurstDist{indz2};
end

NovelBurstDist = BurstDist{9};
FamiliarBurstDist = BurstDist{8};
NormNovelBurstDist = NovelBurstDist/max(NovelBurstDist)*100;
NormFamiliarBurstDist = FamiliarBurstDist/max(FamiliarBurstDist)*100;

figure6name = strcat(animal,'-',channelname,'-','BurstProfileNovelty');
figure('Name',figure6name);
subaxis3 = subplot(2,1,1);
plot(NovelBurstDist,'LineWidth',2,'Color','r')
hold on
plot(FamiliarBurstDist,'LineWidth',2,'Color','b')
xlim([0 900])
set(gca,'xTick',0:60:900)
set(gca,'Xticklabel',[])
ylab1 = ylabel('Total Number of Bursts','fontsize',14);
set(ylab1, 'Units', 'Normalized', 'Position', [-0.08, 0.5, 0]);
set(gca,'FontSize',12);
legend({'Novel','Familiar'},'Location','northwest');
legend boxoff
set(gca,'box','off');
subaxis4 = subplot(2,1,2);
plot(NormNovelBurstDist,'LineWidth',2,'Color','r')
hold on
plot(NormFamiliarBurstDist,'LineWidth',2,'Color','b')
xlim([0 900])
set(gca,'xTick',0:60:900)
set(gca,'xTickLabel',0:1:15)
alpha(gca,0.75)
xlabel('Time (min)','fontsize',14);
ylab2 = ylabel('Percentage of Bursts (%)','fontsize',14);
set(ylab2, 'Units', 'Normalized', 'Position', [-0.08, 0.5, 0]);
set(gca,'FontSize',12);
set(gca,'box','off');
set(gcf, 'Position',  [300, 100, 500, 630])
set(subaxis3,'Position',[0.13 0.55 0.775 0.4]);
set(subaxis4,'Position',[0.13 0.11 0.775 0.4]);
hgsave(figure6name)
```

```
SpectrumBeforeBursts = [EventData(:).SpectrumBeforeBursts]';
fFinterp = linspace(1,120,238);
MMSBB = mean(SpectrumBeforeBursts);
stdSBB = std(SpectrumBeforeBursts);
semSBB = stdSBB/sqrt(size(SpectrumBeforeBursts,1));
SBBLow = MMSBB-semSBB;
SBBHigh = MMSBB+semSBB;
SpectrumDuringBursts = [EventData(:).SpectrumDuringBursts]';
MMSDB = mean(SpectrumDuringBursts);
stdSDB = std(SpectrumDuringBursts);
semSDB = stdSDB/sqrt(size(SpectrumDuringBursts,1));
SDBLow = MMSDB-semSDB;
SDBHigh = MMSDB+semSDB;
SpectrumAfterBursts = [EventData(:).SpectrumAfterBursts]';
MMSAB = mean(SpectrumAfterBursts);
stdSAB = std(SpectrumAfterBursts);
semSAB = stdSAB/sqrt(size(SpectrumAfterBursts,1));
SABLow = MMSAB-semSAB;
SABHigh = MMSAB+semSAB;

figure7name = strcat(animal,'-',channelname,'-','BeforeDuringAfterBurstSpectrums');
figure('Name',figure7name);
SBBbar = patch([fFinterp fFinterp(end:-1:1) fFinterp(1)],[SBBLow SBBHigh(end:-1:1)
SBBLow(1)], 'r');
hold on;
SBBline = line(fFinterp,MMSBB,'LineWidth',1.5);
SDBbar = patch([fFinterp fFinterp(end:-1:1) fFinterp(1)],[SDBLow SDBHigh(end:-1:1)
SDBLow(1)], 'r');
SDBline = line(fFinterp,MMSDB,'LineWidth',1.5);
SABbar = patch([fFinterp fFinterp(end:-1:1) fFinterp(1)],[SABLow SABHigh(end:-1:1)
SABLow(1)], 'r');
SABline = line(fFinterp,MMSAB,'LineWidth',1.5);
alpha(0.3);
set(SBBbar, 'facecolor', [0 1 0.8667], 'edgecolor', 'none');
set(SDBbar, 'facecolor', [0 (12/255) 1], 'edgecolor', 'none');
set(SABbar, 'facecolor', [1 0 (233/255)], 'edgecolor', 'none');
set(SBBline, 'color', [0 0.8 0.8]);
set(SDBline, 'color', [0 0 0.8]);
set(SABline, 'color', [0.8 0 0.8]);
set(gca,'LineWidth',1.5);
set(gca,'FontSize',12)
xlabel('Frequency (Hz)','fontsize',14);
ylabel('Power (DB)','fontsize',14);
legend([SBBline SDBline SABline],{'Before Burst','During Burst','After Burst'});
legend boxoff
set(gca,'box','off');
set(gcf, 'Position',  [400, 100, 600, 500])
% xlim([3 40])
hgsave(figure7name)

%Save the finished data structure as a .mat file for later use
EventFolder = strcat(foldername(1:end-2),'Analysed\','EventData');
mkdir(EventFolder);
cd(EventFolder);
save(strcat('EventData','-',(animal),'-',(channelname),'.mat'),'EventData');

end
```

Published with MATLAB® R2019b

9.3 Phase Amplitude Coupling Analysis (Tort Method) - PhaseAmplitudeCouplingTort

```
function [PACData] = PhaseAmplitudeCouplingTort(Folder,Channel)

folder = Folder;
folder = dir(folder);
foldername = folder.folder;
subfolders = {folder.name};
subfolders = subfolders(contains(subfolders,'Day'));
subfolders = strcat(foldername,'\',subfolders);
sessionnames =
["Day1a","Day1b","Day2a","Day2b","Day3a","Day3b","Day4a","Day4b","Day5a","Day5b"];
cd(foldername);

%Starts a megaloop to analyse and cycle through each session in an animals
%folder.
for ind0 = 1:length(subfolders)

    files = dir(subfolders{ind0});
    files = files(arrayfun(@(x) ~strcmp(x.name(1),'.'),files));
    channels = {files.name};
    channels = channels(contains(channels,Channel));
    channels = strcat(subfolders{ind0},'\',channels);
    channelname = string(channels{1}(end-14:end-11));

    animalnumber = foldername(end-1:end);
    animal = strcat('Mouse',animalnumber);
    session = files.folder;
    session = session(end-4:end);

    %Imports the .continuous data into MatLab
    signal = [];
    [signal(:,1),~,info] = load_open_ephys_data_faster(channels{1});

    %Cuts the signals to the experiment duration ie 15minutes in this case
    ExpDurationMinutes = 15;
    Fs = info.header.sampleRate;
    ExpDurationFrames = (ExpDurationMinutes*60)*Fs;
    ExpDurationSeconds = ExpDurationMinutes*60;
    signal = signal(1:ExpDurationFrames,:);

    %Downsamples the signals and timestamps, to reduce computation time,
    %and detrends to remove any baseline fluctuations
    downsampleX = 10;
    Fs = Fs/downsampleX;
    signalsds = downsample(signal,downsampleX);
    signalsdsdt = detrend(signalsds);
    signalsdsdt(isnan(signalsdsdt)) = [];

    signalsdsdt = signalsdsdt(1:60*Fs);

    %Sets the theta and gamma frequency bins to investigate, and
```

```
    %preallocates the modulation index matrix.
    phasebinstart = 2;
    phasebinstep = 0.25;
    phasebinstop = 12;
    phasebins = (phasebinstart:phasebinstep:phasebinstop);
    numpbins = (length(phasebins)-1);
    amplitudebinstart = 10;
    amplitudebinstep = 2;
    amplitudebinstop = 100;
    amplitudebins = (amplitudebinstart:amplitudebinstep:amplitudebinstop);
    numabins = (length(amplitudebins)-1);

    MI = zeros(numel(amplitudebins)-1,numel(phasebins)-1);
    for indpf = 1:numpbins
        phasefilter{indpf} =
designfilt('bandpassiir','FilterOrder',2,'HalfPowerFrequency1',phasebins(indpf),'HalfPow
erFrequency2',phasebins(indpf+1),'DesignMethod','butter','SampleRate',Fs);
    end
    for indaf = 1:numabins
        amplitudefilter{indaf} =
designfilt('bandpassiir','FilterOrder',2,'HalfPowerFrequency1',amplitudebins(indaf),'Hal
fPowerFrequency2',amplitudebins(indaf+1),'DesignMethod','butter','SampleRate',Fs);
    end

    %For the calculation of a normalised MI value, a number of surrogate
    %MI values are calculated by circularly shifting the signals with
    %random magnitude delays. Here, the number of surrogates calculated, as
    %well as the maximum and minimum delays are given. Fs is used to
    %prevent the data being shifted only one second forward or backward.
    NumberOfPoints = length(signalsdsdt);
    NumberOfSurrogates = 100;
    MinSkip = Fs;
    MaxSkip = NumberOfPoints-Fs;
    phasebars = (0:10:360);
    nphasebars = length(phasebars)-1;
    Q = repmat(1/nphasebars,[1 nphasebars]);

    clear surrogate_amplitude
    for indp = 1:numpbins
        phasesignal = filtfilt(phasefilter{indp},signalsdsdt);
        phase = angle(hilbert(phasesignal));
        phase = rad2deg(phase)+180;
        [phasesorted,phasesort] = sort(phase);
        for inda = 1:numabins
            amplitudesignal = filtfilt(amplitudefilter{inda},signalsdsdt);
            amplitude = abs(hilbert(amplitudesignal));
            amplitudesorted = amplitude(phasesort);
            for ibin = 1:36
                P(ibin) = mean(amplitudesorted(phasesorted >= phasebars(ibin) &
phasesorted < phasebars(ibin+1)));
            end
            P = P./sum(P);
            temp =  P.*log(P./Q);
            temp(isnan(temp)) = 0;
            DKL = sum(temp,2);
            mraw = DKL/log(nphasebars);

            % compute surrogate values
```

```
            skip = randi([MinSkip MaxSkip],[NumberOfSurrogates,1]);
            surrogateamplitude = zeros(length(amplitude),NumberOfSurrogates);
            for inds = 1:NumberOfSurrogates
                surrogateamplitude = circshift(amplitude,-skip(inds));
                surrogateamplitudesorted = surrogateamplitude(phasesort);
                for ibin = 1:36
                    P(ibin) = mean(surrogateamplitudesorted(phasesorted >=
phasebars(ibin) & phasesorted < phasebars(ibin+1)));
                end
                P = P./sum(P);
                temp =  P.*log(P./Q);
                temp(isnan(temp)) = 0;
                DKL = sum(temp,2);
                surrogateM(inds) = DKL/log(nphasebars);
            end

            %Fits gaussian to surrogate data and normalize length using surrogate data
(z-score)
            [surrogatemean,surrogatestd] = normfit(surrogateM);
            mnormlength = (mraw-surrogatemean)/surrogatestd;
            MI(inda,indp) = abs(mnormlength);
        end
    end

    pbt = (phasebinstart+phasebinstep/2:phasebinstep:phasebinstop-phasebinstep/2);
    abt = (amplitudebinstart+amplitudebinstep/2:amplitudebinstep:amplitudebinstop-
amplitudebinstep/2);
    numphaseticks = numpbins;
    numamplitudeticks = numabins;
    interpfactor = 2;
    pbi = phasebinstart:phasebinstep/interpfactor:phasebinstop;
    abi = amplitudebinstart:amplitudebinstep/interpfactor:amplitudebinstop;
    pbti =
(phasebinstart+(phasebinstep/2)/interpfactor:phasebinstep/interpfactor:phasebinstop-
(phasebinstep/2)/interpfactor);
    abti =
(amplitudebinstart+(amplitudebinstep/2)/interpfactor:amplitudebinstep/interpfactor:ampli
tudebinstop-(amplitudebinstep/2)/interpfactor);
    numphaseticksint = interpfactor*numphaseticks;
    numamplitudeticksint = interpfactor*numamplitudeticks;

    phaseticksi = linspace(pbt(1),pbt(end),numphaseticksint);
    amplitudeticksi = linspace(abt(1),abt(end),numamplitudeticksint);
    [PT,AT] = ndgrid(pbt,abt);
    F = griddedInterpolant(PT,AT,MI');
    [PTI,ATI] = ndgrid(pbti,abti);
    MIinterp = F(PTI,ATI)';

    %Sets the theta and gamma frequency bins to investigate, and
    %preallocates the modulation index matrix.
    phasefocus = [4 12];
    amplitudefocus = [30 120];
    phasebars = (0:10:360);
    phasebarstr = string(phasebars);
    phasefocusfilter =
designfilt('bandpassiir','FilterOrder',2,'HalfPowerFrequency1',phasefocus(1),'HalfPowerF
requency2',phasefocus(2),'DesignMethod','butter','SampleRate',Fs);
    amplitudefocusfilter =
```

```
designfilt('bandpassiir','FilterOrder',2,'HalfPowerFrequency1',amplitudefocus(1),'HalfPo
werFrequency2',amplitudefocus(2),'DesignMethod','butter','SampleRate',Fs);

    phasefocussignal = filtfilt(phasefocusfilter,signalsdsdt);
    focusphase = angle(hilbert(phasefocussignal));
    amplitudefocussignal = filtfilt(amplitudefocusfilter,signalsdsdt);
    focusamplitude = abs(hilbert(amplitudefocussignal));
    phasedeg = rad2deg(focusphase)+180;
    [phasesorted,phasesort] = sort(phasedeg);
    amplitudesorted = focusamplitude(phasesort);
    for izz3 = 1:36
        meanamplitude(izz3) = mean(amplitudesorted(phasesorted >= phasebars(izz3) &
phasesorted < phasebars(izz3+1)));
    end
    totalamplitude = sum(meanamplitude);
    meanamplitude = meanamplitude./totalamplitude;
    meanmeanamplitude = mean(meanamplitude);
    meanamplituderep = [meanamplitude meanamplitude];

    TPACFigureFolder = strcat(foldername,'\','ThetaPACHeatMaps');
    mkdir(TPACFigureFolder);
    cd(TPACFigureFolder);
    figurename = strcat(animal,'-',session(end-1:end),'-',channelname,'-','ThetaPAC');
    figure('Name',figurename);
    imagesc(pbti,abti,MIinterp);
    axis xy
    set(gca,'LineWidth',1.5);
    set(gca,'FontSize',12);
    xLabel = xlabel('Phase Frequency (Hz)','fontsize',14);
    yLabel = ylabel('Amplitude Frequency (Hz)','fontsize',14);
    set(gca,'box','off');
    grid off
    CB = colorbar;
    caxis([0 10]);
    CBtitle = get(CB,'Title');
    set(CBtitle,'String','MI');
    CBpos = get(CBtitle,'Position');
    set(CBtitle,'Position',[CBpos(1) CBpos(2)-320]);
    set(CBtitle,'FontSize',14);
    hgsave(figurename)

    PACData(ind0).PhaseBins = phasebins;
    PACData(ind0).AmplitudeBins = amplitudebins;
    PACData(ind0).NumberOfSurrogates = NumberOfSurrogates;
    PACData(ind0).MI = MI;
    PACData(ind0).PhaseBinsinterp = pbi;
    PACData(ind0).AmplitudeBinsinterp = abi;
    PACData(ind0).MIinterp = MIinterp;

end

%Save the finished data structure as a .mat file for later use

PACFolder = strcat(foldername(1:end-2),'Analysed\','PACtData');
mkdir(PACFolder);
cd(PACFolder);
save(strcat('PACtData','-',(animal),'-',(channelname),'.mat'),'PACData');
```

```
end
```

Published with MATLAB® R2019b

9.4 Multi-Unit Activity Analysis - SimpleMUADuringBursts

```
function [BurstMUAData] = SimpleMUADuringBursts(Folder)

%First selects the folder with the data, and locates all the LFP data
folder = Folder;
folder = dir(folder);
foldername = folder.folder;
subfolders = {folder.name};
subfolders = subfolders(contains(subfolders,'Day'));
subfolders = strcat(foldername,'\',subfolders);
sessionnames =
["Day1a","Day1b","Day2a","Day2b","Day3a","Day3b","Day4a","Day4b","Day5a","Day5b"];
cd(foldername);

%Starts a megaloop to analyse and cycle through each session in an animals
%folder.
for ind0 = 1:length(subfolders)

    cd(Folder)
    files = dir(subfolders{ind0});
    files = files(arrayfun(@(x) ~strcmp(x.name(1),'.'),files));
    channels = {files.name};
    channels = channels(contains(channels,'CH'));
    channels = strcat(subfolders{ind0},'\',channels);

    animalnumber = Folder(end-1:end);
    animal = strcat('Mouse',animalnumber);
    session = files.folder;
    session = session(end-4:end);

    [~,~,extension] = fileparts(channels{1});
    signals = [];

    for ich = 1:length(channels)
        if strcmp(extension,'.continuous')
            %Imports the .continuous data into MatLab
            [signals(:,ich),~,info] = load_open_ephys_data_faster(channels{ich});
            channelnames{ich} = channels{ich}(end-14:end-11);
        elseif strcmp(extension,'.mat')
            %Imports the .continuous data into MatLab
            load(channels{ich});
            signals(:,ich) = sig;
            info.header.sampleRate = 30000;
            channelnames{ich} = channels{ich}(end-14:end-11);
        end
    end

    %Cuts the signals to the experiment duration ie 15minutes in this case
    ExpDurationMinutes = 15;
    Fs = info.header.sampleRate;
    ExpDurationFrames = (ExpDurationMinutes*60)*Fs;
    ExpDurationSeconds = ExpDurationMinutes*60;
    signals = signals(1:ExpDurationFrames,:);

    %Downsamples the signals and timestamps, to reduce computation time,
    %and detrends to remove any baseline fluctuations
```

```
    signalsdt = detrend(signals);

    %Set the parameters for Chronux analysis
    params.fpass = [500 5000];

    for ich = 1:length(channels)

        %Common Average Referencing
        refchannels = 1:length(channelnames);
        refchannels(ich) = [];
        refsignal = mean(signalsdt(:,refchannels),2);
        signaldt = signalsdt(:,ich);
        signal = signaldt-refsignal;

        % Creates a filter in the MUA frequency band (600-6000Hz) and applies
        %it to the signal. Then uses a hilbert transform to find the envelope
        %amplitude of the signal, and the instantaneous phase.
        muafilter =
designfilt('bandpassiir','FilterOrder',4,'HalfPowerFrequency1',params.fpass(1),'HalfPowe
rFrequency2',params.fpass(2),'DesignMethod','butter','SampleRate',Fs);
        muasignal = filtfilt(muafilter,signal);

        threshold = 4*median(abs(muasignal)/0.6745);

        %Sets the beta burst detection parameters. The burst must cross 3 standard
        %deviations from the mean for at least 150ms, to be classified.
        [~,peaklocations] =
findpeaks(abs(muasignal),'MinPeakHeight',threshold,'MinPeakDistance',Fs/2000);

        peakstarts = peaklocations - Fs/1000;
        peakstops = peaklocations + Fs/1000;

        peaksbeforesession = peakstarts <= Fs;
        peakstarts(peaksbeforesession) = [];
        peakstops(peaksbeforesession) = [];
        peaksaftersession = peakstops >= (ExpDurationFrames-Fs);
        peakstarts(peaksaftersession) = [];
        peakstops(peaksaftersession) = [];

        peaklength = peakstops-peakstarts;
        peaknumber = length(peaklength);

%         for indpeaks = 1:peaknumber
%             waveforms(:,indpeaks) =
muasignal(peakstarts(indpeaks):peakstops(indpeaks));
%             [~,maxind] = max(abs(waveforms(:,indpeaks)));
%             wfamplitude(indpeaks) = waveforms(maxind,indpeaks);
%         end

        for indpeaks = 1:peaknumber
            waveforms(:,indpeaks) = muasignal(peakstarts(indpeaks):peakstops(indpeaks));
            [~,maxind(indpeaks)] = max(abs(waveforms(:,indpeaks)));
            peakstarts(indpeaks) = peakstarts(indpeaks) + (maxind(indpeaks)-31);
            peakstops(indpeaks) = peakstops(indpeaks) + (maxind(indpeaks)-31);
            if waveforms(maxind(indpeaks),indpeaks)<0
                waveforms(:,indpeaks) =
muasignal(peakstarts(indpeaks):peakstops(indpeaks));
            else
```

```
                waveforms(:,indpeaks) = -
muasignal(peakstarts(indpeaks):peakstops(indpeaks));
            end
            wfamplitude(indpeaks) = waveforms(31,indpeaks);
        end
        peaks = [peakstarts peakstops];
        [~,idx,~] = unique(peaks,'rows');
        peakstarts = peakstarts(idx);
        peakstops = peakstops(idx);
        waveforms = waveforms(:,idx);
        wfamplitude = wfamplitude(idx);

        % Creates a filter in the beta frequency band (20-30Hz) and applies
        %it to the signal. Then uses a hilbert transform to find the envelope
        %amplitude of the signal, and the instantaneous phase.
        betafilter =
designfilt('bandpassiir','FilterOrder',2,'HalfPowerFrequency1',20,'HalfPowerFrequency2',
30,'DesignMethod','butter','SampleRate',Fs);
        betasignal = filtfilt(betafilter,signaldt);
        betasignalmagnitude = abs(hilbert(betasignal));
        noisethreshold = median(betasignalmagnitude)+10*mad(betasignalmagnitude,1);
        betasignalmagnitude(betasignalmagnitude>noisethreshold) = 0;
        zscorebetasignalmagnitude = zscore(betasignalmagnitude);
        betasignalphase = rad2deg(angle(hilbert(betasignal)));

        %Sets the beta burst detection parameters. The burst must cross 3 standard
        %deviations from the mean for at least 150ms, to be classified.
        burststdthreshold = 2;
        minbetaburstdurationms = 150;
        minbetaburstsamples = Fs*(minbetaburstdurationms/1000);
        minburstcycles = 3;

        %The amplitude detection parameter is applied to the beta signal, in order
        %to find indexes of when the burst reaches the detection threshold. A second
threshold of half the detection threshold
        % is also used to find the starts and stops of each putative burst, in
        % order to include the sides of each burst.
        burstdetectionthreshold = zscorebetasignalmagnitude>=burststdthreshold;
        burstsidethreshold = zscorebetasignalmagnitude>=burststdthreshold/2;

        %The two thresholds are combined so that a burst would show as 01210,
        %ie below threshold 1, above threshold 1, above thresholds 1+2, and
        %then back down.
        BdtBst = burstdetectionthreshold + burstsidethreshold;
        difBdtBst = diff(BdtBst);
        %Find is used to find where these changes between threshold levels
        %occur in the signal.
        [blocations,~,bchanges] = find(difBdtBst);
        revblocations = flipud(blocations);
        %strfind is used to find the starts of sequences with the change
        %+1+1-1-1, ie 01210, and also the starts of sequences with the change
        %-1-1+1+1, ie the reverse, to find the stops of these 01210 sequences.
        bpatternseek = strfind(bchanges',[1 1 -1 -1]);
        revbpatternseek = strfind(flipud(bchanges)',[-1 -1 1 1]);
        betaburststarts = blocations(bpatternseek)+1;
        betaburststops = flipud(revblocations(revbpatternseek));
        %These stretches are then removed from the data, to turn it into 01110,
        %so that bursts that don't return to 0, such as 0121210, can be
```

```
        %detected without redetecting the previously discovered bursts. These
        %bursts that don't return to 0 are referred to as "waves" for now.
        for idy = 1:length(betaburststarts)
            burstdetectionthreshold(betaburststarts(idy):betaburststops(idy)) = 0;
        end
        %Bursts that started before recording are discarded, as are those that stopped
after recording.
        if betaburststops(1)<betaburststarts(1)
            betaburststops = betaburststops(2:end);
        end
        if betaburststarts(end)>betaburststops(end)
            betaburststarts = betaburststarts(1:end-1);
        end
        %In order to detect "waves", we can just look at the detection
        %threshold and only pick out the 2's of 0121's, rather than 121's. This
        %method prevents excessive combination of adjacent waves into extra long
        %events.
        difBdt = diff(burstdetectionthreshold);
        [wlocations,~,wchanges] = find(difBdt);
        revwlocations = flipud(wlocations);
        wpatternseek = strfind(wchanges',[1 -1]);
        revwpatternseek = strfind(flipud(wchanges)',[-1 1]);
        wavestarts = wlocations(wpatternseek);
        wavestops = flipud(revwlocations(revwpatternseek)+1);

        %"Waves" that started before recording are discarded, as are those that stopped
after recording.
        if length(wavestops)>1
            if wavestops(1)<wavestarts(1)
                wavestops = wavestops(2:end);
            end
            if wavestarts(end)>wavestops(end)
                wavestarts = wavestarts(1:end-1);
            end

            wavelength = wavestops-wavestarts;
            wavestarts = wavestarts(wavelength>minbetaburstsamples);
            wavestops = wavestops(wavelength>minbetaburstsamples);
        else
        end
        %A previosly assigned MINIMUM DURATION parameter is applied to find bursts with
        %sufficient duration to be classified, while all shorter events are removed.
        betaburstlength = betaburststops-betaburststarts;
        betaburststarts = betaburststarts(betaburstlength>minbetaburstsamples);
        betaburststops = betaburststops(betaburstlength>minbetaburstsamples);

        %The burst starts and "wave" starts are combined and put in
        %ascending order, as are the stops. These starts and stops are now the indexes
of all putative bursts.
        ratiob2w = length(betaburststarts)/length(wavestarts);
        betaburststarts = [betaburststarts;wavestarts];
        betaburststops = [betaburststops;wavestops];
        [betaburststarts,sortI] = sort(betaburststarts);
        betaburststops = betaburststops(sortI);
        betaburstlength = betaburststops-betaburststarts;

        %Artefact removal on a burst by burst basis, by detecting large almost
        %instantaneous changes in the unfiltered LFP.
```

```
        for ib = 1:length(betaburststarts)
            betaburstmagnitude(ib) =
max(betasignalmagnitude(betaburststarts(ib):betaburststops(ib),:));
        end
        discard = isoutlier(betaburstmagnitude);
        betaburststarts(discard) = [];
        betaburststops(discard) = [];
        betaburstlength(discard) = [];
        betaburstmagnitude(discard) = [];

        %Now the burst start and stop indexes of all putative bursts that do
        %not meet these 2 criteria have been removed, all remaining can
        %be counted as bursts, so we can calculate the total number of bursts
        %in this session, as well as the duration of each burst in
        %milliseconds.
        SegLengthF = Fs/2;
        SegStepF = 1500;
        tooearly = betaburststarts < SegLengthF;
        betaburststarts(tooearly) = [];
        betaburststops(tooearly) = [];
        betaburstlength(tooearly) = [];
        betaburstmagnitude(tooearly) = [];
        toolate = betaburststarts + SegLengthF > ExpDurationFrames;
        betaburststarts(toolate) = [];
        betaburststops(toolate) = [];
        betaburstlength(toolate) = [];
        betaburstmagnitude(toolate) = [];

        % Detect beta burst segments (burststart-Fs:burststart+Fs) that
        % overlap with eachother and remove them
        bsegstarts = betaburststarts-SegLengthF;
        bsegstops = betaburststarts+SegLengthF;
        for i = 1:length(bsegstarts)
            burstseg{i} = bsegstarts(i):bsegstops(i);
        end
        for i = 1:length(bsegstarts)
            for i2 = 1:length(bsegstarts)
                overlap(i,i2) = ~isempty(intersect(burstseg{i},burstseg{i2}));
            end
        end
        OL = sum(overlap,1)>1;

        betaburststarts(logical(OL)) = [];
        betaburststops(logical(OL)) = [];
        betaburstlength(logical(OL)) = [];
        betaburstmagnitude(logical(OL)) = [];
        numberofbetabursts = length(betaburststarts);

        if numberofbetabursts > 0

            rasteredges = [-SegLengthF SegLengthF];
            spikeraster = zeros(ExpDurationFrames,1);
            spikeraster(peakstarts) = 1;

            for indbr = 1:numberofbetabursts
                periburstspikeR(indbr,:) = spikeraster(betaburststarts(indbr)-
SegLengthF:betaburststarts(indbr)+SegLengthF);
                periburstbinnedspikeR(indbr,:) =
```

```
histcounts(peakstarts,betaburststarts(indbr)-
SegLengthF:SegStepF:betaburststarts(indbr)+SegLengthF);
            end
            periburstspikeH = sum(periburstbinnedspikeR,1);
            periburstspikeH = periburstspikeH./sum(periburstspikeH);

        else
        end

        %Stores all data of interest as a non-scalar structure, making it easy
        %to look at and compare data from different sessions.
        %First the parameters and settings.
        BurstMUAData(ich).Channel = channelnames{ich};
        %Then Burst Data
        BurstMUAData(ich).NumberOfBetaBursts = numberofbetabursts;
        BurstMUAData(ich).TimeStamps = peakstarts;
        BurstMUAData(ich).Waveforms = waveforms;
        if numberofbetabursts>0
            BurstMUAData(ich).BurstLengths = betaburstlength;
            BurstMUAData(ich).BurstMagnitude = betaburstmagnitude;
            BurstMUAData(ich).RasterEdges = rasteredges;
            BurstMUAData(ich).PeriBurstSpikeRaster = periburstspikeR;
            BurstMUAData(ich).HistogramEdges = -SegLengthF:SegStepF:SegLengthF;
            BurstMUAData(ich).PeriBurstSpikeHistogram = periburstspikeH;
%             BurstMUAData(ich).MeanBurstSpike = meanburstspike;
%             BurstMUAData(ich).MeanNonBurstSpike = meannonburstspike;
        else
        end

    clearvars -except Folder folder foldername subfolders sessionnames ind0 ich animal
channelnames signalsdt Fs params ExpDurationFrames BurstMUAData

    end

    %Save the finished data structure as a .mat file for later use
    MUAFolder = strcat(foldername(1:end-2),'Analysed\','MUAData');
    warning('off', 'MATLAB:MKDIR:DirectoryExists');
    mkdir(MUAFolder);
    cd(MUAFolder);
    save(strcat('BurstMUAData','-',(animal),'-
',sessionnames{ind0},'.mat'),'BurstMUAData');

end

end
```

Published with MATLAB® R2019b

9.5 Beta Burst Cross-Correlation Analysis - BurstXCorr

```
function [BXCData] = BurstXCorr(Folder,RefChannel)

%First selects the folder with the data, and locates all the LFP data
folder = Folder;
folder = dir(folder);
foldername = folder.folder;
```

```
subfolders = {folder.name};
subfolders = subfolders(contains(subfolders,'Day'));
subfolders = strcat(foldername,'\',subfolders);
sessionnames =
["Day1a","Day1b","Day2a","Day2b","Day3a","Day3b","Day4a","Day4b","Day5a","Day5b"];
cd(foldername);

%Starts a megaloop to analyse and cycle through each session in an animals
%folder.
for ind0 = 1:length(subfolders)

    files = dir(subfolders{ind0});
    files = files(arrayfun(@(x) ~strcmp(x.name(1),'.'),files));
    channels = {files.name};
    channels = channels(contains(channels,'CH'));
    channels = strcat(subfolders{ind0},'\',channels);

    animalnumber = Folder(end-1:end);
    animal = strcat('Mouse',animalnumber);
    session = files.folder;
    session = session(end-4:end);

    [~,~,extension] = fileparts(channels{1});
    Fs = 30000;
    ExpDurationMinutes = 15;
    ExpDurationFrames = (ExpDurationMinutes*60)*Fs;

    for indch = 1:length(channels)
        if strcmp(extension,'.continuous')
            %Imports the .continuous data into MatLab
            [signal,~,info] = load_open_ephys_data_faster(channels{indch});
            signals(:,indch) = signal(1:ExpDurationFrames);
        elseif strcmp(extension,'.mat')
            %Imports the .continuous data into MatLab
            load(channels{indch});
            signals(:,indch) = sig;
            info.header.sampleRate = 30000;
        end
    end

    %Downsamples the signals and timestamps, to reduce computation time,
    %and detrends to remove any baseline fluctuations
%     downsampleX = 1;
%     signalsds = downsample(signals,downsampleX);
%     Fs = Fs/downsampleX;
    signalsdsdt = detrend(signals);

    %Set the parameters for Chronux analysis
    params.Fs = Fs;
    params.pad = 2;
    params.tapers = [2 3];
    params.err = 0;
    params.trialave = 0;
    params.segave = 0;

    %Creates a filter in the beta frequency band (20-30Hz) and applies
    %it to the signal. Then uses a hilbert transform to find the envelope
    %amplitude of the signal, and the instantaneous phase.
```

```
    betafilter =
designfilt('bandpassiir','FilterOrder',2,'HalfPowerFrequency1',20,'HalfPowerFrequency2',
30,'DesignMethod','butter','SampleRate',Fs);
    betasignal = filtfilt(betafilter,signalsdsdt);
    betasignalmagnitude = abs(hilbert(betasignal(:,RefChannel)));
    noisethreshold = median(betasignalmagnitude)+10*mad(betasignalmagnitude,1);
    betasignalmagnitude(betasignalmagnitude>noisethreshold) = 0;
    zscorebetasignalmagnitude = zscore(betasignalmagnitude);
    betasignalphase = rad2deg(angle(hilbert(betasignal)));

    %Sets the beta burst detection parameters. The burst must cross 3 standard
    %deviations from the mean for at least 150ms, to be classified.
    burststdthreshold = 2;
    minbetaburstdurationms = 150;
    minbetaburstsamples = Fs*(minbetaburstdurationms/1000);

    %The amplitude detection parameter is applied to the beta signal, in order
    %to find indexes of when the burst reaches the detection threshold. A second
threshold of half the detection threshold
    % is also used to find the starts and stops of each putative burst, in
    % order to include the sides of each burst.
    burstdetectionthreshold = zscorebetasignalmagnitude>=burststdthreshold;
    burstsidethreshold = zscorebetasignalmagnitude>=burststdthreshold/2;

    %The two thresholds are combined so that a burst would show as 01210,
    %ie below threshold 1, above threshold 1, above thresholds 1+2, and
    %then back down.
    BdtBst = burstdetectionthreshold + burstsidethreshold;
    difBdtBst = diff(BdtBst);
    %Find is used to find where these changes between threshold levels
    %occur in the signal.
    [blocations,~,bchanges] = find(difBdtBst);
    revblocations = flipud(blocations);
    %strfind is used to find the starts of sequences with the change
    %+1+1-1-1, ie 01210, and also the starts of sequences with the change
    %-1-1+1+1, ie the reverse, to find the stops of these 01210 sequences.
    bpatternseek = strfind(bchanges',[1 1 -1 -1]);
    revbpatternseek = strfind(flipud(bchanges)',[-1 -1 1 1]);
    betaburststarts = blocations(bpatternseek)+1;
    betaburststops = flipud(revblocations(revbpatternseek));
    %These stretches are then removed from the data, to turn it into 01110,
    %so that bursts that don't return to 0, such as 0121210, can be
    %detected without redetecting the previously discovered bursts. These
    %bursts that don't return to 0 are referred to as "waves" for now.
    for idy = 1:length(betaburststarts)
        burstdetectionthreshold(betaburststarts(idy):betaburststops(idy)) = 0;
    end
    %Bursts that started before recording are discarded, as are those that stopped after
recording.
    if betaburststops(1)<betaburststarts(1)
        betaburststops = betaburststops(2:end);
    end
    if betaburststarts(end)>betaburststops(end)
        betaburststarts = betaburststarts(1:end-1);
    end
    %In order to detect "waves", we can just look at the detection
    %threshold and only pick out the 2's of 0121's, rather than 121's. This
    %method prevents excessive combination of adjacent waves into extra long
```

```
    %events.
    difBdt = diff(burstdetectionthreshold);
    [wlocations,~,wchanges] = find(difBdt);
    revwlocations = flipud(wlocations);
    wpatternseek = strfind(wchanges',[1 -1]);
    revwpatternseek = strfind(flipud(wchanges)',[-1 1]);
    wavestarts = wlocations(wpatternseek);
    wavestops = flipud(revwlocations(revwpatternseek)+1);

    %"Waves" that started before recording are discarded, as are those that stopped
after recording.
    if length(wavestops)>1
        if wavestops(1)<wavestarts(1)
            wavestops = wavestops(2:end);
        end
        if wavestarts(end)>wavestops(end)
            wavestarts = wavestarts(1:end-1);
        end

        wavelength = wavestops-wavestarts;
        wavestarts = wavestarts(wavelength>minbetaburstsamples);
        wavestops = wavestops(wavelength>minbetaburstsamples);
    else
    end

    %A previosly assigned MINIMUM DURATION parameter is applied to find bursts with
    %sufficient duration to be classified, while all shorter events are removed.
    betaburstlength = betaburststops-betaburststarts;
    betaburststarts = betaburststarts(betaburstlength>minbetaburstsamples);
    betaburststops = betaburststops(betaburstlength>minbetaburstsamples);

    %The burst starts and "wave" starts are combined and put in
    %ascending order, as are the stops. These starts and stops are now the indexes of
all putative bursts.
    ratiob2w = length(betaburststarts)/length(wavestarts);
    betaburststarts = [betaburststarts;wavestarts];
    betaburststops = [betaburststops;wavestops];
    [betaburststarts,sortI] = sort(betaburststarts);
    betaburststops = betaburststops(sortI);
    betaburstlength = betaburststops-betaburststarts;

    %Artefact removal on a burst by burst basis, by detecting large almost
    %instantaneous changes in the unfiltered LFP.
    for ib = 1:length(betaburststarts)
        pbm(ib) = max(betasignalmagnitude(betaburststarts(ib):betaburststops(ib),:));
    end
    discard = isoutlier(pbm);
    params.discardrate = sum(discard)/length(betaburststarts);
    betaburststarts(discard) = [];
    betaburststops(discard) = [];
    betaburstlength(discard) = [];

    %Now the burst start and stop indexes of all putative bursts that do
    %not meet these 2 criteria have been removed, all remaining can
    %be counted as bursts, so we can calculate the total number of bursts
    %in this session, as well as the duration of each burst in
    %milliseconds.
    betaburstnumber = length(betaburstlength);
```

```
    burstduration = (betaburstlength/Fs)*1000;
    meanburstduration = mean(burstduration);
    stdburstduration = std(burstduration);
    semburstduration = stdburstduration/sqrt(length(burstduration));
    betaburststartsds = ceil(betaburststarts./Fs);
    betaburststopsds = ceil(betaburststops./Fs);

    %Finally the burst start and stop indexes are used to isolate the
    %filtered and unfiltered bursts, and the peak magnitude of each burst
    %is ascertained. These are averaged, and SEM calculated to gain an
    %idea of the burst dynamics for the session.
    betabursts = cell(betaburstnumber,1);
    betaburstsunfiltered = cell(betaburstnumber,1);
    peakburstmagnitude = zeros(betaburstnumber,1);
    if betaburstnumber>0
        for indb = 1:betaburstnumber
            betabursts{indb} = betasignal(betaburststarts(indb):betaburststops(indb),:);
            betaburstsunfiltered{indb} =
signalsdsdt(betaburststarts(indb):betaburststops(indb),:);
            for indch = 1:length(channels)
                [XCorr{indb}(:,indch),lags] =
xcorr(betabursts{indb}(:,indch),betabursts{indb}(:,RefChannel),'coeff');
                [PeakXCorr(indch,indb),PeakInd] = max(XCorr{indb}(:,indch));
                PeakDelay(indch,indb) = lags(PeakInd)/(Fs/1000);
            end
        end
    else
    end

    load ColorMap7
    ColorMapBurst = interp1(1:7,ColorMap7,linspace(1,7,betaburstnumber));
    ColorMapChannel = interp1(1:7,ColorMap7,linspace(1,7,16));

    figure('Position', [50 200 1200 500])
    subplot(1,2,1)
    plot(PeakXCorr')
    xlim([0 betaburstnumber+1])
    xlabel('Burst Number')
    ylabel('Correlation')
    set(gca,'box','off');
    subplot(1,2,2)
    plot(PeakDelay')
    xlim([0 betaburstnumber+1])
    xlabel('Burst Number')
    ylabel('Delay (ms)')
    set(gca,'box','off');
    colororder(ColorMapChannel)

    %Stores all data of interest as a non-scalar structure, making it easy
    %to look at and compare data from different sessions.
    %First the parameters and settings.
    BXCData(ind0).Session = session;
    BXCData(ind0).Parameters = params;
    BXCData(ind0).Parameters.MinimumBurstDurationms = minbetaburstdurationms;
    BXCData(ind0).Parameters.BurstThreshold = burststdthreshold;
    %Then Burst Data
    BXCData(ind0).NumberOfBetaBursts = betaburstnumber;
    if betaburstnumber>0
```

```
        BXCData(ind0).BurstStarts = betaburststarts;
        BXCData(ind0).BurstStops = betaburststops;
        BXCData(ind0).BurstLength = betaburstlength;
        BXCData(ind0).BurstDuration = burstduration;
        BXCData(ind0).BetaBursts = betabursts;
        BXCData(ind0).BetaBurstsUnfiltered = betaburstsunfiltered;
        BXCData(ind0).PeakXCorr = PeakXCorr;
        BXCData(ind0).PeakDelay = PeakDelay;
    else
    end

    clearvars -except Folder RefChannel folder foldername subfolders sessionnames ind0
animal channelname BXCData

end

%Save the finished data structure as a .mat file for later use
BXCFolder = strcat(Folder(1:end-2),'Analysed\','BurstXCData');
mkdir(BXCFolder);
cd(BXCFolder);
save(strcat('BurstXCData','-',(animal),'-
','Channel',num2str(RefChannel),'.mat'),'BXCData');

end
```

Published with MATLAB® R2019b

9.6 Coherence Analysis - CoherenceWYW (While-You-Work)

```
function [CoherenceStructure] = CoherenceWYW(Folder,Channels)

%First selects the folder with the data, and locates all the LFP data
folder = Folder;
folder = dir(folder);
foldername = folder.folder;
subfolders = {folder.name};
subfolders = subfolders(contains(subfolders,'Day'));
subfolders = strcat(foldername,'\',subfolders);
sessionnames =
["Day1a","Day1b","Day2a","Day2b","Day3a","Day3b","Day4a","Day4b","Day5a","Day5b"];
cd(foldername);

%Starts a megaloop to analyse and cycle through each session in an animals
%folder.
for ind0 = 1:length(subfolders)

    files = dir(subfolders{ind0});
    files = files(arrayfun(@(x) ~strcmp(x.name(1),'.'),files));
    channels = {files.name};
    channels = channels(contains(channels,Channels));
    channels = strcat(subfolders{ind0},'\',channels);
    channelname = string(channels{1}(end-14:end-11));

    animalnumber = foldername(end-1:end);
    animal = strcat('Mouse',animalnumber);
    session = files.folder;
```

```
    session = session(end-4:end);

    [~,~,extension] = fileparts(channels{1});
    signals = [];

    for indch = 1:2
        if strcmp(extension,'.continuous')
            %Performs tracking, calculates speed and total distance travelled in m
            [x,y,~,speed_out,distance] =
TrackingNovelFamiliar(subfolders{ind0},1,'two');
            tsf = fillmissing(speed_out.ts,'linear');
            speed = speed_out.speed;
            %Imports the .continuous data into MatLab
            [signals(:,indch),~,info] = load_open_ephys_data_faster(channels{indch});
        elseif strcmp(extension,'.mat')
            [x,y,ts,speed_out,distance] =
TrackingNovelFamiliarSplitSession(subfolders{ind0});
            tsf = fillmissing(speed_out.ts,'linear');
            speed = speed_out.speed;
            %Imports the .continuous data into MatLab
            load(channels{indch});
            signals(:,indch) = sig;
            info.header.sampleRate = 30000;
        end
    end

    %Cuts the signals to the experiment duration ie 15minutes in this case
    ExpDurationMinutes = 15;
    Fs = info.header.sampleRate;
    ExpDurationFrames = (ExpDurationMinutes*60)*Fs;
    ExpDurationSeconds = ExpDurationMinutes*60;
    signals = signals(1:ExpDurationFrames,:);

    %Downsamples the signals and timestamps, to reduce computation time,
    %and detrends to remove any baseline fluctuations
    downsampleX = 30;
    signalsds = downsample(signals,downsampleX);
    signalsdsdt = detrend(signalsds);

    %Set the parameters for Chronux analysis
    Fs = Fs/downsampleX;
    params.Fs = Fs;
    params.pad = 2;
    params.tapers = [2 3];
    params.err = 0;
    params.trialave = 0;
    params.segave = 0;

    signal1 = signalsdsdt(:,1);
    signal2 = signalsdsdt(:,2);

    %Performs multi-taper spectral analysis, firstly, for the unbinned
    %signal (ie the whole session) then for the binned signal, for each
    %frequency band. As it is not possible to manually set the bandwidth,
    %this allows us to cut off each band at the exact start and end.
    params.fpass = [1 120];
    [CohgFull,~,~,~,~,t,fF] = cohgramc(signal1,signal2,[1 1],params);
```

```
    MeanCoh = mean(CohgFull,1);

    MeanCoh(fF>47 & fF<53) = NaN;
    MeanCoh(fF>97 & fF<103) = NaN;
    MeanCoh = fillmissing(MeanCoh,'linear');
%     params.smoothfactorlow = length(fF(fF>=3 & fF<30))/9;
%     MeanCoh(fF>=3 & fF<30) = smoothdata(MeanCoh(fF>=3 &
fF<30),'gaussian',params.smoothfactorlow);
%     params.smoothfactorhigh = length(fF(fF>=30 & fF<=120))/6;
%     MeanCoh(fF>=30 & fF<=120) = smoothdata(MeanCoh(fF>=30 &
fF<=120),'gaussian',params.smoothfactorhigh);

    fD = fF(fF>=1 & fF<5);
    fT = fF(fF>=5 & fF<12);
    fA = fF(fF>=12 & fF<20);
    fB = fF(fF>=20 & fF<30);
    fG = fF(fF>=30 & fF<=100);
    fLG = fF(fF>=30 & fF<65);
    fHG = fF(fF>=65 & fF<=120);
    MeanDelta = MeanCoh(fF>=1 & fF<5);
    MeanTheta = MeanCoh(fF>=5 & fF<12);
    MeanAlpha = MeanCoh(fF>=12 & fF<20);
    MeanBeta = MeanCoh(fF>=20 & fF<30);
    MeanGamma = MeanCoh(fF>=30 & fF<=100);
    MeanLowGamma = MeanCoh(fF>=30 & fF<65);
    MeanHighGamma = MeanCoh(fF>=65 & fF<=120);

    clearvars CohD CohT CohA CohB CohG CohLG CohHG
    clearvars FreqD FreqT FreqA FreqB FreqG FreqLG FreqHG

    %Calculates the raw power of each speed bin as the mean power in each
    %frequency band, and the freqency, as the frequency at which the power
    %is maximal.
    CohD = mean(MeanDelta);
    CohT = mean(MeanTheta);
    CohA = mean(MeanAlpha);
    CohB = mean(MeanBeta);
    CohG = mean(MeanGamma);
    CohLG = mean(MeanLowGamma);
    CohHG = mean(MeanHighGamma);

    PeakDC = max(MeanDelta,[],2);
    PeaksDC = find(MeanDelta==PeakDC);
    FreqD = median(fD(PeaksDC));
    PeakTC = max(MeanTheta,[],2);
    PeaksTC = find(MeanTheta==PeakTC);
    FreqT = median(fT(PeaksTC));
    PeakAC = max(MeanAlpha,[],2);
    PeaksAC = find(MeanAlpha==PeakAC);
    FreqA = median(fA(PeaksAC));
    PeakBC = max(MeanBeta,[],2);
    PeaksBC = find(MeanBeta==PeakBC);
    FreqB = median(fB(PeaksBC));
    PeakGC = max(MeanGamma,[],2);
    PeaksGC = find(MeanGamma==PeakGC);
    FreqG = median(fG(PeaksGC));
    PeakLGC = max(MeanLowGamma,[],2);
    PeaksLGC = find(MeanLowGamma==PeakLGC);
```

```
    FreqLG = median(fLG(PeaksLGC));
    PeakHGC = max(MeanHighGamma,[],2);
    PeaksHGC = find(MeanHighGamma==PeakHGC);
    FreqHG = median(fHG(PeaksHGC));

    %Stores all data of interest as a non-scalar structure, making it easy
    %to look at and compare data from different sessions.
    CoherenceStructure(ind0).Session = session;
    CoherenceStructure(ind0).Parameters = params;
    CoherenceStructure(ind0).fF = fF;
    CoherenceStructure(ind0).MeanCoherence = MeanCoh;
    CoherenceStructure(ind0).CohgFull = CohgFull;
    CoherenceStructure(ind0).X = x;
    CoherenceStructure(ind0).Y = y;
    CoherenceStructure(ind0).Distance = distance;
    CoherenceStructure(ind0).Speed = speed;
    CoherenceStructure(ind0).DeltaCoherence = CohD;
    CoherenceStructure(ind0).ThetaCoherence = CohT;
    CoherenceStructure(ind0).AlphaCoherence = CohA;
    CoherenceStructure(ind0).BetaCoherence = CohB;
    CoherenceStructure(ind0).GammaCoherence = CohG;
    CoherenceStructure(ind0).LowGammaCoherence = CohLG;
    CoherenceStructure(ind0).HighGammaCoherence = CohHG;
    CoherenceStructure(ind0).DeltaFrequency = FreqD;
    CoherenceStructure(ind0).ThetaFrequency = FreqT;
    CoherenceStructure(ind0).AlphaFrequency = FreqA;
    CoherenceStructure(ind0).BetaFrequency = FreqB;
    CoherenceStructure(ind0).GammaFrequency = FreqG;
    CoherenceStructure(ind0).LowGammaFrequency = FreqLG;
    CoherenceStructure(ind0).HighGammaFrequency = FreqHG;

end

%Session Analysis
MeanCoh = cell2mat({CoherenceStructure.MeanCoherence}');
NovelSpecs = MeanCoh(1:8:9,:);
FamiliarSpecs = MeanCoh([2 3 4 5 6 7 8 10],:);
MeanNovelSpec = mean(NovelSpecs);
MeanFamiliarSpec = mean(FamiliarSpecs);
NovelStd = std(NovelSpecs,0,1);
FamiliarStd = std(FamiliarSpecs,0,1);
NovelSEM = NovelStd/sqrt(size(NovelSpecs,1));
FamiliarSEM = FamiliarStd/sqrt(size(FamiliarSpecs,1));

% %Creates the mean spectrums for Novel and Familiar with SEM.
Coherence = strcat(foldername,'\','Coherence');
mkdir(Coherence);
cd(Coherence);
figure2name = strcat(animal,'-',(strcat(Channels{1},Channels{2})),'-
','CoherenceFamiliarity');
figure('Name',figure2name);
NovelSpec = shadedErrorBar(fF,MeanNovelSpec,NovelSEM);
set(NovelSpec.edge,'LineStyle','none')
NovelSpec.mainLine.LineWidth = 1.5;
NovelSpec.mainLine.Color = [1 0 0];
NovelSpec.patch.FaceColor = [0.6 0 0];
hold on;
FamiliarSpec = shadedErrorBar(fF,MeanFamiliarSpec,FamiliarSEM);
```

```
set(FamiliarSpec.edge,'LineStyle','none')
FamiliarSpec.mainLine.LineWidth = 1.5;
FamiliarSpec.mainLine.Color = [0 0 1];
FamiliarSpec.patch.FaceColor = [0 0 0.6];
alpha(0.3);
ylim([0.5 1]);
set(gca,'LineWidth',1.5);
set(gca,'FontSize',12)
xlabel('Frequency (Hz)','fontsize',14);
ylabel('Coherence','fontsize',14);
legend({'Novel','Familiar'});
legend boxoff
set(gca,'box','off');
hgsave(figure2name)

%Save the finished data structure as a .mat file for later use
CoherenceFolder = strcat(foldername(1:end-2),'Analysed\','Coherence');
mkdir(CoherenceFolder);
cd(CoherenceFolder);
save(strcat('Coherence','-',(animal),'-
',(strcat(Channels{1},Channels{2})),'.mat'),'CoherenceStructure');

end
```

Published with MATLAB® R2019b

9.7 Granger Causality Analysis - GrangerGram

```
function [GGData] = GrangerGram(Folder,Channels)

%First selects the folder with the data, and locates all the LFP data
folder = Folder;
folder = dir(folder);
foldername = folder.folder;
subfolders = {folder.name};
subfolders = subfolders(contains(subfolders,'Day'));
subfolders = strcat(foldername,'\',subfolders);
sessionnames =
["Day1a","Day1b","Day2a","Day2b","Day3a","Day3b","Day4a","Day4b","Day5a","Day5b"];
cd(foldername);

%Starts a megaloop to analyse and cycle through each session in an animals
%folder.
for ind0 = 1:length(subfolders)

    files = dir(subfolders{ind0});
    files = files(arrayfun(@(x) ~strcmp(x.name(1),'.'),files));
    channels = {files.name};
    channels = channels(contains(channels,Channels));
    channels = strcat(subfolders{ind0},'\',channels);
    channelname = string(channels{1}(end-14:end-11));

    animalnumber = foldername(end-1:end);
    animal = strcat('Mouse',animalnumber);
    session = files.folder;
    session = session(end-4:end);
```

```
    [~,~,extension] = fileparts(channels{1});
    signals = [];

    for indch = 1:length(Channels)
        if strcmp(extension,'.continuous')
            %Imports the .continuous data into MatLab
            [signals(indch,:,1),~,info] = load_open_ephys_data_faster(channels{indch});
        elseif strcmp(extension,'.mat')
            %Imports the .continuous data into MatLab
            load(channels{indch});
            signals(indch,:,1) = sig;
            info.header.sampleRate = 30000;
        end
    end

    %Cuts the signals to the experiment duration ie 15minutes in this case
    ExpDurationMinutes = 15;
    Fs = info.header.sampleRate;
    ExpDurationFrames = (ExpDurationMinutes*60)*Fs;
    ExpDurationSeconds = ExpDurationMinutes*60;
    signals = signals(:,1:ExpDurationFrames);


    %Downsamples the signals and timestamps, to reduce computation time,
    %and detrends to remove any baseline fluctuations
    downsampleX = 30;
    Fs = Fs/downsampleX;
    signals = downsample(signals',downsampleX)';

    %Parameters

    regmode   = 'OLS';  % VAR model estimation regression mode ('OLS', 'LWR' or empty
for default)
    icregmode = 'LWR';  % information criteria regression mode ('OLS', 'LWR' or empty
for default)
    morder    = 'AIC';  % model order to use ('actual', 'AIC', 'BIC' or supplied
numerical value)
    momax     = 20;     % maximum model order for model order estimation
    acmaxlags = 50000;     % maximum autocovariance lags (empty for automatic
calculation)
    tstat     = '';     % statistical test for MVGC:  'F' for Granger's F-test (default)
or 'chi2' for Geweke's chi2 test
    alpha     = 0.05;   % significance level for significance test
    mhtc      = 'FDR';  % multiple hypothesis test correction (see routine
'significance')
    fres      = [];     % frequency resolution (empty for automatic calculation)
    segsize   = 15;     % time segment size in seconds
    segsizem  = segsize/60;
    segsizef  = segsize*Fs;
    segedges = [1 segsizef:segsizef:length(signals)];
    Ggram12 = zeros(481,60);
    Ggram21 = zeros(481,60);
    Ggram = zeros(481,60);

    for indseg = 1:ExpDurationMinutes/segsizem

        signalseg = signals(:,segedges(indseg):segedges(indseg+1));
```

```
[nvars,nobs,ntrials] = size(signalseg);

% Model order estimation (<mvgc_schema.html#3 |A2|>)

% Calculate information criteria up to specified maximum model order.
[AIC,BIC,moAIC,moBIC] = tsdata_to_infocrit(signalseg,momax,icregmode,false);

% Select model order.
if strcmpi(morder,'AIC')
    morder = moAIC;
elseif strcmpi(morder,'BIC')
    morder = moBIC;
else
end

% VAR model estimation (<mvgc_schema.html#3 |A2|>)

% Estimate VAR model of selected order from data.

[A,SIG] = tsdata_to_var(signalseg,morder,regmode);

% Check for failed regression
assert(~isbad(A),'VAR estimation failed');

% NOTE: at this point we have a model and are finished with the data! - all
% subsequent calculations work from the estimated VAR parameters A and SIG.

% Autocovariance calculation (<mvgc_schema.html#3 |A5|>)

% The autocovariance sequence drives many Granger causality calculations (see
% next section). Now we calculate the autocovariance sequence G according to the
% VAR model, to as many lags as it takes to decay to below the numerical
% tolerance level, or to acmaxlags lags if specified (i.e. non-empty).

[G,info] = var_to_autocov(A,SIG,acmaxlags);

% The above routine does a LOT of error checking and issues useful diagnostics.
% If there are problems with your data (e.g. non-stationarity, colinearity,
% etc.) there's a good chance it'll show up at this point - and the diagnostics
% may supply useful information as to what went wrong. It is thus essential to
% report and check for errors here.

var_info(info,true); % report results (and bail out on error)

% Granger causality calculation: time domain  (<mvgc_schema.html#3 |A13|>)

% Calculate time-domain pairwise-conditional causalities - this just requires
% the autocovariance sequence.

F = autocov_to_pwcgc(G);

% Check for failed GC calculation

assert(~isbad(F,false),'GC calculation failed');

% Significance test using theoretical null distribution, adjusting for multiple
% hypotheses.
```

```
        pval = mvgc_pval(F,morder,nobs,ntrials,1,1,nvars-2,tstat); % take careful note
of arguments!
        sig  = significance(pval,alpha,mhtc);

        % Granger causality calculation: frequency domain  (<mvgc_schema.html#3 |A14|>)

        % Calculate spectral pairwise-conditional causalities at given frequency
        % resolution - again, this only requires the autocovariance sequence.

        f = autocov_to_spwcgc(G,fres);

        % Check for failed spectral GC calculation

        assert(~isbad(f,false),'spectral GC calculation failed');

        % Plot spectral causal graph.

        gc12 = squeeze(f(2,1,:));
        gc21 = squeeze(f(1,2,:));

        n = size(f,1);
        assert(ndims(f) == 3 && size(f,2) == n,'must be a 3-dim matrix with the first
two dims square');
        h = size(f,3);
        fres = h-1;
        faxis = sfreqs(fres,Fs)';
        fiaxis = 0:0.25:120;
        gc12i = interp1(faxis,gc12,fiaxis);
        gc21i = interp1(faxis,gc21,fiaxis);

        % Granger causality calculation: frequency domain -> time-domain
(<mvgc_schema.html#3 |A15|>)

        % Check that spectral causalities average (integrate) to time-domain
        % causalities, as they should according to theory.

        Fint = smvgc_to_mvgc(f); % integrate spectral MVGCs
        mad = maxabs(F-Fint);
        madthreshold = 1e-5;
        if mad < madthreshold
            fprintf('maximum absolute difference OK: = %.2e (<
%.2e)\n',mad,madthreshold);
        else
            fprintf(2,'WARNING: high maximum absolute difference = %e.2 (>
%.2e)\n',mad,madthreshold);
        end

        Ggram12(:,indseg) = gc12i;
        Ggram21(:,indseg) = gc21i;
        Ggram(:,indseg) = gc12i-gc21i;

    end

    GGData(ind0).Frequency = fiaxis;
    GGData(ind0).Ggram12 = Ggram12;
    GGData(ind0).Ggram21 = Ggram21;
    GGData(ind0).Ggram = Ggram;
```

```
end

%Save the finished data structure as a .mat file for later use
GCFolder = strcat(foldername(1:end-2),'Analysed\','Granger Causality');
mkdir(GCFolder);
cd(GCFolder);
save(strcat('GG','-',(animal),'-',(strcat(Channels{1},Channels{2})),'.mat'),'GGData');

end
```

Published with MATLAB® R2019b

10 Appendix 2

Beta bursting in the retrosplenial cortex is a neurophysiological correlate of environmental novelty which is disrupted in a mouse model of Alzheimer's disease.

Retrosplenial beta bursting in health and amyloidopathy

Callum Walsh, Thomas Ridler, Maria Garcia Garrido, Jonathan Witton, Andrew D. Randall, Jonathan T. Brown

Institute of Biomedical and Clinical Sciences, University of Exeter Medical School, Hatherly Laboratories, Exeter EX4 4PS, United Kingdom

Corresponding Authors: C. Walsh, cw685@exeter.ac.uk, J. T. Brown, J.T.Brown@exeter.ac.uk

Pages: 27

Figures: 6

Abstract: 221 words

Introduction: 646 words

Discussion: 1519 words

Conflict of Interest Statement

The authors declare no competing financial interests.

Acknowledgements

CFW was funded by a University of Exeter and Janssen Pharmaceutica studentship. TR was supported by an ARUK Major Project grant (ARUK-PG2017B-7) awarded to JTB and AR.

Abstract

The retrosplenial cortex (RSC) plays a significant role in spatial learning and memory, and is functionally disrupted in the early stages of Alzheimer's disease. In order to investigate neurophysiological correlates of spatial learning and memory in this region we employed *in vivo* electrophysiology in awake, behaving mice, comparing neural activity between wild-type and J20 mice, a mouse model of Alzheimer's disease-associated amyloidopathy. To determine the response of the RSC to environmental novelty local field potentials were recorded while mice explored novel and familiar recording arenas. In familiar environments we detected short, phasic bursts of beta (20-30 Hz) oscillations (beta bursts) which arose at a low but steady rate. Exposure to a novel environment rapidly initiated a dramatic increase in the rate, size and duration of beta bursts. Additionally, theta-beta cross-frequency coupling was significantly higher during novelty, and spiking of neurons in the RSC was significantly enhanced during beta bursts. Finally, aberrant beta bursting was seen in J20 mice, including increased beta bursting during novelty and familiarity, yet a loss of coupling between beta bursts and spiking activity. These findings, support the concept that beta bursting may be responsible for the activation and reactivation of neuronal ensembles underpinning the formation and maintenance of cortical representations, and that disruptions to this activity in J20 mice may underlie cognitive impairments seen in these animals.

Introduction

The retrosplenial cortex (RSC) is considered to play a critical role in spatial learning and memory. Damage to this region results in severe impairments in navigation and landmark processing (see Mitchell *et al.*, 2018 for review). There is a large body of experimental evidence suggesting the retrosplenial cortex is involved in the encoding, retrieval and consolidation of spatial and contextual memory (see Todd and Bucci, 2015 for review). Optogenetic stimulation of RSC neurons is sufficient to elicit retrieval and consolidation of contextual memories (Cowansage et al., 2014; De Sousa et al., 2019). RSC neurons encode a range of contextual information during navigation (Koike et al., 2017),

and inactivation of the RSC during impairs performance in spatial memory and contextual fear memory tasks (Czajkowski et al., 2014; Kwapis et al., 2015), suggesting the RSC is involved in the storage of spatial information. Finally, Iaria *et al.*, (2007) demonstrated that while hippocampal subregions are differentially involved in the encoding and retrieval of spatial information, the entire RSC is active during both processes. Spatial learning and memory impairments have been shown to be one of the earliest aspects of cognitive impairment in Alzheimer's disease (AD). Patients exhibit disturbances in specific spatial memory processes associated with the RSC (Laczó et al., 2009; Vann et al., 2009; Morganti et al., 2013). During the early stages of AD, the retrosplenial gyrus has been shown to exhibit regional hypometabolism (as measured by FDG-PET), and considerable atrophy (Minoshima et al., 1997; Choo et al., 2010). As such, the RSC is a region of great interest in research into the brain's function in health and AD.

Measurable correlates of brain function can have great value in fundamental neuroscience. They can aid the understanding of the complex ways in which the brain processes information and performs its many tasks, and also indicate how such functionality may be affected in disease. Similarly, these "functional biomarkers" can provide measurable benchmarks against which to test interventions which may affect or restore normal brain function (Walsh et al., 2017). Of the growing number of methodologies available for investigating brain function, *in vivo* electrophysiology remains a powerful tool with a superior temporal resolution to all others. The coordinated firing of large groups of neurons in the brain gives rise to waves of electrical activity, known as neural oscillations, which can be recorded as intracranial local field potentials (LFPs) or extracranial electroencephalograms (EEGs). It is thought that one of the roles of these oscillations in the brain is to coordinate the spiking activity of neurons, allowing computation and communication between potentially distant brain regions (Canolty et al., 2010). The temporal resolution of electrophysiology combined with the spatial specificity afforded by intracranial recordings make *in vivo* electrophysiology an invaluable tool for discovering functional correlates of brain function and disease-associated dysfunction.

In order to investigate the function of the RSC in spatial learning and memory, we recorded LFPs and multi-unit spiking activity from this region, while mice freely explored either a novel or familiar environment. To probe the effects of AD-associated amyloid pathology on RSC function we used J20 mice, a widely employed mouse model of amyloidopathy. In this manuscript, we describe short, phasic bursts of beta (20-30 Hz) oscillations, termed “beta bursts”, that occur within the RSC, while mice freely explore an environment. Beta bursting activity is significantly increased during exposure to a novel environment, and these bursts are correlated with increased neuronal spiking in the RSC. These data demonstrate that beta bursting in the RSC is a robust neurophysiological correlate of environmental novelty and may have a role in the storage and retrieval of cortical spatial representations. Finally, we observed aberrant beta bursting activity and an uncoupling of beta bursting from neuronal spiking in the RSC in J20 mice, which may disrupt its function, and underlie spatial learning and memory deficits seen in these mice (Cheng et al., 2007).

Methods

Ethics

All procedures were carried out in accordance with the UK Animal (Scientific Procedures) Act 1986 and were approved by the University of Exeter Animal Welfare and Ethical Review Body.

Animals

8 male J20 mice and 6 wild-type littermates were bred at the University of Exeter and housed on a 12 hour light/dark cycle. Access to food and water was provided ad libitum. All mice underwent surgery at between 6-8 months of age. Mice were group housed prior to surgery, and single housed post-surgery, in order to prevent damage to the surgical implants.

Surgery

Mice were unilaterally implanted with a 16 channel, single shank silicon probe (NeuroNexus Technologies, A1x16-5mm-100-177-CM16LP), in the right retrosplenial cortex (AP –2 mm, ML +0.5 mm, DV +1.75 mm, 0° Pitch). Mice were anaesthetised using isoflurane and fixed into a stereotaxic frame. A small craniotomy was drilled over the desired co-ordinate, and at least one hole was drilled in each of the major skull plates, in which miniature screws were placed to act as supports (Antrin Miniature Specialties). The probe was slowly lowered into the desired location, and fixed in place with dental cement (RelyX Unicem, 3M). The ground wire from the probe was connected to a silver wire, attached to a screw overlying the cerebellum. Throughout surgery, body temperature was monitored with a rectal probe and regulated by a feedback-controlled heat mat. Animals were kept hydrated by subcutaneous injections of Hartmann's solution once per hour of surgery (0.01 ml/g body weight).

Behaviour

After at least one week of post-surgical recovery, animals underwent a Novel/Familiar environment task, as shown in (Fig. 1). Individual mice were tethered to the recording apparatus, and placed in one of two high-sided recording arenas: one square, with black and white stripes, and one circular and lacking stripes. Both arenas each had two internal visual cues, placed on opposite sides. The animals were allowed to freely explore their environment for 15 minutes, after which, they were returned to their home cage. After 15 minutes in their home cage, the animal was returned to the same recording arena for another 15 minutes, and allowed to freely explore. Following this, the animal was returned to its home cage. This protocol was repeated at the same time of day, for 5 consecutive days, but on the fifth day, the animal was placed in the other, previously unseen arena. The order of exposure to these arenas was counterbalanced between animals. Each session can therefore be described by the experimental day, and the particular session within that day, with session A being the first, and session B being the second. Using this nomenclature, Sessions 1a and 5a were 'novel' sessions, while the remaining sessions were 'familiar' sessions. In order to reduce the stress associated with the recording process, animals were acclimatised to this process during a 10 minute test session 3 days prior to the

start of the experiment, in which the animal was tethered and recorded from while in its home cage. An added benefit of this was to familiarize the animals with this experimental procedure, thus ensuring that perceived novelty during the first experimental session was limited to the environment, and not the experience of being tethered to the recording apparatus.

Data Collection

Throughout experimental sessions, Local Field Potentials (LFPs) were recorded using an Open Ephys Acquisition board (Open Ephys), which was tethered to the probe via a headstage (RHD 16-Channel Recording Headstage, Intan Technologies), and SPI cables (Intan Technologies). LFPs on each channel were sampled at 30 kHz, while the animal's location was monitored using a pair of light-emitting diodes (LED) soldered to the headstage, and a video camera, placed directly above the arena. The location of these LEDs was tracked using Bonsai tracking software, so the location and running speed of the animal could be estimated offline.

Data Analysis

LFPs were down-sampled (Spectral Analysis: 1 kHz, Burst Detection and Phase Amplitude Coupling: 3 kHz, Multi-Unit Activity: N/A) and de-trended, in order to remove any slow linear drift of the baseline that may occur across the session. The Chronux toolbox (Mitra and Bokil, 2008, http://chronux.org/) was used for the mtspecgramc function, as well as a number of built in MATLAB functions. All scripts used in this study were written in house, and are now publicly available (see Software Accessibility). All LFP analyses were performed for a single channel in the dysgranular and a separate single channel in granular RSC, except for multi-unit activity analysis, in which all channels in each region were used. The location of each channel was estimated from post-hoc histology.

Power Spectra

Multi-taper spectral analysis was performed using the mtspecgramc function from the Chronux Toolbox, with a time-bandwidth product of 2 (1 second x 2 Hz), and 3 tapers, resulting in some

smoothing of resulting spectra. The mtspecgramc function generates a power spectrogram by generating multiple power spectra for short segments of time series data, using a moving window; in our case with the window size of 1 s with no overlap. These spectrograms were then logged to the base 10, and multiplied by 10, in order to correct for the tendency of spectral power to decrease with a 1/f distribution. These individual spectra were averaged, resulting in a single mean power spectrum for the entire session, or for the first minute of each session, as specified in the results. Spectral data from 48 to 52 Hz, which incorporates line frequency noise (50 Hz), were removed, and linearly interpolated. The power of each frequency band was calculated as the mean power in each of the following frequency ranges: delta (1-5 Hz), theta (5-12 Hz), alpha (12-20 Hz), beta (20-30 Hz), low gamma (30-65 Hz), and high gamma (65-120 Hz).

Beta Burst Detection

The data were band-pass filtered between 20-30 Hz, to isolate the beta frequency band. The amplitude and phase of this beta signal were calculated as the real and imaginary components of the Hilbert transform, respectively. The amplitude was z-scored, in order to give the instantaneous standard deviation of the beta signal amplitude from the mean. Epochs of the signal where this z-score exceeded 2 standard deviations from the mean amplitude were detected, as were the corresponding “edges” of these epochs, where the signal magnitude surpassed 1 standard deviation either side of the 2 standard deviation threshold. This was done in order to capture the time-course of these high beta amplitude epochs. Events that did not persist longer than a minimum duration of 150 ms (i.e. fewer than 3 oscillation cycles) were discarded. Furthermore, due to the sensitivity of this method to large, amplitude noise artefacts, any event whose peak amplitude exceeded three scaled median absolute deviations from the median of the events detected in that session were discarded as well. These remaining events were then considered beta-bursts. The duration and peak magnitude of each burst was calculated, as well as the distribution and total number of bursts in the session.

Phase-Amplitude Coupling

To calculate phase-amplitude coupling, and create a comodulogram, modulation index was calculated individually for each pair of phase and amplitude frequencies. Modulation index was calculated as described by Canolty *et al.* (2006), with modification and vectorisation of some of the MATLAB code, for phase frequencies in bins of 0.25 Hz from 2 to 12 Hz, and for amplitude frequencies in bins of 2 Hz from 10 to 100 Hz. For each pair, local field potentials were filtered in the phase frequency band and the amplitude frequency band, after which the instantaneous phase and amplitude of each filtered signal was calculated, respectively, using the Hilbert transform. Subsequently, modulation index (MI) was calculated, but in order to attempt to reduce the possibility of spurious coupling, this was normalised through the use of 10 surrogates, created by time shifting the data by a random amount (between 1 and 59 seconds). In order to smooth the resulting comodulograms, the data matrix was linearly interpolated in both dimensions by a factor of 2.

Multi-Unit Activity

Due to the distance between adjacent channels on the recording probe (100 μm) it is highly unlikely that activity of a single neuron would appear on multiple channels. Consequently, each channel was treated as an individual multi-unit. Raw local field potentials were first common average-referenced, using a mean of the signals from all other 15 channels, then filtered in the range of 500-14250 Hz, in order to isolate the spiking frequency band. Spikes were detected as peaks that crossed a threshold given by the median of the absolute voltage values of the signal, multiplied by 0.6745, as suggested by Quiroga, Nadasdy and Ben-Shaul (2004), and had a minimum separation of 0.5 ms. In order to investigate multi-unit activity during beta bursts, bursts were detected as previously mentioned, and bursts that occurred within a second of each other were discarded, to remove overlapping segments. A single peri-burst histogram was created for each channel by taking the total number of spikes in 20 ms time bins from 1 second before burst onset, to 1 second after, for all beta bursts. Each histogram was then normalised by dividing the count in each bin by the total number of spikes in all bins,

averaged across all channels within the region, and then across all sessions, smoothed with a 100 ms moving mean filter, and z-scored with respect to the baseline epoch (1 second pre-burst).

Software Accessibility

All code has been made publicly available at https://github.com/cfle/In-Vivo-Ephys-Code. This code is freely accessible for viewing, or use. If using any of this code in a paper, please, cite this paper as well as the GitHub repository (https://github.com/cfle/In-Vivo-Ephys-Code).

Statistics

All statistical analysis was performed in MATLAB. Fourteen mice in total were used in this study, 6 wild-type and 8 J20, with each mouse undergoing a total of ten recording sessions (5 days, 2 sessions per day). Unfortunately, the local field potential data from Day 3 session 1 (i.e. session 3a) was corrupted for a single wild-type mouse, and therefore data for this mouse from this session was omitted from all figure making and statistics. Therefore the n numbers for all statistics are (wild-type: n = 6 (except from Day3a where n = 5), J20: n = 8). All statistics, unless stated otherwise, were performed using a two-way ANOVA, with genotype (wild-type/J20) and novelty (novel/familiar) as factors. It is important to note that due to the experimental design of our Novel/Familiar environment task, there were multiple novel and familiar sessions (2 novel, and 8 familiar). All sessions were either classified as novel or familiar and analysed accordingly. Following a significant main effect or interaction, Bonferroni-corrected multiple comparisons was performed, to investigate pairwise differences between different levels of either factor.

Histology

Upon completion of the experiments, mice were killed using an overdose of sodium pentobarbital (Euthetal), and an isolated stimulator was used to produce electrolytic lesions at the recording sites. Mice were then transcardially perfused with 40% paraformaldehyde (PFA), and their brains were extracted and stored in PFA for 24 hours, after which they were transferred to phosphate-buffered

saline (PBS) prior to sectioning. Brains were sliced into 100 µm sagittal sections using a vibratome (Leica), and stained with Cresyl Violet. Digital pictures were taken using QCapture Pro 7 software (Qimaging), and electrode sites were verified by comparing the lesion sites in these photographs to The Allen Mouse Brain Atlas (https://mouse.brain-map.org/static/atlas). Due to the high channel count of these probes, as well as their linear geometry, it was possible to account for small differences in the depth of each probe by selecting channels of similar depths across different probes. This resulted in reduced variability between animals in a range of neurophysiological measures.

Results

To investigate neurophysiological correlates of spatial learning and memory in the retrosplenial cortex (RSC), local field potentials were recorded from across the entire dorsoventral axis of the RSC, while animals underwent a novel/familiar environment task. The RSC is made up of two distinct subdivisions: dysgranular (RSCdg), and granular (RSCg). While these regions are strongly interconnected, the neuroanatomical connectivity of these regions has been shown to differ (van Groen and Wyss, 1992; Van Groen and Wyss, 2003a, 2003b), therefore it is possible that the functional neurophysiology may vary as well, especially during a behavioural paradigm such as this, where spatial learning and memory processes may be stimulated. Due to the anatomical positioning of these subdivisions in rodents, it is possible to record from both RSCdg and RSCg at once, using a single, vertical silicon probe (Figure 1C). Therefore for this study, our analyses were performed for both subdivisions. We found very little difference between the electrophysiological activities seen in the two subregions. Furthermore, any changes seen in J20 mice were generally common to both subregions, with marginally greater effects in RSCg. For the sake of conciseness, we have decided to only show the data from RSCg in this paper.

Spectral Analysis

Local field potentials from RSCg show a clear peak in theta frequency band (5-12 Hz) throughout recording sessions (Fig. 2a). In order to investigate any changes in oscillatory activity in RSCg during

environmental novelty, power spectral analysis was performed on the entire 15 minutes of each session. These power spectra were averaged across novel and familiar sessions for wild-type and J20 mice. Beta and low gamma power were significantly higher overall during novel sessions (Main Effect Novelty - Beta: $F(1,135) = 16.4, p = 8.8e\text{-}5$; Low Gamma: $F(1,135) = 10.8$, $p = 0.001$, 2-way ANOVA). Furthermore, while alpha, beta, low gamma and high gamma power were significantly higher overall in J20 mice (Main Effect Genotype – Alpha: $F(1,135) = 21.4$, $p = 8.46e\text{-}6$; Beta: $F(1,135) = 253$, $p = 1.01e\text{-}32$; Low Gamma: $F(1,135) = 43.3$, $p = 9.56e\text{-}10$; High Gamma: $F(1,135) = 14.4$, $p = 2.3e\text{-}4$, 2-way ANOVA), delta and theta power were significantly lower (Main Effect Genotype - Delta: $F(1,135) = 9.23$, $p = 0.03$; Theta: $F(1,135) = 7.92$, $p = 0.006$, 2-way ANOVA). Beta power was significantly higher during novel sessions in J20 (Nov: 17.7 ± 0.18; Fam: 16.9 ± 0.09; $p = 4.7e\text{-}4$) but not wild-type mice (Nov: 15.1 ± 0.21; Fam: 14.7 ± 0.1; $p = 0.4$). Upon closer inspection of power spectrograms (Fig. 2a), it was clear that spectral activity changed within novel sessions. Power in the alpha, beta and low gamma range appeared to be higher in the first minute of the session and diminish over time. As exemplified in (Fig. 2c), transient epochs of high power in the 12-40 Hz range are seen throughout the early stages of the session. By performing the same power spectral analysis as before on only the first minute of each session, clear differences appeared between novel and familiar sessions. Alpha, beta and low gamma power were significantly higher overall during novel sessions (Main Effect Novelty - Alpha: ($F(1,135) = 5.73$, $p = 0.02$; Beta: $F(1,135) = 75.7$, $p = 1.01e\text{-}14$; Low Gamma: $F(1,135) = 35.6$, $p = 1.98e\text{-}8$, 2-way ANOVA). Furthermore, alpha, beta, low gamma and high gamma power were significantly higher overall in J20 mice (Main Effect Genotype - Alpha: $F(1,135) = 40.9$, $p = 2.47e\text{-}9$; Beta: $F(1,135) = 132$, $p = 1.1e\text{-}21$; Low Gamma: $F(1,135) = 14.1$, $p = 2.52e\text{-}4$; High Gamma: $F(1,135) = 12.9$, $p = 4.65e\text{-}4$, 2-way ANOVA). Beta and low gamma power were significantly higher in wild type (Beta: Nov: 17 ± 0.28; Fam: 15 ± 0.14; $p = 5.47e\text{-}8$; Low Gamma: Nov: 14.6 ± 0.26; Fam: 13.2 ± 0.13; $p = 3.62e\text{-}5$) and J20 mice (Beta: Nov: 19.2 ± 0.25; Fam: 17.5 ± 0.12; $p = 3.59e\text{-}8$; Low Gamma: Nov: 15.1 ± 0.23; Fam: 14.2 ± 0.11; $p = 0.002$).

Across these time series, increased beta power occured in brief, discrete epochs, as shown in the expanded power spectrogram in (Fig. 3a). This can also be seen clearly in beta-filtered local field potentials, where these periods of high beta amplitude intersperse an otherwise very low amplitude oscillation. In order to understand the timescale and frequency domains of these events, wavelet analysis was used to investigate them further. As exemplified in (Fig. 3C), these individual events were short in duration, and peaked in the 20-30 Hz, beta band.

Beta Bursting Activity

In order to investigate this phasic beta activity in more depth, an algorithm was written to detect and analyse these "beta bursts"; the basis of this algorithm is illustrated in (Fig. 4a). Once all putative bursts have been detected, the duration and magnitude of these beta bursts was calculated (Fig. 4a). With these transient epochs of high beta power now classified as discrete beta bursts, it is possible to compare this beta activity between sessions. Overall, there were significantly more beta bursts detected during novel sessions compared to familiar sessions (Main Effect Novelty - $F(1,135) = 74$, $p = 1.73e\text{-}14$, 2-way ANOVA). As shown in (Fig. 4b), there were significantly more beta bursts detected during novelty, for wild-type (Nov: 33.7 ± 2.42; Fam: 21.4 ± 1.22; $p = 7.59e\text{-}5$) and J20 mice (Nov: 56.3 ± 2.1; Fam: 37.8 ± 1.05; $p = 4.83e\text{-}12$). Furthermore, on average the number of beta bursts detected was significantly higher in J20 mice (Main Effect Genotype – $F(1,135) = 118$, $p = 3.45e\text{-}20$, 2-way ANOVA). Furthermore, it is possible to investigate the distribution of beta bursts within sessions. As shown in (Fig. 4c), during familiar sessions the rate of beta busting was reasonably steady, as indicated by the linear relationship between time and burst number shown in the cumulative frequency plot, for both wild-type and J20 mice. During novel sessions, however, there was a high rate of beta bursting during the first 1-3 minutes of the session, which gradually decreased over time to a steady rate. The rate of beta bursting was significantly higher in J20 mice during familiar sessions, and during the initial and final part of novel sessions.

The features of these beta bursts may also vary depending on novelty and genotype. Burst magnitude was significantly higher overall during novel sessions (Main Effect Novelty - $F(1,135) = 48.7$, $p = 1.21e\text{-}10$, 2-way ANOVA). Furthermore, burst magnitude was significantly higher overall in J20 mice (Main Effect Genotype - $F(1,135) = 137$, $p = 2.97e\text{-}22$, 2-way ANOVA). As shown in (Fig, 4d), beta bursts were significantly larger in magnitude during novelty, for both wild-type (Nov: 106 ± 2.96; Fam: 90.4 ± 1.5; $p = 2.88e\text{-}5$) and J20 mice (Nov: 131 ± 2.57; Fam: 117 ± 1.28; $p = 5.16e\text{-}6$). There was also a significant interaction between the effects of genotype and novelty on beta burst duration ($F(1,135) = 8.04$, $p = 0.005$, 2-way ANOVA). As shown in (Fig.4e), beta bursts were significantly longer in duration during novel sessions for both wild-type (Nov: 192 ± 2.1; Fam: 176 ± 1.1; $p = 3.32e\text{-}9$) and J20 mice (Nov: 189 ± 1.8; Fam: 182 ± 0.9; $p = 0.005$).

Phase-amplitude Coupling

As elegantly shown by van Ede *et al.* (2018), continuous oscillations may appear as phasic burst events if their amplitude varies greatly over time. The amplitude of high frequency oscillations such as gamma may be modulated by the phase of low frequency oscillations such as theta (Canolty et al., 2006). This interaction is generally thought to allow slow, large amplitude oscillations to coordinate faster, small amplitude local oscillations. For this reason, it was of interest for us to investigate whether the amplitude of beta oscillations was coupled to the phase of theta oscillations, an increase in which may underlie the increased beta bursting activity seen during novelty. As shown in (Fig. 5a), phase-amplitude coupling efficacy was calculated for a range of phase and amplitude frequencies, and the effect of novelty and genotype determined. The strength of phase-amplitude coupling was quantified for theta-alpha, theta-beta and theta-gamma coupling for each session (Fig. 5b). There were significant interactions between the effects of genotype and novelty for theta-alpha coupling ($F(1,135) = 12.8$, $p = 4.72e\text{-}4$) and theta-beta coupling ($F(1,135) = 17.7$, $p = 4.73e\text{-}5$, 2-way ANOVA). Theta-alpha coupling was significantly higher in novel sessions for wild-type (Nov: 2.59 ± 0.15; Fam: 1.6 ± 0.07; $p = 2.4e\text{-}7$) but not J20 mice (Nov: 2.2 ± 0.13; Fam: 1.98 ± 0.06; $p = 1$). Theta-beta coupling was also

significantly higher in novel sessions for wild-type (Nov: 1.65 ± 0.08; Fam: 1.16 ± 0.04; p = 1.04e-6) but not J20 mice (Nov: 1.23 ± 0.07; Fam: 1.23 ± 0.03; p = 1). There were no significant effects of novelty on theta-gamma coupling, but theta-gamma coupling was lower on average, in J20 mice (Main Effect Genotype – F(1,135) = 19.7, p = 1.87e-5). It is important to note that in order to focus on the most physiologically and behaviourally relevant part of the session, this analysis was performed for the first minute of each session. When the same analysis was performed on the last minute of each session, there was no effect of novelty on coupling in any band for either genotype (data not shown).

Spiking Activity

In order to determine whether beta bursting was associated with a change in neuronal firing, multi-unit activity was investigated. Due to the linear geometry of the silicon probes, and the 100 µm distance between channels, it was not possible to reliably identify single unit activity, as activity from a single neuron was unlikely to appear on multiple channels, limiting spatiotemporal clustering methods such as those enabled by tetrodes or higher density silicon probes. Therefore, spikes appearing on a single channel could be from one or more nearby neurons. This, however, does mean that it is possible to treat each individual probe channel as a single multi-unit, to facilitate investigation of the relationship between neuronal spiking activity and beta bursting. As shown in the left panel of (Fig. 6a), individual spike waveforms can be readily discerned, and these spike waveforms are similar in wild-type (black) and J20 (green) mice. Furthermore, there was a trend towards higher multi-unit firing rate in J20 mice compared to wild-type mice (WT: 12.9 Hz ± 4.9; J20: 33.5 Hz ± 7.3; t(12) = -2.18, p = 0.05; unpaired t-test, Fig. 6a, right). The average beta amplitude during beta bursts is shown in (Fig. 6b), averaged across all bursts with non-overlapping time segments. Beta bursts in both genotypes are associated with a brief, monophasic increase in beta amplitude that lasts no more than 200 ms on average. Finally, (Fig. 6c) shows peri-event time histograms for spike rate during beta bursts, as a Z score from the pre-burst baseline (left of the dotted line). In order to investigate statistically significant changes in spike rate during bursts, the maximum z scored spike rate was

318 determined at the peak of beta amplitude (approximately 100 ms after burst onset), for each animal,
319 and compared to the mean pre-burst spike rate (0 due to z scoring of spike rate to baseline) using a
320 one-sample t-test. Beta bursting in the RSCg of wild-type mice was associated with a significant
321 increase in spike rate during beta bursts (Z-scored spike rate from baseline: 2.24 ± 0.46, $t(5) = 4.86$, $p = 0.005$, one-sample t-test; Figure 6c, left). Conversely there was no significant increase in spike rate
322 = 0.005, one-sample t-test; Figure 6c, left). Conversely there was no significant increase in spike rate
323 during beta bursts in J20 mice (Z-scored spike rate from baseline: 0.78 ± 0.39, $t(7) = 1.98$, $p = 0.09$,
324 one-sample t-test; Figure 6c, right). The difference between spike rate during beta bursts in wild-type
325 and J20 mice, as determined by a two-sample t-test, was significant ($t(12) = 2.4$, $p = 0.03$, two-sample
326 t-test). These data indicate that beta bursts are closely coupled to neuronal spiking in RSCg in wild-
327 type mice, and that this relationship is effectively uncoupled in J20 mice.

328 ## Discussion

329 In this study we attempted to identify neurophysiological correlates of environmental novelty in the
330 mouse retrosplenial cortex (RSC), and investigate how these may be affected by amyloid pathology.
331 We observed phasic increases in the amplitude of beta frequency neuronal oscillations, termed beta
332 bursts, which occurred more frequently and with larger amplitude during novelty, and were positively
333 correlated with neuronal spiking. A number of aberrant neurophysiological changes were seen in the
334 RSC in J20 mice. Alpha, beta and low gamma power were significantly increased, and increases in beta
335 bursting activity were seen during both novelty and familiarity. Beta bursts were more frequent, and
336 larger in magnitude, yet the coupling of beta bursts to spiking activity was lost, suggesting a functional
337 uncoupling of beta bursting with local neuronal activity. Finally, theta-beta phase-amplitude coupling
338 was also disrupted, resulting in a loss of an effect of novelty on this activity. These results together
339 indicate that beta bursting activity is a neurophysiological correlate of environmental novelty in the
340 RSC, which is disrupted in J20 mice.

341 Numerous studies have noted changes in beta activity in a range of brain regions, during a variety of
342 behaviours (see Spitzer and Haegens, 2017 for review). It is important to note that due to variability

between groups in the naming and frequency ranges of neural oscillation frequency bands, cross-study comparison is often complicated. What we have referred to as beta, has previously been called upper beta (Spitzer and Haegens, 2017), beta2 (França et al., 2014), or slow gamma (Carr et al., 2012; Remondes and Wilson, 2015). For the sake of clarity, references to beta oscillations in this paper refer to the 20-30 Hz frequency range. Others have noticed similar novelty-induced beta oscillations in the hippocampus: Berke *et al.* (2008) reported a large increase in beta power that appeared when mice explored a novel environment, which persisted for around a minute, before returning to a lower level. The authors concluded that these oscillations may be a "dynamic state that facilitates the formation of unique contextual representations." As shown in Igarashi *et al.* (2014), coherent 20-40 Hz oscillatory activity increased between the hippocampus and lateral entorhinal cortex during odour discrimination, and coincided with the development of odour-specific neural representations in these regions. Work by França *et al.* (2014) demonstrated that beta power was also transiently enhanced in the hippocampus during exploration of novel objects, but not previously experienced familiar items. Furthermore, they found that administration of an amnestic agent, namely haloperidol, resulted in a similar increased beta activity upon re-exposure to previously encountered objects, suggesting they had been "forgotten" and were therefore novel again. This further reinforces the idea that hippocampal beta activity is related to novelty, and extends the previous work by demonstrating that hippocampal-dependent novel object recognition can also elicit beta oscillations. Subsequently, França, Borgegius and Cohen (2020) investigated novelty-associated beta bursting in a larger hippocampal novelty circuit, by simultaneously recording from hippocampus, prefrontal cortex and parietal cortex during environmental and object novelty. Novelty-associated increases in beta power were seen in the prefrontal cortex during environmental novelty, and authors demonstrated significant phase-amplitude coupling of delta and theta to beta oscillations, which were increased in novelty. Similarly, in the RSC we see strong coupling between theta phase and beta amplitude, which is significantly higher during novelty, but only in wild-type mice. Others have noted theta-beta PAC in humans as well, both in the hippocampus during a working memory task (Axmacher et al., 2010), and

in the inferior temporal cortex during object novelty (Daume et al., 2017). Interestingly, the studies mentioned above tend to view beta activity as continuous oscillations, rather than discrete events. This is despite Berke *et al.* (2008) noting that beta appears as pulses, and a brief mention of burst detection and characterisation by França *et al.* (2014). As demonstrated in this study, novelty-associated beta oscillations in the RSC conform well to a model of discrete bursts, where their rate, magnitude and duration can vary depending on environmental novelty. Due to the use of averaging across trials or analysis spanning long temporal segments, the phasic nature of transient oscillatory events can be easily lost. Furthermore, in the somatosensory cortex, beta synchronicity appears in short events in both mice and humans; the features of which, such as duration and frequency range, are highly conserved across tasks and species (Shin et al., 2017).

Beta oscillations have long been associated with motor activity and sensory processing, and a large body of work has also noted changes in beta activity in a range of brain regions during other cognitive tasks (see Engel and Fries, 2010 for review). This gave rise to the hypothesis that the unifying function of beta oscillatory activity in these different regions was the maintenance of the "status-quo", be it the current motor state, sensory stimulus or cognitive set (Engel and Fries, 2010). This theory would suggest that, beta activity would be decreased during novelty, and increased during familiarity. As we have shown, this is not the case. While steady and persistent beta bursting during familiarity may support the maintenance of the contextual "status-quo", in this case the environment, this theory does not reconcile the significant increases in beta activity that occur during novelty.

Many groups have previously shown that information may be rapidly represented and stored in the RSC (Cowansage et al., 2014; Czajkowski et al., 2014; Koike et al., 2017; Vedder et al., 2017). Beta oscillations have also been shown to carry a variety of different forms of contextual information in a range of brain regions, and phasic increases in beta power during working memory maintenance may represent reactivation of encoded information (Spitzer and Haegens, 2017). Supporting this is a study in which the authors employed transcranial magnetic stimulation to activate a currently unattended

memory, as shown by an increase in content-specific beta activity (Rose et al., 2016). The theory put forth by Spitzer and Haegens (2017), is that beta oscillations can activate and reactivate neuronal ensembles to create and recall cortical representations. This theory is consistent with the data shown in this study: high beta bursting activity during perceived novelty activates neurons in the RSC, which may encode content about the novel environment, and subsequent beta bursting may continuously reactivate these ensembles, further consolidating or altering this representation. Recent breakthroughs in real-time burst detection and neurofeedback have made it possible to artificially induce beta bursts in awake behaving animals, creating the possibility of testing this hypothesis directly (Karvat et al., 2020).

A number of neurophysiological changes were seen in the RSC in J20 mice. Increases in alpha, beta and gamma power are indicative of a hyperexcitability phenotype, which has been previously noted in this strain (Palop et al., 2007; Palop and Mucke, 2009). Increases in beta bursting rate and burst magnitude were also notable. Finally, and most importantly, beta bursting activity was effectively uncoupled from neuronal spiking in J20 mice, potentially impairing the ability to form neuronal ensembles that encode and store information in the RSC. At the age point used, amyloid pathology in J20 mice is thought to be predominantly located in the hippocampus in this model, although, amyloid pathology seems to develop in the RSC to a much greater extent than other cortical regions, especially in RSCg (Whitesell et al., 2019). Hyperexcitability of cortical neurons in a mouse model of amyloid pathology was more prevalent in neurones proximal to amyloid plaques (Busche et al., 2008), and inhibitory interneuron dysfunction in J20 mice has been shown to lead to cortical network hypersynchrony and spontaneous epileptiform discharges (Verret et al., 2012). The hippocampus projects directly to RSCg, and indirectly, via the subiculum, to RSCdg (van Groen and Wyss, 1992; Van Groen and Wyss, 2003a, 2003b), so network dysfunction in RSC may be explained by its high levels of amyloid pathology or its anatomical connectivity with an increasingly dysfunctional hippocampus (Palop et al., 2007).

These findings demonstrate a novel form of Alzheimer's disease (AD) related cortical dysfunction, which may underlie or exacerbate cognitive dysfunction seen in these mice, and in people with AD. Erroneous attribution of novelty to familiar environments, could cause memory impairments, and result in wandering and confusion. Interestingly, aberrant beta bursting has long been associated with another progressive neurodegenerative disease, Parkinson's disease. Increased beta oscillatory activity in the basal ganglia and cortex are associated with motor impairments in Parkinson's disease (for review see Brittain, Sharott and Brown, 2014), and administration of levodopa has been shown to improve motor function and reduce beta oscillations (Brown et al., 2001). The loss of coupling between beta bursting and neuronal spiking seen in J20 mice suggest that attenuating bursting without restoring this coupling may be ineffective in AD. Furthermore, the dysfunction in novelty-associated beta bursting identified in this study may be a useful functional biomarker of AD-related amyloidopathy, which could be used to measure the neurophysiological effectiveness of possible disease modifying therapeutics.

In conclusion, phasic bursts of beta oscillations may be a functional means of activating neural ensembles to form, and subsequently reactivate cortical representations. Network dysfunction in J20 mice results in aberrant beta bursting and an uncoupling of beta bursting from spiking, which may underlie cognitive impairments in these mice.

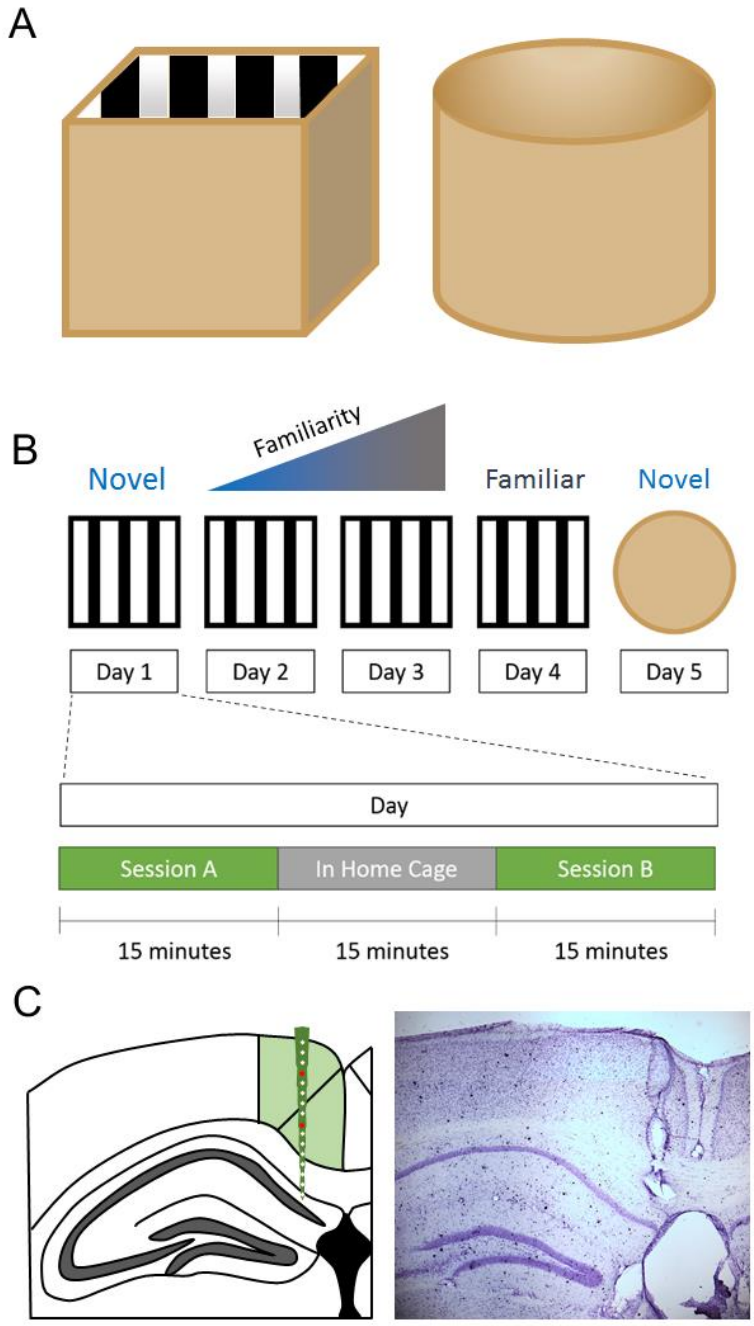

Figure 1. Experimental Design A. Diagrams of the recording arenas used for this study. Both are roughly equal sized, one is square, with black and white stripes along the walls and floor (left) and the other is cylindrical with plain brown floor and walls. B. Experimental procedure for the novel/familiar environment task. A mouse is placed in one of the recording arenas for two 15 minute sessions, referred to as sessions A and B, with a 15 minute break in their home cage between the two sessions. This is repeated in the same arena for 4 consecutive days, after which the arena is switched for the 5th and final day. C. Single shank, 16 channel silicon probe electrodes were implanted in the retrosplenial cortex (green), so that they spanned the dysgranular (upper green section) and granular (lower green section) subregions. In order to verify the location of the electrodes, electrolytic lesions were made prior to perfusion, and slices were histologically prepared using Cresyl Violet stain. An example is shown (right).

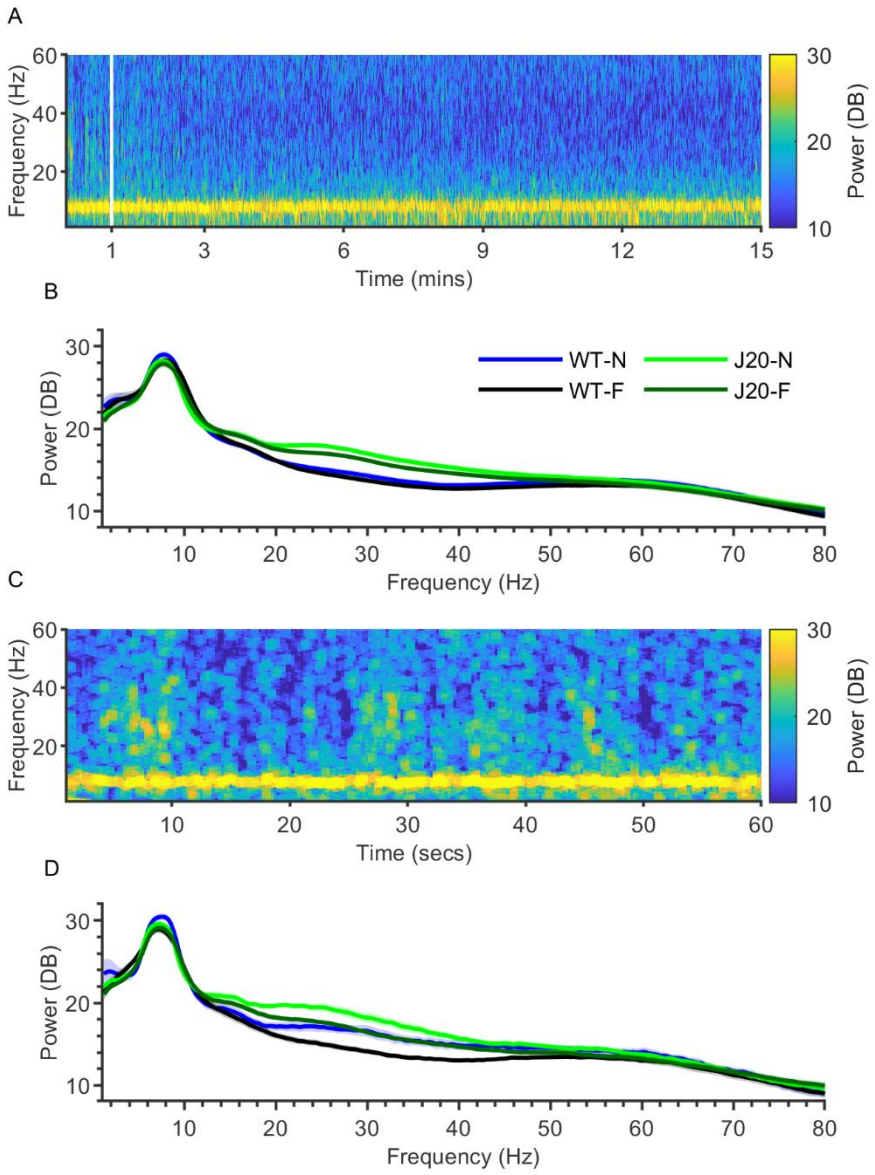

Figure 2. Beta (20-30 Hz) power is significantly higher during novelty in the granular retrosplenial cortex in wild-type and J20 mice. A. Example power spectrogram for an entire novel session in a wild-type mouse. B. Average power spectra for the entire 15 minutes of all novel and familiar sessions, for wild-type and J20 mice. Beta power was significantly higher during novelty in J20 ($p = 4.7e-4$) but not wild-type mice. When compared to WT power in the alpha, beta, low gamma and high gamma bands were significantly higher overall in J20 mice ($p = 8.46e-6$, $p = 1.01e-32$, $p = 9.56e-10$, $2.3e-4$ respectively), whereas power in the delta and theta band were significantly lower ($p = 0.03$, $p = 0.006$ respectively). C. Example power spectrogram shown in A, expanded to show the first 60 seconds of the session. Short epochs of increased power in the 20-40 Hz range can be seen. D. Average power spectra for the first minute of all novel and familiar sessions, for wild-type and J20 mice. Beta and low-gamma power were significantly higher during novelty, for both wild-type ($p = 5.47e-8$, $p = 3.62e-5$ respectively) and J20 mice ($p = 3.59e-8$, $p = 0.002$ respectively). Alpha, beta, low gamma and high gamma power were significantly higher overall in J20 mice ($p = 2.47e-9$, $p = 1.1e-21$, $p = 2.52e-4$, $p = 4.65e-4$ respectively). (Data shown as mean ± SEM, WT: $n = 6$, J20: $n = 8$).

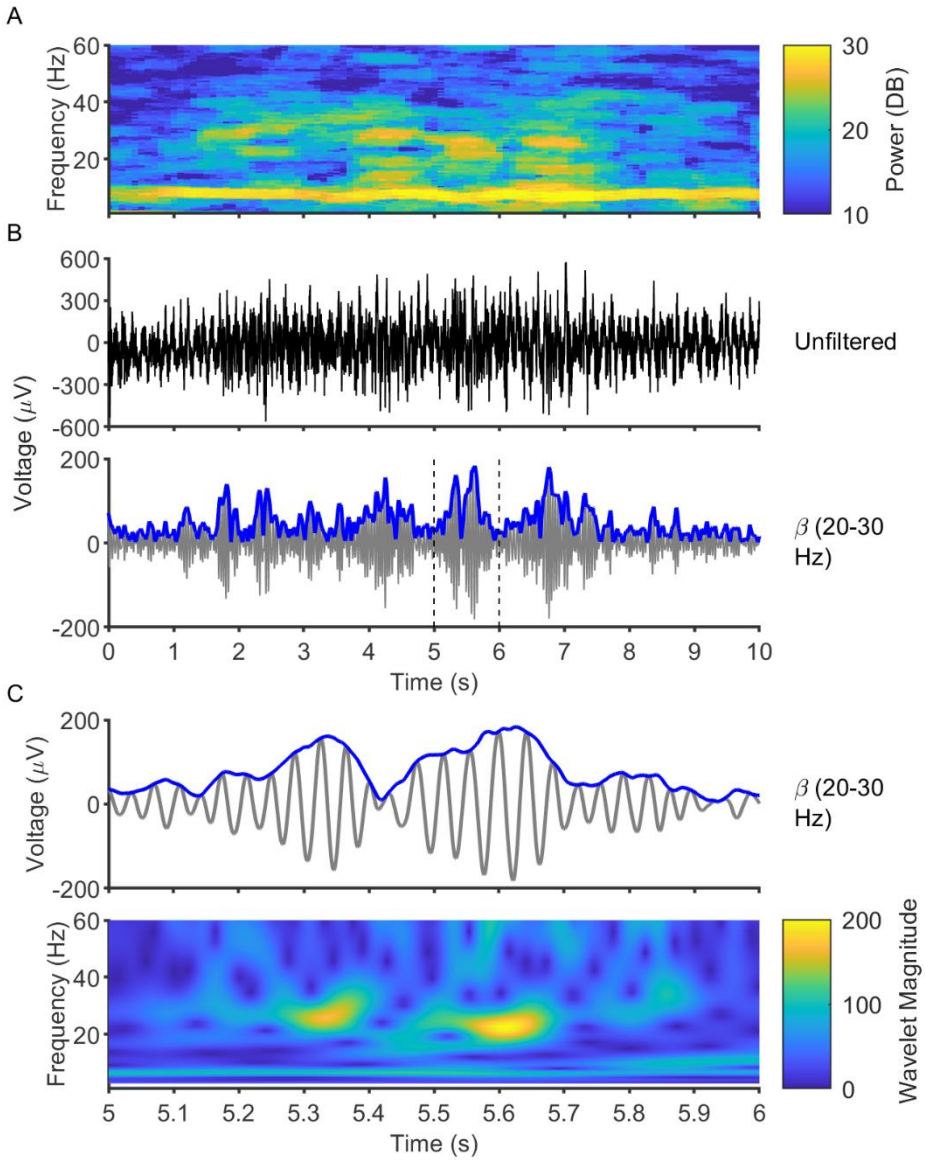

Figure 3. Retrosplenial local field potentials are marked by short, phasic increases in beta power, referred to as beta bursts. A. Example power spectrogram showing transient increases in beta power. B. Local field potentials of data shown in A, both unfiltered (top), and filtered in the beta band (bottom), with the envelope amplitude in blue for clarity. The beta-filtered local field potential shows clear epochs of high beta amplitude, which intersperse a low amplitude continuous beta oscillation. C. Expanded trace of the dashed area in shown in B (top), and a continuous wavelet spectrogram of this time series (bottom). Due to the high temporal resolution of wavelet-based methods, these periods of high beta amplitude can be seen to be brief in duration, only lasting around 100-200ms.

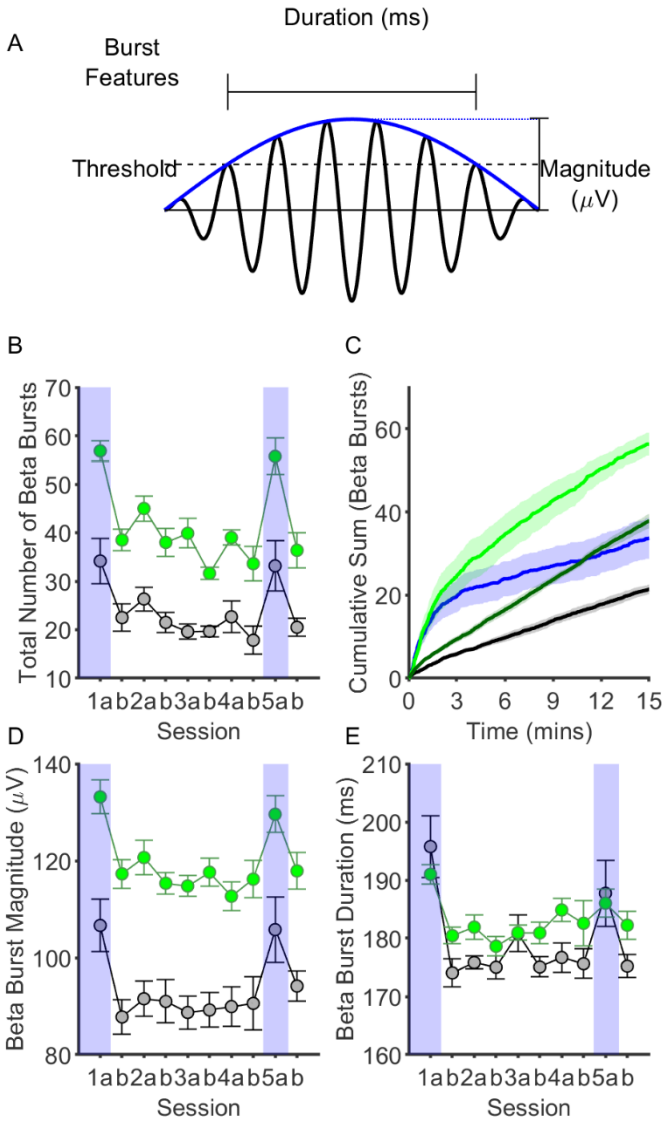

Figure 4. Beta bursting activity in the granular retrosplenial cortex (RSCg) is highly associated with novelty, and dysregulated in J20 mice. A. Diagram illustrating how beta bursts were detected, as well as how the magnitude and duration of these events were calculated. B. Graph showing the average number of beta bursts detected in RSCg in each session, for wild-type (black) and J20 mice (green). Novel sessions Day1a and Day5a are highlighted in blue for clarity. There were significantly more beta bursts in novel sessions as compared to familiar sessions, for both wild-type ($p = 7.59e-5$) and J20 mice ($p = 4.83e-12$). C. Cumulative frequency graphs of number of bursts detected in novel and familiar sessions, for wild-type and J20 mice, showing the time course of bursting activity within sessions. While beta bursting occurred monotonically during familiar sessions, during the first 2-3 minutes of a novel session, beta bursting was substantially increased. D. Graph showing the average magnitude of beta bursts in RSCg in each session, for wild-type and J20 mice. Beta bursts were significantly larger in magnitude in novel sessions, for wild-type ($p = 2.88e-5$) and J20 mice ($p = 5.16e-6$). Beta bursts were also, on average, significantly larger in magnitude in J20 mice ($p = 2.97e-22$). E. Graph showing the average duration of beta bursts in RSCg in each session, for wild-type and J20 mice. Beta bursts were significantly longer in duration in novel sessions, for wild-type ($p = 3.32e-9$) and J20 mice ($p = 0.005$). (Data shown as mean ± SEM, WT: n = 6, J20: n = 8).

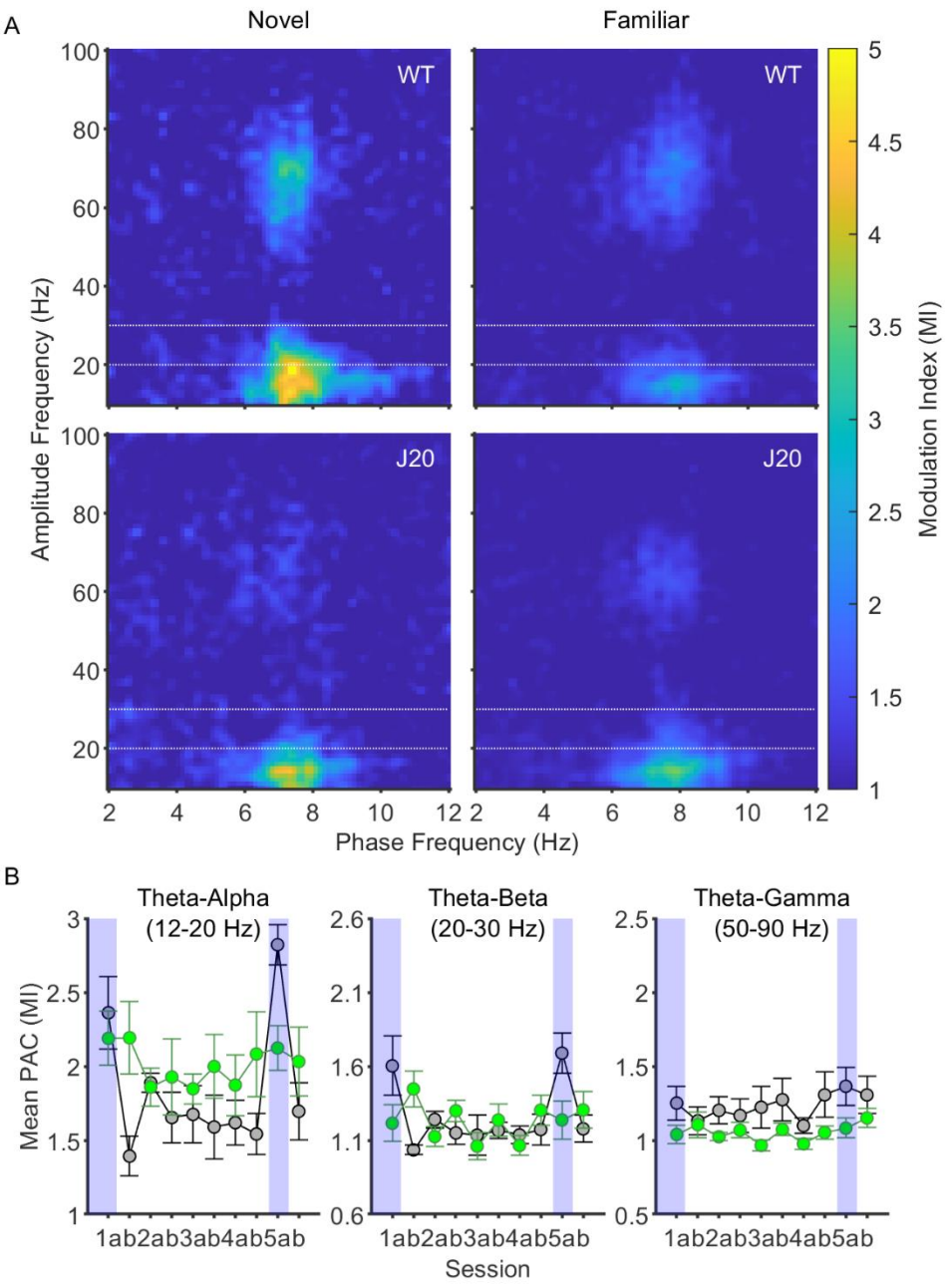

Figure 5. Theta-alpha and theta-beta phase-amplitude coupling are increased during novelty in the granular retrosplenial cortex (RSCg). A. Average comodulograms showing the strength of cross-frequency phase-amplitude coupling in RSCg during the first minute of novel and familiar sessions, for wild-type and J20 mice. Note the presence of three peaks in the first comodulogram, in the theta-alpha, theta-beta and theta-gamma ranges (the boundaries of which are denoted by the dotted lines). B. Average MI in the theta-alpha (left), theta-beta (center) and theta-gamma ranges (right), for each session, for wild-type (black) and J20 mice (green). Novel sessions Day1a and Day5a are highlighted in blue for clarity. Theta-alpha and theta-beta coupling were significantly higher in novel sessions for wild-type mice ($p = 2.4e-7$, $p = 1.04e-6$ respectively), but not J20 mice. (Data shown as mean ± SEM, WT: n = 6, J20: n = 8).

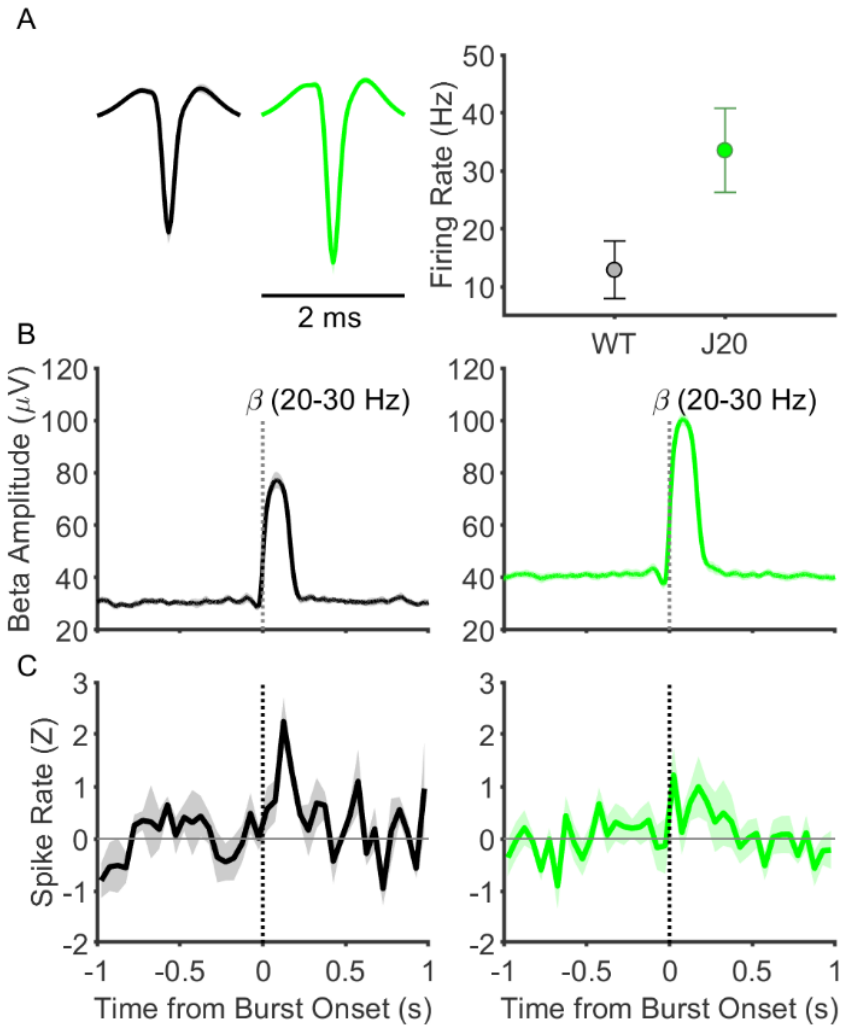

Figure 6. Spiking activity in RSCg is coupled to beta bursting in wild-type mice, but disrupted in J20 mice. A. Average spike waveforms for multi-unit activity in wild-type (black) and J20 (green) mice (left) and graph of average firing rate for detected multi-units across all sessions (right). There was a trend towards increased multi-unit firing rate in J20 mice compared to wild-type mice ($p = 0.052$, unpaired t-test). B. Graphs showing beta amplitude over time for beta bursts, time locked to the onset of the burst (dotted line), and averaged across all detected bursts, for wild-type mice (left) and J20 mice (right). Beta bursting was associated with a monophasic increase in beta amplitude that returns to baseline after around 250 ms. C. Peri-event histograms showing multi-unit activity spike rate during beta bursts, for wild-type (left) and J20 mice (right). Data is shown as Z score from baseline (pre-burst epoch), and averaged across all beta bursts with non-overlapping time segments. Dotted vertical line denotes the burst onset, while the solid horizontal line is shown to indicate the baseline of zero. Spike rate significantly increased during bursts in wild-type mice ($p = 0.005$), but not in J20 mice ($p = 0.09$).

436 ## References

437 Axmacher N, Henseler MM, Jensen O, Weinreich I, Elger CE, Fell J (2010) Cross-frequency coupling
438 supports multi-item working memory in the human hippocampus. Proc Natl Acad Sci
439 107:3228–3233.

440 Berke JD, Hetrick V, Breck J, Greene RW (2008) Transient 23-30 Hz oscillations in mouse
441 hippocampus during exploration of novel environments. Hippocampus 18:519–529.

442 Brittain JS, Sharott A, Brown P (2014) The highs and lows of beta activity in cortico-basal ganglia
443 loops. Eur J Neurosci 39:1951–1959.

444 Brown P, Oliviero A, Mazzone P, Insola A, Tonali P, Di Lazzaro V (2001) Dopamine dependency of
445 oscillations between subthalamic nucleus and pallidum in Parkinson's disease. J Neurosci
446 21:1033–1038.

447 Busche MA, Eichhoff G, Adelsberger H, Abramowski D, Wiederhold KH, Haass C, Staufenbiel M,
448 Konnerth A, Garaschuk O (2008) Clusters of hyperactive neurons near amyloid plaques in a
449 mouse model of Alzheimer's disease. Science (80-) 321:1686–1689.

450 Canolty RT, Edwards E, Dalal SS, Soltani M, Nagarajan SS, Kirsch HE, Berger MS, Barbare NM, Knight
451 RT (2006) High gamma power is phase-locked to theta oscillations in human neocortex. Science
452 (80-) 313:1626–1628.

453 Canolty RT, Ganguly K, Kennerley SW, Cadieu CF, Koepsell K, Wallis JD, Carmena JM (2010)
454 Oscillatory phase coupling coordinates anatomically dispersed functional cell assemblies. Proc
455 Natl Acad Sci U S A 107:17356–17361.

456 Carr MF, Karlsson MP, Frank LM (2012) Transient Slow Gamma Synchrony Underlies Hippocampal
457 Memory Replay. Neuron 75:700–713.

458 Cheng IH, Scearce-Levie K, Legleiter J, Palop JJ, Gerstein H, Bien-Ly N, Puoliväli J, Lesné S, Ashe KH,

Muchowski PJ, Mucke L (2007) Accelerating amyloid-β fibrillization reduces oligomer levels and functional deficits in Alzheimer disease mouse models. J Biol Chem 282:23818–23828.

Choo IH, Lee DY, Oh JS, Lee JS, Lee DS, Song IC, Youn JC, Kim SG, Kim KW, Jhoo JH, Woo JI (2010) Posterior cingulate cortex atrophy and regional cingulum disruption in mild cognitive impairment and Alzheimer's disease. Neurobiol Aging 31:772–779.

Cowansage KK, Shuman T, Dillingham BC, Chang A, Golshani P, Mayford M (2014) Direct Reactivation of a Coherent Neocortical Memory of Context. Neuron 84:432–441.

Czajkowski R, Jayaprakash B, Wiltgen B, Rogerson T, Guzman-Karlsson MC, Barth AL, Trachtenberg JT, Silva AJ (2014) Encoding and storage of spatial information in the retrosplenial cortex. Proc Natl Acad Sci 111:8661–8666.

Daume J, Gruber T, Engel AK, Friese U (2017) Phase-amplitude coupling and long-range phase synchronization reveal frontotemporal interactions during visual working memory. J Neurosci 37:313–322.

De Sousa AF, Cowansage KK, Zutshi I, Cardozo LM, Yoo EJ, Leutgeb S, Mayford M (2019) Optogenetic reactivation of memory ensembles in the retrosplenial cortex induces systems consolidation. Proc Natl Acad Sci U S A 116:8576–8581.

Engel AK, Fries P (2010) Beta-band oscillations-signalling the status quo? Curr Opin Neurobiol 20:156–165.

França ASC, Borgegius N, Cohen MX (2020) Beta2 oscillations in the hippocampal-cortical novelty detection circuit. Cold Spring Harbor Laboratory.

França ASC, do Nascimento GC, Lopes-dos-Santos V, Muratori L, Ribeiro S, Lobão-Soares B, Tort ABL (2014) Beta2 oscillations (23-30 Hz) in the mouse hippocampus during novel object recognition. Eur J Neurosci 40:3693–3703.

Iaria G, Chen JK, Guariglia C, Ptito A, Petrides M (2007) Retrosplenial and hippocampal brain regions in human navigation: Complementary functional contributions to the formation and use of cognitive maps. Eur J Neurosci 25:890–899.

Igarashi KM, Lu L, Colgin LL, Moser MB, Moser EI (2014) Coordination of entorhinal-hippocampal ensemble activity during associative learning. Nature 510:143–147.

Karvat G, Schneider A, Alyahyay M, Steenbergen F, Tangermann M, Diester I (2020) Real-time detection of neural oscillation bursts allows behaviourally relevant neurofeedback. Commun Biol 3.

Koike BDV, Farias KS, Billwiller F, Almeida-Filho D, Libourel PA, Tiran-Cappello A, Parmentier R, Blanco W, Ribeiro S, Luppi PH, Queiroz CM (2017) Electrophysiological evidence that the retrosplenial cortex displays a strong and specific activation phased with hippocampal theta during paradoxical (REM) sleep. J Neurosci 37:8003–8013.

Kwapis JL, Jarome TJ, Lee JL, Helmstetter FJ (2015) The retrosplenial cortex is involved in the formation of memory for context and trace fear conditioning. Neurobiol Learn Mem 123:110–116.

Laczó J, Vlček K, Vyhnálek M, Vajnerová O, Ort M, Holmerová I, Tolar M, Andel R, Bojar M, Hort J (2009) Spatial navigation testing discriminates two types of amnestic mild cognitive impairment. 202:252–259.

Minoshima S, Giordani B, Berent S, Frey KA, Foster NL, Kuhl DE (1997) Metabolic reduction in the posterior cingulate cortex in very early Alzheimer's disease. Ann Neurol 42:85–94.

Mitchell AS, Czajkowski R, Zhang N, Jeffery K, Nelson AJD (2018) Retrosplenial cortex and its role in spatial cognition. Brain Neurosci Adv 2:239821281875709.

Mitra P, Bokil H (2008) Observed Brain Dynamics.

505 Morganti F, Stefanini S, Riva G (2013) From allo- to egocentric spatial ability in early Alzheimer's
506 disease: A study with virtual reality spatial tasks. Cogn Neurosci 4:171–180.

507 Palop JJ, Chin J, Roberson ED, Wang J, Thwin MT, Bien-Ly N, Yoo J, Ho KO, Yu GQ, Kreitzer A,
508 Finkbeiner S, Noebels JL, Mucke L (2007) Aberrant Excitatory Neuronal Activity and
509 Compensatory Remodeling of Inhibitory Hippocampal Circuits in Mouse Models of Alzheimer's
510 Disease. Neuron 55:697–711.

511 Palop JJ, Mucke L (2009) Epilepsy and cognitive impairments in alzheimer disease. Arch Neurol
512 66:435–440.

513 Quiroga RQ, Nadasdy Z, Ben-Shaul Y (2004) Unsupervised spike detection and sorting with wavelets
514 and superparamagnetic clustering. Neural Comput 16:1661–1687.

515 Remondes M, Wilson MA (2015) Slow-γ Rhythms Coordinate Cingulate Cortical Responses to
516 Hippocampal Sharp-Wave Ripples during Wakefulness. Cell Rep 13:1327–1335.

517 Rose NS, LaRocque JJ, Riggall AC, Gosseries O, Starrett MJ, Meyering EE, Postle BR (2016)
518 Reactivation of latent working memories with transcranial magnetic stimulation. Science (80-)
519 354:1136–1139.

520 Shin H, Law R, Tsutsui S, Moore CI, Jones SR (2017) The rate of transient beta frequency events
521 predicts behavior across tasks and species. Elife 6.

522 Spitzer B, Haegens S (2017) Beyond the status quo: A role for beta oscillations in endogenous
523 content (RE)activation. eNeuro 4.

524 Todd TP, Bucci DJ (2015) Retrosplenial Cortex and Long-Term Memory: Molecules to Behavior.
525 Neural Plast 2015.

526 van Ede F, Quinn AJ, Woolrich MW, Nobre AC (2018) Neural Oscillations: Sustained Rhythms or
527 Transient Burst-Events? Trends Neurosci 41:415–417.

van Groen T, Wyss JM (1992) Connections of the retrosplenial dysgranular cortex in the rat. J Comp Neurol 315:200–216.

Van Groen T, Wyss JM (2003a) Connections of the retrosplenial granular b cortex in the rat. J Comp Neurol 463:249–263.

Van Groen T, Wyss JM (2003b) Connections of the retrosplenial granular b cortex in the rat. J Comp Neurol 463:249–263.

Vann SD, Aggleton JP, Maguire EA (2009) What does the retrosplenial cortex do? Nat Rev Neurosci 10:792–802.

Vedder LC, Miller AMP, Harrison MB, Smith DM (2017) Retrosplenial Cortical Neurons Encode Navigational Cues, Trajectories and Reward Locations during Goal Directed Navigation. Cereb Cortex 27:3713–3723.

Verret L, Mann EO, Hang GB, Barth AMI, Cobos I, Ho K, Devidze N, Masliah E, Kreitzer AC, Mody I, Mucke L, Palop JJ (2012) Inhibitory interneuron deficit links altered network activity and cognitive dysfunction in alzheimer model. Cell 149:708–721.

Walsh C, Drinkenburg WHIM, Ahnaou A (2017) Neurophysiological assessment of neural network plasticity and connectivity: Progress towards early functional biomarkers for disease interception therapies in Alzheimer's disease. Neurosci Biobehav Rev 73.

Whitesell JD, Buckley AR, Knox JE, Kuan L, Graddis N, Pelos A, Mukora A, Wakeman W, Bohn P, Ho A, Hirokawa KE, Harris JA (2019) Whole brain imaging reveals distinct spatial patterns of amyloid beta deposition in three mouse models of Alzheimer's disease. J Comp Neurol 527:2122–2145.